



MINISTÉRIO DA CIÊNCIA, TECNOLOGIA, INOVAÇÕES E COMUNICAÇÕES  
**INSTITUTO NACIONAL DE PESQUISAS ESPACIAIS**

sid.inpe.br/mtc-m21c/2019/05.15.19.00-TDI

**IMPACT OF THE REMOVAL OF AMAZON FOREST  
ON THE SOUTHERN HEMISPHERE STORM TRACKS  
IN FUTURE CLIMATE**

Philipp Edson Dias da Silva

Doctorate Thesis of the Graduate  
Course in Terrestrial System  
Science, guided by Drs. Mariane  
Mendes Coutinho, and Kevin Ivan  
Hodges, approved in May 29, 2019.

URL of the original document:

<<http://urlib.net/8JMKD3MGP3W34R/3TAJ4MB>>

INPE  
São José dos Campos  
2019

**PUBLISHED BY:**

Instituto Nacional de Pesquisas Espaciais - INPE  
Gabinete do Diretor (GBDIR)  
Serviço de Informação e Documentação (SESID)  
CEP 12.227-010  
São José dos Campos - SP - Brasil  
Tel.:(012) 3208-6923/7348  
E-mail: pubtc@inpe.br

**BOARD OF PUBLISHING AND PRESERVATION OF INPE  
INTELLECTUAL PRODUCTION - CEPPII (PORTARIA Nº  
176/2018/SEI-INPE):****Chairperson:**

Dra. Marley Cavalcante de Lima Moscati - Centro de Previsão de Tempo e Estudos Climáticos (CGCPT)

**Members:**

Dra. Carina Barros Mello - Coordenação de Laboratórios Associados (COCTE)

Dr. Alisson Dal Lago - Coordenação-Geral de Ciências Espaciais e Atmosféricas (CGCEA)

Dr. Evandro Albiach Branco - Centro de Ciência do Sistema Terrestre (COCST)

Dr. Evandro Marconi Rocco - Coordenação-Geral de Engenharia e Tecnologia Espacial (CGETE)

Dr. Hermann Johann Heinrich Kux - Coordenação-Geral de Observação da Terra (CGOBT)

Dra. Ieda Del Arco Sanches - Conselho de Pós-Graduação - (CPG)

Silvia Castro Marcelino - Serviço de Informação e Documentação (SESID)

**DIGITAL LIBRARY:**

Dr. Gerald Jean Francis Banon

Clayton Martins Pereira - Serviço de Informação e Documentação (SESID)

**DOCUMENT REVIEW:**

Simone Angélica Del Ducca Barbedo - Serviço de Informação e Documentação (SESID)

André Luis Dias Fernandes - Serviço de Informação e Documentação (SESID)

**ELECTRONIC EDITING:**

Ivone Martins - Serviço de Informação e Documentação (SESID)

Cauê Silva Fróes - Serviço de Informação e Documentação (SESID)



MINISTÉRIO DA CIÊNCIA, TECNOLOGIA, INOVAÇÕES E COMUNICAÇÕES  
**INSTITUTO NACIONAL DE PESQUISAS ESPACIAIS**

sid.inpe.br/mtc-m21c/2019/05.15.19.00-TDI

**IMPACT OF THE REMOVAL OF AMAZON FOREST  
ON THE SOUTHERN HEMISPHERE STORM TRACKS  
IN FUTURE CLIMATE**

Philipp Edson Dias da Silva

Doctorate Thesis of the Graduate  
Course in Terrestrial System  
Science, guided by Drs. Mariane  
Mendes Coutinho, and Kevin Ivan  
Hodges, approved in May 29, 2019.

URL of the original document:

<<http://urlib.net/8JMKD3MGP3W34R/3TAJ4MB>>

INPE  
São José dos Campos  
2019

Cataloging in Publication Data

---

Silva, Philipp Edson Dias da.

Si38i      Impact of the removal of Amazon Forest on the Southern Hemisphere Storm Tracks in future climate / Philipp Edson Dias da Silva. – São José dos Campos : INPE, 2019.

xxx + 242 p. ; (sid.inpe.br/mtc-m21c/2019/05.15.19.00-TDI)

Thesis (Doctorate in Terrestrial System Science) – Instituto Nacional de Pesquisas Espaciais, São José dos Campos, 2019.

Guiding : Drs. Mariane Mendes Coutinho, and Kevin Ivan Hodges.

1. Storm track. 2. Land Use change. 3. HadGEM2-ES. 4. Climate Change. 5. Projections. I.Title.

CDU 551.583:332.3(81)

---



Esta obra foi licenciada sob uma Licença [Creative Commons Atribuição-NãoComercial 3.0 Não Adaptada](https://creativecommons.org/licenses/by-nc/3.0/).

This work is licensed under a [Creative Commons Attribution-NonCommercial 3.0 Unported License](https://creativecommons.org/licenses/by-nc/3.0/).

Aluno (a): *Philipp Edson Dias da Silva*

Título: "IMPACT OF THE REMOVAL OF AMAZON FOREST ON THE SOUTHERN HEMISPHERE STORM TRACKS IN FUTURE CLIMATE"

Aprovado (a) pela Banca Examinadora em cumprimento ao requisito exigido para obtenção do Título de *Doutor(a)* em *Ciência do Sistema Terrestre*

Dr. Celso von Randow



---

Presidente / INPE / São José dos Campos - SP

Participação por Video - Conferência

Aprovado  Reprovado

Dra. Mariane Mendes Coutinho



---

Orientador(a) / IAE/DCTA / São José dos Campos - SP

Participação por Video - Conferência

Aprovado  Reprovado

Dr. Kevin Ivan Hodges



---

Orientador(a) / UoR / Reino Unido - UK

Participação por Video - Conferência

Aprovado  Reprovado

Dr. Nelson Jesus Ferreira



---

Membro da Banca / INPE / São José dos Campos - SP

Participação por Video - Conferência

Aprovado  Reprovado

Este trabalho foi aprovado por:

maioria simples

unanimidade

São José dos Campos, 29 de maio de 2019

Aprovado (a) pela Banca Examinadora  
em cumprimento ao requisito exigido para  
obtenção do Título de *Doutor(a)* em  
*Ciência do Sistema Terrestre*

Dr. Roger Rodrigues Torres

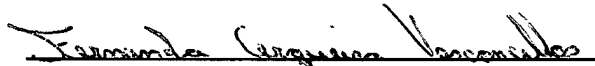


Convidado(a) / UNIFEI / Itajubá - MG

( ) Participação por Vídeo - Conferência

Aprovado ( ) Reprovado

Dra. Fernanda Cerqueira Vasconcellos



Convidado(a) / UFRJ / Rio de Janeiro - RJ

( ) Participação por Vídeo - Conferência

Aprovado ( ) Reprovado

**Este trabalho foi aprovado por:**

( ) maioria simples

( ) unanimidade

**São José dos Campos, 29 de maio de 2019**

*“You think you have a limit, so you try to touch this limit. Something happens, and you can run a bit stronger. Thanks to the power of your mind, your determination, your instinct, and the experience as well, you can fly very high”.*

AYRTON SENNA DA SILVA



*In dedication to my wife Mariana Pallotta and my family  
for patience, comprehension and love.*



## ACKNOWLEDGEMENTS

First, I would like to show my warm thank to Dr. Mariane Coutinho and Dr. Kevin Hodges who supported me at every bit with huge amount of help and guidance, and without whom it was impossible to accomplish the end task. I can't thank you enough for everything you've done.

I would like to pay special thankfulness and appreciation to the persons below who made my research successful and assisted me at every point to cherish my goal:

My wife, Dr. Mariana Pallotta, who helped in all moments at every point during my thesis.

My Mom Lina and Dad Edson, brothers and family members, without whom I was nothing. Thank you so much for your support morally and emotionally.

Dr. Nelson Ferreira, Senior Researcher at INPE, whose reminders and constant motivation always encouraged me in academic life.

Dr. Fernando Ii, whose help me a lot during my period at England.

Friends for helping along the way, in particular to Jójhy Sakuragi, Lincoln Alves, Thiago Veloso, Henri Pinheiro, Ricardo Imai, Majory Imai, Lucas Suzuki, Marcelo Schneider, Leticia Covre, Marcos Covre and Rafael Scremin, for all great times and conversations that encouraged me during this important period of my life.

Friends from England, in particular thanks go to: Manuel, Davi, Flávia, Rachel, Hèlene, Francesca, Ludo, Luca, Michael, Thomas Eldridge, Thomas Hall, William, Veronica and Ying, for all great moments and valuable help of all provided during my PhD Sandwich. I also acknowledge the friends from class of 2014, for all good times that turned my research a success. Friends from ECMWF, in particular thanks go to: Nils, Lorian, Cristiano, Eduardo, Andras and Luke for all the fun football games.

The physical support of National Institute for Space Research (INPE - Brazil) and University of Reading (England - UK) and the technical contribution of PGCST (Angela and Mariana) is highly appreciable. Without their support and assistance, it was impossible to reach the goal. This study was financed in part by the Coordenação de Aperfeiçoamento de Pessoal de Nível Superior - Brasil (CAPES) - Finance Code 001.



## ABSTRACT

The Amazon Forest is one of the most important ecosystems in the world. The forest plays an important role in the global hydrological system. Deforestation affects evapotranspiration, latent heat, river discharges and, consequently, the global climate. In this study, HadGEM2-ES Earth system model is used to investigate the impact of the removal of the Amazon Forest on the storm tracks (STs) of the (HS) in future climate. Firstly, the recent past climate simulated by HadGEM2-ES is compared to that indicated by the Era-Interim reanalysis to evaluate the performance of the model in representing the STs in the HS. Next, experiments with and without the Amazon Forest under two future scenarios Representative Concentration Pathways (RCP) are contrasted against controlled experiments to examine possible future changes in STs. The HadGEM2-ES has the ability to simulate well the mid-latitude storm tracks in the Southern Hemisphere (SH). However, the model tends to represent the austral winter ST position with an equatorward bias and a zonal bias in the spiral towards the pole. The main differences are found during the austral winter and spring, with large track density biases over the Indian Ocean indicating a poor representation of the ST in this specific region. This seems to be related to two factors. First, the large negative genesis biases over South America, Antarctic Peninsula and the Antarctic coast. Second, the model resolution and the representation of the Andes Mountains in South America. The model generally underestimates the extratropical cyclone intensity, which in part is related to low spatial resolution. The future projections show a consistent shift of the STs in the HS toward the pole, and this is reduced when the Amazon Forest is removed. The storm track changes under the RCP4.5 are larger than in the RCP8.5 scenario. In general, the changes are strongly associated with the mean large-scale circulation, although the change in the Amazon Forest is on a regional-scale. When the Amazon Forest is removed, the temperature decreases over northern South America. There is also a decrease in the total number of cyclones in the SH and a slight shift of cyclone intensity distributions toward stronger storms.

Palavras-chave: Storm Track. Land Use Change. HadGEM2-ES. Climate Change. Projections.



# IMPACTO DA REMOÇÃO DA FLORESTA AMAZÔNICA NAS STORM TRACKS DO HEMISFÉRIO SUL NO CLIMA FUTURO

## RESUMO

A Floresta Amazônica é um dos ecossistemas mais importantes do mundo. A floresta desempenha um papel importante no sistema hidrológico global. O desmatamento afeta a evapotranspiração, o calor latente, as descargas dos rios e, conseqüentemente, o clima global. Neste estudo, o modelo do sistema terrestre HadGEM2-ES é utilizado para investigar o impacto da remoção da Floresta Amazônica nas storm tracks (STs) do (HS) no clima futuro. Primeiramente, o clima passado recente simulado pelo HadGEM2-ES é comparado ao indicado pela reanálise Era-Interim para avaliar o desempenho do modelo em representar as STs no HS. Em seguida, experimentos com e sem a Floresta Amazônica, sob dois cenários futuros Representative Concentration Pathways (RCP), são contrastados com experimentos controlados para examinar possíveis mudanças futuras nas STs. O HadGEM2-ES tem a capacidade de simular bem as STs nas latitudes médias no Hemisfério Sul. No entanto, o modelo tende a representar a posição dos ciclones durante o inverno austral com um viés para o equador e apresenta um viés zonal na espiral em direção ao pólo. As principais diferenças foram encontradas durante o inverno e a primavera austral, com grandes vieses de densidade de trajetórias sobre o Oceano Índico, indicando uma representação pobre das STs nessa região específica. Isso parece estar relacionado a dois fatores. Primeiro, o grande viés negativo na gênese sobre a América do Sul, a Península Antártica e a costa da Antártica. Em segundo lugar, a resolução do modelo e a representação da Cordilheira dos Andes na América do Sul. O modelo geralmente subestima a intensidade dos ciclones extratropicais, o que em parte está relacionado à baixa resolução espacial. As projeções futuras mostram um desvio consistente das STs do HS em direção ao polo, e isso é reduzido quando a Floresta Amazônica é removida. As mudanças nas STs sob o cenário RCP4.5 são maiores do que as do RCP8.5. Em geral, as mudanças estão fortemente associadas à circulação média em grande escala, embora a mudança na Floresta Amazônica esteja em escala regional. Quando a Floresta Amazônica é removida, a temperatura diminui no norte da América do Sul. Ocorre, também, uma diminuição no número total de ciclones no HS e um leve deslocamento das distribuições de intensidade de ciclones em direção a tempestades mais fortes.

Keywords: Storm Tracks. Mudanças de Uso da Terra. HadGEM2-ES. Mudanças Climáticas. Projeções.



## LIST OF FIGURES

	<u>Page</u>
2.1 Upper-tropospheric seasonal cycle of the SH storm track. . . . .	13
2.2 Main drivers of climate change. . . . .	16
2.3 Climate feedbacks and timescales. . . . .	18
2.4 Land use as cropland and use of grassland across the RCPs. . . . .	23
2.5 Land use change until the end of each RCP scenario in 2100. . . . .	24
3.1 Methodology overview. . . . .	29
3.2 Processes included in the HadGEM2 model family. . . . .	31
3.3 Representation of each component and interactions in the HadGEM2-ES model. . . . .	34
3.4 Schematic coupling between TRIFFID and HadGEM2-ES. . . . .	36
3.5 Representation of the disturbed fraction in the HadGEM2-ES model. . .	37
3.6 Historical and projected total anthropogenic RF ( $Wm^{-2}$ ) relative to the pre-industrial between 1950 and 2010. . . . .	40
3.7 Land use change for the experiments with and without Amazon Forest. .	42
3.8 Regions for zonal mean of the large-scale fields. . . . .	52
4.1 Extratropical cyclone track climatology for the period 1979-2005. . . . .	55
4.2 Genesis density climatology for the period 1979-2005. . . . .	56
4.3 Lysis density climatology for the period 1979-2005. . . . .	57
4.4 Mean growth decay rate climatology for the period 1979-2005. . . . .	58
4.5 Extratropical cyclone track density biases for the period 1979-2005. . . .	63
4.6 Genesis density biases for the period 1979-2005. . . . .	64
4.7 Lysis density biases for the period 1979-2005. . . . .	65
4.8 Mean growth decay rate biases for the period 1979-2005. . . . .	66
4.9 Orography height biases over Southern Hemisphere. . . . .	67
4.10 Maximum Eady growth rate climatology for the period 1979-2005. . . . .	71
4.11 Maximum Eady growth rate biases at 250hPa for the period 1979-2005. .	75
4.12 Maximum Eady growth rate biases at 850hPa for the period 1979-2005. .	76
4.13 Zonal mean temperature and zonal wind in winter for the period 1979-2005.	77
4.14 Geopotential height anomaly biases at 500hPa for the period 1979-2005.	78
4.15 Sea surface temperature biases for the period 1979-2005. . . . .	79
4.16 Precipitation biases for the period 1979-2005. . . . .	80
4.17 Zonal mean temperature and zonal wind in summer for the period 1979- 2005. . . . .	84
4.18 Zonal mean temperature and zonal wind in spring for the period 1979-2005.	88

4.19	Zonal mean temperature and zonal wind in autumn for the period 1979-2005. . . . .	89
4.20	Maximum intensity distribution for JJA during the period 1979-2005. . .	92
4.21	Maximum intensity distribution for DJF during the period 1979-2005. . .	93
4.22	Maximum intensity distribution for SON during the period 1979-2005. . .	94
4.23	Maximum intensity distribution for MAM during the period 1979-2005. . .	95
4.24	Meridional moisture and kinetic energy biases for period 1979-2005. . . .	98
4.25	Track density biases at 250hPa for the period 1979-2005. . . . .	99
5.1	Storm track density changes in JJA for the period 2070-2099. . . . .	106
5.2	Genesis density changes in JJA for the period 2070-2099. . . . .	107
5.3	Lysis density changes in JJA for the period 2070-2099. . . . .	108
5.4	Mean growth decay rate changes in JJA for the period 2070-2099. . . . .	109
5.5	Storm track density changes in DJF for the period 2070-2099. . . . .	112
5.6	Genesis density changes in DJF for the period 2070-2099. . . . .	113
5.7	Lysis density changes in DJF for the period 2070-2099. . . . .	114
5.8	Mean growth decay rate changes in DJF for the period 2070-2099. . . . .	115
5.9	Storm track density changes in SON for the period 2070-2099. . . . .	118
5.10	Genesis density changes in SON for the period 2070-2099. . . . .	119
5.11	Lysis density changes in SON for the period 2070-2099. . . . .	120
5.12	Mean growth decay rate changes in SON for the period 2070-2099. . . . .	121
5.13	Storm track density changes in MAM for the period 2070-2099. . . . .	122
5.14	Genesis density changes in MAM for the period 2070-2099. . . . .	123
5.15	Lysis density changes in MAM for the period 2070-2099. . . . .	124
5.16	Mean growth decay rate changes in MAM for the period 2070-2099. . . .	125
5.17	Maximum Eady growth rate RCP8.5 changes at 250hPa for the period 2070-2099. . . . .	131
5.18	Maximum Eady growth rate RCP4.5 changes at 250hPa for the period 2070-2099. . . . .	132
5.19	Maximum Eady growth rate RCP8.5 changes at 850hPa for the period 2070-2099. . . . .	133
5.20	Maximum Eady growth rate RCP4.5 changes at 850hPa for the period 2070-2099. . . . .	134
5.21	Zonal mean temperature and zonal wind RCP8.5 changes in JJA. . . . .	135
5.22	Zonal mean temperature and zonal wind RCP4.5 changes in JJA. . . . .	136
5.23	500hPa geopotential height anomaly RCP8.5 changes. . . . .	137
5.24	500hPa geopotential height anomaly RCP4.5 changes. . . . .	138
5.25	Skin temperature RCP8.5 changes. . . . .	139
5.26	Skin temperature RCP4.5 changes. . . . .	140
5.27	Outgoing longwave radiation RCP8.5 changes. . . . .	141

5.28	Outgoing longwave radiation RCP4.5 changes. . . . .	142
5.29	Precipitation RCP8.5 changes. . . . .	143
5.30	Precipitation RCP4.5 changes. . . . .	144
5.31	Zonal mean temperature and zonal wind RCP8.5 changes in DJF. . . . .	149
5.32	Zonal mean temperature and zonal wind RCP4.5 changes in DJF. . . . .	150
5.33	Zonal mean temperature and zonal wind RCP8.5 changes in SON. . . . .	153
5.34	Zonal mean temperature and zonal wind RCP4.5 changes in SON. . . . .	154
5.35	Zonal mean temperature and zonal wind RCP8.5 changes in MAM. . . . .	155
5.36	Zonal mean temperature and zonal wind RCP4.5 changes in MAM. . . . .	156
5.37	Maximum intensity distribution for JJA during the period 2070-2099. . . . .	160
5.38	Maximum intensity distribution for SON during the period 2070-2099. . . . .	163
5.39	Maximum intensity distribution for DJF during the period 2070-2099. . . . .	164
5.40	Maximum intensity distribution for MAM during the period 2070-2099. . . . .	166
5.41	Skin temperature RCP8.5 changes. . . . .	172
5.42	Skin temperature RCP4.5 changes. . . . .	173
5.43	Precipitation RCP8.5 changes. . . . .	174
5.44	Precipitation RCP4.5 changes. . . . .	175
5.45	Outgoing longwave radiation RCP8.5 changes. . . . .	176
5.46	Outgoing longwave radiation RCP4.5 changes. . . . .	177
5.47	Wind RCP8.5 changes at 850hPa. . . . .	178
5.48	Wind RCP4.5 changes at 850hPa. . . . .	179
5.49	Maximum Eady growth rate RCP8.5 changes at 850hPa for the period 2070-2099. . . . .	180
5.50	Maximum Eady growth rate RCP4.5 changes at 850hPa for the period 2070-2099. . . . .	181
5.51	Relative humidity and Omega RCP8.5 changes at 850hPa. . . . .	182
5.52	Relative humidity and Omega RCP4.5 changes at 850hPa. . . . .	183
5.53	Relative humidity and Omega RCP8.5 changes at 500hPa. . . . .	184
5.54	Relative humidity and Omega RCP4.5 changes at 500hPa. . . . .	185
5.55	Latent heat RCP8.5 changes. . . . .	186
5.56	Latent heat RCP4.5 changes. . . . .	187
5.57	Sensible heat RCP8.5 changes. . . . .	188
5.58	Sensible heat RCP4.5 changes. . . . .	189
5.59	Evaporation minus Precipitation RCP8.5 changes. . . . .	190
5.60	Evaporation minus Precipitation RCP4.5 changes. . . . .	191
6.1	Schematic of the positive feedback mechanism after the removal of Ama- zon Forest. . . . .	209
6.2	Schematic of South America circulation for WAMZ experiment in winter.	210
6.3	Schematic of South America circulation for WAMZ experiment in summer.	211



## LIST OF TABLES

	<u>Page</u>
3.1 Summary of main new components in the Earth system configuration from HadGEM1 to HadGEM2-ES. . . . .	32
3.2 Summary of main new couplings in the Earth system configuration from HadGEM1 to HadGEM2-ES. . . . .	32
3.3 HadGEM2-ES experiments for historical period between 1976-2005. . . .	39
3.4 HadGEM2-ES experiments for future projected changes 2006-2100. . . .	41
3.5 Comparison of main features between ERA-40 and ERA-Interim reanalysis. 43	
4.1 Number of cyclones per month for each season that are found in the Southern Hemisphere extratropics (90°S,20°S) for the period 1979-2005. Abbreviations: EM, Ensemble Member. . . . .	91
5.1 Number of cyclones per month for each season in HadGEM2-ES experiments that are found in the SH extratropics (90°S,20°S) for all seasons in RCP8.5 scenario. The period for WAMZ and CTRL experiments is 2070-2099 and for Historical experiment is 1976-2005. Abbreviations: EM, Ensemble Member. . . . .	158
5.2 Number of cyclones per month for each season in HadGEM2-ES experiments that are found in the SH extratropics (90°S,20°S) for all seasons in RCP4.5 scenario. The period for WAMZ and CTRL experiments is 2070-2099 and for Historical experiment is 1976-2005. Abbreviations: EM, Ensemble Member. . . . .	158
5.3 Kolmogorov-Smirnov statistical test for the RCP8.5 experiments in comparison to the Historical experiment and between them. Each experiment comparison shows the Kolmogorov-Smirnov statistic ( $D$ ) for intensity distributions of the relative vorticity in the Southern Hemisphere for the respective seasons (top side); and the percentage of individual HadGEM2-ES ensemble member in a likewise experiment comparison for each member. The period for WAMZ and CTRL experiments is 2070-2099 and for Historical experiment is 1976-2005. Abbreviations: EM, Ensemble Member. 161	

5.4 Kolmogorov-Smirnov statistical test for the RCP4.5 experiments in comparison to the Historical experiment and between them. Each experiment comparison shows the Kolmogorov-Smirnov statistic ( $D$ ) for intensity distributions of the relative vorticity in the Southern Hemisphere for the respective seasons (top side); and the percentage of individual HadGEM2-ES ensemble member in a likewise experiment comparison for each member. The period for WAMZ and CTRL experiments is 2070-2099 and for Historical experiment is 1976-2005. Abbreviations: EM, Ensemble Member. 161

## LIST OF ABBREVIATIONS

4D-Var	–	4D-Variational Data Assimilation Scheme
AGCM	–	Atmospheric General Circulation Model
AMO	–	Atlantic Multidecadal Oscillation
AMZ	–	Amazon
AR4	–	Assessment Report Five
AR5	–	Assessment Report Four
C	–	Celsius
CFSR	–	Climate Forecast System Reanalysis
CMIP4	–	Coupled Model Intercomparison Project Phase 4
CMIP5	–	Coupled Model Intercomparison Project Phase 5
CMIP6	–	Coupled Model Intercomparison Project Phase 6
CTRL	–	Control Experiment
DFRAC	–	Disturbed Fraction
DJF	–	December, January and February
ECHAM5	–	Max Planck Institute for Meteorology AGCM version 5
ECMWF	–	European Centre for Medium-Range Weather Forecasts
EM	–	Ensemble Member
EN	–	El Niño
ES	–	Earth System
ENSO	–	El Niño Southern Oscillation
ERA40	–	ECMWF 40 Year Reanalysis
ERA-Interim	–	ECMWF Interim Reanalysis
ESM	–	Earth System Model
FAR	–	First Assessment Report
GB	–	Gigabytes
GDAS	–	Global Data Assimilation
GGE	–	Greenhouse Gas Emissions
GRIB	–	Gridded Binary
GPCP	–	Global Precipitation Climatology Project
HadGEM1	–	Met Office Hadley Centre ESM Version 1
HadGEM2	–	Met Office Hadley Centre ESM Version 2
HadGEM2-ES	–	Met Office Hadley Centre ESM Version 2 - Earth System
HD	–	Hard Disk
HGT	–	Geopotential Height
HIST	–	Historical Experiment
IAM	–	Integrated Assessment Models
IPO	–	Interdecadal Pacific Oscillation
ITCZ	–	Intertropical Convergence Zone
IPCC	–	Intergovernmental Panel on Climate Change
IS92	–	IPCC scenarios 1992

JJA	–	June, July and August
K	–	Kelvin
KS	–	Kolmogorov-Smirnov
LN	–	La Niña
LUC	–	Land Use Change
LUCC	–	Land Use Cover Change
MAM	–	March, April and May
MGDR	–	Mean Growth Decay Rate
MJO	–	Madden-Julian Oscillation
MOM4	–	Modular Ocean Model Version 4
MOSES2	–	Met Office Surface Exchange Scheme Version 2
NASA	–	National Aeronautics and Space Administration
NCEP	–	National Centers for Environmental Prediction
NH	–	Northern Hemisphere
NHC	–	National Hurricane Center
NOAA	–	National Oceanic and Atmospheric Administration
OSU	–	Oregon State University - Land Surface Model
PB	–	Petabytes
PDO	–	Pacific Decadal Oscillation
PFT	–	Plant Functional Type
PREC	–	Precipitation
R1	–	NCEP Reanalysis version 1
R2	–	NCEP Reanalysis version 2
RCP	–	Representative Concentration Pathways
RCP4.5	–	Representative Concentration Pathways - Stabilization Scenario - Radiative Forcing Level of $4.5 \text{ Wm}^{-2}$
RCP8.5	–	Representative Concentration Pathways - Highest Emissions Scenario - Radiative Forcing Level of $8.5 \text{ Wm}^{-2}$
RF	–	Radiative Forcing
RH	–	Relative Humidity
SA	–	South America
SACZ	–	South Atlantic Convergence Zone
SALLJ	–	South American Low-Level Jet East of the Andes
SAR	–	Second Assessment Report
SAM	–	Southern Annular Mode
SH	–	Southern Hemisphere
SON	–	September, October and November
SPCZ	–	South Pacific Convergence Zone
SRES	–	Special Report on Emissions Scenarios
SST	–	Sea Surface Temperature
ST	–	Storm Track
TAR	–	Third Assessment Report

- TB – Terabytes
- TOA – Top of Atmosphere
- TRIFFID – Top-Down Representation of Interactive Foliage and  
Flora Including Dynamics
- VORT – Vorticity
- WAMZ – Without Amazon Forest Experiment



## LIST OF SYMBOLS

$D$	–	Kolmogorov-Smirnov D Statistics
$f$	–	Coriolis Parameter
$p$	–	P Value
$N$	–	Brunt-Väisälä Frequency
$\psi$	–	Smoothness Constraint
$\sigma_{eady}$	–	Maximum Eady Growth Rate
$\theta$	–	Geopotential Height
$v$	–	Total Wind Vector
$\Xi$	–	Cost Function
$z$	–	Geometric Height
$\zeta$	–	Vorticity
$\zeta_r$	–	Relative Vorticity



# CONTENTS

	<u>Page</u>
<b>1 INTRODUCTION</b> . . . . .	<b>1</b>
1.1 Motivation . . . . .	2
1.2 Aims . . . . .	3
1.3 Structure of thesis . . . . .	4
<b>2 LITERATURE REVIEW</b> . . . . .	<b>7</b>
2.1 Southern hemisphere Storm Tracks . . . . .	7
2.1.1 Definition . . . . .	7
2.1.2 Cyclone formation and intensification mechanisms . . . . .	8
2.1.3 Spatial distribution and characteristics . . . . .	11
2.2 Southern hemisphere storm tracks in climate change scenarios . . . . .	14
2.2.1 Observational evidence of change in the storm tracks - Recent past studies . . . . .	14
2.2.2 Future projections . . . . .	15
2.2.2.1 An overview of climate modeling . . . . .	15
2.2.2.2 Storm track response to climate change scenario . . . . .	19
2.2.2.3 Representative concentration pathways . . . . .	20
2.2.2.4 Land Use Cover Change as a atmospheric change source . . . . .	25
2.2.2.5 Amazon Forest regional climate . . . . .	26
2.3 Storm tracking methods . . . . .	27
<b>3 METHODOLOGY</b> . . . . .	<b>29</b>
3.1 The HadGEM2 model . . . . .	30
3.1.1 Earth system configuration . . . . .	33
3.1.2 Land Use Cover change configuration in HadGEM2 model . . . . .	34
3.1.3 HadGEM2-ES experimental design . . . . .	38
3.1.3.1 Historical . . . . .	38
3.1.3.2 Representative Concentration Pathways . . . . .	39
3.2 Gridded observational data . . . . .	43
3.2.1 ERA-Interim . . . . .	43
3.2.2 Global Precipitation Climatology Project . . . . .	44
3.3 Statistics and analysis by seasons . . . . .	44
3.4 Extratropical cyclone tracking . . . . .	45

3.4.1	Objective feature identification . . . . .	45
3.4.2	Cyclone tracking using TRACK . . . . .	48
3.4.3	Statistics and post-processing . . . . .	48
3.5	Large-scale fields and diagnostics . . . . .	50
3.6	Regional-scale fields and diagnostics . . . . .	52
<b>4</b>	<b>STORM TRACK CLIMATOLOGY AND HADGEM2-ES EN- SEMBLE BIASES . . . . .</b>	<b>53</b>
4.1	Climatology . . . . .	53
4.1.1	Winter . . . . .	53
4.1.2	Summer . . . . .	59
4.1.3	Transition seasons . . . . .	60
4.2	HadGEM2-ES ensemble biases . . . . .	61
4.2.1	Storm track density biases . . . . .	61
4.2.1.1	Winter . . . . .	61
4.2.1.2	Summer . . . . .	68
4.2.1.3	Transition seasons . . . . .	69
4.2.2	Large-scale biases . . . . .	70
4.2.2.1	Winter . . . . .	72
4.2.2.2	Summer . . . . .	81
4.2.2.3	Transition seasons . . . . .	85
4.2.3	Cyclone intensity biases . . . . .	90
4.2.3.1	Cyclone count . . . . .	90
4.2.3.2	Maximum intensity distribution . . . . .	91
4.3	Discussion and conclusion . . . . .	96
<b>5</b>	<b>SOUTHERN HEMISPHERE STORM TRACK FUTURE PRO- JECTIONS . . . . .</b>	<b>101</b>
5.1	HadGEM2-ES ensemble changes . . . . .	102
5.1.1	Storm track density changes . . . . .	102
5.1.1.1	Winter . . . . .	103
5.1.1.2	Summer . . . . .	110
5.1.1.3	Transition seasons . . . . .	116
5.1.2	Large-scale changes . . . . .	126
5.1.2.1	Winter . . . . .	126
5.1.2.2	Summer . . . . .	145
5.1.2.3	Transition seasons . . . . .	151
5.1.3	Cyclone intensity changes . . . . .	157

5.1.3.1	Cyclone count . . . . .	157
5.1.3.2	Maximum intensity distribution . . . . .	159
5.1.4	Regional-scale changes . . . . .	167
5.1.4.1	Winter . . . . .	167
5.1.4.2	Summer . . . . .	192
5.1.4.3	Transition seasons . . . . .	194
5.2	Discussion and conclusion . . . . .	196
<b>6</b>	<b>CONCLUSIONS . . . . .</b>	<b>201</b>
6.1	Overview . . . . .	201
6.2	Conclusions . . . . .	202
6.2.1	How well does the HadGEM2-ES Coupled Model represent the Southern Hemisphere Storm Tracks? . . . . .	202
6.2.2	What are the main factors that contribute to biases in the storm tracks?204	
6.2.3	What are future storm track changes predicted by the HadGEM2-ES model for the two IPCC future climate change scenarios? . . . . .	205
6.2.4	How might Amazon land use cover change affect the storm track and climate over South America? . . . . .	207
6.3	Recommendations and future work . . . . .	212
	<b>REFERENCES . . . . .</b>	<b>213</b>
	<b>APPENDIX A - ARTICLE . . . . .</b>	<b>241</b>



## 1 INTRODUCTION

Extratropical cyclones play an important role in the transport of energy and moisture from low latitudes to Polar Regions. They are synoptic scale<sup>1</sup> weather systems of meteorological, climatic and socioeconomic importance. The preferred region for these systems are the so called Storm Tracks, which according to Blackmon et al. (1977) can be identified as the maximum kinetic energy and characterized by a strong gradient of geopotential and meridional wind. Cyclones that constitute the STs can lead to extreme weather in the middle latitudes, such as cold air outbreaks (SPRENGER et al., 2013), extreme precipitation (SILVA DIAS et al., 2013) and intense winds (PARISE et al., 2009). As the intensity of extreme weather has increased in recent years (INTERGOVERNMENTAL PANEL ON CLIMATE CHANGE (IPCC), 2013), improving our knowledge of STs presents an important challenge. Thus cyclones and the STs have significant impacts on weather and climatic conditions at extratropical latitudes in both hemispheres.

For the Southern Hemisphere (SH) several previous studies such as Taljaard (1972), Gan and Rao (1991), Berbery and Vera (1996), Sinclair (1997), Simmonds and Keay (2000), Hoskins and Hodges (2005), Hodges et al. (2011) and others, using observational data and reanalyses, have found important storm track (ST) patterns and links with the mean flow and large scale circulation. From a climate model perspective, while progress has been made in simulating the Northern Hemisphere (NH) ST features (e.g. (CATTO et al., 2010; CATTO et al., 2011; ZAPPA et al., 2013b; CHANG, 2013)), few studies have explored the role of the STs in the SH (e.g. (BENGTSSON et al., 2006)).

Previous studies, such as Hoskins et al. (1985), Hoskins and Valdes (1990), Ulbrich et al. (2009), Catto et al. (2010), Catto et al. (2011), Hawcroft et al. (2017) and others, have shown that latent heating plays an important role in the evolution and deepening of some of the most damaging cyclones, modifying the potential vorticity structure. Thus, a better representation of latent heating process (location and magnitude) can help to understand how this important process can affect the life cycle, the interaction with the mean flow and the location of extra-tropical cyclones.

Anthropogenic climate change is dependent on several factors that must be considered when investigating the impacts of climate change on the STs. Among these factors, the level of emissions of greenhouse gases (GHG) and land use change are

---

<sup>1</sup>From several hundred kilometers to several thousand kilometers.

considered to be the most important (INTERGOVERNMENTAL PANEL ON CLIMATE CHANGE (IPCC), 2013). Pioneering studies such as that of Charney et al. (1975) have shown that the global climate is very sensitive to changes in the planetary albedo, which is associated with land cover, atmospheric circulation and feedback mechanisms. Changes in the planetary albedo have a strong impact on the radiation budget and can heat or cool regions in the terrestrial surface. In this way, the interaction between the surface and air above these regions may modify processes important in the development of cyclones such as latent heat release and friction which may lead to changes in the SH STs. In summary, it is important to understand how cyclones and the STs will respond to anthropogenic climate change in order to mitigate as much as possible any detrimental effects.

Recent studies that relate the effects of climate change into STs under different climatic scenarios highlight the changes in the location of extratropical cyclones, generally towards the poles, mainly due to the increase in mean temperature and convective static stability, which may result in the expansion of the Hadley Cell circulation (KORTY; SCHNEIDER, 2008; CEPPI; HARTMANN, 2013; ADAM et al., 2014; LEVINE; SCHNEIDER, 2015; MBENGUE; SCHNEIDER, 2017). Thus, studies with a better representation of atmospheric processes can also help to improve the knowledge about the mechanisms that control the large scale interactions between tropical and extratropical regions and the precipitation patterns, cyclones and the STs, and how they might change.

## 1.1 Motivation

Extratropical cyclones modulates the weather and climate in the middle latitudes. The most intense cyclones can cause large socioeconomic impacts through heavy rain, flooding, thunderstorms, strong winds and cold temperatures.

The distribution and variability of this preferred region of extratropical cyclones, the Storm Tracks, is a subject rarely explored in the literature over Southern Hemisphere. Studies in this extensive region are important for a better understanding of the possible impacts and influences of the ST on the precipitation regime during current and future climate (TRENBERTH, 1991; SINCLAIR, 1995; VERA, 2003; HOSKINS; HODGES, 2005; CAVALCANTI, 2009).

The ST are also important component of the general atmospheric circulation, transporting heat and moisture between poles and tropical region. Investigate the past and present climate with the newest reanalysis data sets is important for a better

understanding of the aspects of STs, such as structure, life cycle and the distribution of variability in the current climate and how they also influences the atmosphere and precipitation over South America.

According to last Intergovernmental Panel on Climate Change ([INTERGOVERNMENTAL PANEL ON CLIMATE CHANGE \(IPCC\), 2013](#)) report, studies on the SH Storm Track are currently lacking. Recently, analyze the possible impacts of ST on the future climate has become feasible due to the higher spatial and temporal resolution of the models composing the latest dataset of climate projections, the Coupled Model Intercomparison Project Phase 5 (CMIP5) ([VUUREN et al., 2011](#)). This new data set includes land use cover changes that influence the climate system in many ways, including direct land use change emissions, impacts on the hydrological cycle, and changes in remaining vegetation stock (influencing the removal of  $CO_2$  of the atmosphere), planetary albedo and surface roughness. Therefore, given the importance of ST in climate regulation in South America, investigating the role of land use cover changes in ST pattern in climate projections becomes important not only for a better understanding of the possible impacts in two large interdisciplinary areas, surface and atmosphere, but also to enable the creation of strategies for adaptation and mitigation of natural disasters.

## 1.2 Aims

The aim of this thesis is perform a comprehensive study of the Storm Tracks over the Southern Hemisphere and to investigate the impact on cyclones and the STs in an idealized experiment, using the UK Met Office HadGEM2-ES coupled climate model, that changes the land use change over the Amazon Forest. To this goal, reanalysis data and numerical simulation results will be used to answer the key science questions.

- How well does the HadGEM2-ES Coupled Model represent the Southern Hemisphere Storm Tracks?
- What are the main factors that contribute to biases in the storm tracks?
- What are future Southern Hemisphere storm track changes are predicted by HadGEM2-ES under two IPCC future climate change scenarios?
- How might Amazon land use cover change affect the storm track and climate over South America?

The thesis will be divided into two parts: an evaluation of the SH STs as simulated by the HadGEM2-ES model for the current climate and the second part the determination of how the Amazon land use affects the STs and how they may change in the future.

### 1.3 Structure of thesis

In Chapter 2 a literature review of the properties of cyclones, storm track behaviour and climate change will be presented. The first section presents a literature review of SH storm tracks and their main characteristics, such as baroclinic instability, orography and others. The second section will review the response of SH storm tracks to climate change scenarios and how the land use cover changes affects the climate in a global and regional-scale. In the last section a brief overview is presented of the methods used to analyze cyclones and STs found in the literature.

The numerical model, tools and methods used in this thesis are described in the Chapter 3. In the first section a description of the HadGEM2 model in an earth system configuration is given, followed by a description of the climate change experiments with and the sensitivity experiments with and without Amazon Forest. In the second section the gridded observational datasets are presented, followed by a brief description of the statistics and analysis by season. In fourth section the cyclone tracking method used to analyse the cyclones in the simulations, TRACK, is explained in details. TRACK will be used widely in this thesis to both identify and track cyclones but also to produce statistics of their distribution and properties. Finally, the large-scale fields and diagnostics used to assess the cyclones are presented fifth section, being the regional-scale analyses described in last section.

The climatology and biases of SH extratropical cyclones and the large-scale fields in the HadGEM2-ES model for the current climate are investigated in Chapter 4. The aim of this chapter is to answer the first two science questions of the thesis which are "How well does the HadGEM2-ES Coupled Model represent the Southern Hemisphere Storm Tracks?" and "What are the main factors that contribute to biases in the storm tracks?". In the first section, an overview of the SH storm track climatology in ERA-Interim for winter, summer and the transition seasons is presented. Second section, the biases in terms of storm track distributions, large-scale fields and extratropical cyclones properties compared to the observational datasets are investigated. Finally, in the last section a brief resume of the results are presented and discussed.

The future projections of extratropical cyclones and large and regional-scale fields as predicted by the HadGEM2-ES model and how these are affected by changes to the Amazon land use are investigated in Chapter 5 with the aim of addressing the science questions of "What are future Southern Hemisphere storm track changes are predicted by HadGEM2-ES under two IPCC future climate change scenarios?" and "How might Amazon land use cover change affect the storm track and climate over South America?". This chapter is divided in four and each section has the following structure. The future projected climate with and without Amazon Forest in terms of the storm track distribution, large-scale fields, extratropical cyclones count distribution and regional-scale are investigated under the Representative Concentration Pathways designed for CMIP5 in an idealized experiment.

In the Chapter 6, an overview of the results are presented, followed by a summary of the main conclusions of the thesis in addressing the science questions. Finally, a suggestion of the future works are proposed.



## 2 LITERATURE REVIEW

In this chapter a brief literature review is presented. First, the main characteristics of the cyclones and storm track are described in Section 3.4. Section 2.2 focuses on the storm tracks under climate change observational evidence and future projected climate, including a brief review of how the land use affects the atmosphere. Finally, a review of the tracking methods is presented in Section 2.3.

### 2.1 Southern hemisphere Storm Tracks

In this thesis the term 'cyclone' is defined as the extratropical cyclone at lower levels (850hPa), while genesis and cyclogenesis refer to the initial stage of cyclone development and lysis and cyclolysis refer to the dissipation phase. In addition, the general distribution of extratropical cyclones is referred to as 'storm track', and the path of an individual extratropical cyclone is referred to as 'cyclone track'.

#### 2.1.1 Definition

Spectral analysis was a major advance for the understanding of atmosphere general circulation, since it allowed to identify the variability of meteorological fields in relation to a frequency spectrum. Sawyer (1970) investigated the variabilities of geopotential height at 500hPa for periods of less than 10, in synoptic analyzes on the North Atlantic and found a strong correlation between the regions of extratropical cyclones and the maximum variability of the high frequencies. Blackmon (1976), based on Sawyer (1970), studied nine winters over the Northern Hemisphere and observed a correspondence between the position of the mean vorticity maxima and the maximum geopotential height variance, both in filtered fields. Following the previous study, Blackmon et al. (1977) investigated the geopotential height variance distribution at 500hPa using bandpass filter and found maximums in large areas at medium latitudes, calling them Storm Tracks.

The Storm Track is the region of preference for transient synoptic scale disturbances, which is associated with the average position of maximum winds (jets) in high levels in middle latitudes. This jet is characterized by the zonal component of the west wind at higher levels of the troposphere, which increases with altitude due to southern temperature gradients. The maximum wind flow is so called jet stream, which separates the hot air from the tropics of the cold air from the poles. The analysis of the ageostrophic component within the jet streams allows the identification of preferred regions for formation of extratropical cyclones (HOLTON, 2004). Corre-

sponding to winds at high levels, relative vorticity is another variable widely used in ST analysis, since it expresses the tendency of a quantity of fluid to spin.

Currently, two types of approach are common in ST studies. The first is the filtering of frequency bands associated to synoptic systems as presented above, which is based on simple statistics for a given frequency band (e.g. 2 - 6 days ) in an area (SAWYER, 1970; BLACKMON, 1976; BLACKMON et al., 1977; WALLACE; BLACKMON, 1983; KONIG et al., 1993; BERBERY; VERA, 1996; CHANG; FU, 2002). The second is the system tracking, a lagrangian approach, which identifies and tracks the system over a given period of time, providing statistics of its distribution (e.g. cyclogenesis, cyclolysis, among others) (MURRAY; SIMMONDS, 1991; HODGES, 1994; HODGES, 1999; SINCLAIR, 1997; SIMMONDS et al., 2008; INATSU, 2009). There are also other studies that use both approaches, such as Hoskins and Hodges (2002), Hoskins and Hodges (2005).

### 2.1.2 Cyclone formation and intensification mechanisms

Early studies of synoptic scale transient disturbances are from the beginning of the 19th century, based on mathematical models that disregarded the vertical component of the angular velocity and the vertical shear of the zonal flow. These transient disturbances are perturbations characterized by the passage of cyclones (low pressure) and anticyclones (high pressure) or by the propagation of baroclinic waves between 4000 and 5000 km, in a period of up to 10 days and with an average size of 200 to 2000 km (BLUESTEIN, 1993).

In the 1950s, Charney (1947) and later Eady (1949) solved the quasi-geostrophic equations in different ways using approximations of the  $\beta$  plane and demonstrated that the western winds are unstable in the middle latitudes because of the baroclinicity<sup>1</sup>. In the following decades, the 60s and 70s, ST studies were almost entirely focused on the Northern Hemisphere due to a number of factors, including the advent of meteorological satellites, technological evolution of computers, and evolution of mathematics and physics of numerical models for weather forecasting. Studies on the dynamics of ST formation in the SH emerged in the 1980s and 1990s and can be divided into three parts: baroclinic instability, downstream development and the orography.

The main mechanism of ST formation is baroclinic instability, which occurs due to

---

<sup>1</sup>is a measure of fluid stratification. A baroclinic atmosphere is where the density depends on the temperature and pressure (HOLTON, 2004).

an instability in the jet stream flow caused by the temperature difference between the pole and the equator (HOLTON, 2004). The jets are located on a region where polar cold air meets tropical hot air, called the polar frontal zone, and the vertical wind shear occurs associated with the horizontal temperature gradient, generating the jet streams. The relation between vertical wind shear and horizontal temperature gradient is explained by the thermal wind balance. This theory states that the higher the temperature gradient between pole and equator, the greater is the intensity of the jet stream and the amplification of the baroclinic wave in the flow (HOSKINS; VALDES, 1990).

The baroclinic wave develops due to the conversion of potential energy into kinetic energy through the advection of cold air. This results in the decrease of the geopotential height and intensifies the horizontal gradient of temperature and pressure, causing the convergence within the low pressure and aiding the ascending movement of the hot air and descending of the cold air (HOSKINS; VALDES, 1990; HOLTON, 2004). This movement characterizes a secondary circulation and plays a key role in maintaining cyclones life cycle. Barry and Carleton (2001) point out that the secondary circulation in baroclinic wave development is fundamental for conversion of potential energy of the disturbance into kinetic energy. In addition, the authors emphasize that for this conversion to be more efficient, there should be a disturbance inclination with the height to the west, implying in the increase of potential energy by the longitudinal advection of temperature. On the other hand, Lorenz (1955) has shown that the latitudinal temperature gradient implies in the transport of sensible heat from the poles to the equator and vice versa, converting potential energy of the basic state to potential energy of the perturbation. Thus, when the cold air is conveyed from the pole towards the equator there is a decrease of geopotential height, and, in the opposite situation, an increase in geopotential height. Therefore, baroclinic instability is one of the most important mechanisms not only for ST formation but also for terrestrial climate regulation, because it tends to balance the gradient between these regions of high temperature contrast.

Downstream development is another important mechanism for the formation of ST on the SH. When a cyclone within a baroclinic wave is dissipating, it transfers kinetic energy downstream this wave amplifying it, which favors the formation of a new cyclone (CHANG, 1993; ORLANSKI; CHANG, 1993). Trenberth (1991) investigated downstream development and observed that in the SH, different from the Northern Hemisphere, the proportion of ocean is much larger than the continent and there is greater influence of downstream development in baroclinic waves through the

transfer of kinetic energy downstream of the dissipating cyclone. Similar results were also found in [Loon \(1965\)](#).

[Berbery and Vera \(1996\)](#) investigated ST during the winter season and concluded that downstream development is very important for extratropical cyclones, because influences their formation mainly alongside the subtropical jet where the baroclinicity has lower intensity. Subsequently, [Chang and Yu \(1999\)](#) concluded that downstream development is also important during austral summer and [Rao et al. \(2002\)](#) have shown that it also has a significant contribution in the transition seasons (autumn and spring).

In South America, the orography of the Andes Mountains directly influences the atmospheric circulation and is another important mechanism for the STs. [Gan and Rao \(1994\)](#), in a study about the influence of the Andes Mountains in synoptic scale systems, observed that when the western flow crosses the mountains at the top (when the air rises) the movement tends to be anticyclonic and at the bottom (when the air descends) the movement tends to be cyclonic. The authors also observed a strong correlation between the baroclinic disturbances of west and the stationary wave formed by the movement of the descent of the mountain air that warms the air, known as Thermal-orographic Low of the Northwest of Argentina (LNOA). In a later study, [Gan and Rao \(1996\)](#) also showed that the orography of the Andes Mountains has a favorable effect for cyclogenesis in SA.

The region of the Andes Mountains was also considered in other studies, such as [Seluchi \(1995\)](#). The author suggests that the low-pressure centering in the east of the mountains, associated with the advection of hot and humid northern air, and the displacement in middle levels of the cyclonic disturbance favors the intensification of the semi-stationary baroclinic zone east of northern of Argentina, Uruguay and south of Brazil. [Inatsu and Hoskins \(2004\)](#) and [Hoskins and Hodges \(2005\)](#) highlight the results obtained by [Seluchi \(1995\)](#) and also the importance of the low-level jet at east of the mountains in the intensification of systems, because of the moisture supply from the Amazon especially during the austral summer, which agrees with [Berbery and Barros \(2002\)](#) and [Cavalcanti \(2009\)](#).

Next Section 2.2 several features related to dynamics formation and aspects such as the variability, climatology and geography of ST in the Southern Hemisphere will be addressed.

### 2.1.3 Spatial distribution and characteristics

The SH storm tracks were earliest investigated by [Taljaard \(1972\)](#) in a comprehensive study of their structure from the perspective of weather observations, however, this study had similar results to those already known for the Northern Hemisphere. One year later, using satellite imagery, [Streten and Troup \(1973\)](#) identified and tracked vortices and cyclones subjectively, creating their own climatology. Further, [Carleton \(1981\)](#) used a similar approach to study cyclonic activity during winter and identified favorable regions for passage of these cyclones.

The study of [Trenberth \(1991\)](#) was important in terms of defining with detail the Southern Hemisphere ST. Using analysis of zonal means of synoptic scale transient systems and their components, the author verified the correlation between these regions and the polar jet, which was associated with baroclinicity at lower levels. In addition, the author pointed out important features that were previously unknown, such as ST persistence throughout the year and low meridional variability during the summer. The strong relation between jet position and the strongest intensity in the South Indian Ocean and weaker in the Southern Pacific Ocean was another important feature identified.

[Berbery and Vera \(1996\)](#) used ECMWF reanalysis data to identify structure and evolution of synoptic scale waves in mid-latitudes during the winter of 1983 and 1988. The spatial distribution of jet streams showed maximum magnitude and higher frequency of the ST in the Indian Ocean at 50°S and 30°S, which is associated respectively to the polar and subtropical jets. For the Pacific Ocean, in the same latitudes, there is a lower ST frequency, confirming the results of [Trenberth \(1991\)](#). Furthermore, the evolution of synoptic scale wave packets showed lower amplitude upstream low pressure centers and higher amplitude downstream.

[Chang and Yu \(1999\)](#) studied the variations and waves propagation in ST during winter and austral summer between 1980 and 1993. They aimed to identify the basic features of wave packets in both hemispheres with ECMWF reanalysis data. In austral summer, the ST is zonally symmetric, located in the latitude range of 50°S and the systems follow the jet streams flow. On the other hand, in austral winter, ST consists of a spiral around the poles, starting in Australia and ending in New Zealand, which is similar to the observed by [Berbery and Vera \(1996\)](#).

Similar to [Chang and Yu \(1999\)](#), but with 19 years of NCEP/NCAR reanalysis data focusing on autumn and spring, [Rao et al. \(2002\)](#) analyzed the standard deviation

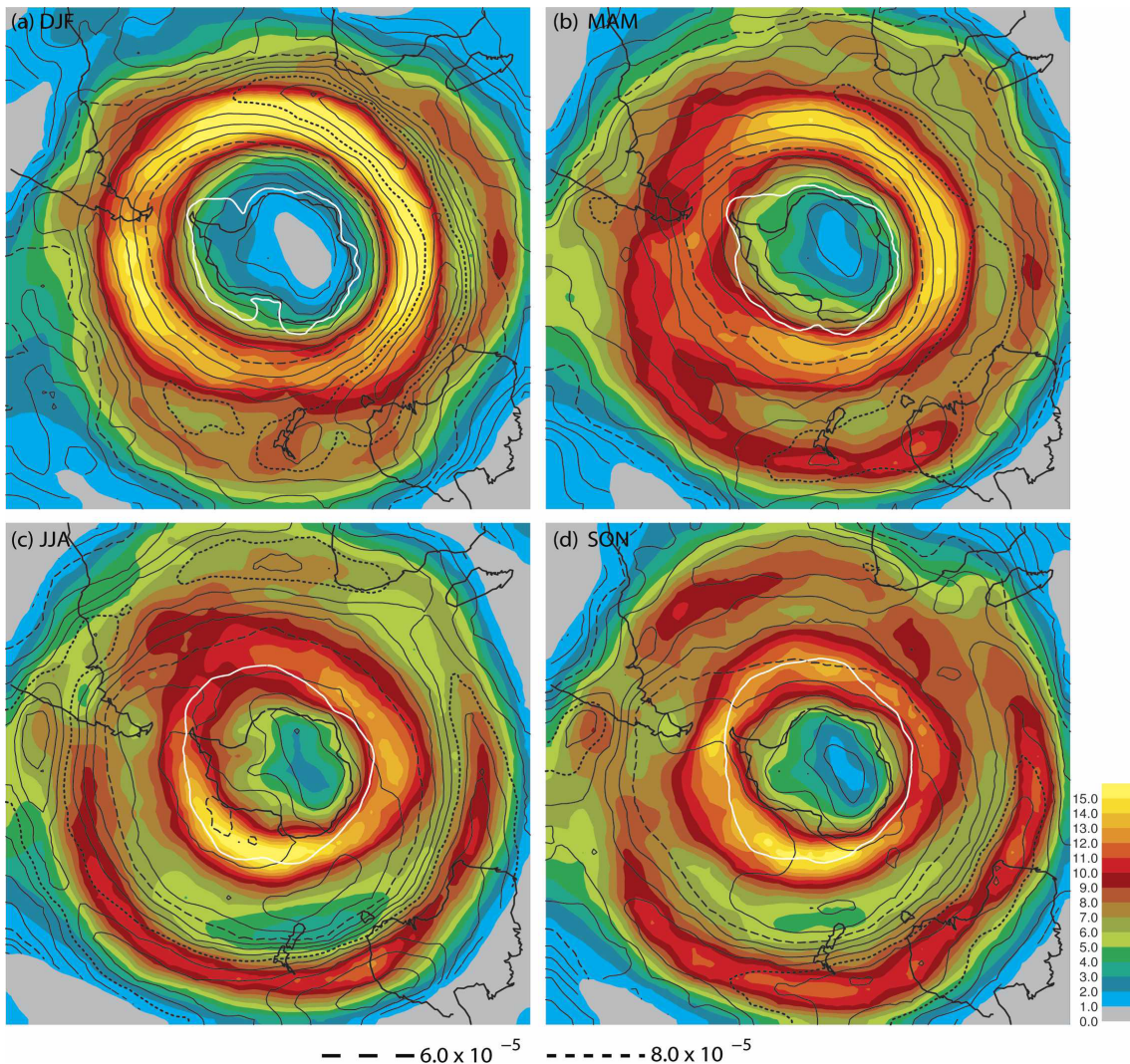
of the southern wind component for high troposphere in response to the change in direction caused by the passage of synoptic scale transient systems. During autumn, ST have higher frequency and intensity than in spring, besides pronounced features in the high troposphere. Despite these differences, the preferential trajectory of transient disturbances did not present significant changes for transition seasons.

Inatsu and Hoskins (2004) used the Hadley Center Atmospheric Model Version 3 (HadAM3) to investigate zonal asymmetry in ST during austral winter. The authors found that zonal asymmetry in jet streams and the associated baroclinicity play a key role in the seasonal variations of ST. In austral summer and autumn, the subtropical jet is less intense and the ST of the Pacific Ocean is attached to the ST around the pole. In winter and austral autumn, the subtropical jet intensifies and forks in high levels in the region of greater intensity of the winds (nucleus), shifting the ST to north during these seasons. This same result was also found by Gallego et al. (2005) in his study about jets in the Southern Hemisphere.

In the same research line, Nakamura and Shimpo (2004) investigated the relation between ST and high level jets using NCEP (R1) reanalysis data between 1979 and 1995. The authors have shown that regional and seasonal features are determined by subtropical and polar jets. In winter, the polar jet is intense and vertically extensive, and it is associated with a baroclinic zone near the surface, which favors the growth of transient systems. Due to these factors, ST in HS are strongly correlated to jets.

Hoskins and Hodges (2005) studied in a new perspective the ST in the HS using 40 years of ECMWF reanalysis data, the ERA-40. ST asymmetry is greater during the winter and almost nil in the summer, opposite of what is observed in the Northern Hemisphere. Similar to the results of Rao et al. (2002), the transition seasons ST similarity with those in preceding season was also found (autumn with summer and spring with winter), as shown in Figure 2.1. Cyclogenesis during summer tends to move eastward, contributing to the precipitation regime in the South and Southeast regions of Brazil. In addition, at this time of year low pressure systems tend to move in the northwest/southeast direction to southwest of the semi-permanent anticyclones, contributing to the convergence zones observed in the South Atlantic and South Pacific. The authors emphasize that, in general, few differences were found in relation to the previous studies so the general concept of ST in SH remained the same.

Figure 2.1 - Upper-tropospheric seasonal cycle of the SH storm track.



Track density (color) and mean intensity (line contour) for (a) DJF (summer), (b) MAM (autumn), (c) JJA (winter), and (d) SON (spring). Track density is number density per month per unit area.

SOURCE: From Hoskins and Hodges (2005).

Mendes et al. (2010) analyzed the cyclogenesis climatology at surface using NCEP/NCAR reanalysis data between 1979 and 2003 and an objective method of cyclone track. The preferred region of cyclone formation in south-eastern South America observed by Gan (1992), Hoskins and Hodges (2005), and others, was also documented in this study. In addition, the authors also observed a strong correlation in this region between the propagation of baroclinic waves embedded in the western flow at high levels and the Andes Mountains, which contributes to the higher frequency of cyclogenesis.

Recent studies such as Bengtsson et al. (2006), Reboita et al. (2010a), Silva (2010), Catto et al. (2010), Catto et al. (2011), Lee (2014), Catto (2016), Shaw et al. (2016), Reboita et al. (2018), among others, investigated the cyclones and ST under a climate change perspective and found that the future position and intensity of storm tracks depend on processes that alter temperature gradients.

## 2.2 Southern hemisphere storm tracks in climate change scenarios

### 2.2.1 Observational evidence of change in the storm tracks - Recent past studies

Hartmann (2013) highlighted that may be direct observational evidence of change in the storm tracks given that the average global temperature of the land and ocean surface shows a mean warming of  $0.85^{\circ}\text{C}$  between 1880-2012, with around  $0.72^{\circ}\text{C}$  during over the period 1951-2002. The ocean has experienced less warming than land, with SST showing a warming trend between  $0.68\text{-}0.72^{\circ}$  (Hartmann (2013), table 2.5). Depending on the dataset used, land temperatures show a warming trend (two climatology periods) of  $1.14 - 1.26^{\circ}$  (Hartmann (2013), table 2.4).

The IPCC AR5 (IPCC WORKING GROUP 1 et al., 2013) concludes that “there is also low confidence for a clear trend in storminess proxies over the last century due to inconsistencies between studies or lack of long-term data in some parts of the world (particularly in the SH)”. In Southern Hemisphere, the quality and consistency of storm data vary, which also results in low confidence of large-scale changes in the intensity of extreme winds and extratropical cyclones of the 1900s.

The observational datasets are divided into observational (*in situ*) data (observations of stations) and reanalysis data (assimilated data). In relation to *in situ* data, measurement practices and instruments change/errors are the main source of errors over the time. The reanalysis datasets have quality variations, including large quality jumps when new observing systems (e.g. satellite data from 1979) are implemented. Thus, any methods of identifying the ST cannot provide homogeneous long-term information. Hodges et al. (2011) show that the newer reanalyses (e.g. ERA-Interim, CFSR) are more similar than the older ones, including relevant improvements over southern hemisphere. The new generation of reanalyses (e.g. ERA 20th century (1900-2010)) are likely to homogenize timeseries, making possible long-term analysis of STs.

## 2.2.2 Future projections

### 2.2.2.1 An overview of climate modeling

Climate models are built from different points of view and different models should be interpreted as complementary rather than incompatible.

There are two different ways to think and build a climate model, the complexity and performance. Basically, in the complexity way the models are built to represent very complex physical processes, complete and high resolution manner, and the most likely outcomes are expected. On the other hand, in the performance way, simpler and low resolution models are expected to quantify the uncertainties due to the greater number of models that can be executed. Knutti (2010) argues that with a larger number of models pushing the edges of what is plausible, less observational data can restrict the likely range of simulation and eliminate extreme or improbable values, while few models can lead to overconfidence if all are based on the same assumptions.

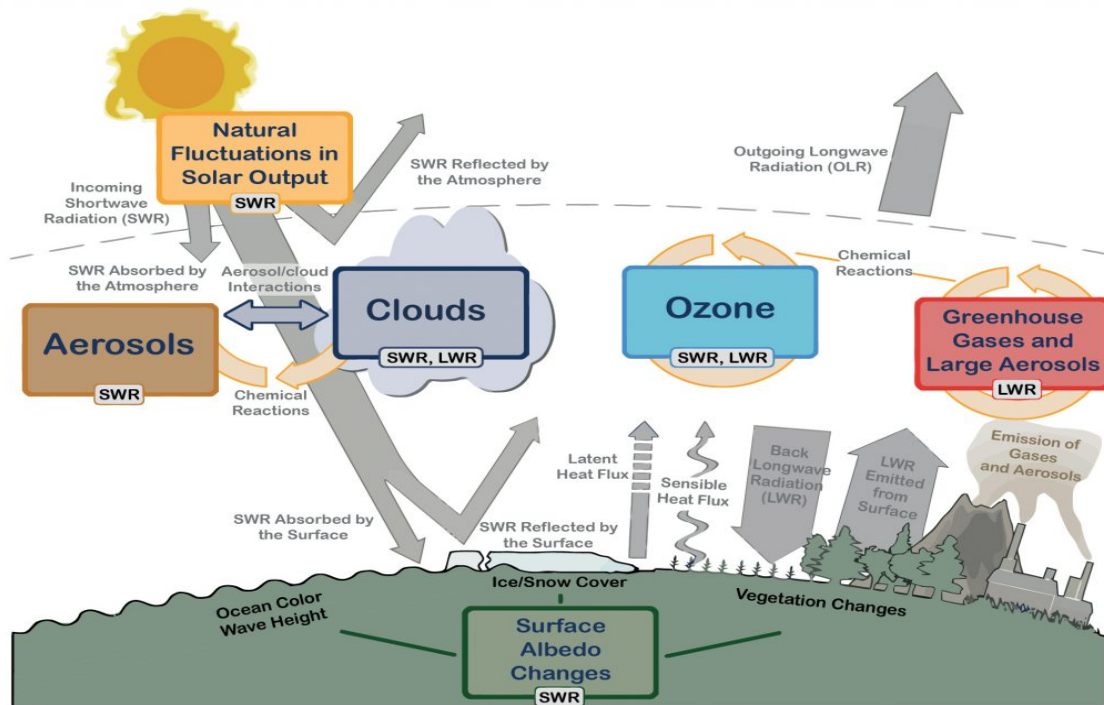
Since the 1970s, climate models have become increasingly complex through the evolution of computational power. The aim of this is to model in more detail (e.g. atmosphere-ocean) and to capture more of the drivers and feedbacks of climate change. The radiative balance between incoming shortwave solar radiation (SWR) and outgoing longwave radiation (OLR) is influenced by global climate 'drivers', as shown in Figure 2.2, which are:

- Surface albedo is modified by changes in vegetation (e.g. natural death of trees) or land surface properties (e.g.: desertification), snow/ice cover and ocean colour. These changes are driven by natural seasonal and diurnal changes, as well as human influence (e.g., land use/land cover changes) (PIELKE et al., 2011);
- Human activity changes the emissions of gases and aerosols (e.g. fossil fuel), which are involved in atmospheric chemical reactions, resulting in modified  $O_3$  and aerosol amounts;
- $O_3$  and aerosol particles absorb, scatter and reflect SWR, changing the energy balance. Some aerosols act as cloud condensation nuclei modifying the properties of cloud droplets and possibly affecting precipitation;
- Anthropogenic changes in GHGs (e.g.,  $CO_2$ ,  $CH_4$ ,  $N_2O$ ,  $O_3$ , CFCs) and

large aerosols modify the amount of outgoing LWR by absorbing outgoing LWR and re-emitting less energy at a lower temperature;

- Cloud interactions with SWR and LWR are large, because their small changes in the properties of clouds have important implications for the radiative budget;
- Natural fluctuations (e.g. sunspot, solar cycles) in the amount of incoming SWR can cause changes in the energy balance.

Figure 2.2 - Main drivers of climate change.



SOURCE: Cubasch et al. (2013).

The most important feedbacks and the timescales are shown in Figure 2.3. Feedback is defined as a process which there are changes in inflows and outflows in a system through a change in the system itself (MEADOWS; WRIGHT, 2008). There are many feedback mechanisms that determine the response of the climate system. Positive feedbacks act to reinforce/amplify the effects of a change in climate drivers, on the other hand, negative feedbacks act to reverse/diminish the climate trend, whatever direction of change is imposed on the system. Positive (+) feedbacks includes:

- Water vapor;
- Snow/ice albedo;
- Peat and permafrost decomposition.

Negative (-) feedbacks includes:

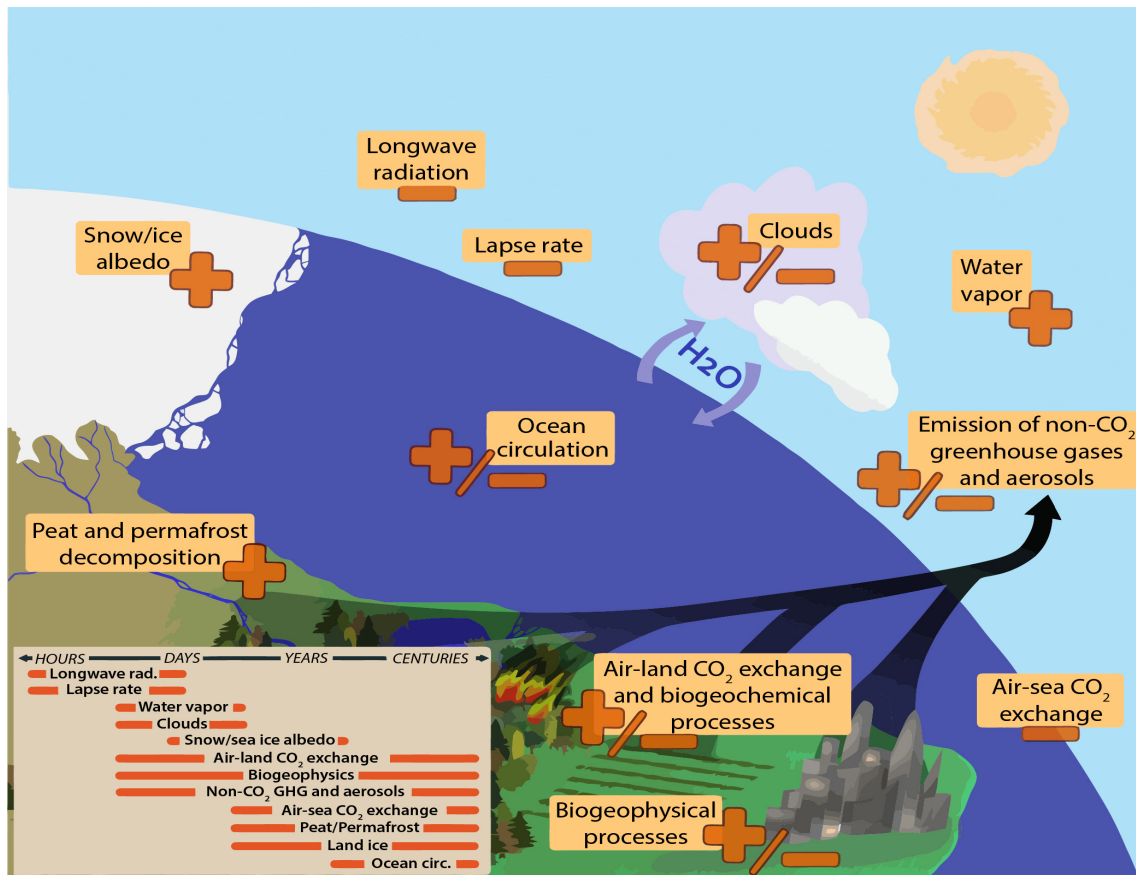
- Longwave radiation;
- Lapse rate;
- Air-sea  $CO_2$  exchange.

Sometimes feedbacks can be positive or negative ( $\pm$ ) and includes:

- Clouds;
- Ocean circulation;
- Emission of non- $CO_2$  greenhouse gases and aerosols;
- Air-land  $CO_2$  exchange and biogeochemical processes;
- Biogeophysical processes.

The climate feedback timescales (Figure 2.3, inbox) may be hours (e.g. longwave radiation) or centuries (e.g. ocean circulation) depending of the interactions and/or processes.

Figure 2.3 - Climate feedbacks and timescales.



SOURCE: Cubasch et al. (2013).

In the 1980s, given the range of climate drivers, feedbacks, timescales, physical process improvements, climate models have increased in complexity adding more coupling components and developed the first generation of Atmosphere-Ocean General Circulation Models (AOGCMs). These models were later increased in complexity adding full ocean models, physical processes and timescales, capturing more of the climate drivers and feedbacks. From 1990s, the next generation of climate models added the biogeochemical cycles (highlighted carbon and nitrogen), land use and dynamic vegetation, atmospheric chemistry and some interactions between gases, land ice, stratosphere clouds and ocean biogeochemistry (EDWARDS, 2011), called Earth System Models (ESMs). These climate model improvements were important to represent better the component interactions and climate drivers, feedbacks and timescales.

After 2000s, the climate models have been improved but the computational power increased faster, making possible a resolution increase. Most climate model in an earth system configuration have a good improvements, which has consequences for dynamic and vertical processes (increase the number of vertical levels and height of model top).

### 2.2.2.2 Storm track response to climate change scenario

Different dynamical mechanisms are responsible for the future projections in storm track position and intensity under global warming scenarios. These mechanisms produces competing effects between them, which result in multiple mechanisms to explain how the storm tracks respond to the large-scale changes. [Shaw et al. \(2016\)](#) have reviewed the recent understanding of ST response to climate change and discussed the challenges of quantifying the influence and feedbacks of different processes, such as latent heat release and the shortwave and longwave radiation associated with clouds, under future emission scenarios.

The earliest studies about the storm track response to climate change was made by [Held \(1993\)](#) through several experiments using baroclinic models to project an increase in the SH equator-to-pole temperature gradients under increasing  $CO_2$  concentration. These experiments were designed to shows a response of faster warming in lower latitudes compared to higher latitudes. The authors found that the projected changes in temperature gradients differ at upper and lower levels and that the storm tracks are affected differently according to each level of temperature gradient change. Recently, [Harvey et al. \(2014\)](#) studied the equator-to-pole temperature differences at lower levels and found this relation with the temperature gradient. Thus, when the lower level tropical temperature increase in relation to the pole, this acts to shift the storm track towards equator.

[Lorenz and DeWeaver \(2007\)](#) and most recently [Butler et al. \(2010\)](#) found the relation between the rise in the tropopause height and mid-latitude circulation changes as a result of the strengthening and poleward shift of the tropospheric zonal jets. In addition, [Butler et al. \(2010\)](#) also found that the tropical troposphere warming plays a key role in the poleward reduction of the storm tracks. Moreover, [Held and Soden \(2006\)](#) investigated the horizontal moisture transport in the CMIP3 coupled climate models and found that the moisture in the atmosphere produce two competing effects on extratropical latitudes, first more intense storms due to greater latent release, and second decreased eddy amplitudes (in order to maintain the same temperature gradient) due to greater transport of energy and moisture poleward.

While the latent heat has an important role to storm track changes, [Fyfe \(2003\)](#), [Orlanski \(2013\)](#), [Sun et al. \(2014\)](#) and [Barnes et al. \(2014\)](#) found that the stratospheric ozone also acts to shift the storm track and change the circulation. They investigate the role of Ozone in the storm tracks and the relation found was that during the Ozone depletion there is a poleward shift in the tropospheric circulation, while during the Ozone replace there is an equatorward shift. For Southern Hemisphere, [Barnes et al. \(2014\)](#) investigated the CMIP5 experiments and found that the Southern Annular Mode (SAM) is also affected by stratospheric Ozone changes. The SAM phases are very important to the climate patterns (e.g. precipitation) over the South America.

Finally, studies such as [Lu et al. \(2010\)](#) indicates an increase in the subtropical and extratropical static stability that contribute to a poleward shift, while [Raible \(2007\)](#) highlight the static stability importance to the NH genesis regions. Moreover, another studies such as [Korty and Schneider \(2008\)](#), [Ceppi and Hartmann \(2013\)](#), [Adam et al. \(2014\)](#), [Levine and Schneider \(2015\)](#), [Mbengue and Schneider \(2017\)](#), found that the changes in the location of extratropical cyclones are generally towards the poles, which occur mainly due to the increase in mean temperature and convective static stability and are directly related to the expansion of the Hadley Cell circulation.

### **2.2.2.3 Representative concentration pathways**

The representative concentration pathways (RCPs) are referred to as pathways in order to emphasize that their primary purpose is to provide time-dependent projections of atmospheric greenhouse gas (GHG) concentrations. The term pathway was chosen to meant to emphasize that it is not only a specific long-term concentration or radiative forcing outcome, such as a stabilization level, that is of interest, but also the trajectory that is taken over time to reach that outcome ([IPCC Expert Meeting Report, 2007](#)). In addition, they are representative in that they are one of several different scenarios that have similar radiative forcing and emissions characteristics.

The RCPs are composed of four future projection scenarios that were developed for CMIP5 from a range of projections of future population growth, technology evolution and societal responses ([VUUREN; RIAHI, 2011](#)). The criteria for choose the four scenarios was, among others, the fact that they were sufficiently separated from each other in terms of the radiative forcing (RF) of approximately  $2 \text{ Wm}^{-2}$ . The purpose of this choice is to provide distinguishable climatic results ([IPCC Expert Meeting Report, 2007](#)). These estimated radiative forcing is based on forcing of greenhouse

gases and other forcing agents (e.g.  $O_3$ ), but does not include direct impacts of land use (e.g. albedo) and mineral dust forcing (DAVIES-BARNARD et al., 2014).

The main characteristics of each RCP (VUUREN; RIAHI, 2011) are present as follows:

#### RCP2.6

- This scenario was developed by IMAGE from Netherlands Environmental Assessment Agency, Netherlands (VUUREN et al., 2007);
- The pathway is peak ( $3.1 \text{ Wm}^{-2}$ ) about 2050 and decline ( $2.6 \text{ Wm}^{-2}$ ) in 2100 of radiative forcing;
- The use of cropland and grasslands increases mostly driven by an increasing global population, bio-energy production, and production of animal products;

#### RCP4.5

- Developed by GCAM from Pacific Northwest National Laboratory's Joint Global Change Research Institute (JGCRI), United States (WISE et al., 2009);
- The pathway is stabilization without overshoot ( $4.5 \text{ Wm}^{-2}$ ), which total radiative forcing is stabilized shortly after 2100 due the use of new technology. See Clarke et al. (2007) for more details;
- The land use consider the preservation of large terrestrial carbon stocks in forests and a global expansion of the forest area throughout the 21st century;
- Agricultural land slightly decreases due to regeneration. Demand for food declines due to improved production, food changes and the efficiency of production and international trade.

#### RCP6.0

- This scenario was developed by AIM modeling team at the National Institute for Environmental Studies (NIES), Japan (FUJINO et al., 2006; HIJIOKA et al., 2008);

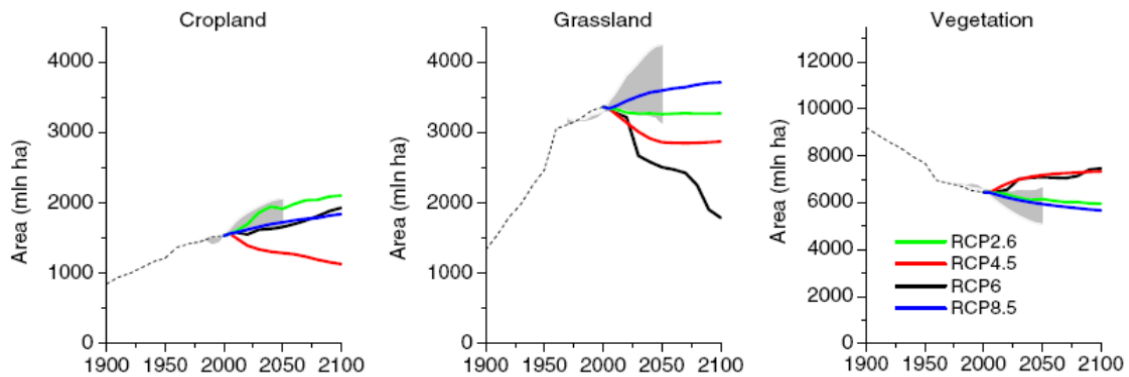
- The pathway is also stabilization without overshoot ( $6.0 \text{ Wm}^{-2}$  in 2100), with the application of a range of technologies and strategies for reducing greenhouse gas emissions;
- The land productivity has been extended from historical trends, but does not exceed regional potential, while urban land use increases due to population and economic growth;
- Agriculture cultivated area expands due to growing food demand, while pasture area declines as the extent of total forested areas remains constant throughout the century.

## RCP8.5

- Developed by MESSAGE and Integrated Assessment Framework at the International Institute for Applied Systems Analysis (IIASA), Austria (RIAHI et al., 2007);
- The pathway is rising, increasing greenhouse gas emissions over time which is representative of scenarios in the literature that lead to high greenhouse gas concentration levels;
- The use of cropland and grasslands increases in RCP8.5, mostly driven by an increasing global population;
- There is an increase of cultivated land of approximately 185 million hectares in the period 2000-2050 and another 120 million hectares in the period 2050-2100;
- Agriculture land use in developed countries declines slightly and all increases (net) occur in developing countries;
- Forest cover declined over the course of the century by 300 million hectares of 2000-2050 and another 150 million hectares by 2050-2100.

Land use is a crucial element of the new scenarios because it influences the global climate system in many different ways, including direct emissions due to land management, hydrological impacts, biogeophysical impacts (e.g. albedo, surface roughness and other changes) and also vegetation growth, which influences the removal of the atmosphere  $CO_2$  simulated by models that include the dynamic vegetation (SMITH et al., 2010). The Figure 2.4 resume the land use in each RCP scenario.

Figure 2.4 - Land use as cropland and use of grassland across the RCPs.



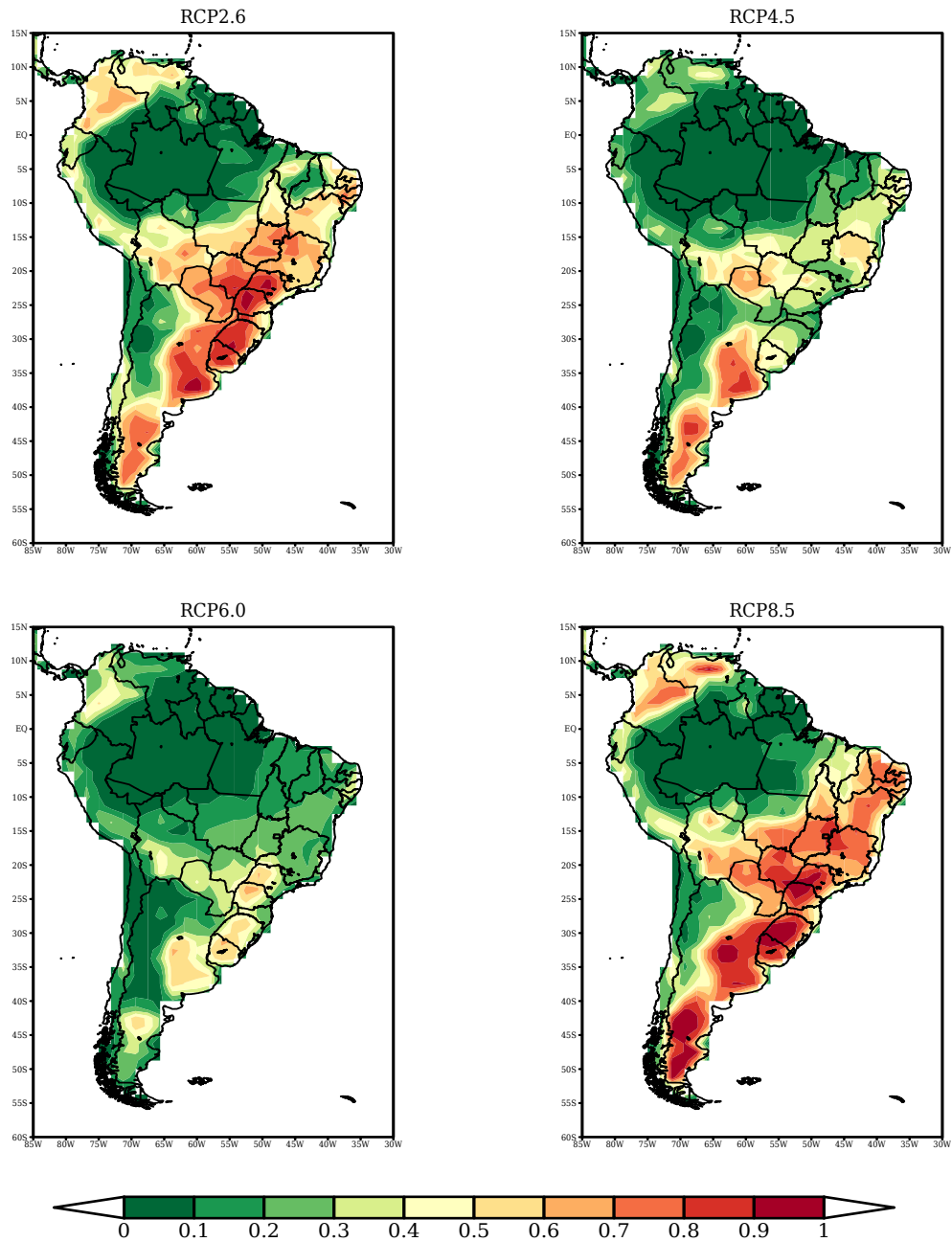
Grey area indicates the 90th percentile of scenarios reported in the literature (see [Smith et al. \(2010\)](#)). Vegetation is defined as the part not covered by cropland or anthropogenically used grassland.

SOURCE: From [Vuuren and Riahi \(2011\)](#).

The land use change is forced in the climate model for each RCP and it is shown in [Figure 2.5](#) as the disturbed fraction of vegetation. The disturbed fraction in 2100 over the Amazon Forest is similar in all of the RCP scenarios, which motivates experimental design with and without this important ecosystems for future projections.

Recent studies, such as [Hurtt \(2011\)](#), [Pitman \(2009\)](#), [Brovkin et al. \(2013\)](#), among others, highlighted that farmland and pasture have increased greatly in the last century, driven by population growth, food standards and modern agriculture. In addition, studies on the use of short-term RCPs (up to 2050) show that there is an increasing demand for cropland and pasture. There are still few papers in the literature and few models that present an explicit treatment of land use. Thus, research on the use of land use scenarios in Earth System Models (ESM) has a great potential.

Figure 2.5 - Land use change until the end of each RCP scenario in 2100.



Disturbed fraction over South America simulated by the HadGEM2-ES Earth System Model for four future scenarios at 2100: RCP2.6 (high mitigation), RCP4.5, RCP6.0, and RCP8.5 (high emissions).

SOURCE: Author's production.

#### 2.2.2.4 Land Use Cover Change as a atmospheric change source

The climatic system can not be studied through experimental methods because it has immense size and long-term scales. The scientists have made great efforts to create representations and projections of the Earth's climate based on numerical models of general circulation of the atmosphere and the terrestrial system (LEVIS, 2010). The advent of climate projections was an important step in global socioeconomic awareness of climate change, which is possible through the use of possible scenarios of greenhouse gas emissions in the form of climate scenarios.

The land surface modeling was invented to represent the atmosphere lower boundary over continental areas in climate models (MANABE et al., 1965). Mass, momentum, and energy cross this boundary via biogeochemical and biogeophysical processes, which includes the interactions with plants (SELLERS et al., 1996). Thus, the scientific research with models focuses to refine how the changing face of the land interacts with climate change. Currently, there is an estimative that about one-third to one-half of the Earth's surface has been modified by human (ELLIS, 2011). Investigate the effects of land cover<sup>2</sup> and use<sup>3</sup> on the past climate is important to explain historical changes, distinguish anthropogenic and natural influences on climate and improve future projections (VUUREN; RIAHI, 2011).

Each component of the Earth's climate system impacts life and climate on earth in different ways. The surface of the earth influences the climate through biogeophysical and biogeochemical effects (LEVIS, 2010). The biogeophysical effects on climate arise from land surface such as:

- characteristics: albedo, roughness, and;
- processes: evaporation, transpiration and others.

In comparison, biogeochemical effects arise mainly from interactions of plant ecosystems, including their soils and microorganisms associated with:

- greenhouse gases (e.g. carbon dioxide (CO<sub>2</sub>)) and related biogeochemical cycles, for example, such as carbon and plant nutrients, and;

---

<sup>2</sup>Coverage of the earth, it is meant the physical, chemical, or biological categorization of the terrestrial surface, e.g. grassland, forest, or concrete (MEYER; TURNER, 1994; MCCONNELL, 2002)

<sup>3</sup>Land use refers to the human purposes that are associated with that cover, e.g. extraction of wood and latex, raising cattle, recreation, or urban living (MEYER; TURNER, 1994)

- the cycles of mineral compounds (e.g. dust) and organic compounds (e.g. isoprene).

The terrestrial surface biogeophysical and biogeochemical effects may be due to human activity, such as land use changes (LUC), which include the conversion of natural land cover to generate energy and food, manufacturing and construction products for houses and cities, besides the use of fossil fuels (BROVKIN et al., 2013). Although these processes are so important in the correct representation of the Earth's climate, only the latest generation of climate models used in the latest climate change report (INTERGOVERNMENTAL PANEL ON CLIMATE CHANGE (IPCC), 2013) is able to represent the impacts caused by the LUC.

The new generation of Earth System Models (ESMs) may represent the combined biogeophysical and biogeochemical effects of changes in land use and greenhouse gas (GHG) emissions in the climate system. The representation of these effects is a very important advance in climate modeling because, as a comparison, in the Assessment Report Fourth (AR4), only 3 of 23 models used to compile the IPCC report incorporated land use changes into the simulations, which were still inconsistent, incomplete and with many problems to reconcile the historical land use reconstructions and future projections (HURTT, 2011). In addition, one of the major problems found to use the land use scenarios in the previous generation of ESMs was the format of the information that came from diverse sources in different formats.

### 2.2.2.5 Amazon Forest regional climate

The Amazon basin region covers an area of about 7 million  $km^2$ , while the Amazon Forest covers about 5.3 million  $km^2$  and represents approximately 40% of the global tropical forest area (NOBRE, 2014; MARENGO et al., 2018). The annual precipitation regime is about  $2200\text{ mm}\cdot\text{year}^{-1}$  which makes the Amazon basin region an important latent heat source for the atmosphere. This generates a river discharge estimated in  $210,000\text{ m}^3\text{s}^{-1}$  (from Amazon River) and it contributes with 15% of the freshwater input into the global oceans (MARENGO; ESPINOZA, 2016; NOBRE et al., 2016).

Several studies show the importance of the Amazon Forest under a climate overview, including from moisture recycling, water and carbon cycles, to deforestation, such as Salati et al. (1979), Nobre et al. (1991), Betts et al. (2004) and many others. Moreover, the rainfall spatial and temporal variability have been discussed in present climate (MARENGO; ESPINOZA, 2016) and future projected climate changes (MAGRIN et al., 2014; ALVES et al., 2017). The cycle of precipitation over the Amazon region

has different spatial distribution during the year. The rainfall in southern Amazon has the maximum during austral summer, which contrasts to the north (above the the Equator) where the maximum occurs in winter season, while in central Amazon and near the Amazon delta maximums occur during autumn (FIGUEROA; NOBRE, 1990; FISCH et al., 1998; ALVES, 2016). These seasonal and spatial variability occurs due to the meridional migration of the Intertropical Convergence Zone (ITCZ). Only the northwest Amazon not present these variabilities, this region is the wettest and shows no dry season, however, the rainfall in southern Amazon shows values lower than 100 mm during the winter season.

Recent studies such as (TORRES et al., 2012; TORRES, 2014), investigated the uncertainties involved in the future projections of temperature and precipitation changes over the South America, being all of them in CMIP3 and CMIP5 models under seven different scenarios. The authors highlight that the simulations of CMIP3 and CMIP5 models are able to represent well the observed climatological aspects, such as seasonal mean and annual cycle, although some biases are identified close to the Andes Mountains, northwest of South America, Amazon basin, and northeast of Brazil. In addition, the CMIP5 models represent the precipitation better in relation to the observations when compared to CMIP3 models.

The land use cover change is a key mechanism of climate change and it may have impacts in the regional and global-scale climate. Studies such as Nobre et al. (1991), Betts et al. (2004), D’Almeida et al. (2007), Sampaio et al. (2007), Costa et al. (2007), Pires and Costa (2013) and Spracklen and Garcia-Carreras (2015), have shown these impacts under observational and modelling overview. The main changes related to the deforestation occur in the water availability and may also have impacts in the agriculture in some regions (LAWRENCE; VANDECAR, 2015). Also, studies such as Dai et al. (2009), Nobre et al. (2016) and Marengo et al. (2018), highlight that the deforestation effects in the climate system are important to the global hydrological system, acting in many ways to reduce the river discharges, latent heat, and freshwater availability. In general these studies show that the deforestation causes a warmer climate, with less evapotranspiration and moisture convergence, over the areas affected.

### **2.3 Storm tracking methods**

In literature there are two major methods for objectively measuring the storm tracks, the Eulerian and Lagrangian methods.

The Eulerian approach focuses on the properties of the flow at a given point in space as a function of time, the properties of the field in the flow are described as the functions of the spatial and temporal coordinates. The Eulerian approach is commonly called a frequency band filter and was applied in several studies, such as Sawyer (1970), Blackmon (1976), Blackmon et al. (1977), Wallace and Blackmon (1983), Konig et al. (1993), Berbery and Vera (1996), Chang and Fu (2002). On the other hand, the Lagrangian approach evidences the tracking of mass elements and, in many cases, is unfeasible due to the complexity of the analysis to be performed. The Lagrangian approach is commonly called only track and was also applied several studies, such as Murray and Simmonds (1991), Hodges (1994), Hodges (1999), Sinclair (1997), Simmonds et al. (2008), Inatsu (2009).

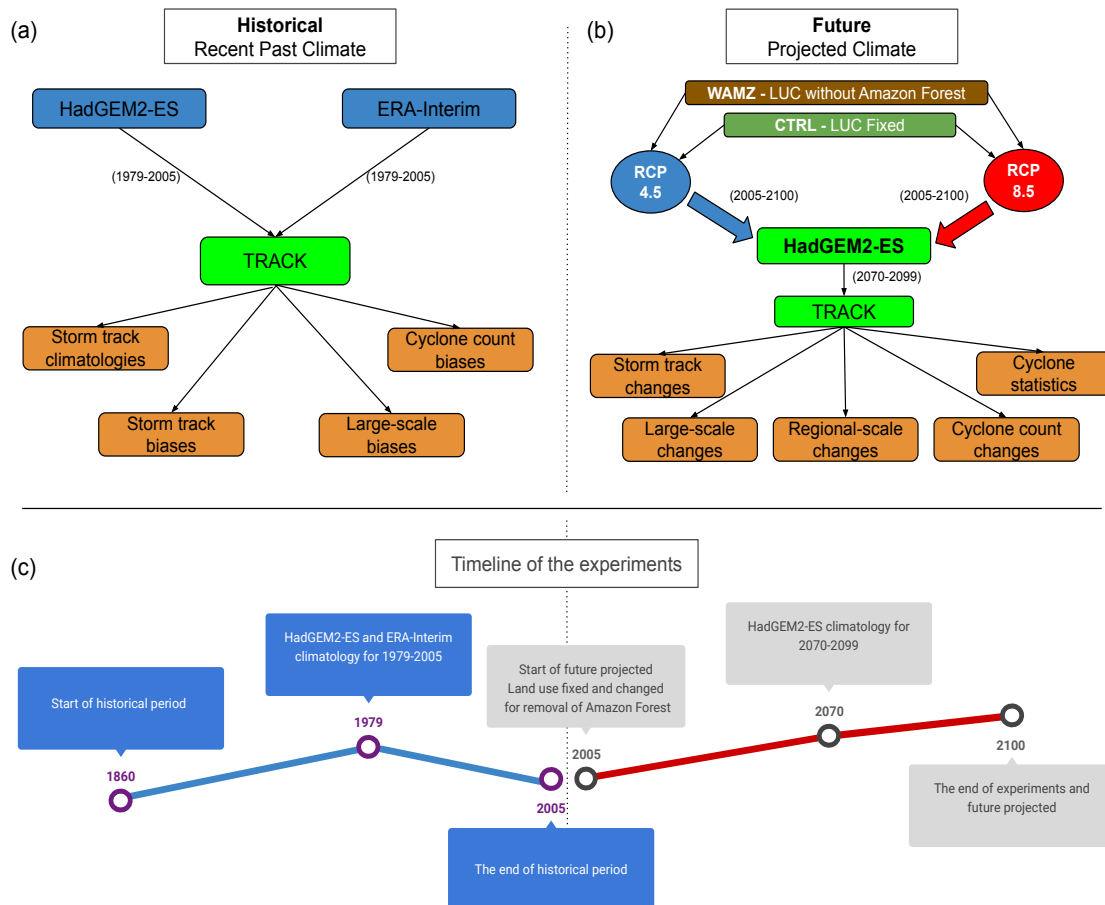
In addition to the approaches, the methods can also be classified into two classes: subjective, or manual, and objective. The first, subjective, is characterized by the recognition of the features of the cyclones, being used mainly in the decades of 70s and 80s when the information was arranged in the form of synoptic charts and satellite images, that is, non-digital form. The second method, the objective, is distinguished by the establishment of thresholds for one or more fields to identify the cyclone and/or their features. This method is the most used since the beginning of the 90s, which enable the analysis of several fields simultaneously with efficiency due to the use of the computer. In addition, this allow the comparison between the different methods and analyses.

### 3 METHODOLOGY

In this chapter the methodology for answering the scientific questions is described. The aims of this thesis required powerful computational resources and large amounts of data to run the Earth system model and to objectively identify the cyclones. The supercomputer installed at CPTEC was used to run the model. The CPTEC supercomputer is a Cray XE6, called TUPÁ, which has 30720 cores capable of 258 TFlop/s, 40 Terabytes of memory and 5 Petabytes of storage. For a more detailed overview of the supercomputer see <https://www.cptec.inpe.br/supercomputador>.

Figure 3.1 gives a schematic overview of the methodology applied in this study, which includes the historical (Figure 3.1a) and future (Figure 3.1b) setups and the timeline of the experiments associated with each one (Figure 3.1c).

Figure 3.1 - Methodology overview.



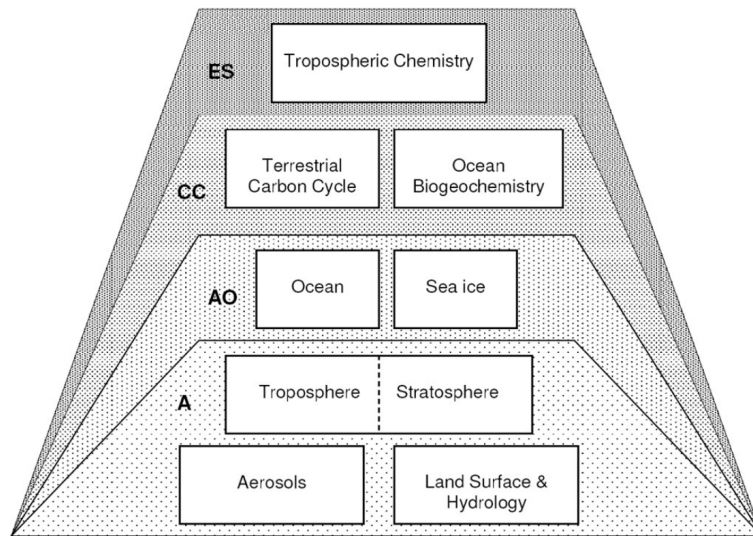
SOURCE: Author's production.

The first section of this chapter (Section 3.1) gives a technical overview of the Earth system model used in this study and the main characteristics, including the model setup, land use change configuration and the experiment design for the removal of Amazon Forest. Section 3.2 gives a description of the observational gridded datasets, such as the reanalysis and precipitation data, used in this study to assess the model performance during the historical period and analyse the extratropical cyclone biases. This is followed by a discussion of seasonal separation (Section 3.3) for the statistics and analyses. Section 3.4 provides a detailed overview of the objective cyclone tracking which is widely used in this study, including a description of the statistical methods used to compute the spatial statistics and their differences. Section 3.5 describes the large-scale and diagnostic fields used to give the dynamical background to the storm track analyses, and finally Section 3.6 describes the regional analysis over South America.

### 3.1 The HadGEM2 model

The Hadley Centre Global Environment Model version 2 (HadGEM2) is the second-generation family of models of the United Kingdom Meteorological Office (UK - Met Office), created for the purpose of performing the Coupled Model Intercomparison Project Phase 5 (CMIP5) simulations (JONES, 2011). While there is no strict definition of which processes and what level of complexity are required for an Earth system model, there is a consensus that the climate model needs to a minimum of components to be considered an Earth system model, which includes terrestrial and oceanic carbon cycles. Specifically, the HadGEM2 Earth system model includes, in addition to the atmospheric and oceanic components, representations of the terrestrial and oceanic ecosystems and tropospheric chemistry. Although the HadGEM2 model was designed from the outset to include the Earth system components, they can be disabled and the data they would produce replaced with climatological mean values. Thus, the combination of model components representing different processes allows different levels of model complexity up to the full Earth System configuration. Bellouin (2011) describe how HadGEM2 components can be combined to create different configurations, as shown in Figure 3.2.

Figure 3.2 - Processes included in the HadGEM2 model family.



Each rectangle represent a process of model, while each trapezoid represents a model configuration where the lower is contained in higher. The HadGEM2 configurations are: A - Atmosphere; AO - Atmospheric Ocean; CC - Carbon Cycle; and ES - Earth System.

SOURCE: From [Bellouin \(2011\)](#).

The earlier Hadley Centre Global Environment Model version 1 (HadGEM1) ([JOHNS et al., 2006](#)) did not include biogeochemical feedbacks, and the carbon cycle model, HadCM3LC ([COX et al., 2000](#)), used artificial correction terms to the ocean heat fluxes. Therefore, the HadGEM2 Earth system (HadGEM2-ES) configuration is the first version to run without the need for flux corrections ([COLLINS et al., 2011](#)). In comparison to previous versions, HadGEM2 includes new components with important improvements to the processes and couplings, which are described in [Tables 3.1 and 3.2](#).

Table 3.1 - Summary of main new components in the Earth system configuration from HadGEM1 to HadGEM2-ES.

New Components	Description	Reason for inclusion
Terrestrial Carbon cycle	TRIFFID dynamic vegetation scheme (COX, 2001).	To model the exchange of $CO_2$ between the atmosphere and the terrestrial biosphere, and to model changes in the vegetation distribution.
Ocean carbon cycle	diat-HadOCC ocean biology scheme (PALMER; TOTTERDELL, 2001).	To model the exchange of carbon dioxide between the atmosphere and the oceanic biosphere.
Atmospheric Chemistry	UKCA tropospheric chemistry scheme.	To allow the ozone and methane radiative forcing fields, and the sulphate oxidant fields to vary with meteorology and climate.
Aerosols	Fossil-fuel organic carbon, ammonium nitrate, dust and biogenic organic aerosols added.	These important anthropogenic and natural aerosol species are now represented in the model.

SOURCE: Adapted from Collins et al. (2011).

Table 3.2 - Summary of main new couplings in the Earth system configuration from HadGEM1 to HadGEM2-ES.

New couplings	Description	Reason for inclusion
Chemistry-radiation	Radiative effects of $O_3$ and $CH_4$ are taken from the interactive chemistry.	This allows the concentrations of these species to vary with climate and tropopause heights.
Chemistry-hydrology	The emissions of methane from wetlands are supplied from the hydrology scheme to the chemistry scheme.	The emissions and hence concentrations of methane will vary as climate impacts on the extent of wetlands.
Chemistry-Aerosols	Sulphate oxidation scheme takes its oxidants from the interactive chemistry.	The sulphur oxidation will now be affected by meteorology and climate.
Ocean carbon cycle-DMS	DMS emission now interactively generated by the ocean biology.	This important source of sulphate aerosol will now vary as climate change affects the plankton.
Vegetation-Dust	Dust emissions depend on the bare soil fraction generated by the vegetation scheme.	Dust production will vary as climate change affects the vegetation distribution.
Dust-Ocean carbon cycle	Dust deposition affects plankton growth.	The supply of nutrients to the plankton varies with the dust production. This coupling also allows geo-engineering experiments to be simulated.

SOURCE: Adapted from Collins et al. (2011).

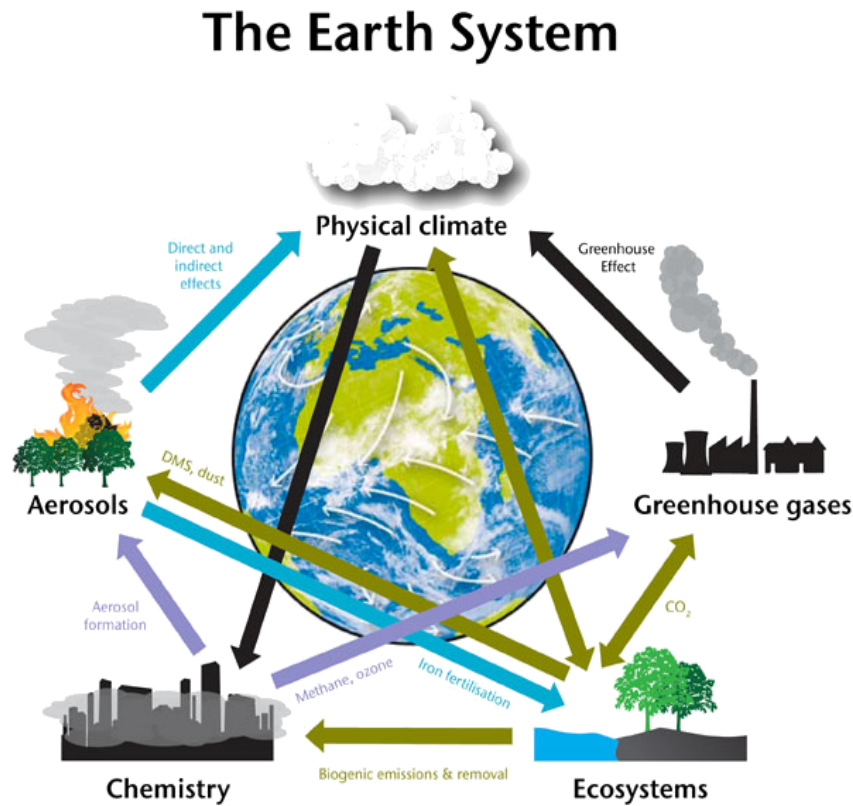
### 3.1.1 Earth system configuration

For this study the HadGEM2 Earth system model (HadGEM2-ES), the most complete configuration available, is used to simulate the historical period and the projected future climate and impact of removing the Amazon. HadGEM2-ES is a coupled Atmospheric Ocean Global Circulation Model in which the atmospheric component usually runs at N96 horizontal resolution ( $1.875^\circ \times 1.25^\circ$ ) with 38 vertical levels (hybrid coordinates); and the ocean component resolution is  $1.0^\circ$  (increasing to  $1/3^\circ$  at the equator) with 40 vertical levels. The HadGEM2-ES simulations use a timestep of 30 minutes for the atmosphere/land and 1 hour for the ocean. The model also includes interactive ocean and land carbon cycles and dynamic vegetation with prescribed or simulated  $CO_2$  concentrations (MARTIN, 2011). An interactive tropospheric chemistry scheme is also included to simulate the interactions with atmospheric aerosols and the evolution of atmospheric composition (BELLOUIN, 2011; COLLINS et al., 2011). In particular, the representation of the tropospheric Ozone ( $O_3$ ) is very important for the Southern Hemisphere because the  $O_3$  depletion/recovery directly affects the storm track variability (BARNES et al., 2014).

The Earth system can be represented by five components in the HadGEM2-ES model: the physical climate, greenhouse gases, ecosystems, atmospheric chemistry and aerosols (COLLINS et al., 2011). The interactions between these components of the earth system are shown in Figure 3.3. Different feedbacks seen in the figure can be investigated using the HadGEM2-ES model. For example, HadGEM2-ES includes a dust aerosol scheme whose emissions are coupled to a dynamic vegetation model (see Table 3.1). The dust affects the climate through its influence on radiation and ocean biogeochemistry (affects plankton growth). Dust production, in turn, varies as climate change affects the vegetation (Table 3.2). Another example is the loop from the climate impacts on ecosystems that change the carbon dioxide concentration in the atmosphere and the greenhouse effect which, in turn, impact back on climate.

HadGEM2-ES has an extensive diagnostic output and in this study the variables were chosen according to the Coupled Model Intercomparison Project Phase 5 (CMIP5) protocol archive. Thus, the output is available either at certain prescribed frequencies or as time-averaged values over certain periods, as detailed in the CMIP5 output guidelines (for more details see the CMIP5 design in Taylor et al. (2012)).

Figure 3.3 - Representation of each component and interactions in the HadGEM2-ES model.



SOURCE: Adapted from MetOffice (2015).

### 3.1.2 Land Use Cover change configuration in HadGEM2 model

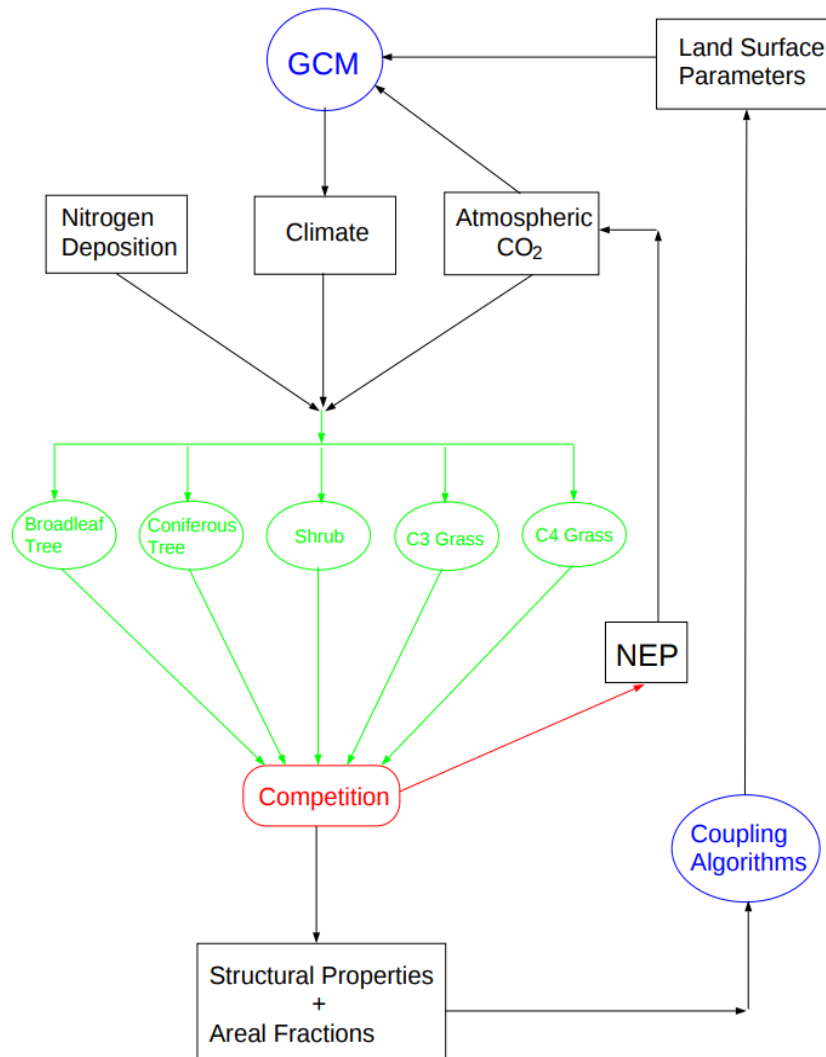
In the HadGEM2 model the terrestrial carbon cycle is represented by the second version of the “Met Office Surface Exchange Scheme” (MOSES2) (ESSERY *et al.*, 2003), which simulates the water cycle, energy and carbon balances between the land surface and atmosphere, coupled to the global dynamic vegetation model “Top-Down Representation of Interactive Foliage and Flora Including Dynamics” (TRIFFID) (COX, 2001). The TRIFFID model simulates the coverage and competition between five Plant Functional Types (PFT): broadleaf tree, needle leaf tree, C3 grass, C4 grass and shrub. MOSES2 recognises the five TRIFFID vegetation types and four types of non-vegetated land cover: bare soil, urban area, lakes and land ice.

The PFTs compete with each other on the basis of competition rules and the net carbon uptake of each PFT simulated within the land-surface scheme closely coupled

with the water budget (COX, 2001). For natural disturbance, the model prescribes a uniform disturbance rate, so that there is no representation of the effects of climate on disturbance regimes such as wind throw, fire, disease or insect attack, and no explicit representation of herbivory. The implicit assumption in the model, therefore, is that natural disturbance regimes remain constant over time. The competition between PFTs is based on the Lotka-Volterra competition equations (prey and predator) and on a hierarchy of dominance in which shrub dominates grasses (i.e. it always displaces fractional coverage of grass), and trees dominate both grasses and shrub (COX, 2001). For more details on the competition between the PFTs, see Cox et al. (2000), Cox (2001).

A schematic of the coupling between the global dynamic vegetation model (TRIFFID) and the global climate model (HadGEM2-ES) is shown in Figure 3.4. The distribution and structure changes of the PFTs can provide a feedback to climate via two routes. First, the vegetation determines the biophysical land-surface parameters (e.g. albedo, roughness length, stomatal conductance), which in turn affect the land-atmosphere fluxes of heat, water and momentum. Second, changes in the carbon stored in vegetation and soil (measured by the net ecosystem productivity (NEP)) can modify the atmospheric  $CO_2$ , and thus the climate through the greenhouse effect. In addition, for completeness nitrogen deposition is also shown as a driver for vegetation change, although this version of TRIFFID does not include an interactive nitrogen cycle.

Figure 3.4 - Schematic coupling between TRIFFID and HadGEM2-ES.

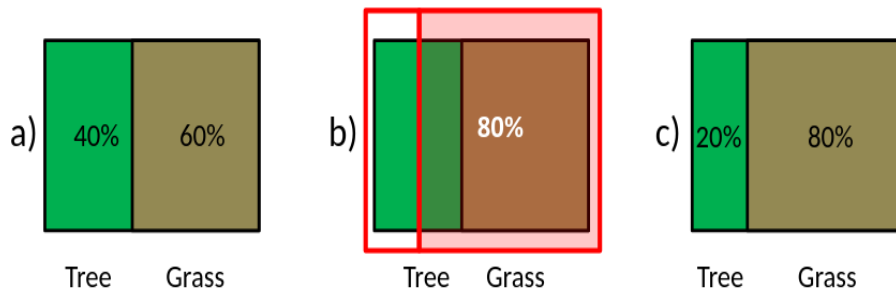


SOURCE: Cox (2001).

Under the RCP scenarios, HadGEM2-ES simulates the crop and pasture fraction from harmonized land-use change (LUC) scenarios through the imposition of a mask called agriculture mask or, as termed in this study, “disturbed fraction“ (DFRAC). Basically, the DFRAC designates a specific fraction of the grid box in which the dynamical vegetation is unavailable to tree and shrub PFTs, therefore all agricultural land, including the croplands, is represented as C3 or C4 grass. These grass types are chosen according to the local climate conditions. Figure 3.5 illustrates how HadGEM2-ES designates the DFRAC. For example, if a grid box would naturally have 40% tree and 60% grass (Figure 3.5a), but the DFRAC is 80% (Figure 3.5b), then the tree fraction is limited to 20% (Figure 3.5c). The TRIFFID vegetation dynamics module simulates growth of grass or not (i.e., allocates bare soil) in the

remaining 20% area depending on the local climate. Therefore, when the DFRAC mask increases, the natural vegetation is removed, however, when the DFRAC decreases, TRIFFID simulates regrowth of trees and grasses in that place, depending on whether the climate is propitious. The disturbed fraction mask varies between 0 and 1 and is forced to the dynamic vegetation every 10 days.

Figure 3.5 - Representation of the disturbed fraction in the HadGEM2-ES model.



SOURCE: Author's production.

Another important feature of HadGEM2-ES is that terrestrial ecosystems and hydrology are tightly coupled, thus a climatic or anthropogenic perturbation can change the vegetation cover and affect the surface evaporation and transpiration rate, resulting in changes in soil moisture and runoff. [Betts et al. \(2007\)](#) highlighted that changes in vegetation due to increased availability of  $CO_2$  affect hydrology through changes in transpiration. When  $CO_2$  concentration increases, plant stomata generally open less widely, therefore the transpiration is reduced and soil moisture and runoff increase. Also, the physical properties of the surface, such as albedo, roughness, and factors that affect the availability of moisture to evaporation, are directly influenced by the distribution of PFTs, the simulated leaf area index for each PFT and the fractional cover of ice, water and bare soil. Therefore, land use changes in the HadGEM2-ES model alter the vegetation cover which directly affects the surface energy and moisture budgets ([BETTS et al., 2015](#)).

In this section the land use concept and configuration in the HadGEM2-ES model was presented. For the experimental design of the removal of Amazon Forest, see Section 3.1.3.2.

### 3.1.3 HadGEM2-ES experimental design

This section presents an overview of the HadGEM2-ES experiments under CMIP5 experimental design that are used in this study. For a detailed overview of the implementation of CMIP5 simulations in HadGEM2-ES, see [Jones \(2011\)](#).

#### 3.1.3.1 Historical

The HadGEM2-ES Historical experiment is forced by the observed atmospheric composition, which reflect both the anthropogenic and natural sources, and the time evolution of land cover. [Flato et al. \(2014\)](#) highlighted that a comprehensive set of historical data of anthropogenic emissions and land use change (LUC) has been assembled for CMIP5 experiments in order to produce a relatively homogeneous ensemble of historical simulations with a common time series of forcing agents. The forcing agents are given in the form of both emissions and concentrations of gases aerosols, LUC and natural forcings (e.g. solar radiation) ([INTERGOVERNMENTAL PANEL ON CLIMATE CHANGE \(IPCC\), 2013](#)). For a more detailed overview of the forcing agents, see [Flato et al. \(2014\)](#), page 760, and [Meinshausen et al. \(2011\)](#).

The HadGEM2-ES historical simulations produced at the Met Office Hadley Centre consist of four model runs generated from different initial conditions, each one referred to as an ensemble member. The initial condition ensembles are required by the CMIP5 protocol in order to estimate if any apparent changes in climate may occur due to internal variability in the simulations ([VUUREN et al., 2011](#)). Simulations obtained from small perturbations in the initial conditions may be influenced by a long-term memory of the initial state associated with multidecadal oceanic processes. Thus, care must be taken in selecting a sufficient range of initial states in relation to the decadal modes, so that the ensemble mean provides an unbiased estimate of the model's response to imposed forcings. The initial conditions for individual ensemble members in the HadGEM2-ES historical simulations were selected using an objective method at 50-year intervals (years 1860, 1910, 1960 and 2010) from a long pre-industrial control run. However, indices of long-term variability, associated with the main modes of decadal variability of the climate system - the Atlantic Multidecadal Oscillation (AMO) ([ENFIELD et al., 2001](#)) and the Pacific Decadal Oscillation (PDO) ([POWER et al., 1999](#)), were used to monitor whether these initial states are independent of each other. For more details on this methodology to select the initial conditions, see [Jones \(2011\)](#).

In this study, the four ensemble members of the HadGEM2-ES Historical simulation

produced at the Met Office Hadley Centre are together referred to as HadGEM2-ES HIST. Table 3.3 shows the list of HadGEM2-ES ensemble members for the Historical experiment.

As a reference, there is another member of the HadGEM2-ES historical ensemble that was later produced at INPE. This member has been assessed according to the CMIP5 protocol and is available on the CMIP5 data portal (Mariane Coutinho personal communication).

Table 3.3 - HadGEM2-ES experiments for historical period between 1976-2005.

	<b>Experiment</b>	<b>Ensemble member</b>	<b>Name</b>
<b>HadGEM2-ES</b>	Historical (HIST)	1	aabna
		2	aabnm
		3	aabny
		4	aabnz

SOURCE: Author's production.

The HadGEM2-ES Historical experiment is forced from the start of the second industrial revolution to the present day, years 1860-2005. In this study the climatological periods are calculated as the mean of:

- the last 30 years of the historical experiment (1976-2005) that will be used to represent the present day in comparisons with the RCP experiments (see Section 3.1.3.2);
- the last 27 years of the historical experiment (1979-2005) that will be used for verification against the ERA-Interim reanalysis, which is the common period between these two datasets.

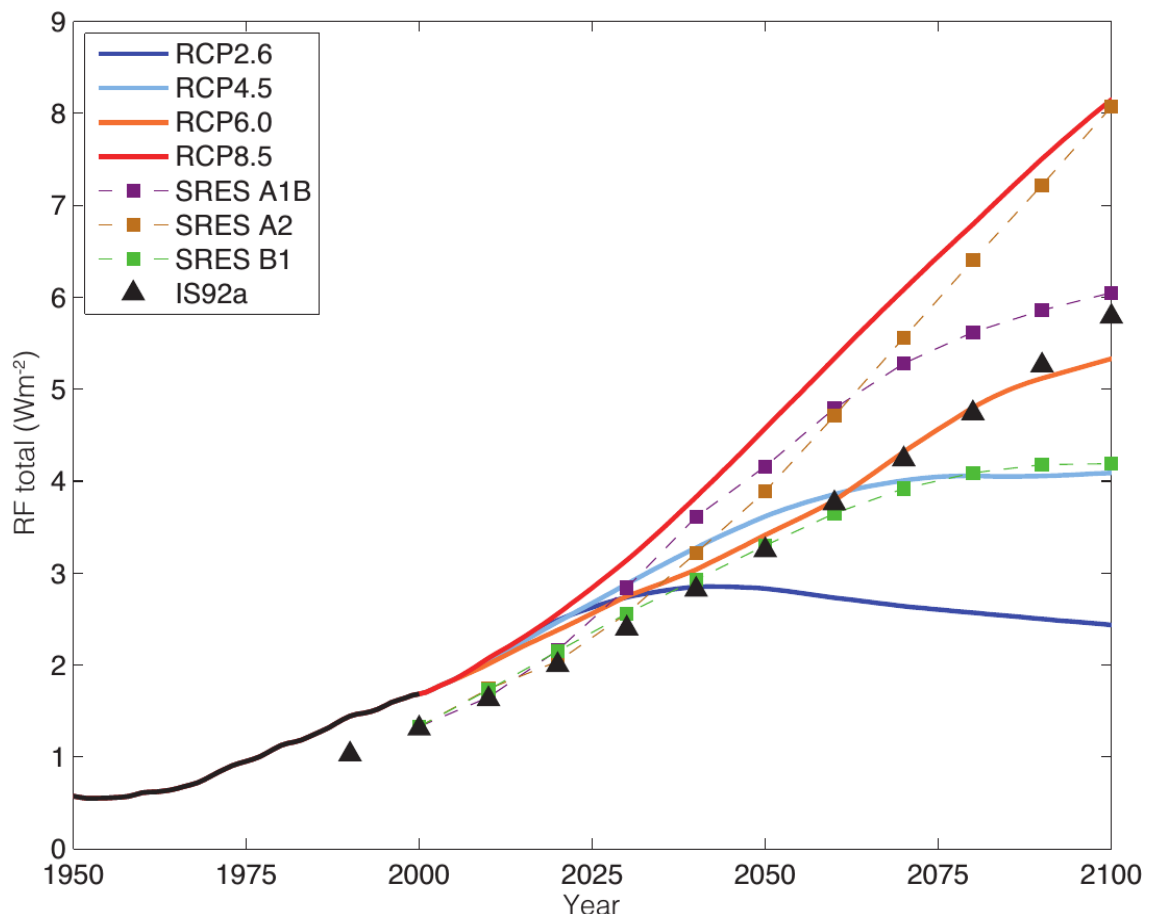
### 3.1.3.2 Representative Concentration Pathways

The Representative Concentration Pathways (RCPs) are composed of four future projection scenarios that were developed for CMIP5 from a range of projections of future population growth, technology evolution and societal responses (TAYLOR et al., 2012). These RCPs were designed to facilitate interactions among scientific working communities on climate change, adaptation and mitigation (HURTT, 2011).

For more details on scenario development, see Section 2.2.2.

While the IPCC Special Report on Emissions Scenarios (SRES) used for both IPCC TAR (INTERGOVERNMENTAL PANEL ON CLIMATE CHANGE (IPCC), 2001) and AR4 (INTERGOVERNMENTAL PANEL ON CLIMATE CHANGE (IPCC), 2007), does not allow options for policy intervention, the RCPs are mitigation scenarios and internally consistent sets of time-dependent forcing projections, that assume policy actions will be taken to achieve certain emission targets (MOSS, 2007; MOSS et al., 2010; TAYLOR et al., 2012). The four RCPs have a rough estimate of the radiative forcing (RF) in the year 2100 (relative to pre-industrial conditions), from 2.6 to  $8.5 \text{ Wm}^{-2}$ , each labeled according to the RF, as shown in Figure 3.6.

Figure 3.6 - Historical and projected total anthropogenic RF ( $\text{Wm}^{-2}$ ) relative to the pre-industrial between 1950 and 2100.



Previous IPCC assessments (SAR IS92a, TAR/AR4 SRES A1B, A2 and B1) are compared with the IPCC 2013 - AR5 RCP2.6, RCP4.5, RCP6.0 and RCP8.5

SOURCE: From Cubasch et al. (2013).

Despite there being four RCPs in CMIP5, in this study only the RCP4.5 and RCP8.5 were chosen because they are the respective medium-low and highest emission scenarios. Similar to the Historical experiment, the HadGEM2-ES under these two RCP scenarios is executed according to the CMIP5 protocol for emissions and concentrations, however the LUC is fixed to 2005. In addition, two experiments for the RCPs are designed to simulate the impact of the removal of the Amazon Forest and are shown in Table 3.4. A total of 16 runs were executed using the TUPÃ - Cray Supercomputer. For more details on the RCPs, see Section 2.2.2.3.

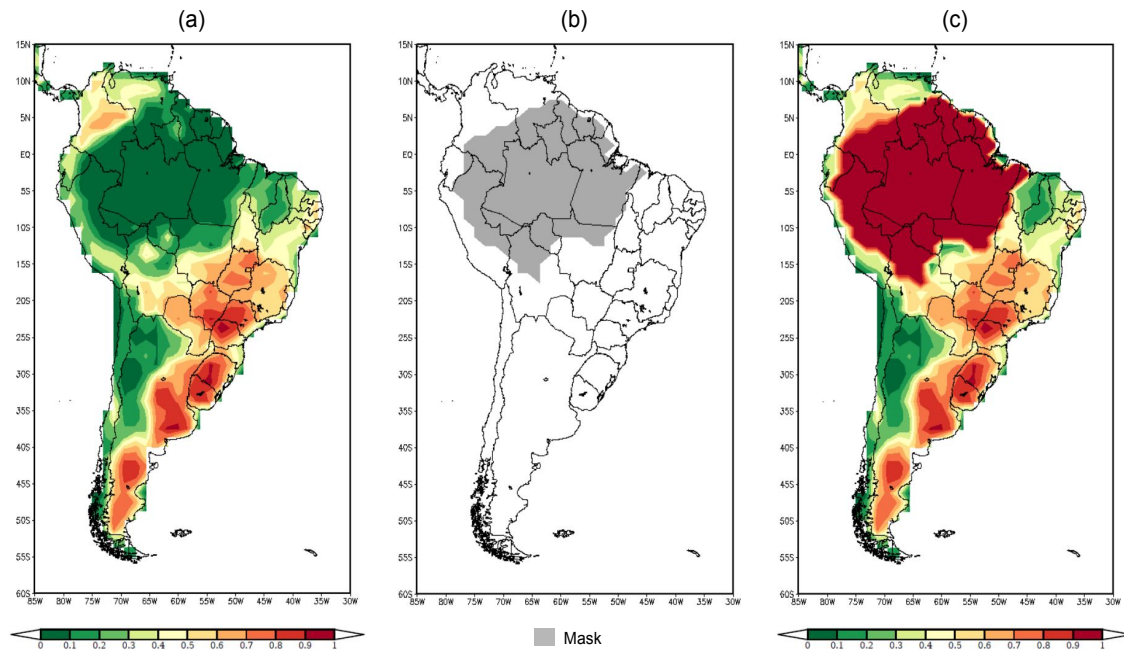
Table 3.4 - HadGEM2-ES experiments for future projected changes 2006-2100.

	Experiment	Land use change	Ensemble member	Name
<b>RCP8.5</b>	Without Amazon Forest (WAMZ)	DFRAC = 1 over Amazon Forest	1	aacdh
			2	aacdi
			3	aacdj
			4	aacdk
	Fixed 2005 (CTRL)	DFRAC fixed	1	aacdd
			2	aacde
			3	aacdf
			4	aacdg
<b>RCP4.5</b>	Without Amazon Forest (WAMZ)	DFRAC = 1 over Amazon Forest	1	aacdp
			2	aacdq
			3	aacdr
			4	aacds
	Fixed 2005 CTRL	DFRAC fixed	1	aabsb
			2	aabsn
			3	aabsf
			4	aabsj

SOURCE: Author's production.

To configure the removal of the Amazon Forest, a program using python/R was developed to change the disturbed fraction for the HadGEM2 input file (ancillary file in Met Office pp format) and the result is shown in Figure 3.7. Further, the program Mkuncil (version 0.55) from the Met Office Hadley Centre was used to create the modified ancillary input file for the HadGEM2 model.

Figure 3.7 - Land use change for the experiments with and without Amazon Forest.



The land use change is modified by the parameter disturbed fraction in the HadGEM2-ES model. Disturbed fraction is fixed on 2005 (a) for the CTRL experiments; and a mask is applied to change the disturbed fraction only over Amazon Forest (b); the result (c) is used to force dynamic vegetation module to remove the Amazon Forest for WAMZ experiments.

SOURCE: Author's production.

The WAMZ and CTRL experiments in both the RCP scenarios are run from 2005-2100. In this study, the climatology for a 30-year period was chosen to be 2070-2099. These experiments will be compared, (WAMZ minus CTRL for each respective RCP), and with the Historical experiment, analyzed in Chapter 4, for the 30-year period of 1976-2005.

## 3.2 Gridded observational data

### 3.2.1 ERA-Interim

The second dataset used in this study is the ERA-Interim reanalysis (DEE et al., 2011). This is used to provide verification of the model results. The ERA-Interim reanalysis uses the Cy31r2 version of the ECMWF atmospheric model that includes a revised cloud scheme, including treatment of ice supersaturation, implicit computation of convective transports, modified orographic drag, salinity effect on saturation at ocean surface and gust fix for orography. The data assimilation used is a 4D-Variational data assimilation scheme (4D-Var) that includes a variational bias adjustment of the observations prior to assimilation (DEE et al., 2011). These improvements in the reanalysis system are important especially for the SH where the observations are less dense than in the NH, particularly the terrestrial observations.

ERA-Interim is an evolution from the ERA-40 reanalysis (UPPALA et al., 2005), which improves some key aspects of the data assimilation, such as variational bias correction of satellite radiance data. Table 3.2.1 presents some of the main features of ERA-40 in relation to the ERA-Interim reanalysis. The main advances of the ERA-Interim are a better representation of the hydrological cycle, the stratospheric circulation and temporal consistency across multiple time-scales (DEE et al., 2011).

Table 3.5 - Comparison of main features between ERA-40 and ERA-Interim reanalysis.

	<b>ERA-40</b>	<b>ERA-Interim</b>
<b>Horizontal resolution</b>	~125 km	~79 km
<b>Levels</b>	60	60
<b>Data Assimilation</b>	3D-VAR	4D-VAR
<b>Surface Model</b>	TESSEL - 4 layers	TESSEL - 4 layers

SOURCE: Adapted from Uppala et al. (2005) and Dee et al. (2011).

However, there are a few known quality issues in the ERA-Interim reanalysis, which are:

- Some spurious shifts along time-series associated with changes in the observation system, for example, the different satellite ozone instruments and their availability;

- Underestimation of low and medium cloud cover when there is high cloud cover;
- Overestimation of the incident solar radiation at the top of atmosphere (TOA) around  $3 \text{ Wm}^{-2}$  due to forecast calculation error.

These errors, reported in [Dee et al. \(2011\)](#), are considered to have a small impact on the 27-year climatologies computed in this study.

### 3.2.2 Global Precipitation Climatology Project

The gridded precipitation dataset from the current Global Precipitation Climatology Project (GPCP), version 2.3 ([ADLER et al., 2018](#)), is used to assess the HadGEM2-ES for the historical period (1979-2005). This dataset was used because the precipitation from reanalysis is a product of the forecast model inside the assimilation system, which can be subject to spin-up from the initial conditions. The GPCP is based on observation datasets such as gauge measurements and satellite estimates of rainfall, including a variety of calibration and validation methods. The data is available at a spatial resolution of  $2.5^\circ$ .

In relation to the earlier version (2.2) ([ADLER et al., 2003](#)), the improvements of GPCP v2.3 are:

- Corrections in cross-calibration of satellite data inputs and updates to the gauge analysis;
- Improvements in the ocean from 2003 resulted in an overall precipitation increase of 1.8% after 2009;
- Updating the gauge analysis to its final, high-quality version increases the global land total by 1.8% for the post-2002 period.

Therefore, these changes correct a small and incorrect underestimation in the estimated global precipitation over the last decade ([ADLER et al., 2018](#)).

### 3.3 Statistics and analysis by seasons

The statistics and analyses for all data in this study are made for meteorological seasons, June, July and August (JJA) for winter; September, October and November (SON) for spring; December, January and February (DJF) for summer; and March,

April and May (MAM) for autumn. While other studies use longer periods, such as cold and warm periods, the three-month climatology periods are chosen because it allows a comparison with the majority of other older studies that use the same methodology for climatologies.

However, [Hoskins and Hodges \(2005\)](#) highlighted two particular aspects that should be considered in this kind of analysis over the Southern Hemisphere. First, the average lag in the temperature response which is higher ( $\sim 44$  days) than in the Northern Hemisphere ( $\sim 33$  days) ([HURRELL et al., 1998](#)). The second, and more important, is the strong semiannual oscillation in the Southern Hemisphere, particularly in the latitude and strength of the circumpolar surface pressure trough and mid-tropospheric temperature gradients, which mainly impact the transition seasons ([LOON, 1967](#)). Both of these occur due the large thermal inertia of the oceans which has a greater influence in the SH climate.

### **3.4 Extratropical cyclone tracking**

In this study the objective feature tracking of [Hodges \(1994\)](#), [Hodges \(1995\)](#), [Hodges \(1996\)](#), [Hodges \(1999\)](#), called TRACK is used. TRACK is described in the Sections 3.4.1 and 3.4.2, followed by the method to compute the track statistics in Section 3.4.3. This methodology has been widely used and improved in [Hoskins and Hodges \(2002\)](#), [Hodges et al. \(2003\)](#), [Hoskins and Hodges \(2005\)](#), [Bengtsson et al. \(2006\)](#), [Hodges et al. \(2011\)](#). Also, the methodology has been applied in many studies for the Southern Hemisphere such as [Silva \(2010\)](#), [Guia \(2010\)](#), [Pinheiro \(2010\)](#), [Lima \(2011\)](#), [Parise \(2014\)](#), [Pinheiro \(2018\)](#) and [Oliveira \(2019\)](#). For a comparison between the main characteristics of other methods for identifying the storm tracks, see Section 2.3. As discussed in Section , the distribution of extratropical cyclones is to be referred to as the 'storm track', similar to previous studies such as [Hoskins and Hodges \(2005\)](#), while the term 'cyclone track' refers to the path of an individual cyclone.

#### **3.4.1 Objective feature identification**

The TRACK is designed to run in a sphere to avoid the need to use projections which can introduce biases ([HODGES, 1995](#)), however the initial cyclone identification is performed on a polar stereographic projection to avoid bias introduced when using a latitude-longitude projection, particularly in middle and high latitudes.

The tracking is applied to 6 hourly relative vorticity at 850 hPa to identify the

cyclones. The benefits of using the relative vorticity are that it focuses on smaller spatial scales than other fields, however, it is a noisy field. Hence the vorticity is spectrally filtered by truncation to T42 and the large-scale background is removed for total wavenumbers  $\leq 5$ . Cyclones are initially identified as minima in the filtered vorticity field, for the SH, and then refined by determining the off-grid locations using B-spline interpolation and steepest descent minimization, this produces smoother tracks.

TRACK identifies all the feature points of the cyclones in the gridded dataset, so they will be grouped into cyclone tracks. First, the algorithm uses the nearest neighbor approach, which checks the nearest point within the same features and associate with the trajectory, but this imposes a constraint on the maximum distance between these points. Thus, these are improved by minimizing a cost function which depends on the local smoothness function to obtain the minimal set of smoothest tracks, as shown in Hodges (1994). This smoothness function is measured in terms of changes in direction and speed and requires a minimum of three consecutive frames of the track (HODGES, 1999).

While a set of tracks is initialized from the identified feature points for the required time sequence (subject to the constraints), the incomplete tracks are padded out with “phantom” feature points so that all tracks have the same number of points and span the length of the time series. This is important because the optimization swaps points on the tracks to give the greatest gain in smoothness and proceeds both backward and forward in time to ensure that there is no feature point ordering dependence in the final result (HODGES, 1999). In addition to the objective feature identification and tracking, the track algorithm also uses thresholds to remove stationary systems which have a timelife less than a time interval (e.g. two days) and displacement less than a interval in kilometers (e.g. 500km).

The execution of the Track is given as follows:

- a) Feature points are then identified as maxima or minima on the grid. These are refined using B-spline interpolation and steepest ascent/descent optimization.
- b) After the objects are identified, the diagnostic process is started and the object points are analyzed and compared to their neighbors. If they are similar, the Track performs the grouping, detection of the center and choice of the representative point of the group, termed as feature point. Thus,

the location (latitude and longitude) and field value relative to the feature point are stored;

- c) Finally, the TRACK will perform the steps described above for the next time step and apply the nearest neighbor approach and cost function optimization to solve the problem of matching the time steps and smoothest tracks. The cost function is given by

$$\Xi = \sum_{i=1}^m \sum_{k=2}^{n-1} D(P_i^{k-1}, P_i^k, P_i^{k+1}) \quad (3.1)$$

where  $D(P_i^{k-1}, P_i^k, P_i^{k+1})$  is called the local deviation in time step  $k$ , with  $m$  the total number of *tracks* and  $n$  the total number of time steps. Also,  $P_i^k$  is the position vector in Cartesian space (a point on the sphere is represented as a unit vector in Cartesian space) for a feature point on track  $i$  at time step  $k$ . The local deviation implemented in Hodges (1999) is defined by thresholds:

$$D(P_i^{k-1}, P_i^k, P_i^{k+1}) = \begin{cases} 0 & \text{if } P_i^{k-1} \text{ is a phantom feature} \\ & \text{point, and } P_i^k \text{ and } P_i^{k+1} \\ & \text{are real or phantom;} \\ \psi(P_i^{k-1}, P_i^k, P_i^{k+1}) & \text{if } P_i^{k-1}, P_i^k \text{ and } P_i^{k+1} \text{ are real} \\ & \text{feature points and;} \\ \Psi & \text{otherwise,} \end{cases}$$

where  $\psi(P_i^{k-1}, P_i^k, P_i^{k+1})$  is a measure of the change of speed and direction over three time steps and  $\Psi$  is now a global upper bound of smoothness constraint that is applied when there is no position information and intensity of track under review, as follows:

$$\psi(P_i^{k-1}, P_i^k, P_i^{k+1}) = 0.5w_1(1 - \hat{T}_i^{k-1,k} \cdot \hat{T}_i^{k,k+1}) + w_2 \left( 1 - \frac{2[||P_i^{k-1}P_i^k|| ||P_i^kP_i^{k+1}||]^{1/2}}{\partial[||P_i^{k-1}P_i^k|| + ||P_i^kP_i^{k+1}||]} \right)$$

where the first term measures directional similarity and the second term measures speed similarity. The unit vector  $\hat{T}_i^{k-1,k}$  represent the direction from point  $P_i^{k-1}$  to point  $P_i^k$  with  $||P_i^{k-1}P_i^k||$  as defined above. Both  $\hat{T}_i^{k-1,k}$

and  $\|P_i^{k-1}P_i^k\|$  will depend on the domain of application, here taken as spherical domain. See Hodges (1995) for further details.

### 3.4.2 Cyclone tracking using TRACK

The spatial statistics are computed using the spherical kernel method, which reduces the biases in relation to a conventional system of projection (HODGES, 1996). Tracks are initialised using a nearest neighbour method and then refined by minimising a cost function for track smoothness subject to constraints on displacement distance in a time step and the track smoothness. The minimization is performed subject to adaptive constraints on the local displacement and track smoothness (HODGES, 1999). This is the same methodology as previously used by Hoskins and Hodges (2002). On completion of the tracking, the tracks are filtered to retain only the mobile systems that, in this study, last at least 2 days (8 time steps) and travel further than 1000km. Spatial statistics are computed using the spherical kernel method (HODGES, 1996). The main advantage of this statistical method is that the statistics are computed directly on the sphere, which reduces the biases that can occur if computing the statistics on a projection using grid boxes.

### 3.4.3 Statistics and post-processing

The spatial statistics are computed directly on the sphere using spherical kernel estimators with local kernel functions, as described in Hodges (1996). The advantage of this method is it remove the needs to use projections or to perform corrections or normalizations (HOSKINS; HODGES, 2002).

The track diagnostics consist of the cyclone maximum intensity, track, genesis and lysis densities and the mean growth and decay rates. The tracking and statistics are computed for the seasonal periods as explained in Section 3.3.

The densities indicate the spatial distribution of cyclones and are scaled to number density per month per unit area, where the unit area is  $5^\circ$  spherical cap ( $\approx 10^6 km^2$ ). The spatial statistics are:

- a) Track density: is similar to the total number of systems passing through a grid box per unit area found in the literature. This field is calculated by using a single point from each track that is closest to the display grid-point;
- b) Genesis density: show the density of where the cyclones initiate (in portuguese *ciclogênese*). It is calculated from the starting points of the tracks,

however any track that starts at the first time step of each season is excluded (to remove the trajectories that cross the season);

- c) Lysis density: is similar to the genesis, but it shows the density of where the cyclones disappear (in portuguese *ciclólises*). This field is calculated from the end points of the tracks, however any track that ends at the last time step of each season is excluded (also to remove the trajectories that cross the season);
- d) Mean growth/decay rates: show where there is strong growth (decay) due to genesis (lysis) and storm increases (decreases), however the growth and decay of them tends to cancel in the middle of storm tracks due to cyclolysis and secondary generation. It is calculated from relative vorticity at 850hPa. Different of previous fields, the mean rates are  $day^{-1}$ .

These fields are shown for both the historical and future projected periods. While the historical period shows large differences between the model and reanalysis, indicating the biases of the models representation of the storm tracks, the future projected changes between the WAMZ and CTRL experiments show small differences, making it necessary to use a statistical significance test. Only for the projected future changes, the Student's t-test was applied to show if the small differences were statistically significant. This methodology was also applied by [Ulbrich et al. \(2013\)](#). The Student's t-test is given by equation

$$t = \frac{\bar{x}_1 - \bar{x}_2}{\sqrt{\frac{S_1^2}{N_1} + \frac{S_2^2}{N_2}}} \quad (3.2)$$

where  $\bar{x}$  is the mean,  $S$  is the standard deviation and  $N$  is the sample size; 1 and 2 are the samples. The degrees of freedom is the sum of the sample sizes of both groups minus 2, thus the result is 238. Therefore, the differences between two samples have statistical significance at 90% ( $p$ -value = 0.1), 95% ( $p$ -value = 0.05) and 99% ( $p$ -value = 0.01) level for two-tailed tests of 1.651281, 1.969982 and 2.596644, respectively.

While the densities show the spatial distributions of the cyclones, the maximum intensity distribution is a useful tool for comparing differences in the strength of cyclones between datasets and seasons. This methodology was applied by [Hodges et al. \(2011\)](#) to study the cyclone intensities in reanalysis datasets. They are calculated through a simple search for the minimum value (negative vorticity) within the search

radius, which was chosen here to be 5° geodesic spherical cap. After, the maximum intensity in each track is found and it is then binned, for all cyclones below 20°S to isolate the extratropical cyclones and consider the subtropical cyclones. Finally, the maximum intensity distributions are then constructed from these binned data for relative vorticity.

The maximum intensity distributions for relative vorticity at 850hPa are presented for historical and future projected periods. However, as the maximum intensity differences are small for future projected period, the two-sided Kolmogorov-Smirnov (*KS*) test was applied to test when and if they are statistically different. Similarly, this methodology was also performed by Hodges et al. (2011) to test cyclone maximum intensity distributions in reanalysis datasets. The *KS* test is a nonparametric method that does not depend on any distributional assumptions and is sensitive to the location and shape of the empirical cumulative distribution functions (ECDFs), however it has less statistical power than parametric methods. In this study, the *KS* test is used to calculate the *KS D* statistic, which measures the maximum distance between the ECDFs of the two samples and is given by equation

$$D = \max_x | F_n(x) - F_m(x) | \quad (3.3)$$

where  $F_n(X)$  is the empirical cumulative probability of distribution  $n$ , estimated as  $F_n(x_i) = i/n$  for the  $i^{th}$  smallest data value and likewise  $F_m(x)$  is the empirical cumulative probability of distribution for  $m$ . For this test, large  $p$ -values are expected the differences are calculated for the same climate model for the same experiment type which have similar storm maximum intensity distributions despite ensemble members having different initial conditions. Thus, relatively high values of  $D$  results in smaller  $p$  values.

### 3.5 Large-scale fields and diagnostics

The large-scale fields are explored to investigate their relationship with the cyclone statistics. Diagnostic fields have been calculated using monthly means from the HadGEM2-ES ensemble members and ERA-Interim data, which are:

- 500 hPa geopotential height anomaly;
- baroclinicity, such as maximum Eady growth rate;

- temperature;
- global skin temperature, which also represents the sea surface temperature (SST);
- zonal winds;
- outgoing longwave radiation;
- precipitation.

These fields and diagnostics were chosen to aid the understand of how the large-scale dynamical fields associated with the storm tracks can give insights in to the mechanisms behind the biases and future projected changes in the storm tracks.

The 500 hPa mean geopotential height anomaly is calculated by first subtracting the zonal mean from the full 500 hPa geopotential height field for each month and then averaging over all months for each season. The geopotential anomalies will be used to explore the stationary wave patterns.

The baroclinicity is computed as the Eady growth rate maximum (EADY, 1949) and is given in Hoskins and Valdes (1990) by equation:

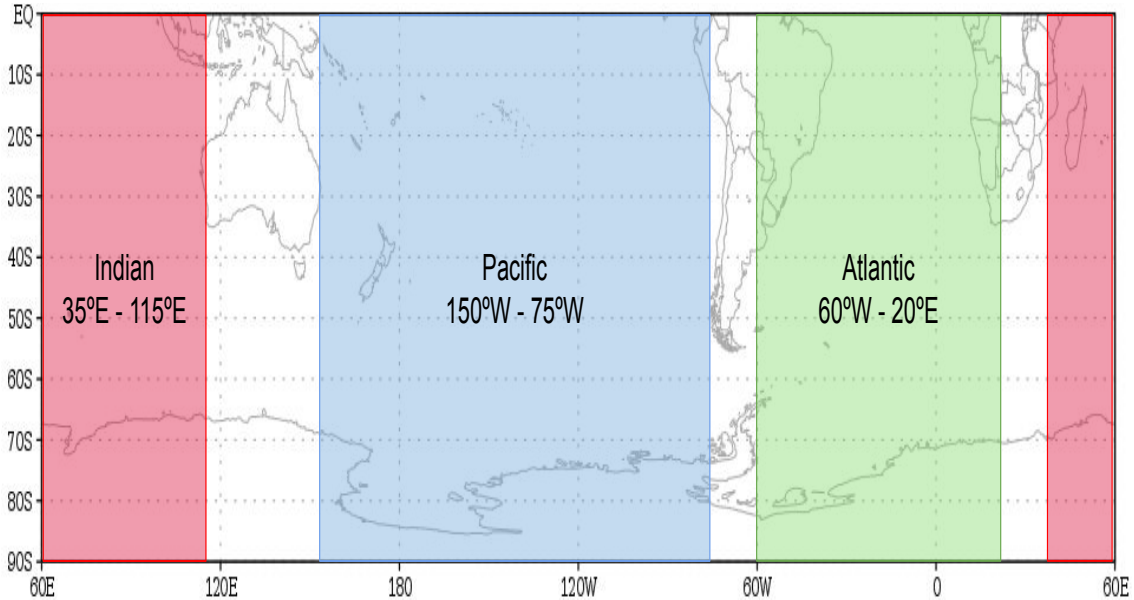
$$\sigma_{eady} = 0.31f \left| \frac{\partial v}{\partial z} \right| N^{-1} \quad (3.4)$$

where  $f$  is the Coriolis parameter,  $v$  is the total wind vector,  $z$  is the geometric height (estimated by geopotential height) and  $N$  is the Brunt-Väisälä frequency (calculated from temperature). The baroclinicity is analyzed at the 850 hPa level, referred to as lower level, and 250 hPa, referred to as upper level, and for the Southern Hemisphere is multiplied by -1 so that growth is positive. The adjacent levels used in the calculation of the vertical gradients are the 925 hPa and 700 hPa, and 300 hPa and 200 hPa, respectively. This analysis will be used to show an energetic perspective of the STs.

The sectorial zonal means of the zonal wind and temperature have been calculated for latitudes between 90°S and 0° for longitudes between 60°W and 20°E, 35°E and 115°E, and 150°E and 75°W, which represent the Atlantic, Indian and Pacific Oceans, respectively, as shown in Figure 3.8. These sectors were chosen with a focus on the circulation over the major water masses and, in the case of the Atlantic sector,

to capture circulation changes and biases leeward of the Andes Mountains - South America (SA)- to Cape Agulhas - South Africa. These diagnostic fields will be used to show a vertical perspective of the STs.

Figure 3.8 - Regions for zonal mean of the large-scale fields.



SOURCE: Author's production.

As a complementary analysis, some diagnostics fields were calculated to aid within large-scale analyses, which are the kinetic energy ( $v'u'$ ), meridional heat transport ( $v't'$ ) and meridional moisture transport ( $v'q'$ ), all of these at 700hPa level.

### 3.6 Regional-scale fields and diagnostics

The regional-scale analysis have the almost fields analyzed in the large-scale, but also were included the fields as follows:

- humidity;
- omega;
- surface latent and sensible heat;
- solar radiation;
- evaporation.

## 4 STORM TRACK CLIMATOLOGY AND HADGEM2-ES ENSEMBLE BIASES

The aim of this chapter is to determine how well storm tracks are represented in the historical experiment of the Hadley Centre Global Environment Model version 2 Earth System (HadGEM2-ES) when contrasted with the European Centre for Medium-Range Weather Forecasts (ECMWF) Interim Reanalysis (ERA-Interim) for the period 1979-2005. This will then provide confidence in using HadGEM2-ES to investigate the importance of the Amazon Forest to the Southern Hemisphere (SH) Storm Tracks (ST) under future climate scenarios of greenhouse gas emissions, to be presented in the chapter 5.

The key science questions which will be addressed in this chapter are:

- How well does the HadGEM2-ES Coupled Model represent the Southern Hemisphere Storm Tracks?
- What are the main factors that contribute to biases in the storm tracks?

This chapter will be divided into three sections, Section 4.1 introduces the storm track features for the ERA-Interim climatology from 1979-2005 over the Southern Hemisphere. Section 4.2 focuses on HadGEM2-ES model biases, examining the cyclone track density, large-scale mean circulation and cyclone intensity biases. Finally, Section 4.3 summarizes the chapter with a discussion about the main identified ST biases.

### 4.1 Climatology

In this section a ST climatology overview based on the ERA-Interim reanalysis for the period of 1979-2005 is presented for the SH. A comparison of the ST climatologies between ERA-Interim with other reanalyses, such as MERRA (RIENECKER *et al.*, 2011), NCEP-CFSR (SAHA *et al.*, 2010) and others, are presented in Hodges *et al.* (2011) while studies of the SH storm track features are presented in Hoskins and Hodges (2005), Silva (2010), Guia (2010), based on the ERA-40 reanalysis (UPPALA *et al.*, 2005).

#### 4.1.1 Winter

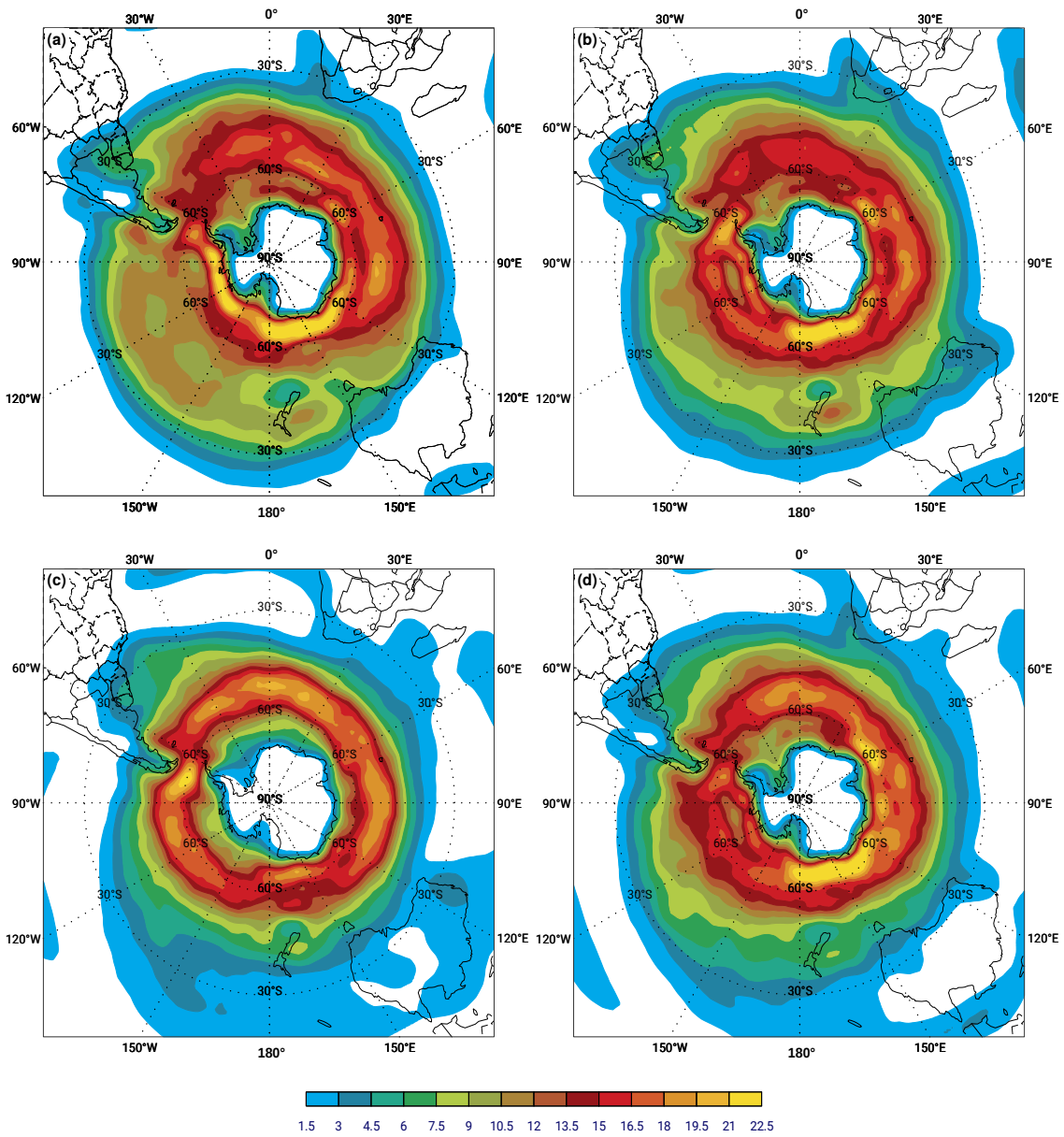
The ST track densities in winter are presented in Figure 4.1a for ERA-Interim. The main characteristic of the ST is the spiral from South America, around Antarctic,

through the Atlantic and Indian Oceans, and to the Antarctic Peninsula (FYFE, 2003; HOSKINS; HODGES, 2005). The largest track density region can be seen around the Antarctic coast between 120°E, and 80°W due to secondary development around the Antarctic coast associated with decaying systems moving in from lower latitudes. The lowest track densities tend to be found to the south of New Zealand and are most apparent in the winter, and are related to the presence of Rossby waves sources in the Indian Ocean (INATSU; HOSKINS, 2006).

The genesis density in winter is shown in Figure 4.2a. In general cyclogenesis occurs throughout the main ST region due to secondary cyclogenesis and downstream development (CHANG, 1993; INATSU; HOSKINS, 2004; HOSKINS; HODGES, 2005; HODGES et al., 2011). More concentrated cyclogenesis occurs in two well-known regions in the southeast of South America (SA), specifically leeward of the natural barrier of the Andes Mountains, one stronger in the northeast of Argentina related with the Subtropical Jet and mountain effect, where strong but shallow cyclonic systems on the subtropical jet cross the Andes (HOSKINS; HODGES, 2005), and the other in the extreme south of SA, which is related to where the ST from the Pacific Ocean crosses the mountains, causing a decay cyclonic systems upstream of the Andes Mountains and the Antarctic Peninsula, enhanced by ocean-continent temperature contrast (GAN; RAO, 1991; GAN; RAO, 1994; GAN; RAO, 1996; HOSKINS; HODGES, 2005; REBOITA et al., 2010b). Other major genesis density maxima are found on the Antarctic coast, the first with center at 65°S e 165°E and a second near to Drake Passage, with both associated with upstream decay and lysis (Figures 4.4a and 4.3a), which enhances the local baroclinicity resulting in reinvigoration or secondary cyclogenesis. Another cyclogenesis region can be seen close to the Australian coast, also found by Hoskins and Hodges (2005), and is related with the winter split jet. The region between 20°S and 50°S is dominated by cyclone growth rates (Figure 4.4a, positive values) where the maximum can be seen on the east side of Andes Mountains.

Finally, the lysis density in winter is presented in Figure 4.3a. The cyclolysis maximum regions are concentrated around the Antarctic coast, with a maximum near to the Antarctic Peninsula and another at the same longitude of Australia. Also an important region can be seen on the windward side of the South America related to where the ST intercepts the Andes Mountains, causing a lysis on the upslope. The cyclone decay rate regions (Figure 4.4a, negative values) are seen in tropical and high latitudes around the SH, with a maximum close to the Andes Mountains and Antarctic coast.

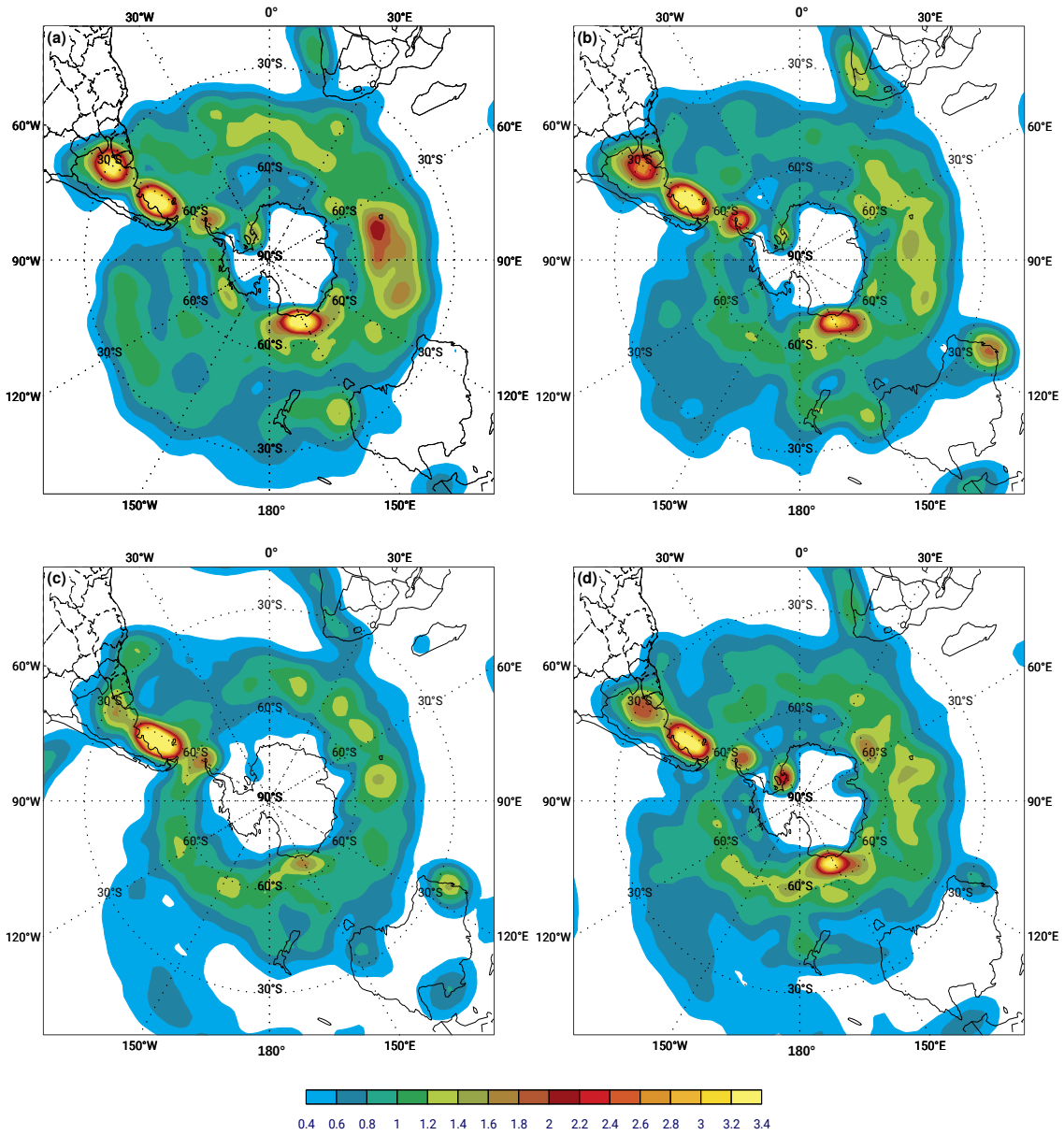
Figure 4.1 - Extratropical cyclone track climatology for the period 1979-2005.



ERA-Interim extratropical cyclone track climatology for the period 1979-2005 over Southern Hemisphere in: (a) JJA; (b) SON; (c) DJF; and (d) MAM. Densities are in units of number density per month per unit area, where the unit area is equivalent to a  $5^\circ$  spherical cap ( $\sim 10^6 km^2$ ).

SOURCE: Author's production.

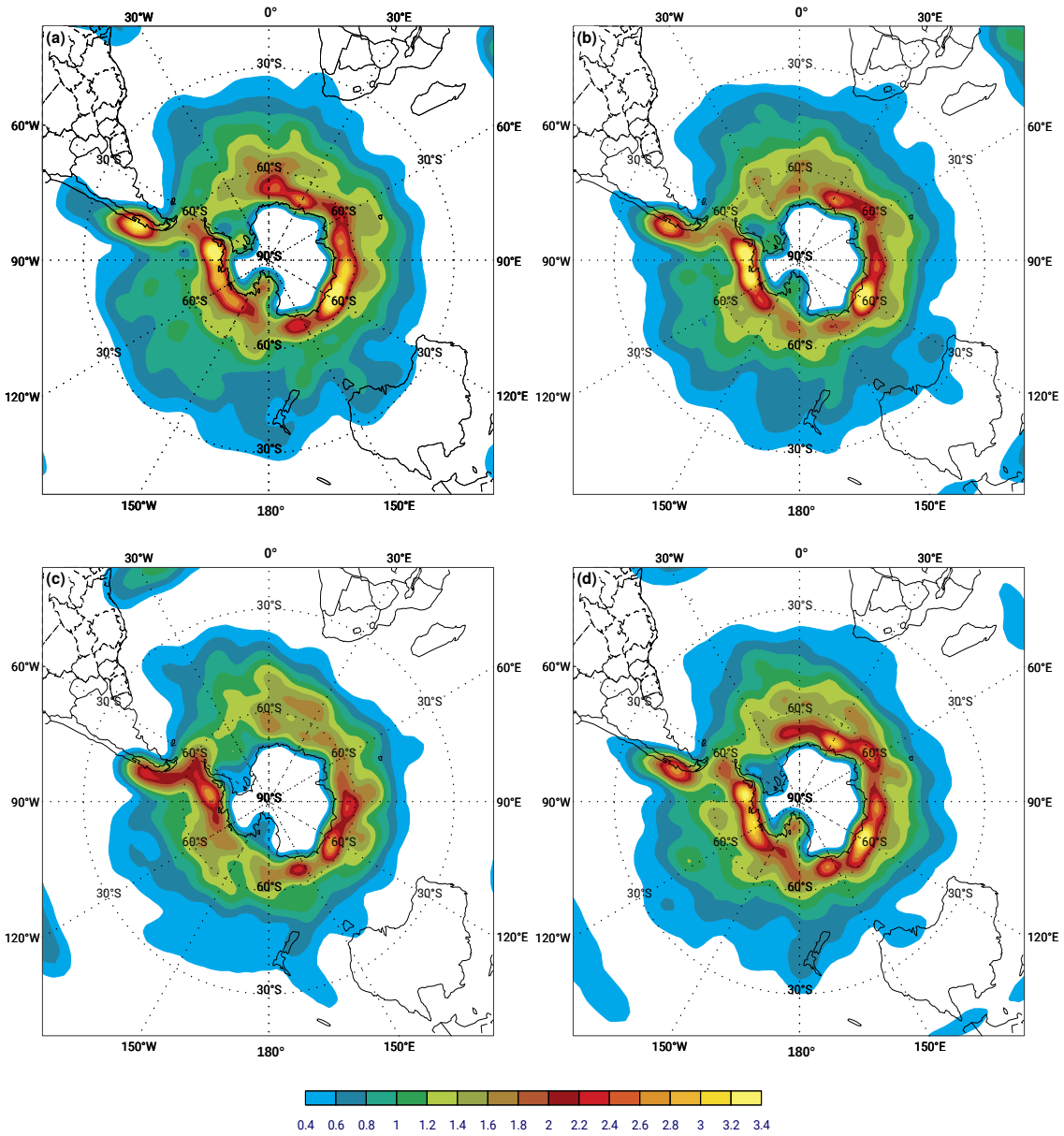
Figure 4.2 - Genesis density climatology for the period 1979-2005.



ERA-Interim genesis density climatology for the period 1979-2005 over Southern Hemisphere in: (a) JJA; (b) SON; (c) DJF; and (d) MAM. Densities are in units of number density per month per unit area, where the unit area is equivalent to a  $5^\circ$  spherical cap ( $\sim 10^6 km^2$ ).

SOURCE: Author's production.

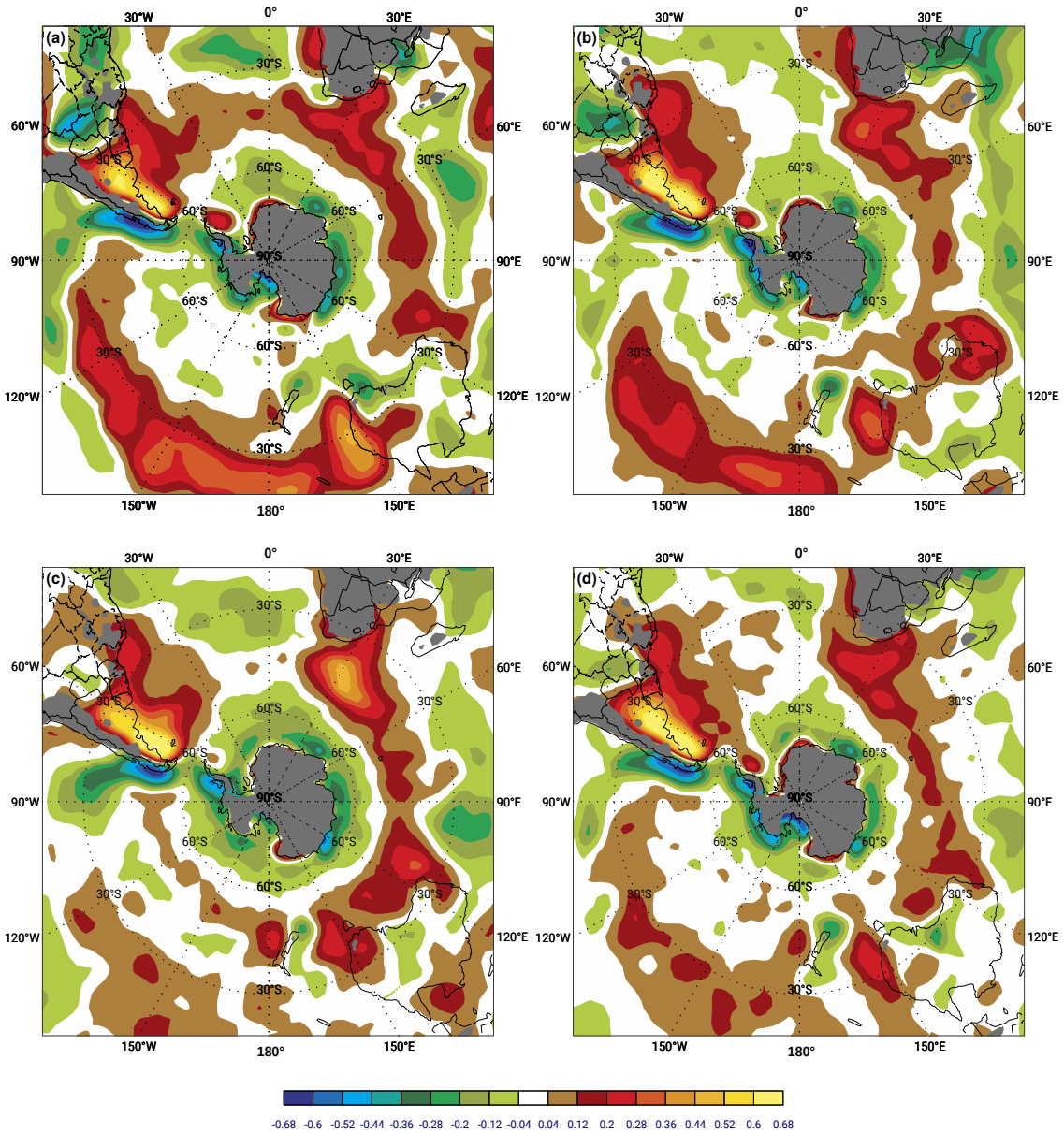
Figure 4.3 - Lysis density climatology for the period 1979-2005.



ERA-Interim genesis density climatology for the period 1979-2005 over Southern Hemisphere in: (a) JJA; (b) SON; (c) DJF; and (d) MAM. Densities are in units of number density per month per unit area, where the unit area is equivalent to a  $5^\circ$  spherical cap ( $\sim 10^6 km^2$ ).

SOURCE: Author's production.

Figure 4.4 - Mean growth decay rate climatology for the period 1979-2005.



ERA-Interim mean growth decay rate climatology for the period 1979-2005 over Southern Hemisphere in: (a) JJA; (b) SON; (c) DJF; and (d) MAM. Mean rate are  $day^{-1}$ .

SOURCE: Author's production.

### 4.1.2 Summer

The track density for the austral summer is shown in Figure 4.1c for ERA-Interim. The main characteristics of the STs are that they are narrower, more zonal and symmetric than in the winter season. These differences are associated mainly with a single eddy-driven jet (Figure 4.17, right column), in contrast with the split jet during the winter (Figure 4.13, right column), and also with cyclonic systems at high levels, such as cold vortices, that are less intense and in general have trajectories over regions of higher latitudes (not shown). The track density maximum is located between South America and the Antarctic Peninsula, which is related with the single eddy-driven jet over the South Pacific Ocean and the orography of the Andes Mountains that tends divert it to the south.

Figure 4.2c shows the regions of cyclogenesis. The two main peaks of genesis density can be seen over Argentina on the eastern side of the Andes Mountains, one stronger to the south that occurs mainly as the jet stream moves to a poleward position during the summer and the other in the northeast, both are also related to mountains effect (HOSKINS; HODGES, 2005).

Another region of cyclogenesis is seen near the southeast of Brazil around 25°S (Figure 4.2c), which generates cyclones different from those of the classical model of Bjerknes and Solberg (1922) and the cyclones have subtropical features (hybrid). Cyclone formation in this region has the same mechanisms as in winter, however they are weaker due to the poleward jet stream position. This condition is enhanced by the continent-ocean temperature contrast (GAN; RAO, 1991), the low-level jet east of the Andes (MARENGO et al., 2004), and moisture advection from northern Brazil associated with the upper-level circulation, such as a low over northeast of Brazil and a high over Bolivia and the centre of Brazil. These conditions favour cyclogenesis and makes the cyclones move poleward and eastward along the southern edge of the South Atlantic Convergence Zone (SACZ) (TALJAARD, 1972; HOSKINS; HODGES, 2005). Similarly, a genesis region can be seen around 150°W along the southern edge of the South Pacific convergence zone (SPCZ). There are other cyclogenesis maxima on the Antarctic Peninsula, that are weaker than those in the winter, near to Western Australia and over the Indian Ocean as described in Hoskins and Hodges (2005).

The cyclone growth rates (Figure 4.4c, positive values) are, in general, smaller than those in the winter with the peak areas found near to the genesis areas. However, over the cyclogenesis regions close to South Africa, the growth rates are larger than

in the winter.

Finally, the lysis density is shown in Figure 4.3c. Generally, the lysis pattern in the summer is similar to the winter season with a slightly reduced maxima in the main regions near to Antarctic. The cyclolysis peak over South America in this season is shifted slightly to the south and has smaller magnitude in comparison to the winter season. Other lysis peaks can be seen in the Eastern Northeast of Brazil related to the propagation of Easterly Wave Disturbances (GOMES *et al.*, 2015). During the summer season the mean decay rates (Figure 4.4c) are qualitatively similar in most parts of the SH, however they have a smaller maximum rate. In comparison with winter, the decrease of decay rate can be seen in the Andes Mountains, and is slightly moved to the south.

### 4.1.3 Transition seasons

The track density climatology for the spring season (Figure 4.1b) has similar features to the winter and summer seasons. This pattern was observed by Hoskins and Hodges (2005), where the transition seasons tend to have similarity with those in the preceding season, and Shaw (2013), where the less abrupt changes in the SH, in comparison with the NH, are related to the lack of a leading-order monsoon-anticyclone transport via planetary-scale waves. The ST over the SH is more zonal than in winter, however some features over the Pacific and Atlantic are somewhat similar to the winter season and the spiral tends to be more poleward. The genesis (Figure 4.2b), lysis (Figure 4.3b) and mean growth decay rate (MGDR) (Figure 4.4b) densities are similar to the patterns discussed in Section 4.1.1 for winter.

The ST during the autumn (Figure 4.1d) is also similar to the spatial pattern in austral summer, however slightly broader in latitude and less zonal and symmetric. The genesis (Figure 4.2d) and mean growth decay rate (Figure 4.4d) densities are similar to summer though the lysis (Figure 4.3d) seems more similar to the winter season around the coast of Antarctic. These differences will be discussed in Section 4.2.1.

## 4.2 HadGEM2-ES ensemble biases

This section compares the SH climatology from the 4 HadGEM2-ES ensemble members under the Historical experiment with ERA-Interim to assess biases for the period 1979-2005 in each season. Storm track statistics are analysed together with the means of large-scale fields to improve the understanding of the extratropical cyclone statistics throughout the discussion. The experimental setup of the historical experiment is described in Section 3.1.

### 4.2.1 Storm track density biases

The STs track density biases are calculated for each HadGEM2-ES ensemble member individually and for the HadGEM2-ES ensemble mean, referred to as HadGEM2-ES, as the difference between the HadGEM2-ES and the ERA-Interim reanalysis (HadGEM2-ES - ERA-Interim). The climatology period is 1979 to 2005 for both datasets.

#### 4.2.1.1 Winter

The austral winter season storm track density biases are shown in Figure 4.5a. In this season, the model overestimates the cyclone density near to southern Australia and underestimates the cyclone density around the coast of Antarctic. This reveals that the HadGEM2-ES model does not represent well the climatological track spiral (HODGES et al., 2011) over these regions, as shown in Figure 4.1a. In the region between the Indian and Pacific Ocean, near to 45°S and 120°E, positive biases are associated with the presence of more cyclones in HadGEM2-ES. This positive bias region occurs because the ST is too zonal due to not enough of the cyclones moving polewards. Similar results were found using older generations of models, such as the ECHAM5 climate model (BENGTSSON et al., 2006). This insufficient poleward motion is associated with the wrong representation of the stationary wave (Figure 4.14a). In addition, large temperature biases in extratropical latitudes (Figure 4.13, left column) contribute to enhance the local baroclinicity (Figure 4.12a), as will be discussed in Section 4.2.2.1.

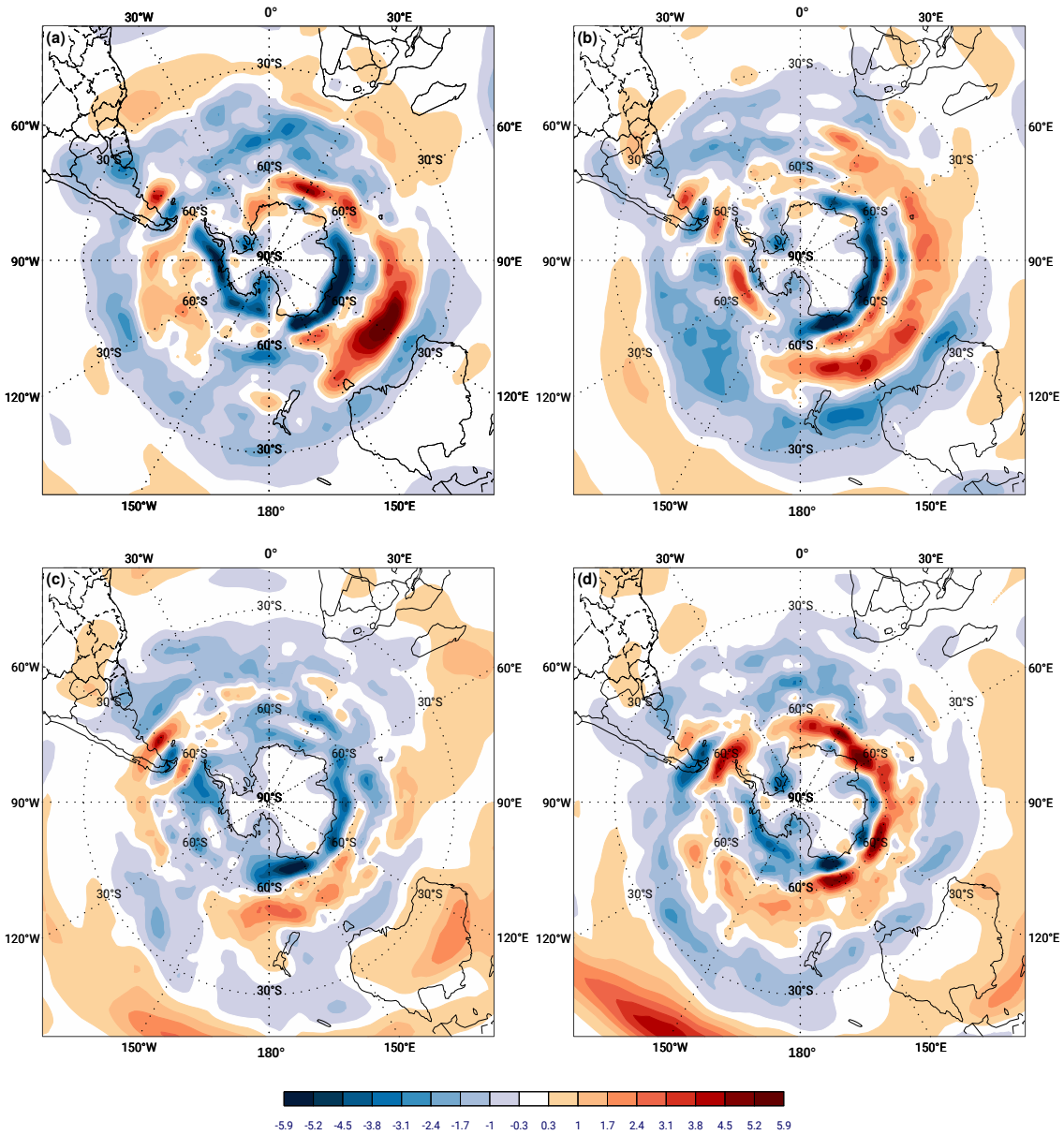
The winter cyclogenesis biases are shown in Figure 4.6a. Two strong bias regions are seen over the south of SA during the winter and both occur due to magnitude, size and position differences of the cyclogenetic regions between the model and the reanalysis. The negative bias over Northeast Argentina and Uruguay occurs because HadGEM2-ES represents the location of the cyclogenesis well in relation

to ERA-Interim climatology (Figure 4.2a), but with lower density that also extends further into the Southern Atlantic Ocean. On the other hand, in the central-south region of Argentina a positive bias can be seen which is more related to a difference in location rather than differences in magnitude. Further south, between 50°S and 70°S, there is another concentrated genesis/lysis biases associated with the peak of cyclogenesis (Figure 4.6a) and lysis/decay (Figures 4.7a and 4.8a), that results in differences associated with location in both fields. These negative biases are also seen around Antarctic. The biases seen in SA may be related to the model spatial resolution, which can impact the representation of the orography and cyclone diabatic processes especially when the cyclones cross the Andes Mountains. To test this hypothesis, the orography biases were investigated to determine how well the model represents the SH mountains with the result shown in Figure 4.9. HadGEM2-ES represents most parts of the Andes Mountains and Transantarctic Mountains (over Antarctic Peninsula) that are lower than that used in ERA-Interim (negative biases), in particular, in the peak regions, such as Mount Aconcagua, the difference is more than 1250 meters.

Further genesis biases (Figure 4.6a) can be seen over the southeast of Brazil and South Africa associated with stronger cyclone growth in the HadGEM2-ES model (Figure 4.8a). Positive biases can also be seen near to the south coast of Australia indicating that the model represents more cyclogenesis in relation to ERA-Interim (Figure 4.2a) in this region although the low track densities are well represented mainly over New Zealand.

For cyclolysis (Figure 4.7a) there are negative biases around Antarctic, which are related to the incorrect simulation of the spiral of activity towards the Antarctic coast. On the other hand, a positive bias is found between the south of SA and the Antarctic Peninsula related to the larger decay rate found in HadGEM2-ES (Figure 4.8a). The results found for the cyclone growth/decay rate biases (Figure 4.8a) are related to the same spiral pattern. The problem to represent the spiral pattern toward Antarctic during the winter is directly associated with the track and genesis underestimation leeward of the mountains, indicating that the cyclones are not well represented in the Andes Mountains region. Previous studies such as [Tamarin and Kaspi \(2017\)](#) show that the stationary wave pattern is opposing the transient nonlinear advection and latent heat release, thus the poleward tendency of the storms is reduced. In addition, this reduction occurs due the poor representation of orography and the stationary wave pattern.

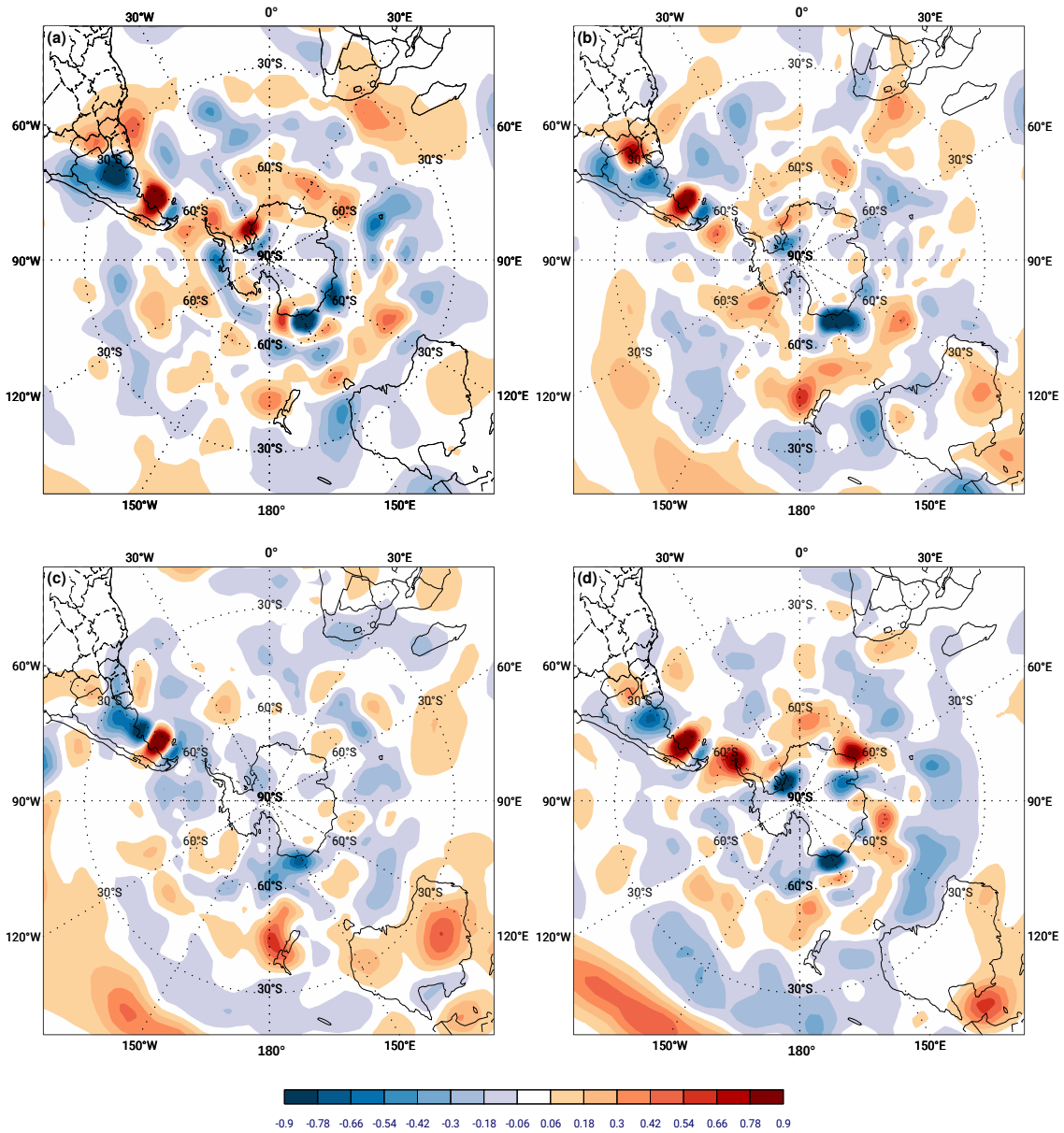
Figure 4.5 - Extratropical cyclone track density biases for the period 1979-2005.



Differences (HadGEM2-ES minus ERA-Interim) in extratropical cyclone track densities for the period 1979-2005 over Southern Hemisphere in: (a) JJA; (b) SON; (c) DJF; and (d) MAM. In figure (d) the locations where orography is above 850hPa are shaded with grey color. Densities are in units of number density per month per unit area, where the unit area is equivalent to a  $5^\circ$  spherical cap ( $\sim 10^6 km^2$ ).

SOURCE: Author's production.

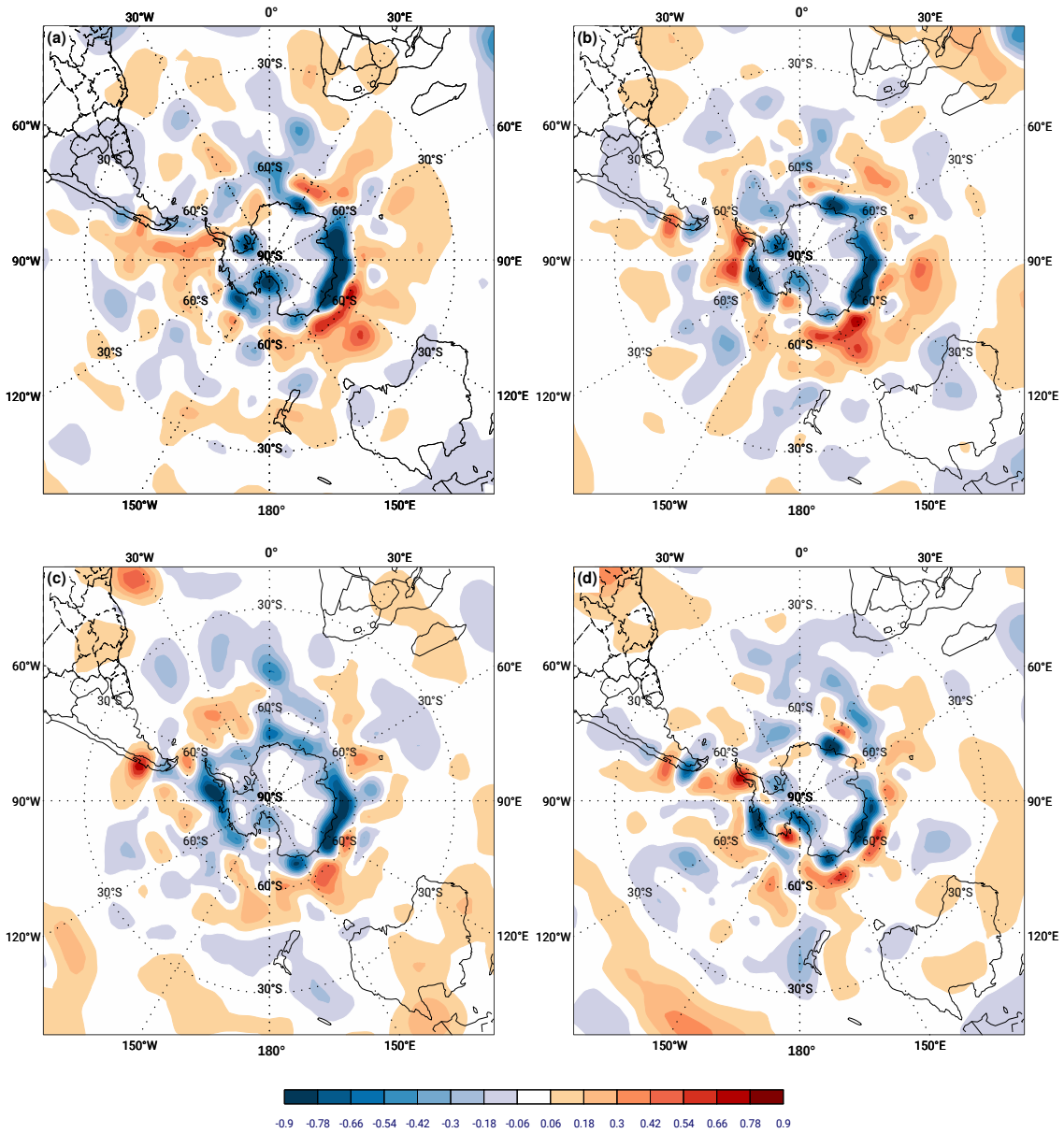
Figure 4.6 - Genesis density biases for the period 1979-2005.



Differences (HadGEM2-ES minus ERA-Interim) in genesis densities for the period 1979-2005 over Southern Hemisphere in: (a) JJA; (b) SON; (c) DJF; and (d) MAM. Densities are in units of number density per month per unit area, where the unit area is equivalent to a  $5^\circ$  spherical cap ( $\sim 10^6 \text{ km}^2$ ).

SOURCE: Author's production.

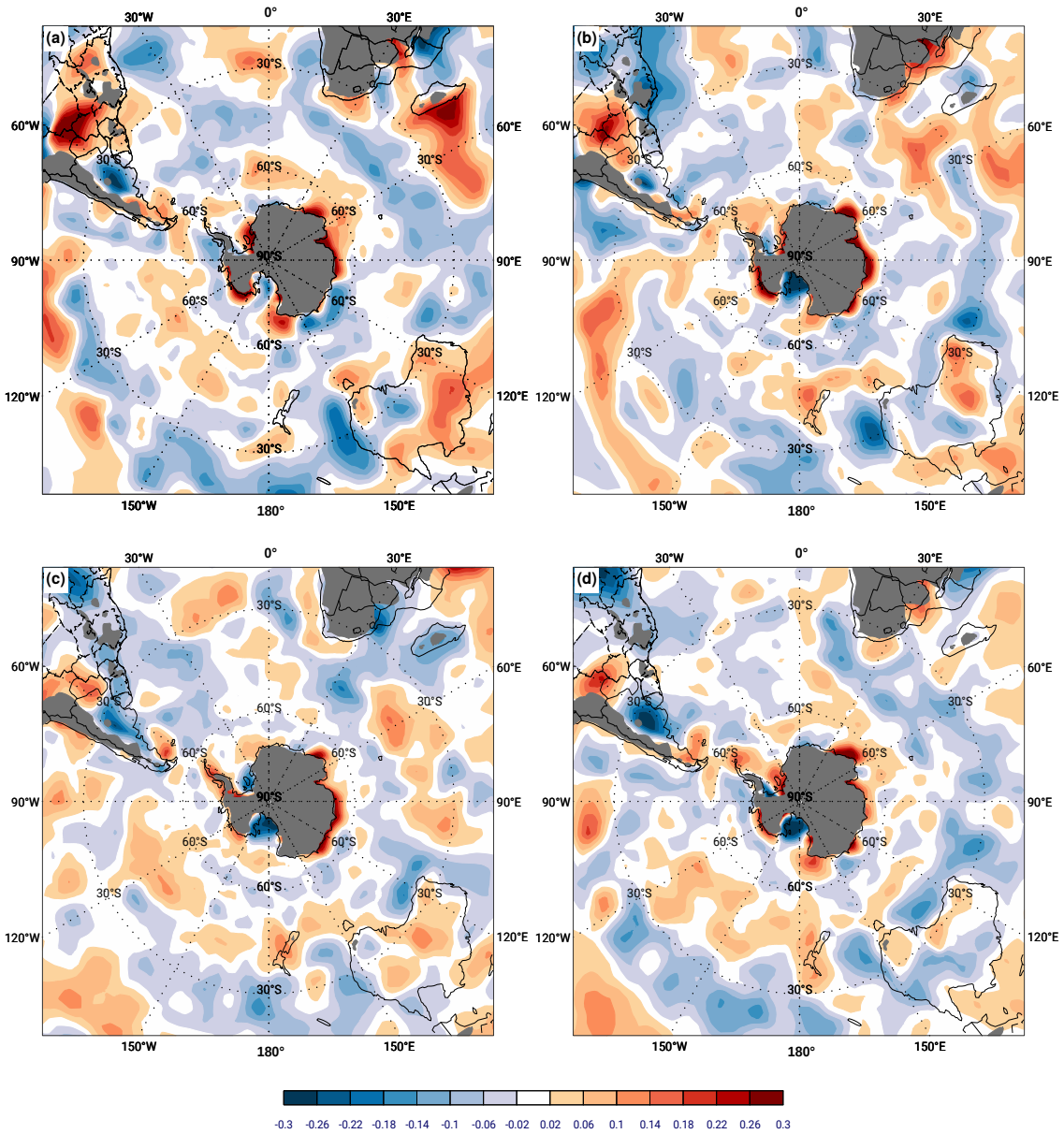
Figure 4.7 - Lysis density biases for the period 1979-2005.



Differences (HadGEM2-ES minus ERA-Interim) in lysis densities for the period 1979-2005 over Southern Hemisphere in: (a) JJA; (b) SON; (c) DJF; and (d) MAM. Densities are in units of number density per month per unit area, where the unit area is equivalent to a  $5^\circ$  spherical cap ( $\sim 10^6 km^2$ ).

SOURCE: Author's production.

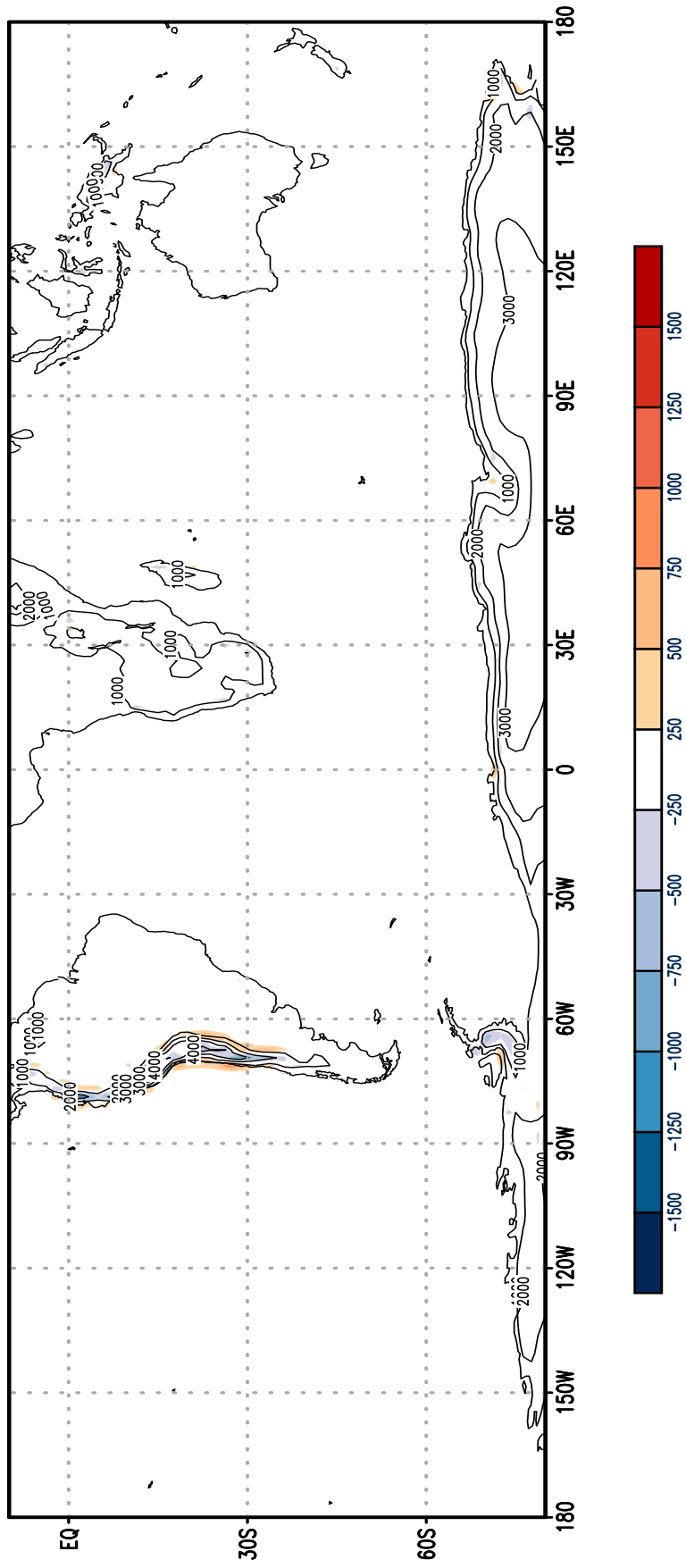
Figure 4.8 - Mean growth decay rate biases for the period 1979-2005.



Differences (HadGEM2-ES minus ERA-Interim) in mean growth decay rates for the period 1979-2005 over Southern Hemisphere in: (a) JJA; (b) SON; (c) DJF; and (d) MAM. In figure (d) the locations where orography is above 850hPa are shaded with grey color. Densities are in units of number density per month per unit area, where the unit area is equivalent to a  $5^\circ$  spherical cap ( $\sim 10^6 km^2$ ).

SOURCE: Author's production.

Figure 4.9 - Orography height biases over Southern Hemisphere.



Orography height biases (HadGEM2-ES minus ERA-Interim) over Southern Hemisphere. Black line contours show ERA-Interim orography height with 1000 meter intervals.

SOURCE: Author's production.

#### 4.2.1.2 Summer

The cyclone track density differences between HadGEM2-ES and ERA-Interim in the summer season are shown in Figure 4.5, and show relatively small magnitudes of bias possibly because the storm track is more zonal than in the winter (Figures 4.1c and a). In summary, the summer storm tracks are more concentrated between the latitudes 60°S and 50°S with the exception of the Atlantic Ocean that is slightly wider near to SA.

The track density differences (Figure 4.5c) are slightly smaller than winter though the distribution is more concentrated. The main differences can be seen around the Antarctic and in equatorward latitudes. In the Pacific Ocean can be seen biases around the Antarctic coast and a larger positive bias towards New Zealand, which is explained by fewer cyclones that move from the South Australia coast and Tasman Sea in comparison with ERA-Interim. The bias magnitudes are similar to the winter season in this region. In the Atlantic sector the storm tracks have similar bias magnitudes to the winter season, with the main biases close to SA. In summer, according to the climatology, cyclones tend to cross the Andes Mountains slightly to the north which can reduce the model overestimation of tracks in this region. HadGEM2-ES tends to represent more cyclones on the equatorward flank of the ST over the Indian and Pacific Oceans.

Figure 4.6c shows the summer genesis density differences, this indicates a negative bias over the Northeast of Argentina, Uruguay and the extreme south of SA though the model represents the position of this cyclogenesis well. The summer genesis climatology in this region shows a decrease in comparison with the winter season (Figures 4.2c and a). The other two cyclogenesis regions, in the southeast of Brazil and south of Argentina, shows the model represents the position and magnitude well, however with some small differences.

For other cyclogenesis regions (Figure 4.6c), the HadGEM2-ES has a good representation of the position of the cyclogenesis around the Australia coast though with stronger values in relation to ERA-Interim (Figure 4.2c). In these regions, the model also tends to underestimate the growth rate as shown in Figure 4.8c. As discussed before, this pattern is related to the zonal temperature differences that will be discussed further in Section 4.2.2.2.

The lysis density biases for the summer season are shown in Figure 4.7c. The results indicate that the main negative biases occur in the Indian Ocean, near to Antarctic,

and over the Antarctic Peninsula. A positive bias can be seen to the west of the Andes Mountains and over the Drake Passage. As discussed before, these patterns are associated with the track distribution narrowing and with the difficulty of the model to represent the cyclones that cross the Andes Mountains (mountain effect and lysis on the upslope, Section 4.2.1.1). This indicates that the HadGEM2-ES tends to reduce the cyclones before and underestimate them after the Andes Mountains, which can also be explained by the negative bias cyclone decay rate in the Figure 4.8c.

#### 4.2.1.3 Transition seasons

The biases during the spring and autumn season are similar to those in the preceding season. The track density biases in the spring (Figure 4.5b) show the same but weaker positive bias area over southern Australia during the winter, however with an addition of increased positive/negative biases south of New Zealand. Negative track density biases over the Pacific Ocean around 40°S are stronger than winter, which are related to the rapid disappearance of two waveguides, as will be discussed further in Section 4.2.2). Genesis density biases in the spring (Figure 4.6b) show the positive/negative peaks over South America. In addition, the region around the Antarctic coast is weaker than winter. Positive lysis biases (Figure 4.7b) over south of the Tasman Sea in spring is stronger than other seasons. The MGDR is more similar to the winter season, except in the southeast of Brazil where there is a decay.

The autumn season track density biases (Figure 4.5d) are similar to the summer season (Figure 4.5c), but increased positive bias peaks are observed in the latitude of 60°S. The genesis biases (Figure 4.6d) are more similar to the winter season, but in the region over Weddell Sea the bias signal is opposite. This pattern is related to the model resolved orography over the Transantarctic Mountains and the latitudinal tilt of the ST which begins to appear during the autumn. Lysis biases (Figure 4.7d) are concentrated around the Antarctic coast and are similar to the winter and spring seasons. The autumn MGDR biases (Figure 4.8d) are opposite on the east coast of Africa and over the Weddell Sea in comparison with summer, however the spatial pattern is somewhat similar to the summer. Negative MGDR bias east of Argentina are weaker than winter only.

### 4.2.2 Large-scale biases

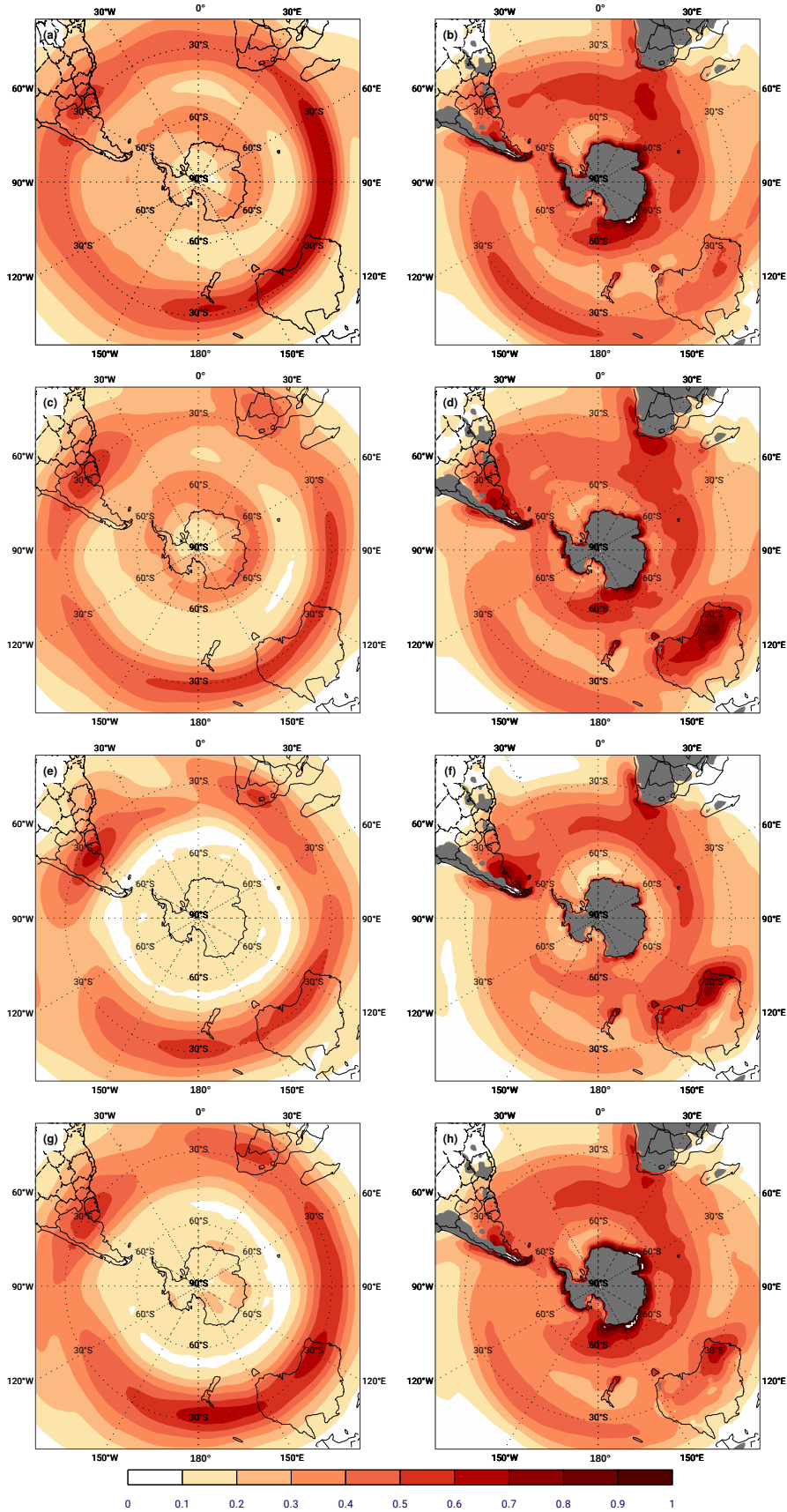
Before presenting the large-scale bias results comparing the mean flow, the maximum Eady growth rate for the ERA-Interim climatology was calculated to provide a frame of reference to the HadGEM2-ES biases, which will be discussed in the next sections. The baroclinic instability represents the growth of cyclones in extratropical regions and, in this way, it is possible to link regions of cyclogenesis and cyclone growth rate with the large-scale environment.

The maximum Eady growth rate for ERA-Interim in the SH winter is shown in Figures 4.10a and 4.10b for 250 and 850hPa respectively. This shows that the baroclinicity is largest in the winter season when contrasted with summer, shown in Figures 4.10e and 4.10f, with peak values found in the vicinity of the subtropical jet. Also seen are strong values around Antarctic that are linked to the strong polar vortex during the austral winter. The strong values found in the vicinity of the Madagascar Island, South coast of Australia and South America correspond with the climatological cyclogenesis and cyclolysis features. The spiral pattern found in the track density is also seen in the latitude of maximum Eady growth rate at 850hPa (Figure 4.10f), which is largest in the vicinity of the SH ST. The winter bias (Figures 4.11a and 4.12b) indicates the model tends to underestimate the baroclinicity in the subtropical jet over all the SH, on the other hand, there is an overestimate at the latitudes of the polar jet. These results will be discussed in Section 4.2.2.1.

The summer baroclinicity is shown in Figures 4.10e and 4.10f. In this season the baroclinicity is more zonally symmetric and weaker than winter at both levels with some track features, such as genesis and growth rate, also found close to the Eady-growth rate peaks. Strong baroclinicity at 850hPa is found in the southeast of SA, south of South Africa and in the region that extends from Australia towards New Zealand. Although the main patterns are well represented, HadGEM2-ES tends to underestimate the baroclinicity at 850hPa, as shown in Figure 4.12c. The positive summer biases at 250 hPa (Figure 4.11c) indicate a model overestimation of the jets in the SH, which can be related with the narrowing of the storm tracks. Also, the bias values at the same level in high latitudes, over 50°, are close to zero. These results will also be discussed in Section 4.2.2.2.

The baroclinicity during the transition seasons have similarity with those in the succeeding seasons, as shown in Figures 4.10c and d for spring and Figures 4.10g and h for autumn, and will be compared in Section 4.2.2.3.

Figure 4.10 - Maximum Eady growth rate climatology for the period 1979-2005.



ERA-Interim maximum Eady growth rate ( $day^{-1}$ ) at 250hPa (left) and 850hPa (right) for the period 1979-2005 over Southern Hemisphere: (a) and (b) JJA; (c) and (d) SON; (e) and (f) DJF; and (g) and (h) MAM.  
SOURCE: Author's production.

#### 4.2.2.1 Winter

The upper level winter biases in baroclinicity (Figure 4.11a) indicate three bias rings, one in the climatological polar jet region at extratropical latitudes where the model tends to overestimate the baroclinicity and the other two rings, on the subtropical flank jet region and another around Antarctic, where there is an underestimation. In the Antarctic region the model indicates less baroclinicity which may be related to the representation of the polar vortex in this season (SIMPSON et al., 2013a).

During the winter season the jets are split with the polar jet between 60°S and 40°S, and the subtropical jet, between 30°S and 20°S, as shown in the Figure 4.13 (black lines contour) for Atlantic (b), Indian (d) and Pacific (f) Oceans for ERA-Interim. HadGEM2-ES tends to show a decrease in the wind speed associated with the eddy-driven jet, however the subtropical jet has positive speed biases and is further equatorward in relation to the climatological position. These biases correspond with the strong positive baroclinicity bias at 250 hPa (Figure 4.11a), and over the Indian Ocean towards New Zealand are related to the poor representation of the winter split jet which is quite typical in climate models.

The zonal mean temperature biases are shown for the Atlantic (Figure 4.13a), Indian (Figure 4.13c) and Pacific (Figure 4.13e) Oceans, where the model indicates negative biases in all oceans from the high-middle troposphere levels at the pole towards lower levels in tropical regions. The peak negative biases are found at upper levels (300-100 hPa) in latitudes between 60°S to 40°S, which are associated with the displaced representation of the polar jet at upper levels in the HadGEM2-ES over the southern oceans. On the other hand, positive maxima can be seen in the Indian Ocean (Figure 4.13c) near to the pole that extends from lower to middle levels, which indicates that the HadGEM2-ES tends to overestimate the temperature in the Antarctic region. Previous studies such as Jones and Harpham (2013) found that temperature biases are largest at polar latitudes in the ERA-Interim reanalysis mainly in the autumn and winter seasons, which is much colder than direct measurements. This indicates that biases could be larger than shown in Figure 4.13c. These patterns, associated with the split jet speed bias and the bias in the spiral representation of the ST in the model, corresponds with the Eady growth negative bias observed around the Antarctic, and the positive bias observed in the Indian Ocean between the latitudes of 40°S and 30°S.

Previous studies such as Taljaard (1972), Rao et al. (2002), Hoskins and Hodges (2005), Inatsu and Hoskins (2006), Woollings (2010), show that the jets commonly split in the time mean in this region and act as two waveguides for most of the time, which create two branches of the storm tracks over the SH (BERBERY; VERA, 1996; CHANG, 1999; RAO et al., 2002; NAKAMURA; SHIMPO, 2004; INATSU; HOSKINS, 2006). Inatsu and Hoskins (2006) show that the split jet occurs due to propagation of Rossby Waves associated with the cross equatorial flow and the monsoon in the subtropical Indian Ocean. Also, Hoskins and Ambrizzi (1993) show that a slower jet can reduce the meridional shear which results in a less poleward waveguide, which could contribute in HadGEM2-ES (Figure 4.13b, d and f) to more dissipation at the poles and more waves propagating out of the jet towards tropical latitudes. The combination of these factors associated with track density biases (Figure 4.5a) indicate that HadGEM2-ES does not represent the jet spatial and seasonal variability, such that more biases occur in this region and extend through the Pacific and Atlantic Oceans.

The slow and equatorward shift of the eddy-driven jet and track density biases are supportive of the hypothesis that HadGEM2-ES may have different Rossby Wave trains than seen in reanalyses. To test this hypothesis, the sea surface temperatures (SST), 500hPa geopotential height zonal anomaly and precipitation were investigated to indicate biases that can affect directly the stationary wave patterns.

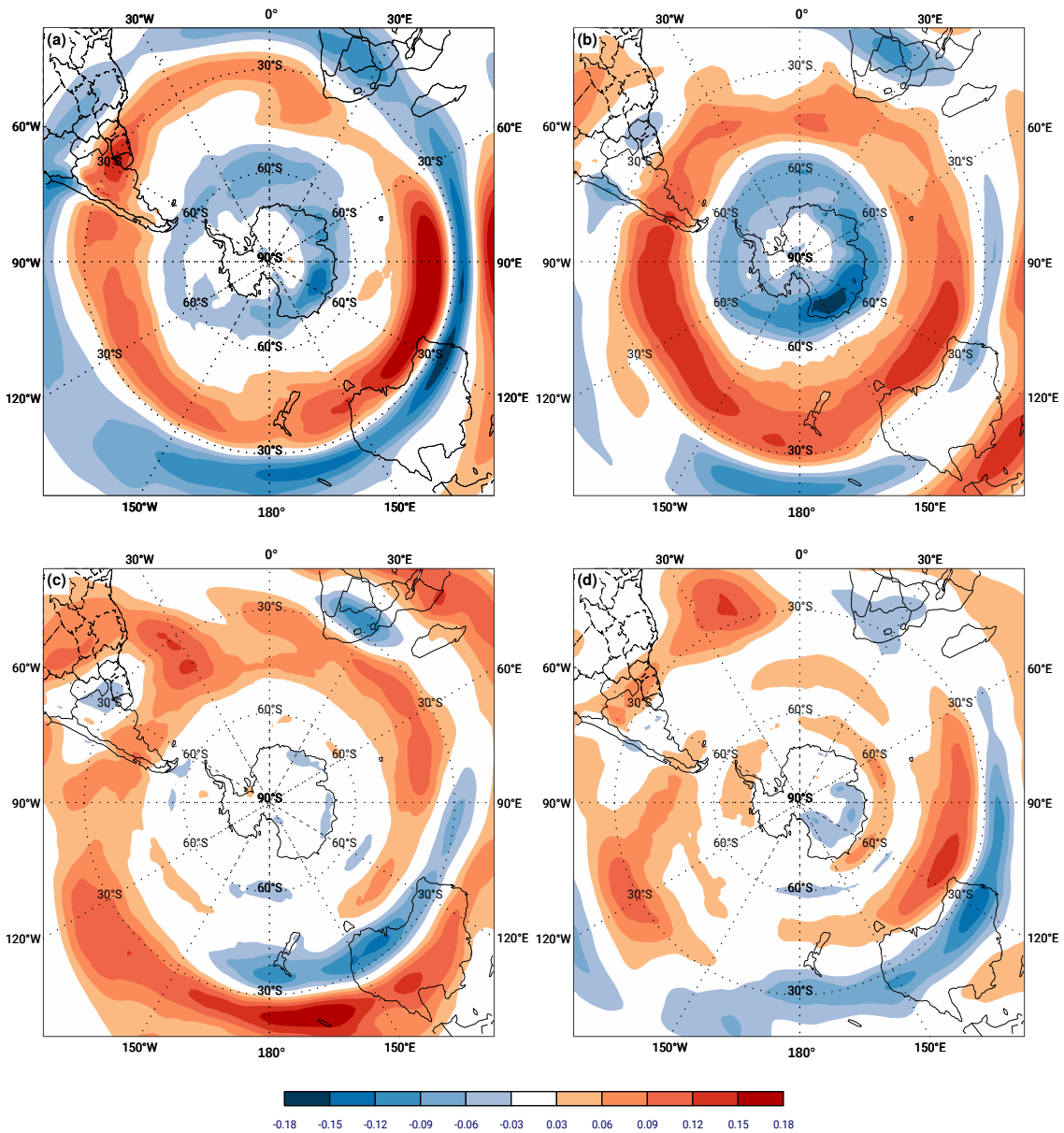
Figure 4.15a show an SST positive bias at extratropical latitudes over the Atlantic towards the Indian Ocean which corresponds with the positive geopotential anomaly biases (Figure 4.14a) over this region during the winter. This seems to indicate that the SSTs contribute to a change in the Rossby Wave train (CAI et al., 2011), which results in a change of the location of centres of geopotential anomalies (Figure 4.14a) and consequently of the waveguides over the southern oceans. Besides, the precipitation biases (Figure 4.16a) in the Indian Ocean, associated with the monsoon, and Indonesia region may partially contribute to a change the split nature of the SH jets, occasioning jet and track density biases via Rossby wave biases over the Indian and Pacific Oceans in particular. Kidston and Vallis (2012) have discussed the relationship between the speed and the latitude of an eddy-driven jet in a simple barotropic model. They found that when the wind speed is increased the jet shifts poleward because of increase of the meridional shear and reduces the absolute vorticity gradient on the flanks of the jet. Therefore, the results found here are consistent with the Kidston and Vallis (2012) results.

The 500hPa geopotential height zonal anomaly biases and ERA-Interim geopotential height climatology (black lines) are shown in Figure 4.14. During the winter (Figure 4.14a) the negative biases between latitudes of 40°S and 20°S in the Atlantic Ocean are related to the representation of the cyclogenesis over the northeast of Argentina/Uruguay which is slightly displaced to the adjacent ocean (Figure 4.6a) and consequently more cyclones propagate toward Africa. Although the model shows more baroclinicity at the 250hPa level (Figure 4.11a) and less geopotential height (Figure 4.14a), this storm track pattern is observed mainly above 30°S (Figure 4.5a). Other negative biases (Figure 4.14a) are observed at extratropical latitudes, one in the Indian Ocean (80°E and 150°E) that corresponds with the track density positive bias peaks (Figure 4.5a) and the model reduced spiral toward the Antarctic (Figures 4.1a and 4.5a), and the other in the Pacific Ocean (140°W and 80°W), where a positive bias in track density is seen (Figure 4.5a). However, the geopotential positive biases (Figure 4.14a) are also found in the three ocean basins, where the maximum is over the extratropical region between 40°W and 60°E, near to south of South Africa. This region has two common problems seen in climate models, the ocean currents and the sea surface temperature (WOOLLINGS *et al.*, 2010).

According to O'Reilly and Czaja (2015) in the North Pacific Ocean there is a relation between the ocean fronts and the downstream dynamics. In this way, they suggest there can be a similar pattern over the South Atlantic, with the Agulhas Front having a direct relation with the interaction between the variability of the Agulhas Current and the downstream dynamics, thus influencing the lower level baroclinicity. This relation was also found by Nakamura (2012). The poor representation in the models, associated with the SST biases (Figure 4.15a), may also contribute to the strong storm track biases found in the Indian Ocean.

Continuing the discussion of Figure 4.14a, two other positive biases are found in the Pacific Ocean, one near to New Zealand towards Antarctic and the other close to South America, that contribute to the track density negative biases (Figure 4.5a) observed over these regions.

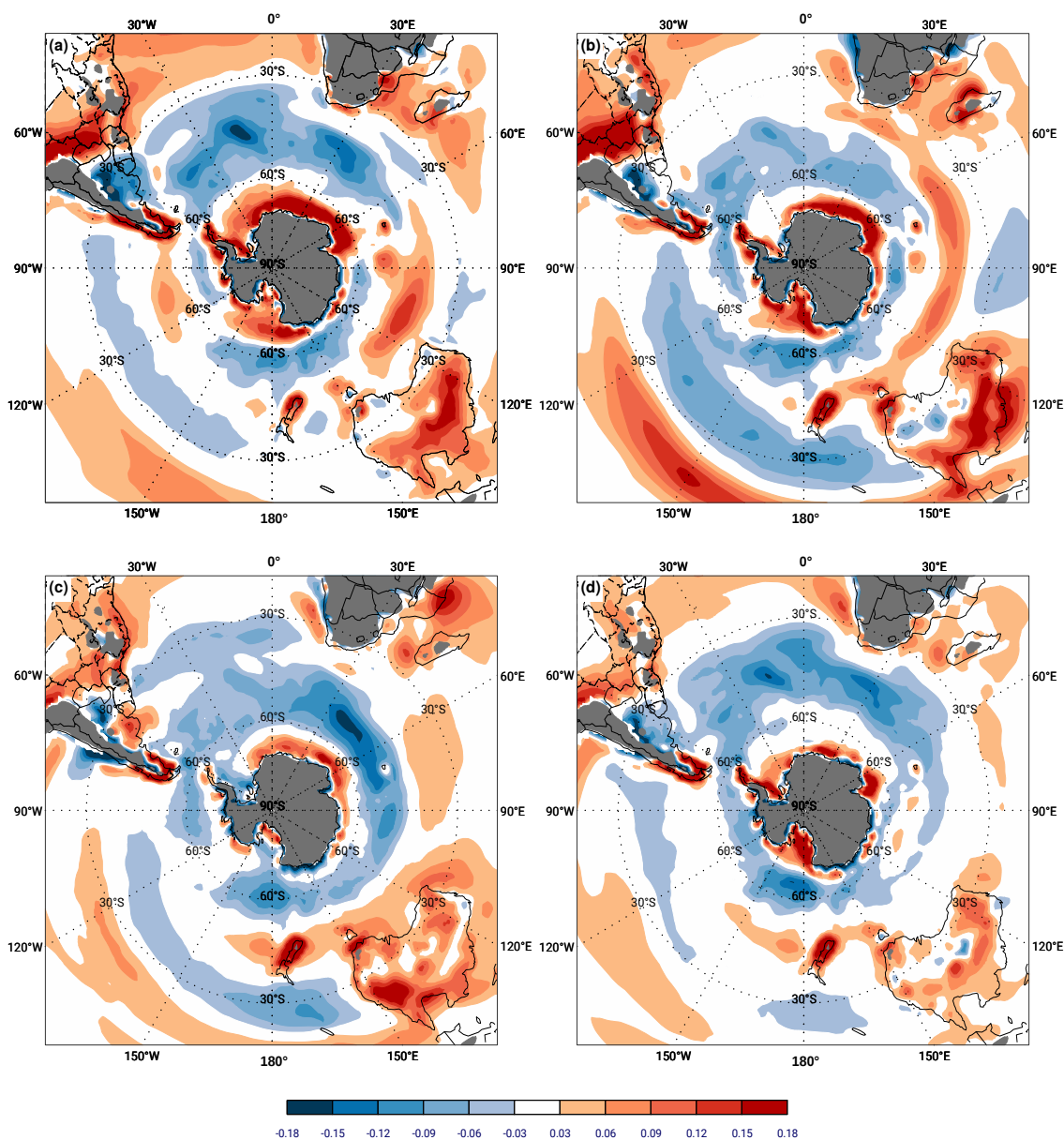
Figure 4.11 - Maximum Eady growth rate biases at 250hPa for the period 1979-2005.



Maximum Eady growth rate ( $day^{-1}$ ) biases (HadGEM2-ES minus ERA-Interim) at upper levels (250hPa) for the period 1979-2005 over Southern Hemisphere: (a) JJA; (b) SON; (c) DJF; and (d) MAM.

SOURCE: Author's production.

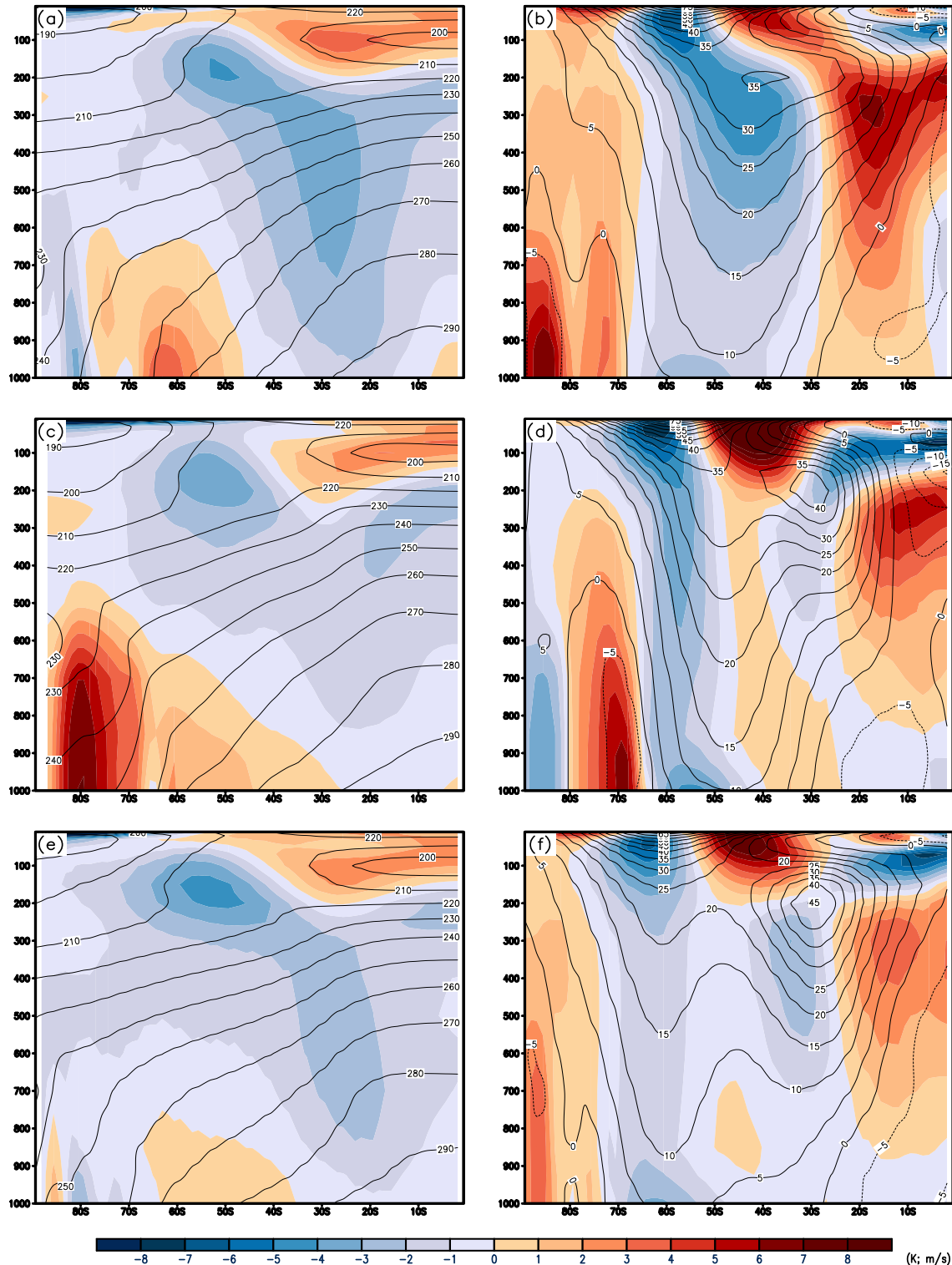
Figure 4.12 - Maximum Eady growth rate biases at 850hPa for the period 1979-2005.



Maximum Eady growth rate ( $day^{-1}$ ) biases (HadGEM2-ES minus ERA-Interim) at lower levels (850hPa) for the period 1979-2005 over Southern Hemisphere: (a) JJA; (b) SON; (c) DJF; and (d) MAM. The locations where orography is above 850hPa are shaded with grey color.

SOURCE: Author's production.

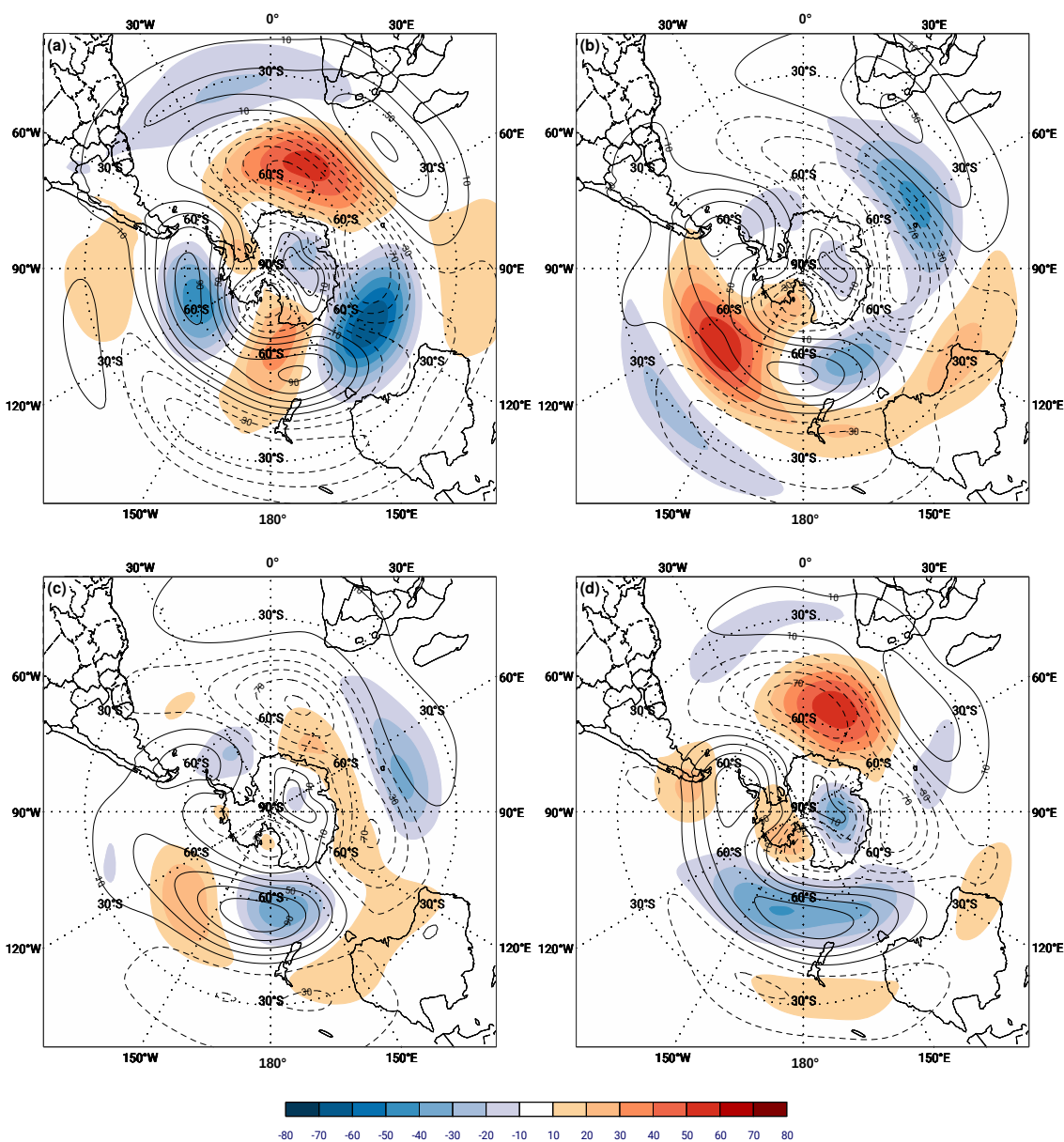
Figure 4.13 - Zonal mean temperature and zonal wind in winter for the period 1979-2005.



Zonal mean temperature (K) (left column) and zonal mean zonal wind ( $m/s$ ) (right column) biases (HadGEM2-ES minus ERA-Interim) in JJA for the Southern Hemisphere Oceans: (a) and (b) Atlantic; (c) and (d) Indian; and (e) and (f) Pacific. Black line contours show ERA-Interim climatology for the period 1979-2005.

SOURCE: Author's production.

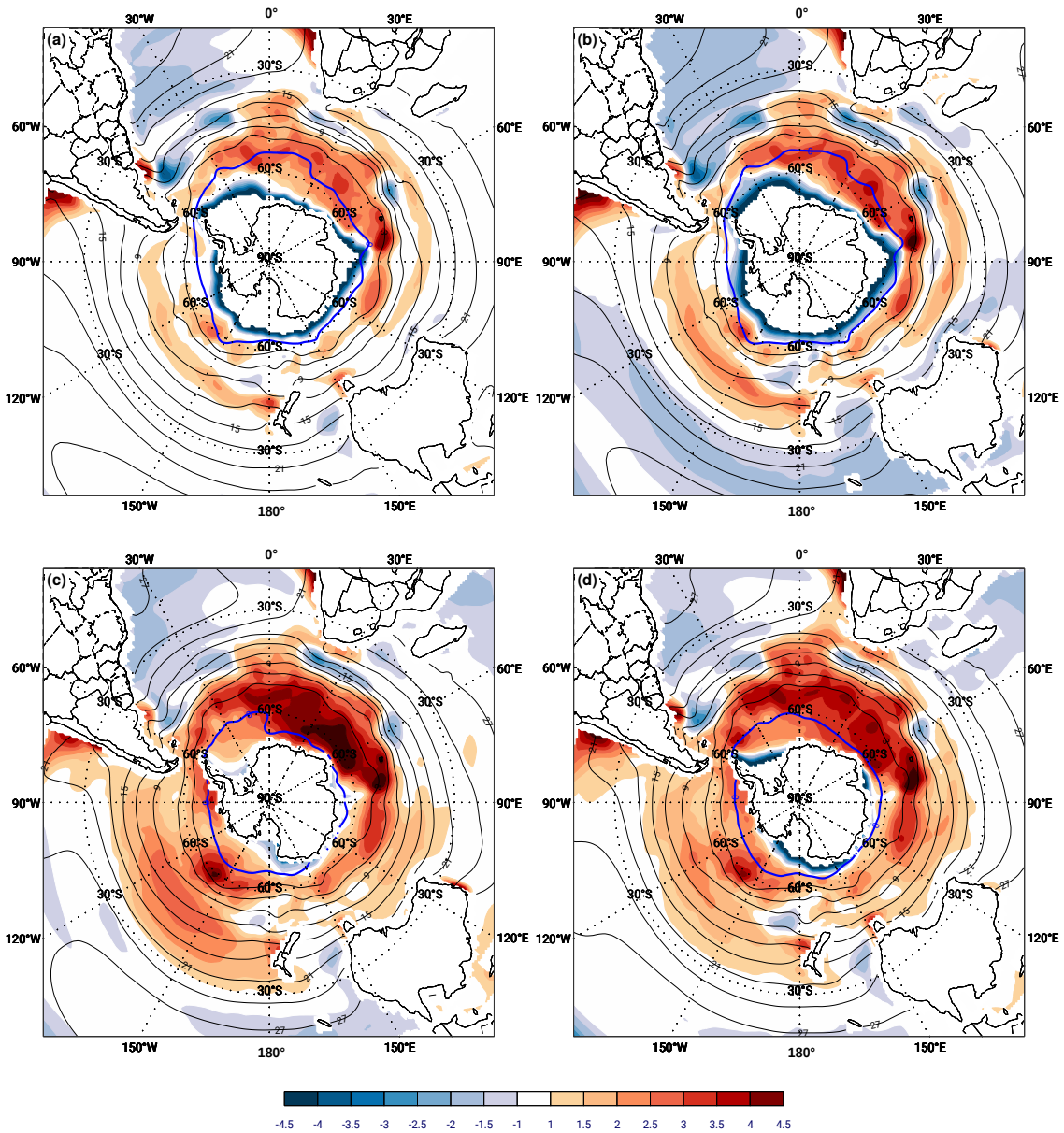
Figure 4.14 - Geopotential height anomaly biases at 500hPa for the period 1979-2005.



500hPa geopotential height anomaly (meters) biases (HadGEM2-ES minus ERA-Interim) from the zonal mean for the period 1979-2005 over Southern Hemisphere: (a) JJA; (b) SON; (c) DJF; and (d) MAM. Black line contours show ERA-Interim climatology for the same period and dashed contours indicate negative values.

SOURCE: Author's production.

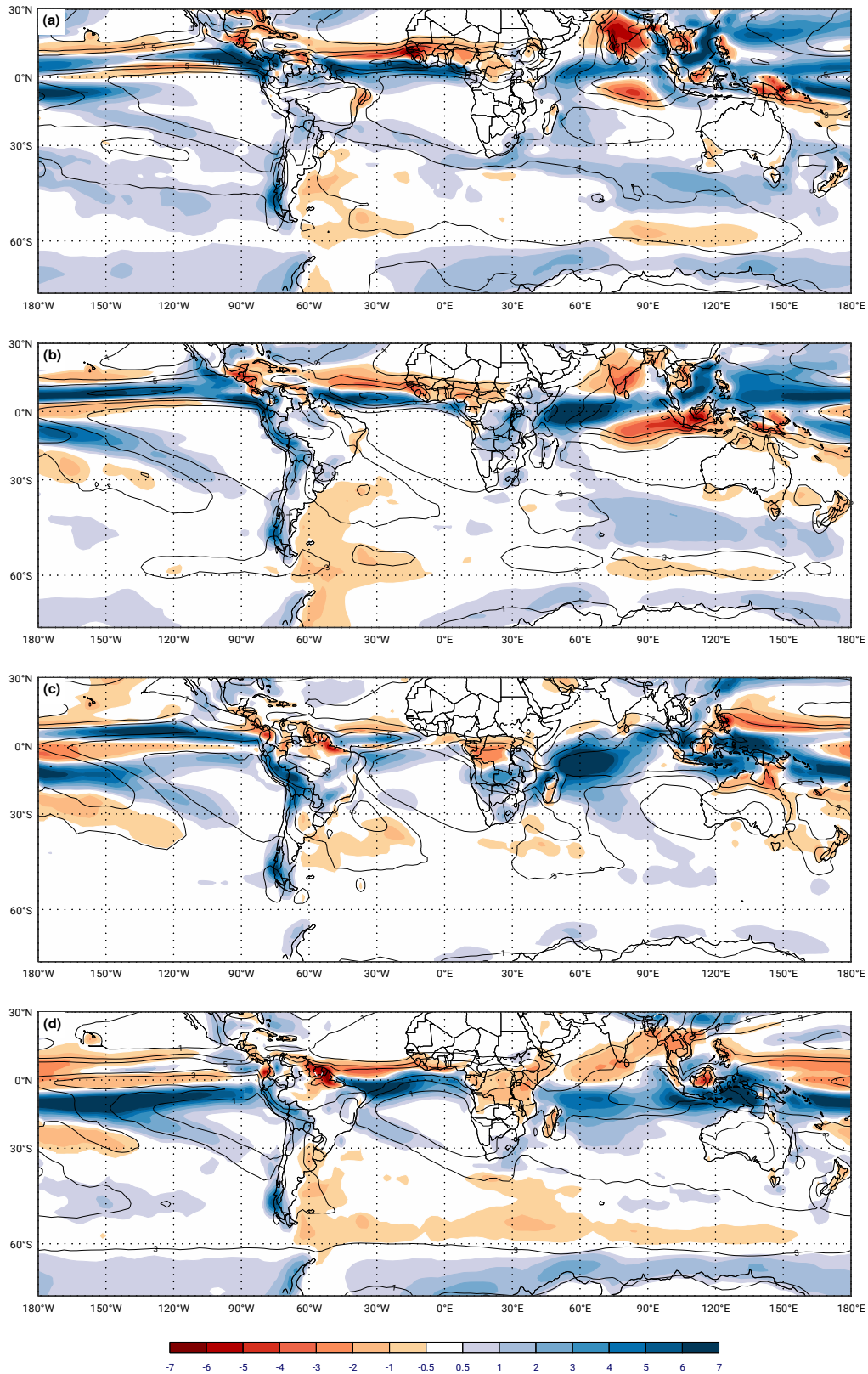
Figure 4.15 - Sea surface temperature biases for the period 1979-2005.



Sea surface temperature ( $^{\circ}\text{C}$ ) biases (HadGEM2-ES minus ERA-Interim) for the period 1979-2005 over Southern Hemisphere: (a) JJA; (b) SON; (c) DJF; and (d) MAM. Black line contours show ERA-Interim climatology for the same period and blue line contour indicate  $0^{\circ}\text{C}$ .

SOURCE: Author's production.

Figure 4.16 - Precipitation biases for the period 1979-2005.



Precipitation (mm) biases (HadGEM2-ES minus GPCP) for the period 1979-2005 over SH: (a) JJA; (b) SON; (c) DJF; and (d) MAM. Black line contours show GPCP climatology with 1, 3, 5 and 10 intervals. SOURCE: Author's production.

#### 4.2.2.2 Summer

During the austral summer the jets (Figures 4.17b, d and f) tend to move poleward and as a result the two wave patterns disappear, with this change being reflected directly in the storm track pattern (Figure 4.1c) (CHANG, 1999; RAO et al., 2002; HOSKINS; HODGES, 2005; INATSU; HOSKINS, 2006; RIVIÈRE, 2011). Although the main ST pattern is well represented in HadGEM2-ES it tends to underestimate the baroclinicity in tropical and extratropical latitudes, as shown in Figure 4.11c and 4.12c.

In contrast with the winter baroclinicity biases (Figure 4.11a), where the maximum biases were found in the Indian Ocean, during the summer the largest biases are found in the Pacific Ocean (Figure 4.11c) at upper levels. Positive biases can be seen on the equatorward side of the climatological position of the ST which may be related to the narrowing of the storm tracks at 250hPa. Two negative bias peaks are found to the south of South Africa and Australia and adjacent oceans (Figure 4.11c). In the northeast of Argentina and Uruguay other minor negative baroclinicity bias is observed and this area corresponds with the track (Figure 4.5c), genesis (Figure 4.6c) and mean growth negative biases (Figure 4.8c). The baroclinicity biases at 250 hPa in the high latitudes, over 50°S, are close to zero.

The maximum Eady growth rate biases at lower levels (850hPa) for the summer season are shown in Figure 4.12c. There is a positive baroclinicity bias over the east of Argentina that are associated with the poleward movement of the ST caused by the single eddy-driven jet in this season. This does not correspond with the genesis and MGDR density biases (Figures 4.6c and 4.8c), which are opposite in sign (positive for baroclinicity at 850hPa and negative for genesis density), however are similar to the winter season. Other positive biases are observed at equatorward latitudes and these correspond well with the positive track density biases (Figure 4.5c). The New Zealand positive biases also occur during the summer and may be related to the stationary wave pattern that will be discussed further later. The negative baroclinicity biases are found in the extratropical latitudes of the Atlantic Ocean and between 45°S and 60°S in the other oceans, which also correspond well with the negative track density biases (Figure 4.5c).

The summer temperature zonal mean (Figure 4.17a, c and e) indicates that the cold biases at upper levels (300-100 hPa) are weaker and more poleward (around 70°S) than in winter over the southern oceans. The temperature positive bias pattern persists at the tropopause (above 50hPa) over tropical latitudes in the summer

season, and may indicate a systematic error because it can also be seen in autumn and spring (Figures 4.19 and 4.18).

The zonal mean zonal wind biases (Figures 4.17b,d and f) show that the jet biases extend from upper levels toward lower levels. Simpson et al. (2013a), Simpson et al. (2013b) found the same pattern which may indicate a link with the Southern Annular Mode (SAM) during the summer season because of a lack of negative feedbacks from planetary waves and a delay in the breakup of the polar vortex. In general, the summer zonal wind biases are smaller than in other seasons related with the better representation of the single eddy-driven jet in this period. Another possibility is suggested by Sun et al. (2014), who found that ozone depletion can delay the polar vortex breakup, inducing a deep response in planetary wave drag and associated eddy-driven circulation. Vasconcellos (2012) investigated the ozone extreme concentration impacts in a GCM idealized experiment and found that under ozone maximum scenario a SAM negative phase for January and April and SAM positive phase for July and November, while opposite phases were found under minimum  $O_3$  scenario. Therefore, the jet position biases seem associated with upper temperature negative biases with the probable effects on the track density biases (Figure 4.5c) in the SH oceans.

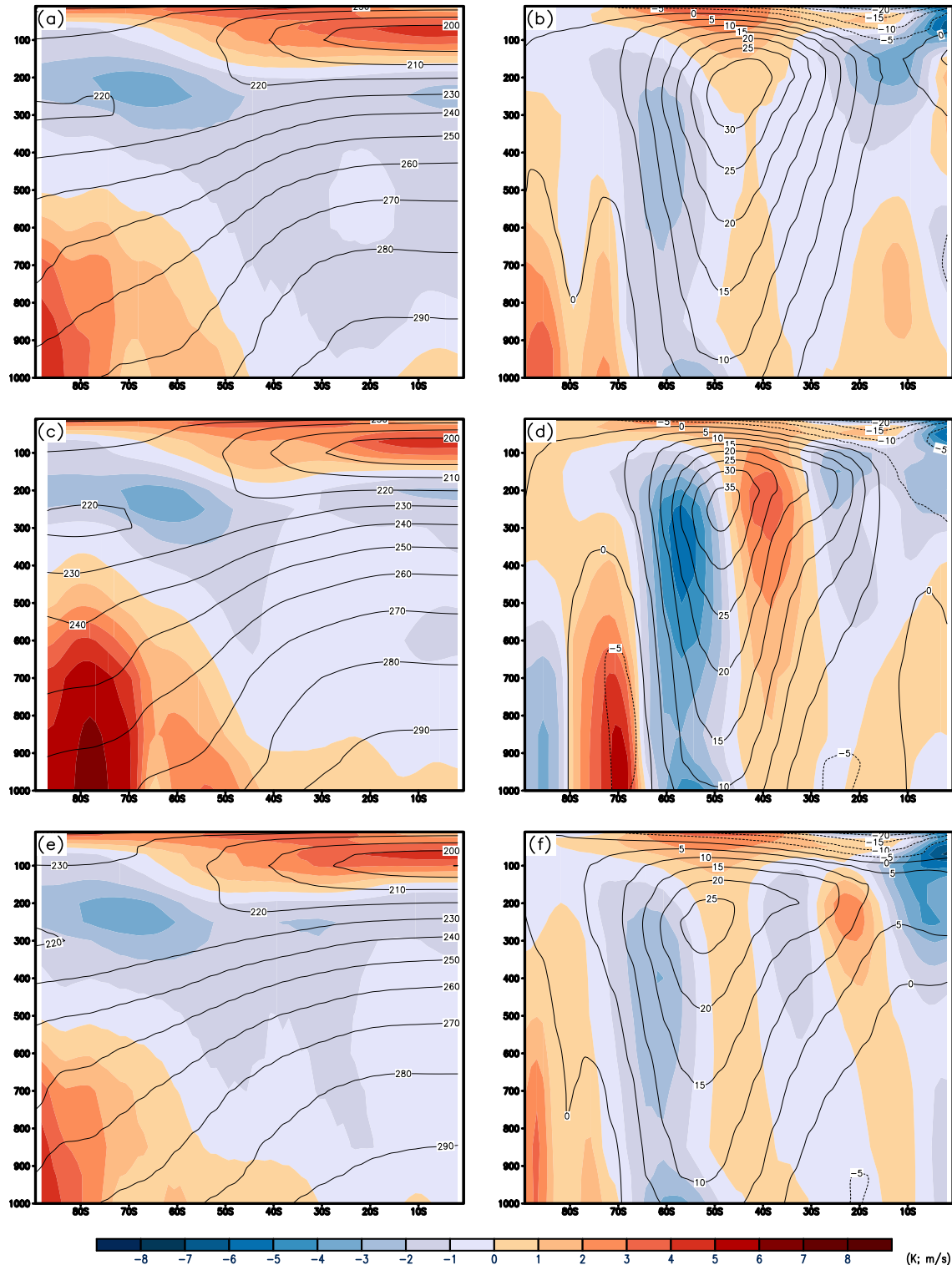
The results during the summer also support the hypothesis that HadGEM2-ES has a different Rossby waveguide compared with ERA-Interim, as described above for winter. During the summer, SST positive biases peaks over the Atlantic and Indian oceans at a latitude of  $70^\circ\text{S}$  (Figure 4.15c). Consequently, a strong zonal wind bias over the Indian Ocean that extends from surface to high levels, is strong on the equatorward side of the jet and weaker on poleward side around 250hPa (Figure 4.17d). This jet cross the Indian Ocean toward Pacific Ocean and enhance the baroclinicity at upper levels mainly over Australia and New Zealand, as shown in Figure 4.11c. These differences occur over a well-known region of the Rossby Wave source during DJF (SHIMIZU; CAVALCANTI, 2011) and it seems to indicate a change of the waveguide, storm track and precipitation (Figure 4.16c) over the Southern Hemisphere.

Similar to the other large-scale biases, the 500 hPa geopotential biases (Figure 4.14c) in the summer are also much weaker than in winter, however, only the SST biases (Figure 4.15c) are stronger. The large negative geopotential bias peak near to New Zealand is related to the positive bias in the lower troposphere over high latitudes that result in a geopotential slightly higher relative to ERA-Interim. This result

corresponds with previous studies, such as Hoskins and Hodges (2005) that found the same region near to New Zealand is also a region with a maximum of anticyclone genesis, which is more intense in the autumn and summer. In this way, the zonal wind anomalies around this low height bias can increase the flow equatorward of south Australia and poleward of  $50^{\circ}\text{S}/60^{\circ}\text{S}$ , which are consistent with the track density bias dipole (Figure 4.5c) close to New Zealand in a region where the storm track densities are most polewards (Figure 4.1c). These results are consistent with the patterns at 500hPa found by Ummenhofer et al. (2013) using a GCM model where it seems to be related to the blocking systems displaced over this region (Figure 4.14c). Besides, this pattern is also consistent with the negative lysis biases (Figure 4.7c) on the Antarctic coast around  $150^{\circ}\text{W}$  and the positive genesis biases (Figure 4.6c) over the east of New Zealand and the Tasman Sea. Also, HadGEM2-ES tends to represent larger geopotential height anomalies in this region and this pattern can help to explain the fewer cyclones near to Antarctica and more cyclones over the equatorward side of the ST in the track density biases (Figure 4.5c).

During the austral summer the SST biases are stronger than in winter as shown in Figure 4.15c. The positive bias peaks over the Atlantic and Indian oceans seem similar to the winter season, however, those in the Pacific Ocean are amplified towards the equator between longitudes of  $90^{\circ}\text{W}$  and  $180^{\circ}\text{W}$ . These regions correspond with the negative track density biases (Figure 4.5c) and baroclinicity at the lower level (Figure 4.12c). Over tropical latitudes the negative biases are weaker than winter, particularly in the Atlantic and Pacific oceans, and other peaks are found over the Indian Ocean close to southern South Africa.

Figure 4.17 - Zonal mean temperature and zonal wind in summer for the period 1979-2005.



Zonal mean temperature (K) (left column) and zonal mean zonal wind ( $m/s$ ) (right column) biases (HadGEM2-ES minus ERA-Interim) in DJF for the Southern Hemisphere Oceans: (a) and (b) Atlantic; (c) and (d) Indian; and (e) and (f) Pacific. Black line contours show ERA-Interim climatology for the period 1979-2005.

SOURCE: Author's production.

### 4.2.2.3 Transition seasons

The baroclinicity biases at upper levels (250hPa) (Figure 4.11b) for the spring season have a symmetric, zonal and extensive biases over the SH, similar to the winter season, with a negative bias ring at high latitudes (over 60°S) and positive biases over extratropical latitudes (between 60°S and 30°S). The HadGEM2-ES model tends to represent the SSTs that are warmer over extratropical latitudes (Figure 4.15b) and it may be related to problems in the model physics to represent cloud feedbacks (LIN et al., 2014). The biases over the Pacific Ocean and Antarctic are stronger than winter. The autumn upper level baroclinicity biases (Figure 4.11b) are somewhat similar to the summer, except in the Australia region, which has the same bias features as the winter.

Different from other fields analysed, the baroclinicity spatial pattern at lower levels (850hPa) during the transition seasons are similar with those in the following seasons. Spring season baroclinicity bias peaks (Figure 4.12b) over South America, Australia and Pacific are stronger than any other season. Indian Ocean positive bias peaks are observed from the southern sector of South Africa toward New Zealand (approximately 45°S), however an increased negative biases over Pacific middle latitudes are stronger than any other season. The autumn lower level baroclinicity biases (Figure 4.12d) are smallest of the all the seasons and the spatial pattern is similar to winter. The Atlantic Ocean has the largest negative biases during autumn, which is related to the start of the twin waveguide patterns discussed in this Section for the winter season (4.2.2.1).

Spring temperature biases are similar to the winter season with cold biases around the middle and high latitude tropopause and warm biases in both regions at lower levels. Upper level cold biases are larger than in the other seasons over the high latitude stratosphere and are related to a delay in the stratospheric final warming, breakup of the polar vortex, in the models (CHARLTON-PEREZ et al., 2013; GARFINKEL et al., 2013; SIMPSON et al., 2013a). Charlton-Perez et al. (2013) used the CMIP5 ensemble dataset, including the HadGEM2-ES model used here, and found this bias in both hemispheres. Barnes and Garfinkel (2012) and Garfinkel et al. (2013) studied the dynamical mechanism of eddy momentum flux convergence and found a link between the delay in the vortex breakup to a lack of parametrized surface roughness mainly over the Indian Ocean, which results in a wind bias that affects the stratosphere.

Recent studies show that the links between some aspects of the increase in the

surface drag with the poleward shift of the eddy-driven jet (ROBINSON, 1997; CHEN et al., 2007) link the jet latitude with the speed (KIDSTON; VALLIS, 2012). In this way, studies such as Garfinkel et al. (2013) and Edson et al. (2013), highlighted the importance of changing the Charnock parameter <sup>1</sup> (CHARNOCK, 1955) to larger values based on recent observations with the resultant increase in surface drag and decrease in wind speed. McLandress et al. (2011) studied the systematic bias of a delayed springtime breakdown of the SH stratospheric polar vortex and found that it is linked with the missing orographic gravity wave drag associated with subgrid scale islands near 60°S in the southern oceans. Garfinkel and Oman (2018) applied the McLandress et al. (2011) methods using the NASA Goddard Earth Observing System Chemistry-Climate Model and found that the orographic drag from these small islands over the SH has impacts for the surface climate, since biases in tropospheric jet position are also partially improved. Butchart et al. (2011) investigated the stratospheric climate and variability from simulations of chemistry-climate models and found similar cold biases in the lower stratosphere. Therefore, the previous results are similar to those discussed here for the spring season.

The temperatures cross sections during the autumn season (Figure 4.18) are similar to summer, however the warm biases at lower levels over middle and high latitudes are weaker. This warm bias pattern corresponds with the SST warm biases (Figure 4.15) and are very similar to the summer season but slightly weaker.

The zonal wind cross sections in the transition seasons have similar features to austral winter, which show a split jet in the Indian (Figures 4.18d and 4.19d) and Pacific Oceans (Figures 4.18f and 4.19f) (see Section 4.2.2.1 for winter), with the autumn split jet less well defined than spring. Spring season biases are negative on the poleward side of the polar jet core (between 60°S and 50°S) at all levels, which indicates a poor representation of the climatological split jets mainly over the Indian and Pacific Oceans, also similar to the winter season. The spring season (Figure 4.18) has the largest upper level biases of any season, with increased biases throughout the stratosphere, and seems also associated with the cold stratospheric biases discussed before and helps to explain the large track density biases (Figure 4.5b) over southern Australia. On the other hand, the autumn season has the smallest biases and the main negative peak over the Atlantic indicates a weaker representation of the jet stream.

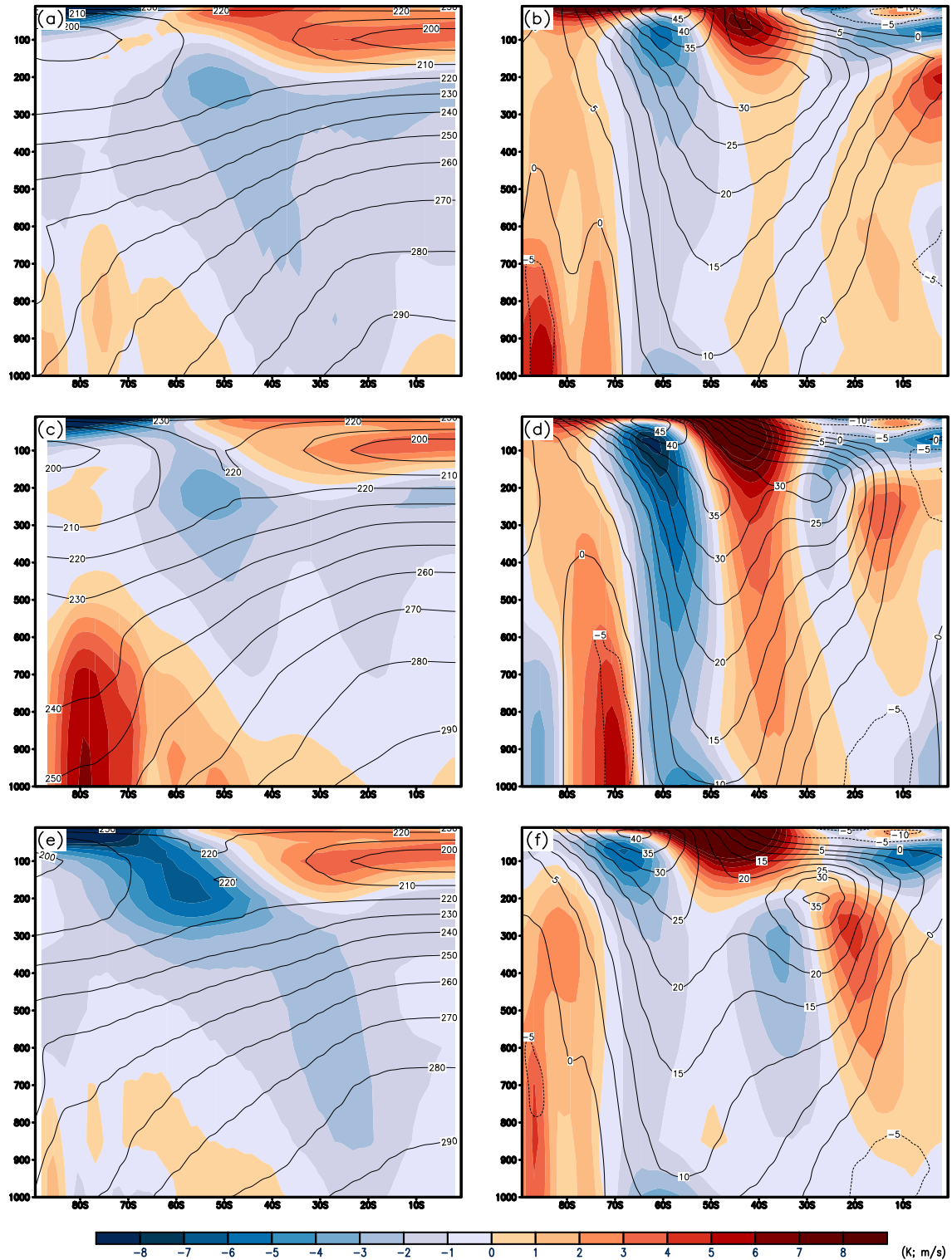
Finally, the geopotential height anomaly biases for the transition seasons (Figures

---

<sup>1</sup>It accounts for increased roughness as wave heights grow due to increasing surface stress.

4.14b and d) are spatially different to the other seasons. The spring biases (Figure 4.14) are concentrated from the Indian Ocean towards the Pacific Ocean. Negative height peaks are found in the Indian Ocean, however there are positive height biases mainly in the Pacific, thus both regions correspond with the extension of the large storm track tilt biases (Figure 4.5b).

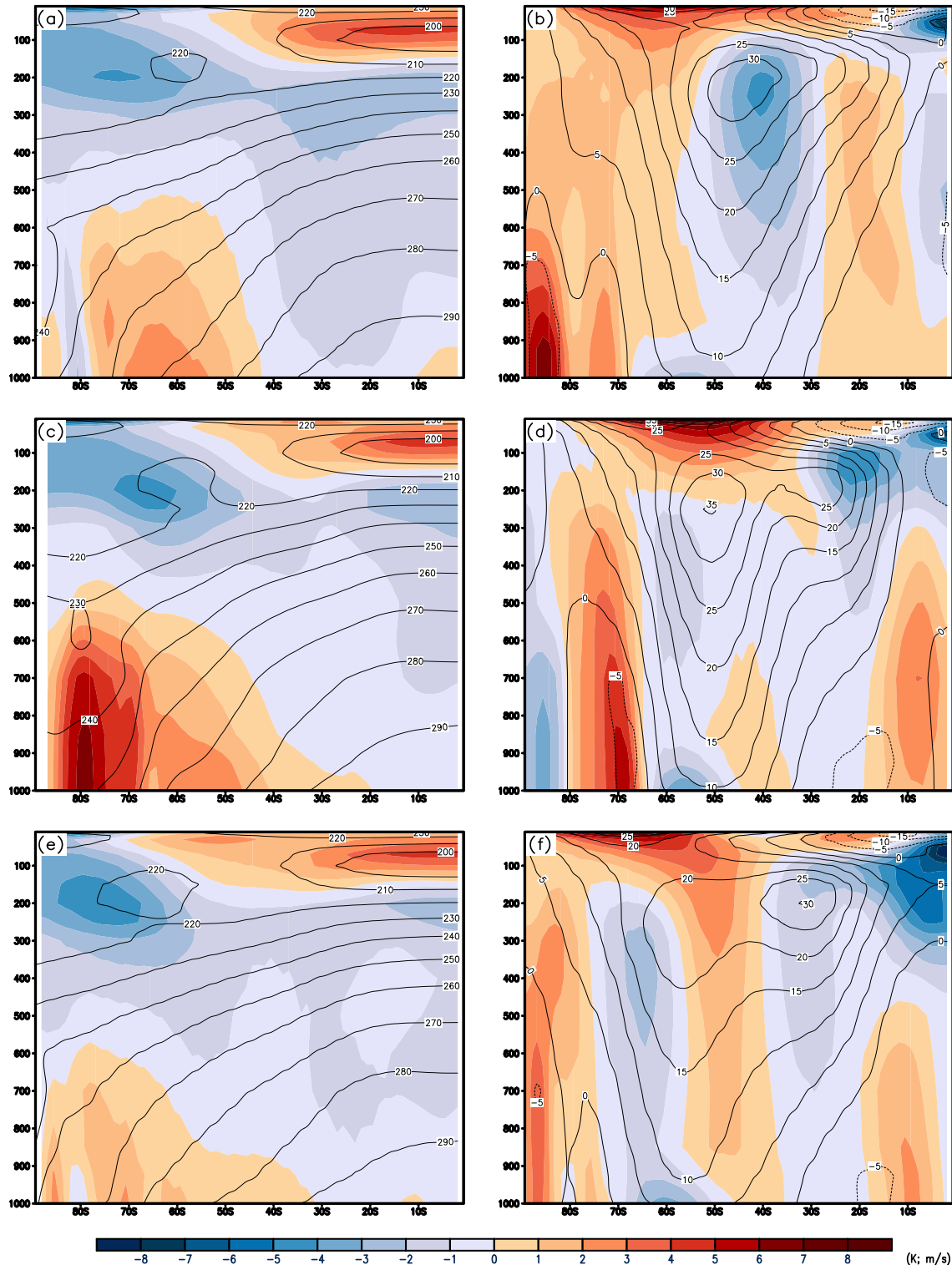
Figure 4.18 - Zonal mean temperature and zonal wind in spring for the period 1979-2005.



Zonal mean temperature (K) (left column) and zonal mean zonal wind ( $m/s$ ) (right column) biases (HadGEM2-ES minus ERA-Interim) in SON for the Southern Hemisphere Oceans: (a) and (b) Atlantic; (c) and (d) Indian; and (e) and (f) Pacific. Black line contours show ERA-Interim climatology for the period 1979-2005.

SOURCE: Author's production.

Figure 4.19 - Zonal mean temperature and zonal wind in autumn for the period 1979-2005.



Zonal mean temperature (K) (left column) and zonal mean zonal wind ( $m/s$ ) (right column) biases (HadGEM2-ES minus ERA-Interim) in MAM for the Southern Hemisphere Oceans: (a) and (b) Atlantic; (c) and (d) Indian; and (e) and (f) Pacific. Black line contours show ERA-Interim climatology for the period 1979-2005.

SOURCE: Author's production.

### 4.2.3 Cyclone intensity biases

The cyclone intensity biases are calculated using the vorticity field at 850hPa for each HadGEM2-ES ensemble member individually and for the HadGEM2-ES average as the difference between the HadGEM2-ES and the ERA-Interim reanalysis (HadGEM2-ES - ERA-Interim). The climatology period is 1979 to 2005 for both dataset.

#### 4.2.3.1 Cyclone count

Results show that the number of cyclones identified, shown in Table 4.1, in HadGEM2-ES are less than in ERA-Interim in all seasons, with greater biases during MAM. In general, the differences in numbers are relatively small and may be associated with two main factors. First, the model tends to represent fewer cyclones possibly due to the lower spatial resolution when compared with the reanalysis. Hodges et al. (2011) shows that ERA-Interim with higher resolution compared to older reanalyses (low resolution) has a significant improvement in cyclone representation especially over the SH. These biases may also be related to the representation of the Andes that can affect directly the genesis number. Secondly, the model tends to simulate a single jet stream during SON, which causes a faster disappearance of the winter split jet and reduces the number of cyclones and cyclogenesis mainly over the Pacific and Atlantic Ocean (Figure 4.18b,d). However, the inverse occurs in the autumn season, which shows a split jet over Pacific Ocean in the ERA-Interim climatology (Figure 4.19f, black contour lines) while the model tends to single jet (Figure 4.19f, negative biases in the split jet core). Therefore, these biases partially contribute to the underestimation of the number of cyclones over the Southern Hemisphere.

Table 4.1 - Number of cyclones per month for each season that are found in the Southern Hemisphere extratropics (90°S,20°S) for the period 1979-2005. Abbreviations: EM, Ensemble Member.

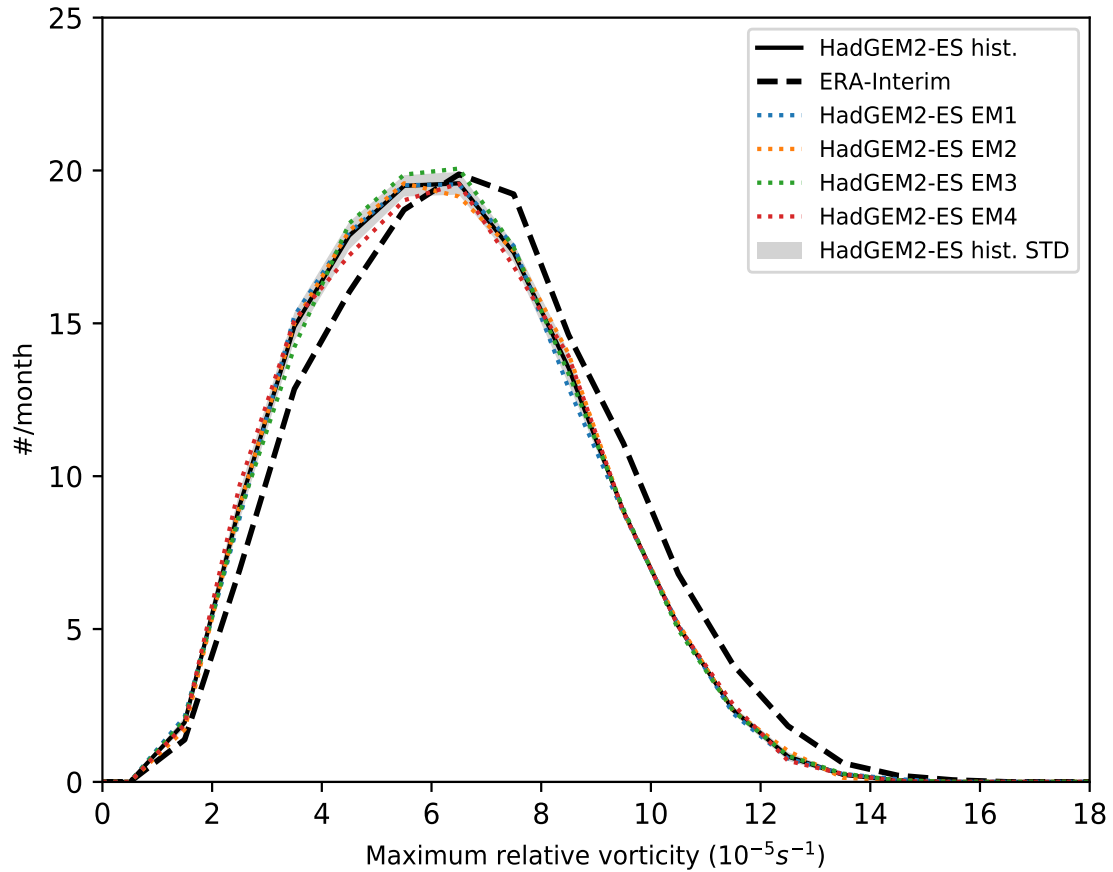
Experiment	JJA	SON	DJF	MAM
HadGEM2-ES EM 1	130.7	124.1	109.0	122.5
HadGEM2-ES EM 2	131.4	121.2	108.4	120.8
HadGEM2-ES EM 3	131.5	121.8	108.8	122.1
HadGEM2-ES EM 4	130.7	123.1	108.1	122.9
HadGEM2-ES	131.1	122.6	108.6	122.1
ERA-Interim	134.0	124.9	111.9	126.0
Differences	-2.9	-2.4	-3.3	-3.9

SOURCE: Author's production.

#### 4.2.3.2 Maximum intensity distribution

The austral winter has the highest number and intensity of cyclones of all seasons, shown in Figure 4.20. The ERA-Interim (dashed black line) has larger intensity magnitudes and higher numbers of cyclones of 19.87 per month for cyclones with vorticity of  $-6.5 \times 10^{-5} s^{-1}$ . These results are consistent with Hodges et al. (2011). The HADGEM2-ES (Figure 4.20, solid black line) represents very well the number of cyclones during the winter season, however tends to underestimate the intensity of cyclones, indicating that the distribution is shifted to weaker intensity values. The winter storm track has the largest biases discussed in the results (see Section 4.2.1.1 and 4.2.2.1). The maximum standard deviation is 0.53 cyclones per month for this distribution. HadGEM2-ES EM3 (Figure 4.20, dashed green line) has the maximum number of cyclones (20.06) for vorticity of  $-6.5 \times 10^{-5} s^{-1}$  and the most near to the total cyclones (131.5) in relation to climatology (134.0) in this season, as shown in Table 4.1.

Figure 4.20 - Maximum intensity distribution for JJA during the period 1979-2005.

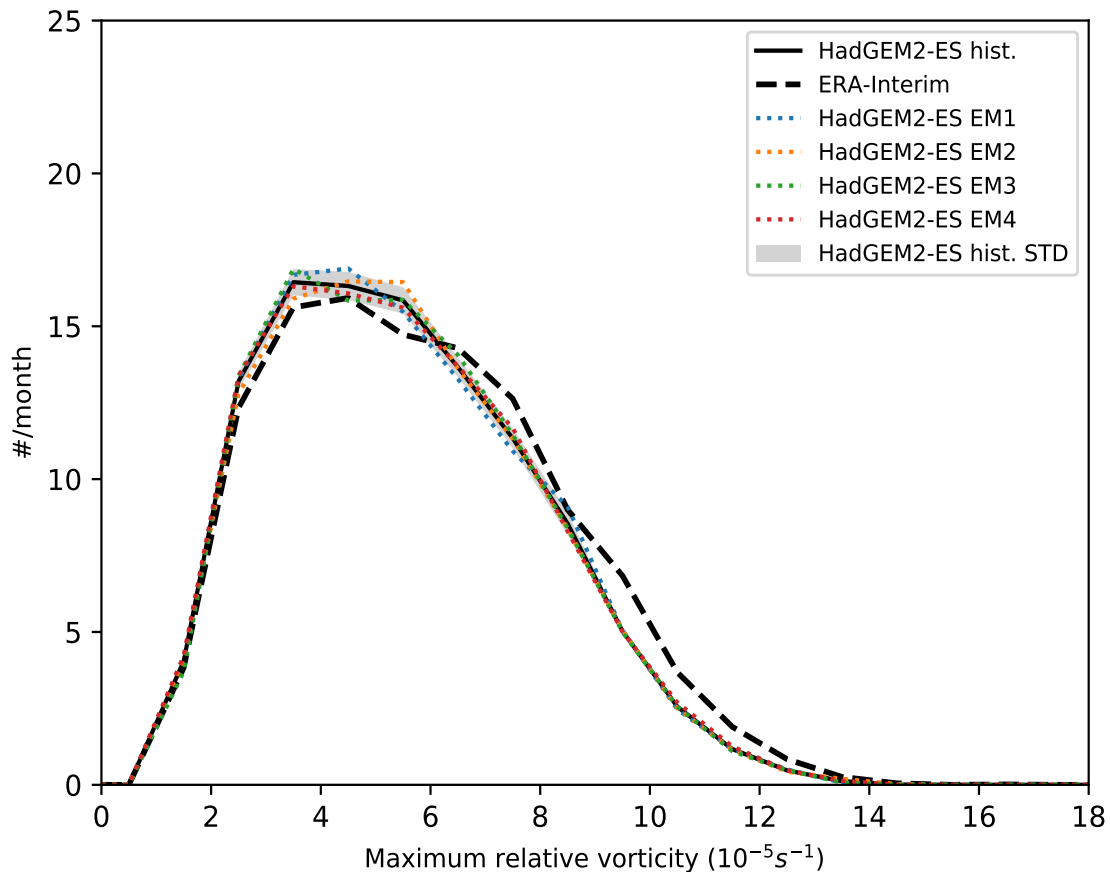


Maximum intensity distribution based on 850hPa relative vorticity for austral winter (JJA) over SH extratropics ( $90^{\circ}\text{S} - 20^{\circ}\text{S}$ ). Values are number per month for the period 1979-2005 for the HadGEM2-ES experiments and ERA-Interim reanalysis. Black solid line represents HadGEM2-ES historical, dashed black line represents ERA-Interim, HadGEM2-ES ensemble members are represented with the dashed thin lines, standard deviation of climatology across the 4 HadGEM2-ES ensemble members is represented by light grey shading. The vorticity is scaled by -1 and the bin widths are  $1 \times 10^{-5} \text{ s}^{-1}$ .

SOURCE: Author's production.

The summer season ERA-Interim intensity distribution (Figure 4.21, dashed black line) is narrower and weaker than all seasons. Hodges et al. (2011) also obtained similar results for other reanalyses. In contrast to the austral winter (Figure 4.20), the HadGEM2-ES (Figure 4.21, solid black line) distribution is also slightly shifted to weaker cyclones, but overestimates the number of cyclones particularly for vorticity between  $-2$  and  $-6 \times 10^{-5} s^{-1}$ , where the maximum number of cyclones (15.92) for the summer season occurs (Figure 4.21, dashed black line). Although HadGEM2-ES has more cyclones during the peak (16.88), fewer cyclones are simulated during the summer season and the total difference is  $-3.3$  cyclones per month in relation to ERA-Interim, as shown in Table 4.1. The maximum standard deviation is 0.46 cyclones per month for this distribution.

Figure 4.21 - Maximum intensity distribution for DJF during the period 1979-2005.

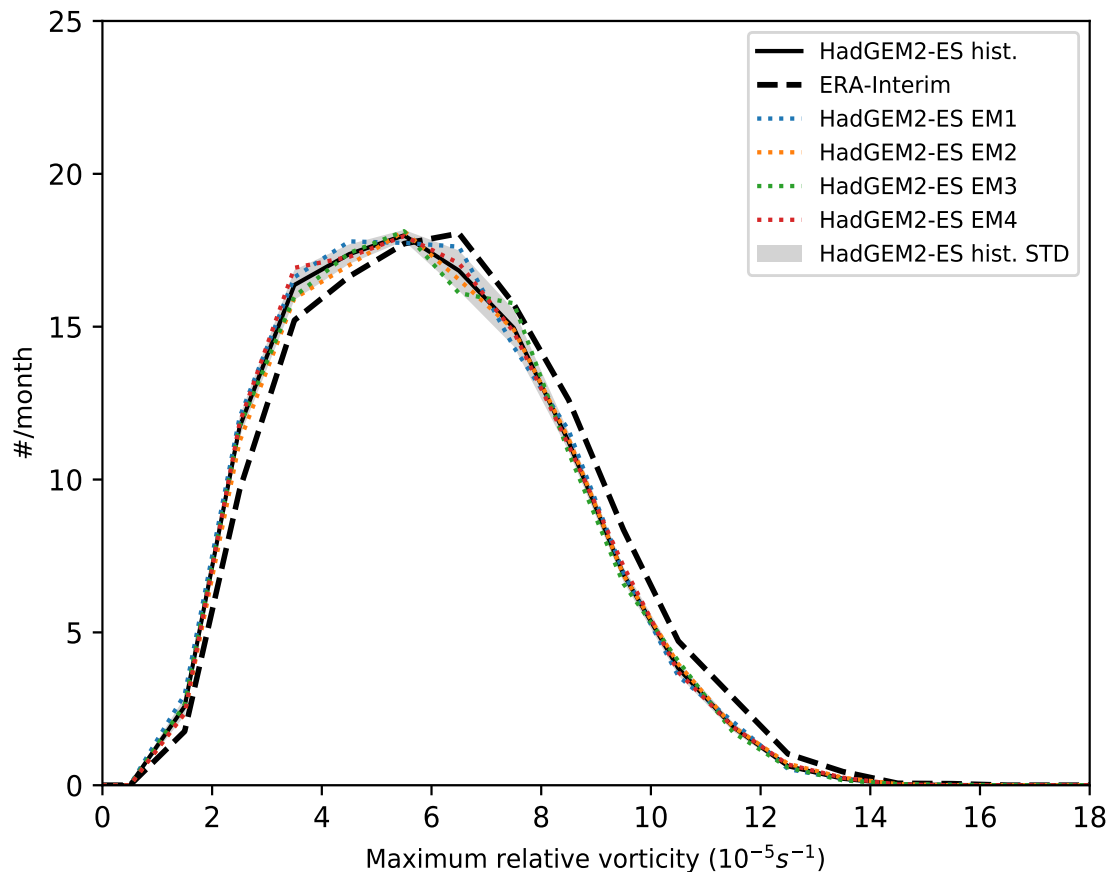


As in Figure 4.20 but for austral summer (DJF).

SOURCE: Author's production.

The spring maximum intensity distribution is shown in Figure 4.22. In general, the spring season is very similar to the winter season, but with fewer cyclones during the peak of the season, 18.05 against 19.87 (winter), for vorticity  $-6.0 \times 10^{-5} s^{-1}$ . The HADGEM2-ES (Figure 4.22, solid black line) also represents well the number of cyclones in this season and the total difference in relation to ERA-Interim is the smallest, -2.4 cyclones per season (Table 4.1). Though the smallest difference, the spring storm track has some of largest biases discussed in the results (see Section 4.2.1.3 and 4.2.2.3). The model also tends to underestimate the intensity of cyclones and the distribution is shifted to weaker intensity values. The maximum STD is 0.66 cyclones per month for this distribution, the largest of all seasons.

Figure 4.22 - Maximum intensity distribution for SON during the period 1979-2005.



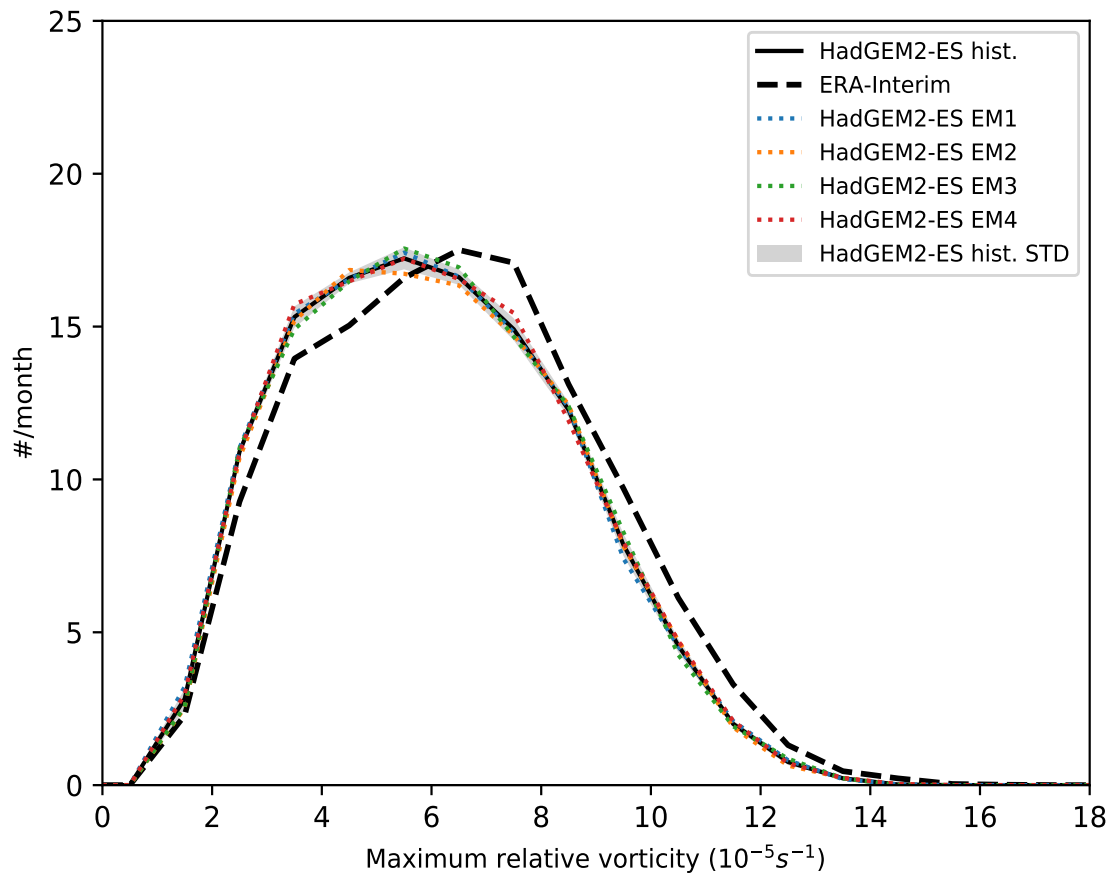
As in Figure 4.20 but for spring (SON).

SOURCE: Author's production.

HadGEM2-ES EM2 (Figure 4.22, dashed orange line) and EM3 (Figure 4.22, dashed green line) has the maximum number of cyclones (18.12) for vorticity of  $-5.5 \times 10^{-5} s^{-1}$ , although the HadGEM2-ES EM1 (Figure 4.22, dashed blue line) total cyclones (124.1) has the smallest difference (0.8) in relation to climatology (124.9) of all seasons (Table 4.1).

The autumn season ERA-Interim intensity distribution (Figure 4.21, dashed black line) is similar to the summer season, but less narrow and stronger. The HadGEM2-ES (Figure 4.23, solid black line) distribution is also shifted to weaker cyclones and the maximum number of cyclones is 17.23 for vorticity  $-5.5 \times 10^{-5} s^{-1}$ , while for ERA-Interim is 17.5 for vorticity  $-6.5 \times 10^{-5} s^{-1}$ .

Figure 4.23 - Maximum intensity distribution for MAM during the period 1979-2005.



As in Figure 4.20 but for autumn (MAM).

SOURCE: Author's production.

In contrast with the spring season, the autumn total cyclone difference is the largest of all seasons, -3.9 cyclones per season (Table 4.1), but the storm track has fewer biases (see Section 4.2.1.3 and 4.2.2.3). The maximum standard deviation is 0.36 cyclones per month for this distribution, the smallest of all seasons, indicating that the HadGEM2-ES ensemble members agrees between their.

### 4.3 Discussion and conclusion

In summary, the ST activity is constrained between 20°S and 70°S over the SH and the maximum track densities can be seen on the poleward side. The genesis densities and growth rates tends to be found at equatorward latitudes and the lysis densities and decay rates at poleward latitudes, close to the Antarctic coast. These figures show the cyclone distributions are very similar to that obtained from previous studies from synoptic charts analysis (TALJAARD, 1972; GAN; RAO, 1991), older reanalyses (SINCLAIR, 1994; SINCLAIR, 1995; SINCLAIR, 1997; HOSKINS; HODGES, 2005; HODGES et al., 2011) and climate models (BENGTSSON et al., 2006; CHANG et al., 2013).

The use of HadGEM2-ES, a modern earth system climate model and the ERA-Interim reanalysis together with objective cyclone tracking techniques has enabled a detailed view of the Southern Hemisphere storm tracks and an assessment of the performance of HadGEM2-ES with respect to cyclones and the STs. The comparison of the cyclone tracking statistics were performed for winter (JJA), spring (SON), summer (DJF) and autumn (MAM). The results show that in general the Southern Hemisphere storm tracks correspond well between the model and reanalysis, with some regions slightly displaced in the variables analyzed. However, zonal biases in the track density were found, mainly around Antarctica and in the Indian Ocean. A summary of the results are outlined below.

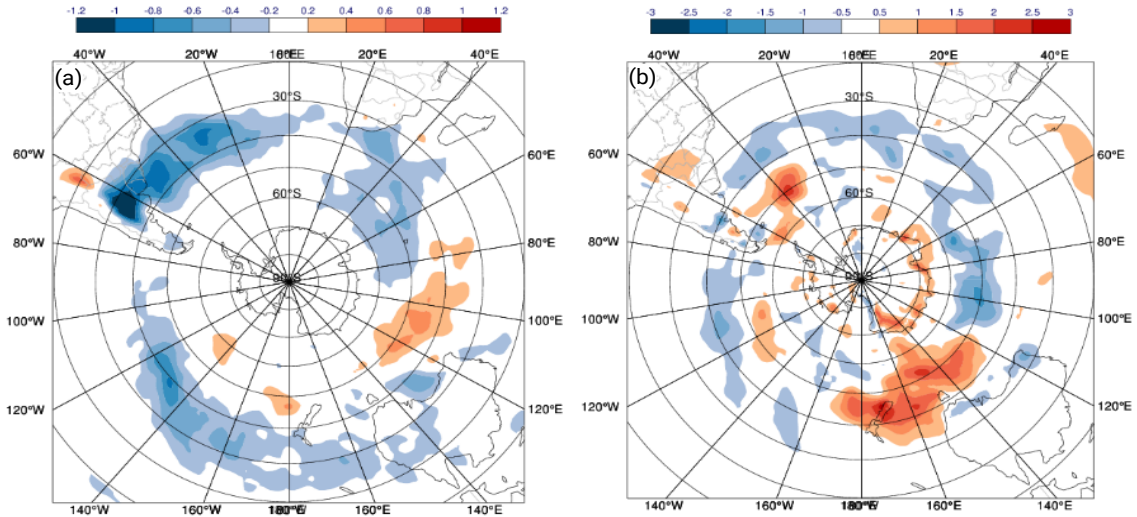
- The storm tracks in the Southern Hemisphere have larger width with more cyclones on the equatorward side and less over the poleward side in HadGEM2-ES. This equatorward bias pattern has high correspondence with the upper level jet differences. These results were also found by Lambert et al. (2002), Bengtsson et al. (2006) using the previous generations of climate models. Roeckner et al. (2006) conducted experiments with the ECHAM5 model (atmospheric only) to investigate the impacts of better horizontal and vertical resolution and found, in higher horizontal resolution, a zonal temperature increase and poleward shift and intensification of

the westerlies in extratropical latitudes. Thus, the results show that there is a link between the equatorward bias and the low resolution in the historical experiments of HadGEM2-ES. This specific issue will be explored in a further study.

- The greatest differences in the track density is observed in the Indian Ocean, between Antarctica and Australia, during the winter season. These biases indicate a poor spatial representation of the winter storm track spiral towards Antarctic in the HadGEM2-ES experiment. The results indicate that this problem is partially caused by two regional factors, the first is because of the negative genesis biases in the climatological cyclogenesis regions over South America, Antarctic Peninsula and the Antarctic coast approximately on longitude  $150^{\circ}\text{E}$ , that is reflected in the number of cyclones in the ST. The second factor is due to model resolution and the representation of the Andes Mountains, which show biases above 1000 meters. In general, both factors affect all seasons but are evidenced during the austral summer because of the single eddy-driven jet, as shown in Figure 4.24. The meridional moisture transport at 700hPa (Figure 4.24a) has the largest biases leeward of the Andes Mountains, indicating an underestimate of moisture for this important cyclogenetic region over South America. Consequently, this negative bias impacts the cyclone energy balance reducing the kinetic energy at 700hPa (Figure 4.24b) along the Atlantic and Indian oceans. Therefore, these meridional biases aid to explain the HadGEM2-ES weaker cyclones distribution observed in all seasons.
- In general, the HadGEM2-ES large-scale biases tend to have a similar pattern to the ST biases. In the upper levels, large cold biases were found over the extratropical and Polar Regions, which is a result of the equatorward jet position bias of the subtropical jet and a negative bias in the polar jet (eddy-driven). The analysis shows that the split jet during the autumn and particularly winter and spring is a model problem linking these biases and the reason seems directly related to wrong representation of the stationary wave pattern which, for example, impacts the SAM. The additional field, track density biases at upper level (250hPa), is shown in Figure 4.25 and illustrate the jet biases pattern spatially for winter (a) and spring (b).
- The breakup delay of the polar vortex in the spring season associated with the negative temperature biases in the upper and lower levels can be related with parametrization problems, such as the lack of orographic gravity wave

drag and ozone depletion.

Figure 4.24 - Meridional moisture and kinetic energy biases for period 1979-2005.



Meridional moisture transport (a) and kinetic energy (b) biases (HadGEM2-ES minus ERA-Interim) in 700hPa for DJF over Southern Hemisphere. Black line contours show ERA-Interim climatology for the period 1979-2005.

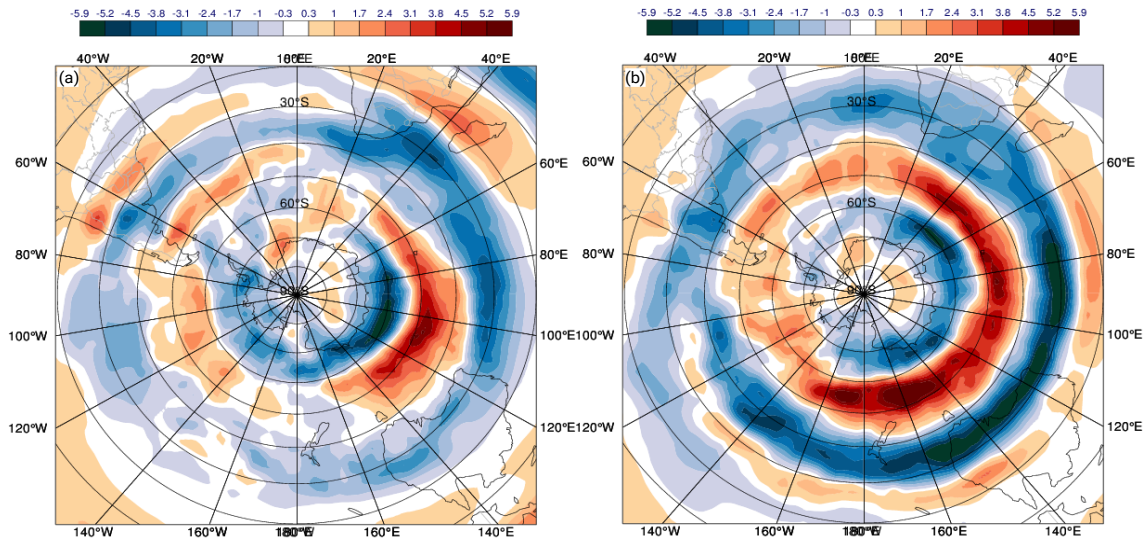
SOURCE: Author's production.

- Over the oceans, the track, genesis, mean growth/decay rate densities biases are possibly associated with the poor representation of location and variability of ocean fronts and stratocumulus clouds.

These results show that there is a considerable agreement between the climate model and the reanalysis, however, there are differences and it is important to be aware of these when using the model to study the impact of perturbation experiments such as removing the Amazon Forest. An important feature that needs to be considered is, although the reanalyses representation of some patterns has seen considerable improvements in recent years, some patterns such as the cyclogenesis in the lee of Andes Mountains continue to be not well represented (HODGES et al., 2011). In addition, differences are still apparent in the storm track density during the winter season. These biases were already found in previous storm tracks studies using previous generation of climate models (e.g. Bengtsson et al. (2006), Ulbrich et al.

(2009), Chang et al. (2013)), and also in the new model generation of CMIP5 models for the North Atlantic (e.g. Zappa et al. (2013a), Zappa et al. (2014)). In this study, using the HadGEM2-ES historical simulations for CMIP5, a similar pattern of zonal biases for the Southern Hemisphere was found.

Figure 4.25 - Track density biases at 250hPa for the period 1979-2005.



Differences (HadGEM2-ES minus ERA-Interim) in extratropical cyclone track densities at 250hPa for the period 1979-2005 over Southern Hemisphere in: (a) JJA and (b) SON.

SOURCE: Author's production.

In summary, the ST comparison between the historical experiment of HadGEM2-ES and the ERA-Interim reanalysis showed that the HadGEM2-ES has a good representation of extratropical cyclones in the Southern Hemisphere. The total difference in terms of number of cyclones per season is fewer than 4%. The storm track features in HadGEM2-ES are consistent in many aspects with ERA-Interim. These results provide confidence for using HadGEM2-ES for future climate studies, as will be investigated in the Chapter 5.



## 5 SOUTHERN HEMISPHERE STORM TRACK FUTURE PROJECTIONS

The previous chapter of this thesis emphasized the biases in the representation of extratropical cyclones and storm tracks in the past recent climate when contrasted with cyclones identified in the ERA-Interim reanalysis. The previous analyses has shown that there are biases and errors in both the climatological position of the Southern Hemisphere (SH) Storm Track (ST) and cyclone intensities in the HadGEM2-ES ensemble mean. In this chapter two idealised scenarios with and without the Amazon Forest are simulated under two future projection scenarios, called Representative Concentration Pathways (RCP), in the HadGEM2-ES model. The experiment with the Amazon Forest are referred to as the Control (CTRL) and without the Amazon as WAMZ, are simulated in idealised experiments for both the radiative forcing scenarios RCP8.5 and RCP4.5. For a detailed overview about the experiments, see Chapter 3 - Section 3.1.3.2 (Table 3.4). The RCP8.5 scenario is a scenario with the highest greenhouse gas emissions for which radiative forcing achieves  $> 8.5 W/m^2$  by 2100 and continues to rise after this, while the RCP4.5 scenario is an intermediate pathway where radiative forcing is stabilized at approximately  $4.5 W/m^2$  after 2100 (MOSS et al., 2010; VUUREN et al., 2011). The results of these experiments are analysed with respect to the changes in the SH storm track for the climatological period of 2070-2099, with a particular focus on the regional-scale changes in South America (SA). Also, the experiments CTRL and WAMZ in both the RCPs will be compared with the Historical scenario, analysed in Chapter 4, for the climatological period of 1976-2005. The detailed overview of the scenarios, configurations and experiments used in this chapter are presented in the Chapter 2 and 3.

The aim of this chapter is to determine how storm tracks are changed in an idealised HadGEM2-ES experiment that contrast the existence of the Amazon Forest for the future climate projections. This will then provide new results about the importance of the Amazon Forest to the SH climate, specially over SA, when simulated with a climate model using an earth system configuration.

The key science questions which are addressed by this chapter are:

- What are future Southern Hemisphere storm track changes are predicted by HadGEM2-ES under two IPCC future climate change scenarios?
- How might Amazon land use cover change affect the storm track and climate over South America?

This chapter will be divided into two sections in a similar way to the previous one. The chapter will primarily highlight the RCP8.5 scenario experiments, but with the RCP4.5 scenario experiments shown where differences are found. Section 5.1 focuses on HadGEM2-ES changes relative to the historical period for the WAMZ and CTRL experiments, by examining the storm track density, large-scale mean circulation and cyclone intensity over the Southern Hemisphere. An further subsection highlights the regional-scale climate changes over SA. Finally, Section 5.2 summarizes the chapter with a discussion about the main ST and climate changes found.

## 5.1 HadGEM2-ES ensemble changes

This section compares the SH cyclone and storm track climatology from the 4 HadGEM2-ES ensemble members for each experiment under the RCP8.5 and RCP4.5 scenarios for the 30-year period of 2070-2099. The WAMZ and CTRL experiments are first contrasted with the Historical experiment (1976-2005) to give a background for the projected future changes, then the experiments are compared between each other to show more clearly the impact of the removal of the Amazon Forest on the SH cyclones and storm tracks. Storm track statistics are analysed using the means of large-scale fields to aid the understanding and discussion of the changes in the extratropical cyclone statistics. Some additional fields are shown to link these impacts with the regional-scale changes. The experimental setup of the idealised and historical experiments are described in Section 3.1.

### 5.1.1 Storm track density changes

The STs density biases are calculated for each HadGEM2-ES ensemble member individually and then for the HadGEM2-ES ensemble mean, as the difference between each idealised experiment and the Historical experiment (WAMZ–Historical and CTRL–Historical) and between them (WAMZ–CTRL) for each RCP. The discussion focuses first on the results for the CTRL experiment, followed by the WAMZ experiment and finally with the difference WAMZ–CTRL. The differences between the experiments and the historical period are important to give an idea of the magnitude of change in relation to the past climate and in relation to the projected future climate when the Amazon Forest is removed.

### 5.1.1.1 Winter

The SH storm track future projected changes during the austral winter are shown in Figure 5.1 for RCP8.5 (left) and RCP4.5 (right) scenarios in terms of the cyclone track densities. In general, the storm track changes in the CTRL experiment (Figures 5.1c and d) show a consistent poleward shift for both of the RCPs, with the track density decreasing on the equatorward side and increasing on the poleward side of the main ST, which is similar to the results found with the CMIP5 climate models (CHANG, 2013; HARVEY et al., 2014). However, the ST changes in the WAMZ experiment show a consistent reduction in the poleward shift, compared with the CTRL experiment, with the track density showing smaller increases on the equatorward side and decreases on the poleward side of the main storm track (Figures 5.1a and b). During the austral winter season the ST density for RCP8.5 future changes seem stronger than for RCP4.5, however some positive changes are stronger for RCP4.5. The ST changes are similar for both RCPs (Figure 5.1) and the largest changes are commonly negative over southern Australia, northern New Zealand and towards south of South America. Positive areas are found around Antarctica and in the Atlantic Ocean ( $\sim 50^\circ\text{S}$ ) mainly in the CTRL experiment. The same positive region over the Atlantic also occurs in the WAMZ experiment (Figure 5.1a) but is slightly displaced and stronger.

The differences (WAMZ–CTRL) are shown in Figures 5.1e and f, which highlight the smaller poleward shift in the WAMZ experiment for both the RCPs, but RCP8.5 has stronger changes than RCP4.5. Track density increases dominate the extratropical latitudes and the main changes occur over the southern oceans, with the Atlantic larger changes. Although both the HadGEM2-ES experiments agree with the decreases on the equatorward side of the ST (Figures 5.1a,b,c and d), the comparison shows a consistent increase on equatorward side of the ST in the WAMZ experiment (Figures 5.1e and f), which supports the hypothesis of the poleward shift reduction (above  $60^\circ\text{S}$ ) when the Amazon Forest is removed. The poleward shift found in the WAMZ experiment will be discussed further in Section 5.1.2.

The RCP8.5 genesis density changes are larger than for those of RCP4.5 in both the experiments, as shown in Figure 5.2 for RCP8.5 (left) and RCP4.5 (right). In SA, the region leeward of the Andes Mountains (Figures 5.2a and b) shows a decrease in genesis over the usual climatological winter maximum region over the south of Argentina of up to 20% relative to the Historical experiment for both the WAMZ and CTRL. Over this same region in SA, the HadGEM2-ES model tends to overestimate

the genesis density for the Historical experiment compared with the reanalysis (see Section 4.2.1.1 for the winter season biases), which may indicate that the projected future changes may have a larger decrease than shown in Figure 5.2. Further north, over the second climatological maximum between northeast Argentina and the south of Brazil, there are increases in genesis density of up to 20% over a region extending eastwards to the Atlantic Ocean in the WAMZ RCP8.5 experiment (Figure 5.2a). This area of genesis density increase can be seen in the other experiments for both the RCPs (Figures 5.2b,c and d). Over the Atlantic Ocean, close to the southeast of Brazil, the future genesis changes indicate a decrease that corresponds to the decrease on the equatorward side of the ST (Figure 5.1) in both the experiments. On the Antarctic coast, the region of the Ross Sea has a decrease in the genesis density of up to 20% relative to the Historical experiment. The Southern Oceans genesis density shows a consistent reduction and seems also related to the decrease of the ST track density.

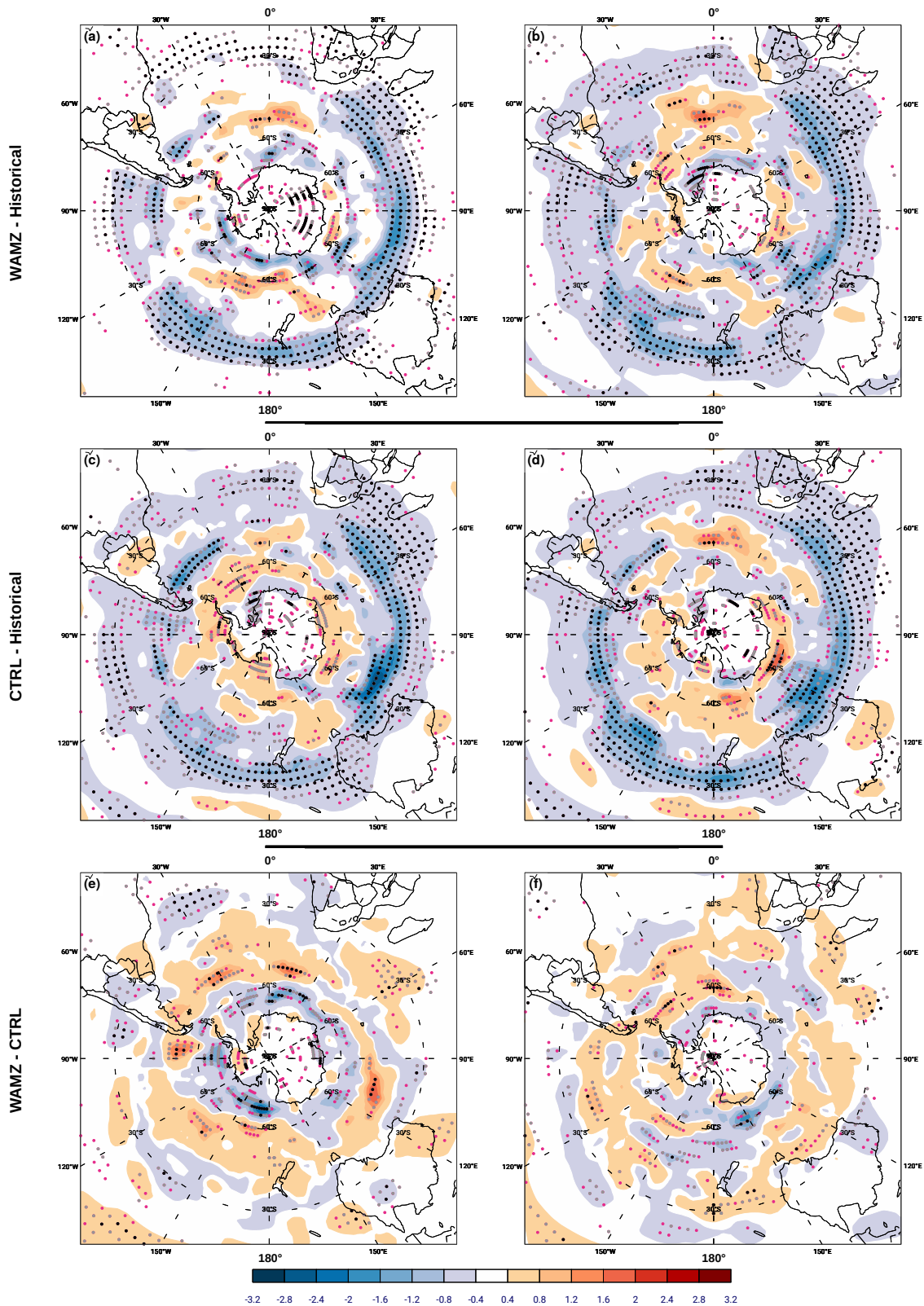
The inter-comparison of the experiments (Figures 5.2e and f) highlight the increase of the genesis density changes over SA in the experiment without the Amazon Forest, which is larger in the RCP8.5 experiments, and over the ocean close to southwest of Australia ( $\sim 45^{\circ}\text{S}$ ,  $105^{\circ}\text{E}$ ), which may be related to the HadGEM2-ES largest biases in this region, as shown in Section 4.2.1.1. Lysis density changes are shown in Figure 5.3 and show a consistent decrease in extratropical latitudes, while there are some increases in regions around the Antarctica coast. The WAMZ–CTRL comparison (Figures 5.3e and f) shows a lysis decrease on the poleward side of the ST and an increase at extratropical latitudes, which correspond to the track future projected changes for both the RCPs. The main changes occur between the south of SA and the Antarctic Peninsula, which the WAMZ RCP8.5 experiment contrast the sign of the projected future change in relation to the RCP4.5 scenario. This contrast seems related to the ST position which is more equatorward for RCP8.5 than RCP4.5 (Figures 5.3, left and right side), causing lysis when the cyclones meet the Andes and Transantarctic Mountains. The mountain effect and lysis on the upslope were discussed in Chapter 4, Section 4.2.1.1.

The mean growth and decay rate (MGDR) changes shown in Figure 5.4 are condensed mainly above the extratropical latitudes in both the experiments. The changes add little to the density change results discussed previously, but the WAMZ–CTRL comparison shows growth changes increasing over SA when the Amazon is removed, especially for RCP4.5. These changes will be discussed further in the regional section (5.1.4). The MGDR future projected changes below  $30^{\circ}\text{S}$  will

be discussed further in the Section 5.1.2.1.

The pattern of changes discussed above contrast with those using older CMIP/AMIP climate models such as used by Yin (2005) using the older IPCC A1B scenario, where kinetic energy was used to define the ST, and found a poleward ST shift but without the equatorward decrease. Similar results have also been found for more recent CMIPs such as by Chang et al. (2013) for AR4/CMIP3 and Chang et al. (2012) for CMIP5, which found changes in the multi-model mean similar to that found here for the CTRL experiment. However, in this study it is necessary to consider only the CTRL experiment to compare with results from the CMIP5 simulations, since they are similar to the CMIP5 simulations. The differences found by Bengtsson et al. (2006) (Figure 10a and b) are the most similar to those found for the CTRL experiment for the winter and summer seasons, which may be associated with the fact that both of the studies uses a single model.

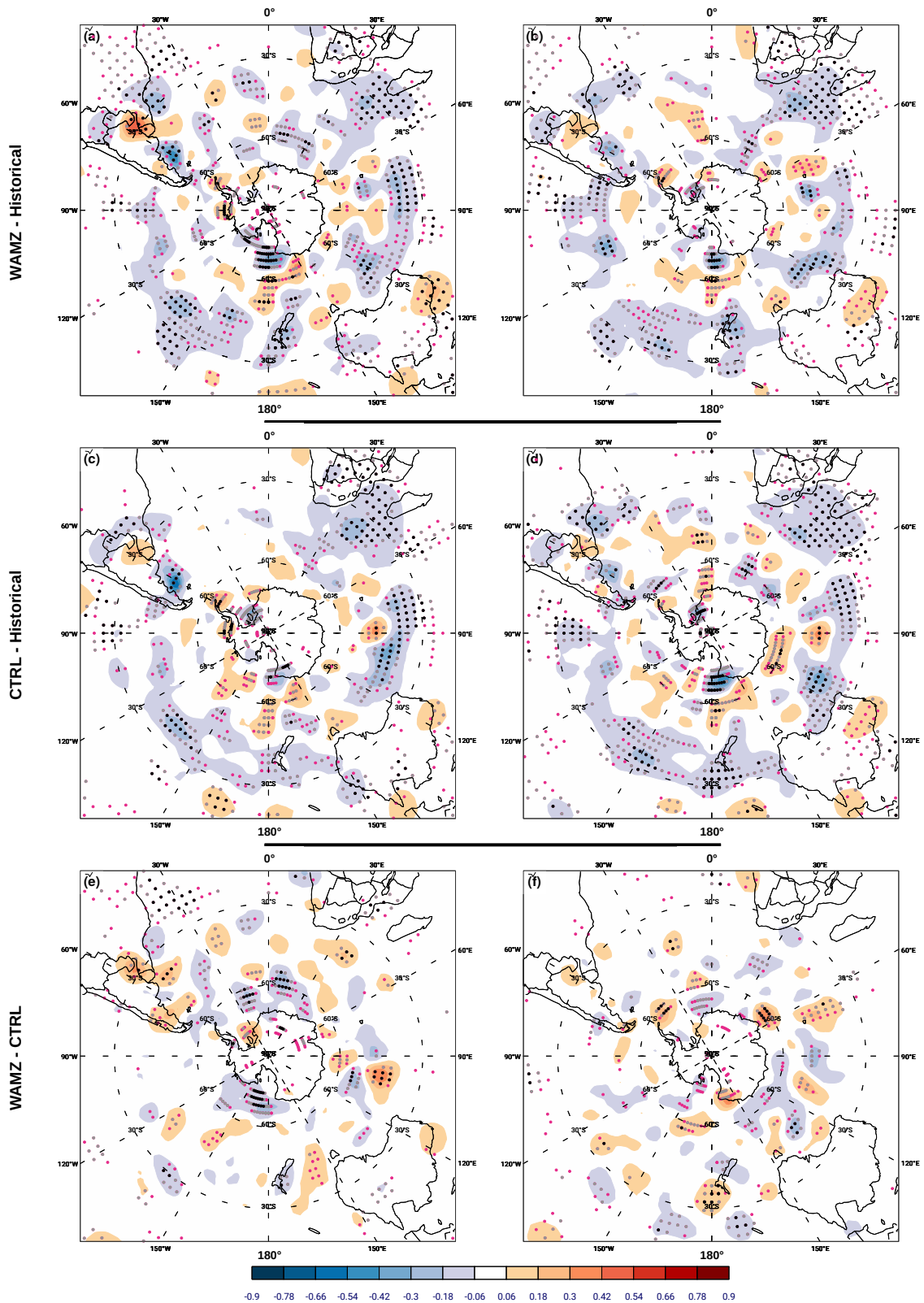
Figure 5.1 - Storm track density changes in JJA for the period 2070-2099.



Future projected changes in cyclone track density for RCP8.5 (left) and RCP4.5 (right) scenarios in JJA: (a) and (b) WAMZ–Historical, (c) and (d) CTRL–Historical, and (e) and (f) WAMZ–CTRL. HadGEM2-ES experiments for period of 2070-2099 and Historical for period of 1976-2005. Densities are in units of number density per month per unit area, where the unit area is equivalent to a  $5^\circ$  spherical cap ( $\sim 10^6 km^2$ ). Stippling shows Student’s t-test significance at 90% (pink), 95% (grey) and 99% (black) levels.

SOURCE: Author’s production.

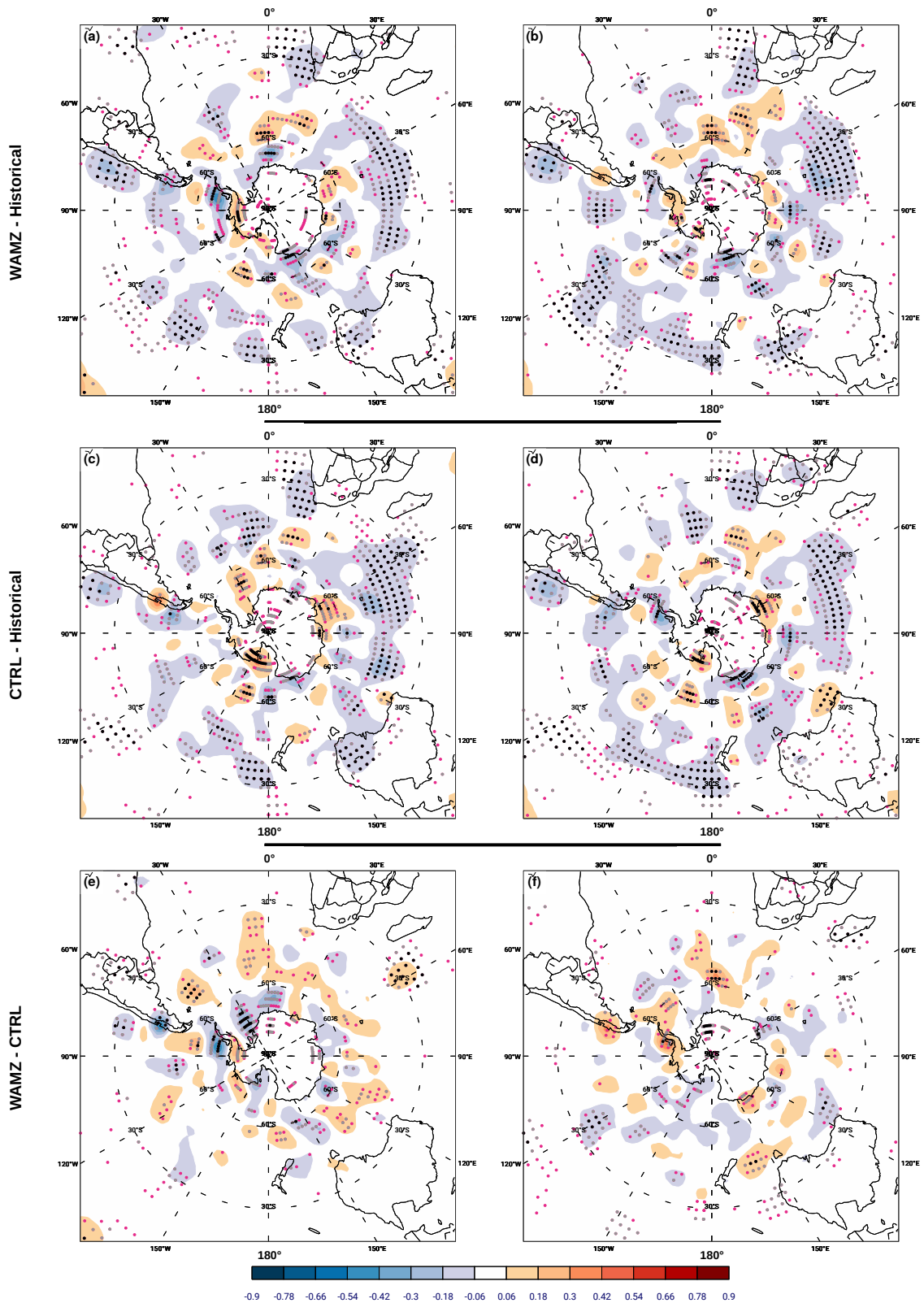
Figure 5.2 - Genesis density changes in JJA for the period 2070-2099.



Future projected changes in cyclone genesis density for RCP8.5 (left) and RCP4.5 (right) scenarios in JJA: (a) and (b) WAMZ–Historical, (c) and (d) CTRL–Historical, and (e) and (f) WAMZ–CTRL. HadGEM2-ES experiments for period of 2070-2099 and Historical for period of 1976-2005. Densities are in units of number density per month per unit area, where the unit area is equivalent to a  $5^\circ$  spherical cap ( $\sim 10^6 km^2$ ). Stippling shows Student’s t-test significance at 90% (pink), 95% (grey) and 99% (black) levels.

SOURCE: Author’s production.

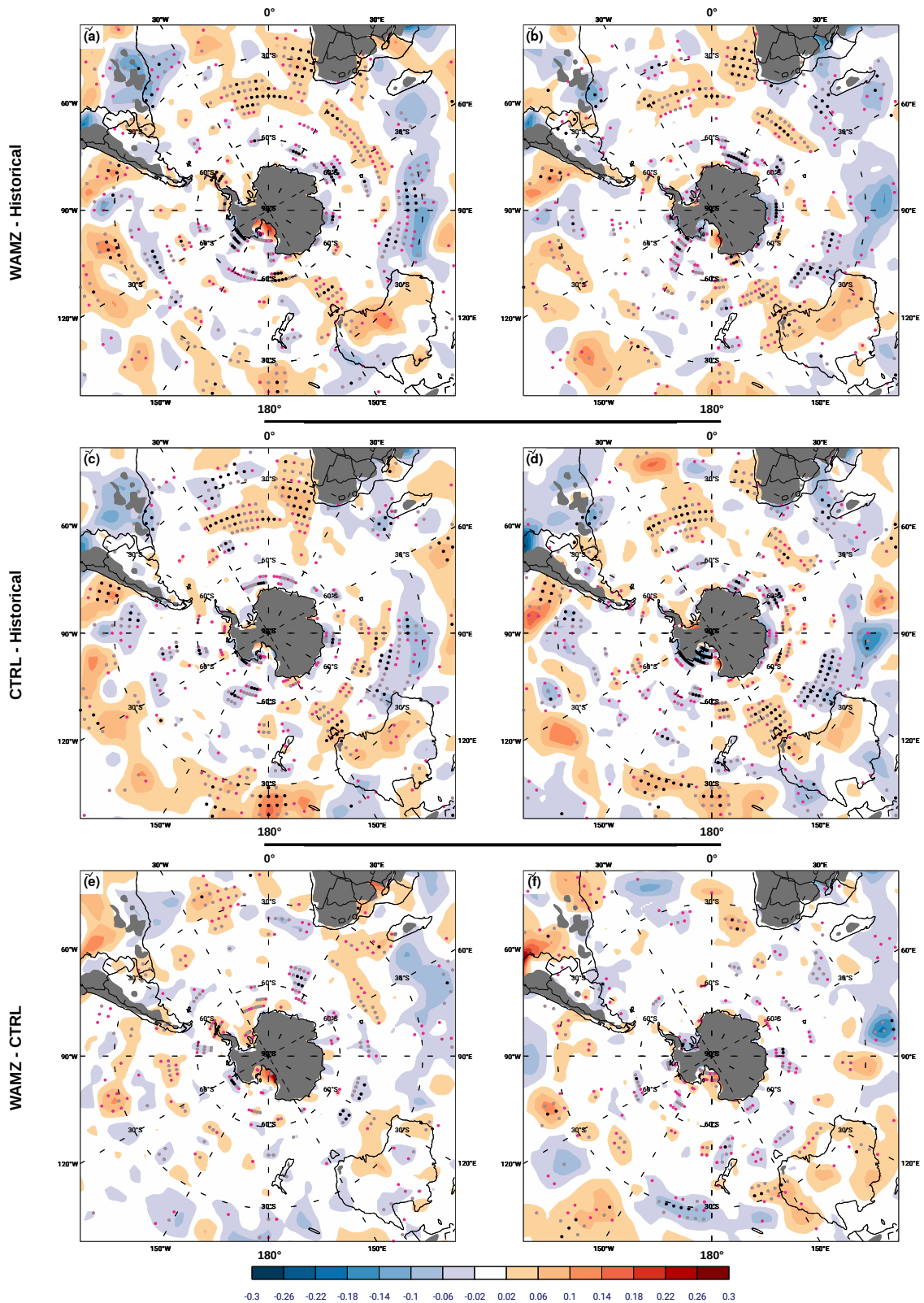
Figure 5.3 - Lysis density changes in JJA for the period 2070-2099.



Future projected changes in cyclone lysis density for RCP8.5 (left) and RCP4.5 (right) scenarios in JJA: (a) and (b) WAMZ–Historical, (c) and (d) CTRL–Historical, and (e) and (f) WAMZ–CTRL. HadGEM2-ES experiments for period of 2070-2099 and Historical for period of 1976-2005. Densities are in units of number density per month per unit area, where the unit area is equivalent to a  $5^\circ$  spherical cap ( $\sim 10^6 km^2$ ). Stippling shows Student’s t-test significance at 90% (pink), 95% (grey) and 99% (black) levels.

SOURCE: Author’s production.

Figure 5.4 - Mean growth decay rate changes in JJA for the period 2070-2099.



Future projected changes in cyclone mean growth and decay rate ( $day^{-1}$ ) for RCP8.5 (left) and RCP4.5 (right) scenarios in JJA: (a) and (b) WAMZ–Historical, (c) and (d) CTRL–Historical, and (e) and (f) WAMZ–CTRL. HadGEM2-ES experiments for period of 2070-2099 and Historical for period of 1976-2005. Densities are in units of number/month/area, where the unit area is equivalent to a  $5^\circ$  spherical cap ( $\sim 10^6 km^2$ ). Stippling shows Student's t-test significance at 90% (pink), 95% (grey) and 99% (black) levels.

SOURCE: Author's production.

### 5.1.1.2 Summer

The main difference between the winter and summer season storm track changes is the more poleward latitudes where the summer changes occur. This is highlighted by the cyclone track density changes (Figure 5.5) which are concentrated around the Antarctic region.

The second largest difference between the austral winter and summer seasons can be seen by comparing the RCP8.5 results with those of the RCP4.5 scenario (Figure 5.5, left and right side). The WAMZ and CTRL experiments shows the largest changes under the RCP4.5 scenario. Considering only the CTRL experiment where the land use change is fixed, which is similar to the CMIP5 simulations, the summer pattern of changes found in this study contrast to (CHANG et al., 2012) once the largest changes were found for the RCP4.5 scenario. These changes indicate that the removal of the Amazon Forest impact the atmosphere over the Southern Hemisphere and a minor radiative forcing (RCP4.5) may contributes to enhance the ST future projected changes by climate feedbacks (see feedback mechanisms in Section 2.2).

Cyclone track density changes are similar in both the experiments (Figure 5.5), but only in the WAMZ RCP8.5 experiment (Figure 5.5a) are the changes spatially concentrated in latitudes above 30°S. The projected future changes show increases around Antarctica ( $\sim 60^\circ\text{S}$ ) of up to approximately 15% relative to the Historical experiment. Although the HadGEM2-ES experiments have shown a poleward shift in the future experiments, the comparison between them shown a reduced poleward shift in the WAMZ RCP8.5 (Figure 5.5e), however this pattern in WAMZ experiment is smoothed in the RCP4.5 scenario (Figure 5.5f). Regionally, both experiments under RCP4.5 changes show increases over the Atlantic, through the Indian Ocean towards the Pacific Ocean at a latitude of ( $\sim 45^\circ\text{S}$ ). In addition, over the Atlantic Ocean there is a growth of the RCP4.5 changes which correspond to the genesis density increases over the northeast of Argentina in SA for the RCP4.5 scenario (Figure 5.6f). Also, there are increases in the track density changes over the Pacific Ocean at high latitudes in both the RCPs (Figure 5.5e and f).

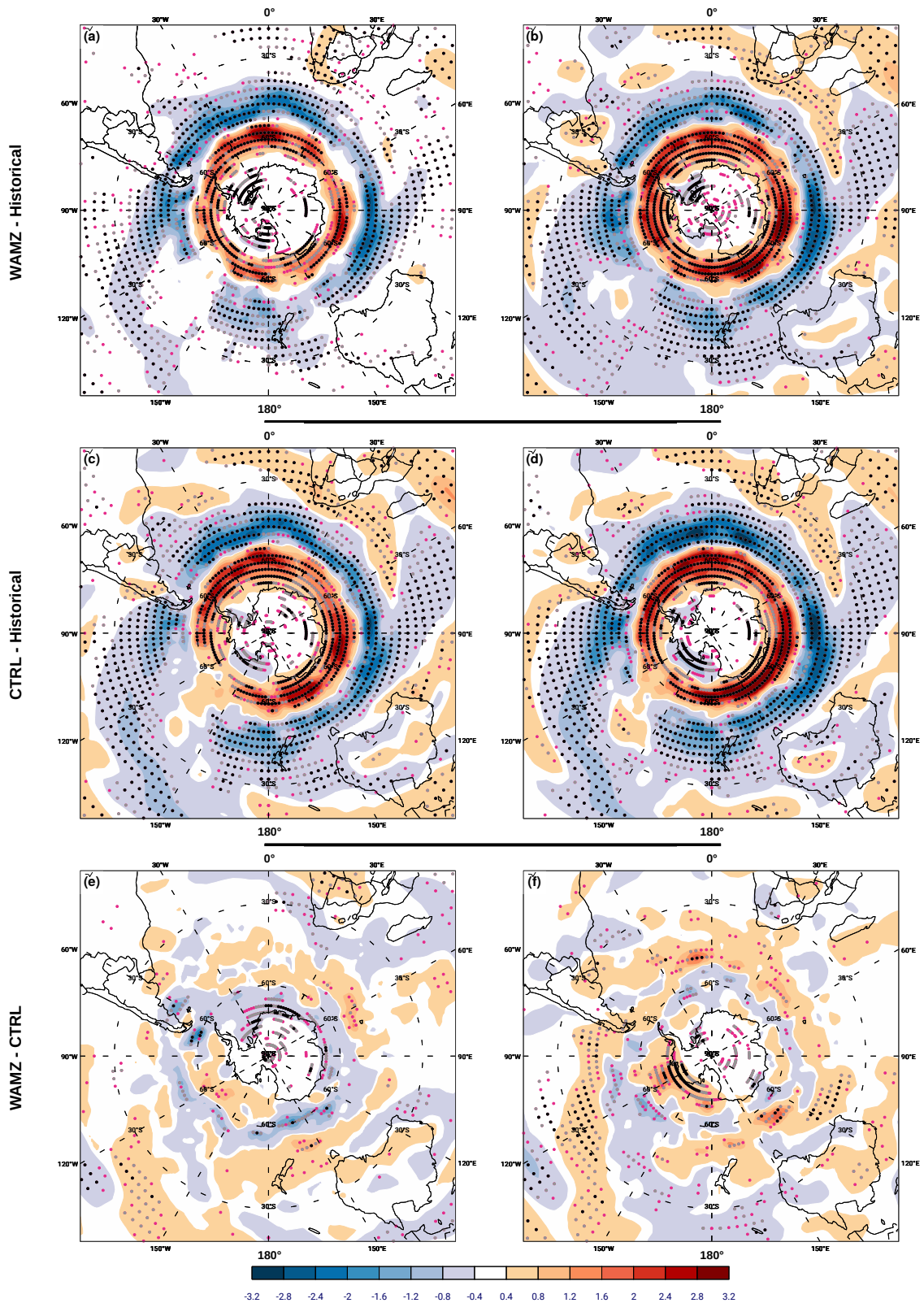
Changes in the genesis densities (Figure 5.6) are also linked to the future projected changes in cyclone track density discussed above. The genesis density decreases over tropical latitudes of the Pacific Ocean and in two of the three climatological cyclogenesis regions in SA, in the south of Argentina and in the Atlantic Ocean close to the southeast of Brazil, compared to the Historical experiment (Figure 5.6a,b,c and d). The genesis changes over the Pacific Ocean seem associated to changes in

the large-scale circulation and will be discussed further in Section 5.1.2.2. However, the HadGEM2-ES experiments shows an increase in the future projected changes of genesis density around the Antarctic coast and on the west coast of Australia. The comparison between the experiments with and without the Amazon Forest (Figure 5.6e and f) show the decrease of genesis over the south of Argentina in both the RCPs and near to the southeast of Brazil in the RCP4.5 scenario. On the other hand, the genesis density increases in the north of Argentina and corresponds to the increase of the track density changes over the Atlantic Ocean, which is more evident in the RCP4.5 experiment (Figure 5.6f).

The lysis densities around the Antarctic coast have the largest projected increases under both the RCPs, with the maximum change near to the Antarctic Peninsula (Figure 5.7a,b,c and d). The main differences WAMZ–CTRL occurs in the region of the Drake Passage and correspond to the track density changes (Figure 5.5e and f).

Cyclone growth decay rates (Figure 5.8) are also closely associated with the track, genesis and lysis density changes in the southern oceans, which correspond to the poleward motion of the ST during the summertime. This also correspond to the small growth/decay changes observed in tropical latitudes in relation to the winter season. The main changes are concentrated in the Antarctic region, particularly over the Ross Sea, and contrast between the experiments and also the RCP scenarios (Figure 5.8a;d and b;c). Thus, the difference WAMZ–CTRL shows this region with opposite change sign between the RCPs (Figure 5.8e and f).

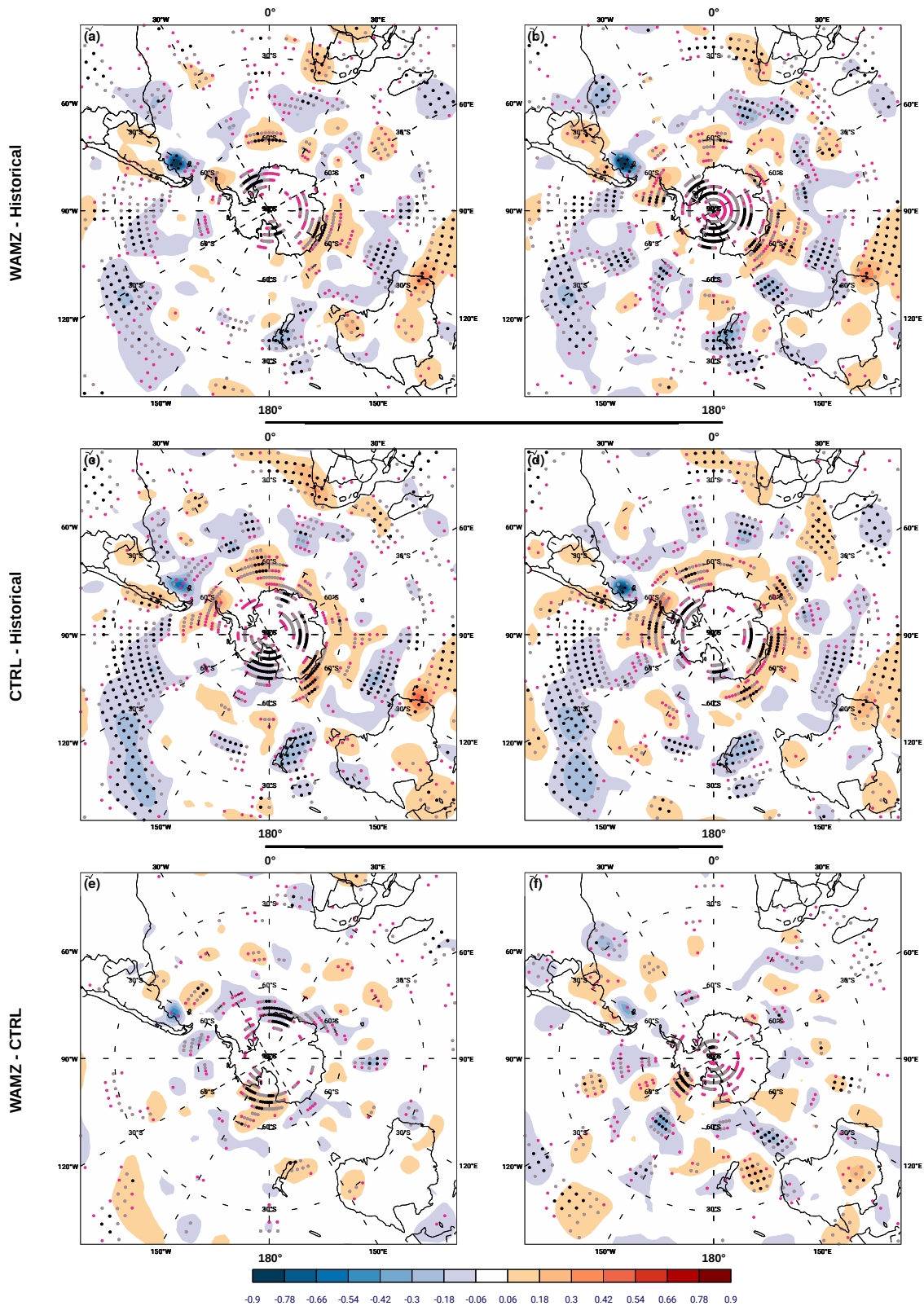
Figure 5.5 - Storm track density changes in DJF for the period 2070-2099.



Future projected changes in cyclone track density for RCP8.5 (left) and RCP4.5 (right) scenarios in DJF: (a) and (b) WAMZ–Historical, (c) and (d) CTRL–Historical, and (e) and (f) WAMZ–CTRL. HadGEM2-ES experiments for period of 2070-2099 and Historical for period of 1976-2005. Densities are in units of number density per month per unit area, where the unit area is equivalent to a  $5^\circ$  spherical cap ( $\sim 10^6 km^2$ ). Stippling shows Student’s t-test significance at 90% (pink), 95% (grey) and 99% (black) levels.

SOURCE: Author’s production.

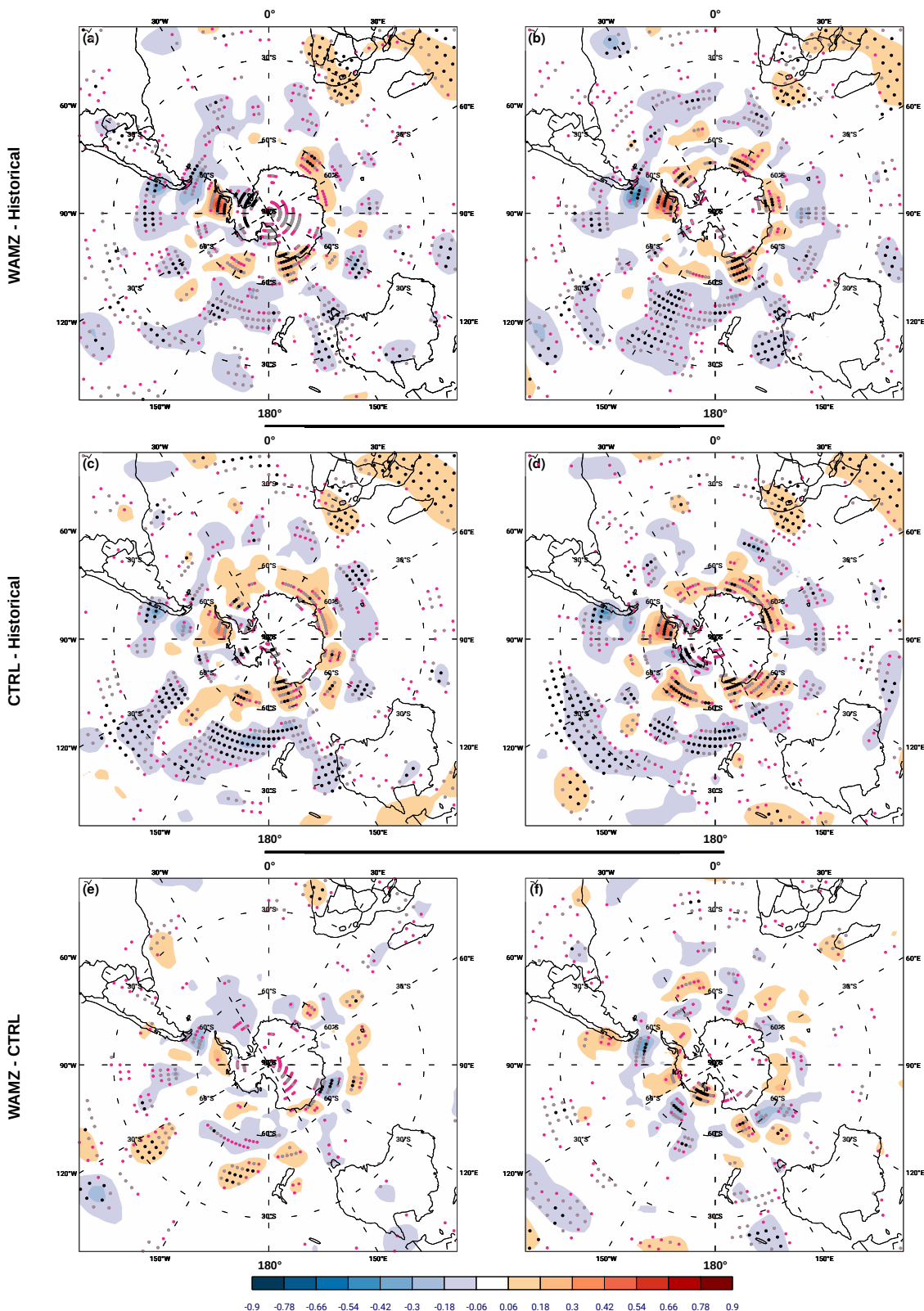
Figure 5.6 - Genesis density changes in DJF for the period 2070-2099.



Future projected changes in cyclone genesis density for RCP8.5 (left) and RCP4.5 (right) scenarios in DJF: (a) and (b) WAMZ–Historical, (c) and (d) CTRL–Historical, and (e) and (f) WAMZ–CTRL. HadGEM2-ES experiments for period of 2070-2099 and Historical for period of 1976-2005. Densities are in units of number density per month per unit area, where the unit area is equivalent to a  $5^\circ$  spherical cap ( $\sim 10^6 km^2$ ). Stippling shows Student’s t-test significance at 90% (pink), 95% (grey) and 99% (black) levels.

SOURCE: Author’s production.

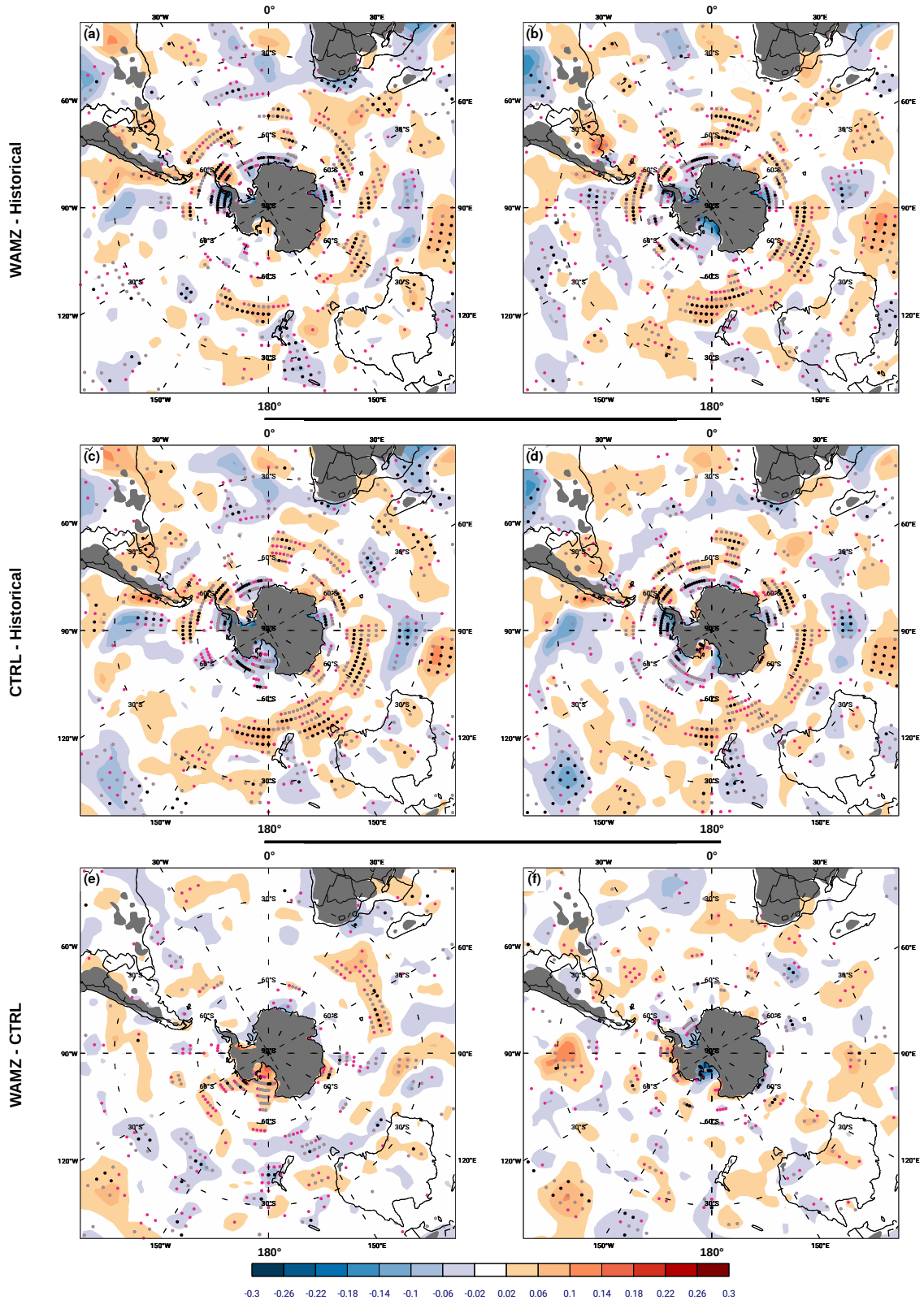
Figure 5.7 - Lysis density changes in DJF for the period 2070-2099.



Future projected changes in cyclone lysis density for RCP8.5 (left) and RCP4.5 (right) scenarios in DJF: (a) and (b) WAMZ–Historical, (c) and (d) CTRL–Historical, and (e) and (f) WAMZ–CTRL. HadGEM2-ES experiments for period of 2070-2099 and Historical for period of 1976-2005. Densities are in units of number density per month per unit area, where the unit area is equivalent to a  $5^\circ$  spherical cap ( $\sim 10^6 km^2$ ). Stippling shows Student’s t-test significance at 90% (pink), 95% (grey) and 99% (black) levels.

SOURCE: Author’s production.

Figure 5.8 - Mean growth decay rate changes in DJF for the period 2070-2099.



Future projected changes in cyclone mean growth and decay rate ( $day^{-1}$ ) for RCP8.5 (left) and RCP4.5 (right) scenarios in DJF: (a) and (b) WAMZ–Historical, (c) and (d) CTRL–Historical, and (e) and (f) WAMZ–CTRL. HadGEM2-ES experiments for period of 2070-2099 and Historical for period of 1976-2005. Densities are in units of number/month/area, where the unit area is equivalent to a  $5^\circ$  spherical cap ( $\sim 10^6 km^2$ ). Stippling shows Student's t-test significance at 90% (pink), 95% (grey) and 99% (black) levels.

SOURCE: Author's production.

### 5.1.1.3 Transition seasons

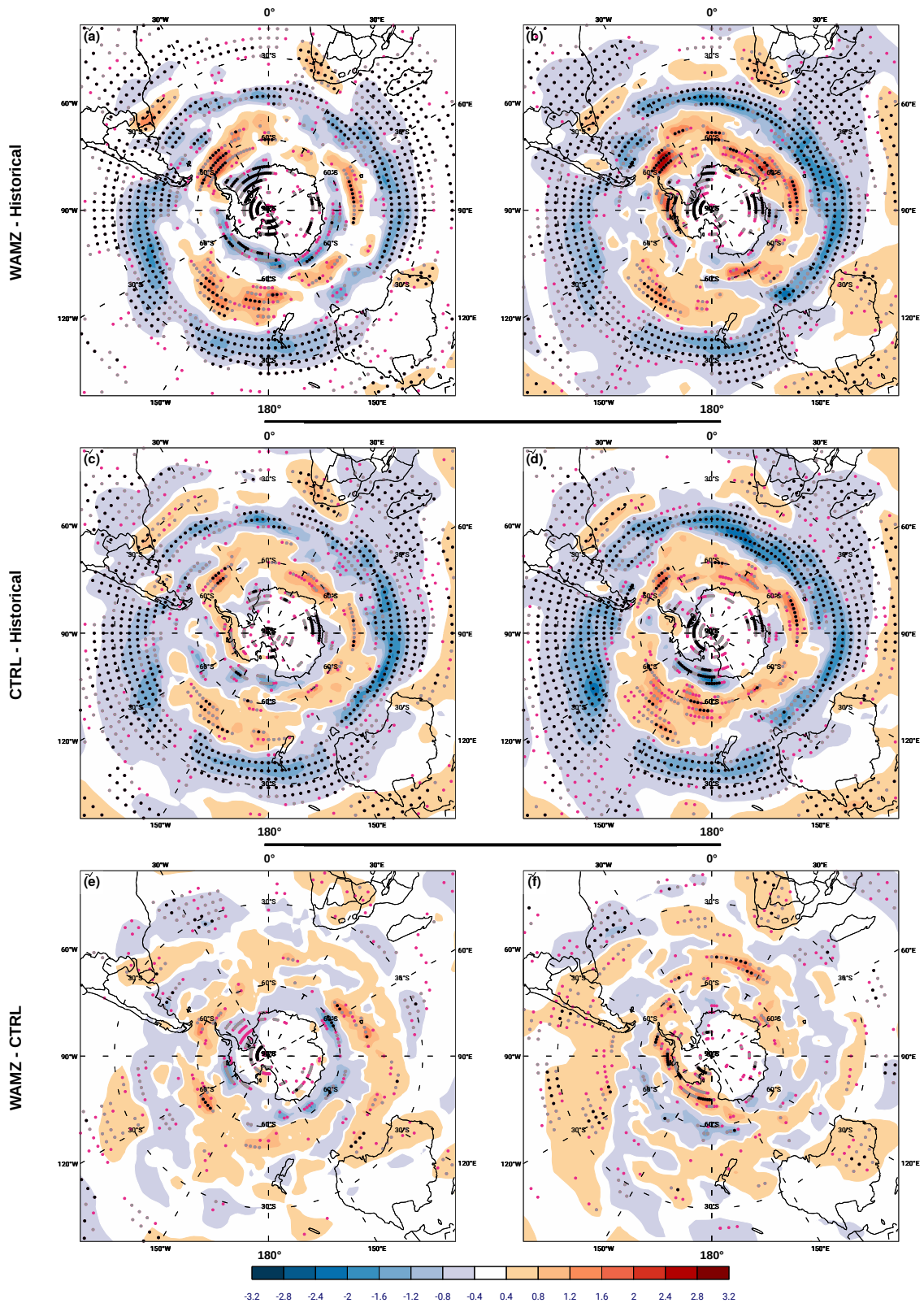
The differences for the transition seasons of the projected changes under both the RCPs are similar to the winter and summer seasons, with the spring season similar to the winter season (e.g. (Figure 5.9 with (Figure 5.1), while the autumn season is similar to the summer season (e.g. (Figure 5.13 with (Figure 5.5). This is somewhat similar to the climatological patterns found in the Southern Hemisphere (Chapter 4, Section 4.1) and seems associated with the large thermal inertia of the oceans. Under the WAMZ RCP4.5 scenario, the transition season patterns (Figures 5.9f and 5.13f) are spatially similar to the summer season around the Antarctic region (Figure 5.5f). However, there is a reduction of poleward trend in the track density response in all seasons under the RCP8.5 scenario (Figures 5.1e, 5.5e, 5.9e and 5.13e). These projected future changes in the RCP4.5 (minor radiative forcing) support the hypothesis that the feedback mechanisms may partially link to these larger ST density changes in this scenario.

The spring season changes differ only in a few features compared to the winter season for both the WAMZ and CTRL experiments. There are larger regions of track density increases over the southern oceans and the main ST latitudinal belt which seems closer to the Antarctic than in the winter season, corresponding to the ST climatological change in this season and the reduced WAMZ RCP8.5 poleward shift. There is also a decline in genesis though the sign continues positive over the northeast of Argentina (Figures 5.10e and f) and, in addition, the climatological cyclogenesis over the south of Argentina decreases by up to 20% compared to the winter season (Figures 5.2e and f). This contributes to the ST future projected decreases from the south of SA the towards Atlantic Ocean ( $\sim 45^\circ\text{S}$  - Figures 5.9e and f). Lysis density changes in the comparison WAMZ–CTRL (Figures 5.11e and f) are similar to the winter season, with the same differences between the RCPs, and the regions of changes concentrated on the Antarctic Peninsula. The storm growth decay rate changes have opposite sign between the RCP scenarios over the east Pacific and South America (Figures 5.12e and f), which will be discussed further in the regional-scale changes (Section 5.1.4).

There are also only a few features in the autumn season changes which differ from the summer season changes. Under the RCP4.5 scenario, the autumn season has the largest projected future changes of all seasons. The track density changes in RCP4.5 (Figure 5.13f) increases over the East Antarctic coast compared to the summer season (Figure 5.5f), however this is the main region of decrease in the

WAMZ experiment (Figure 5.13a and e). In general, both the RCPs reduces the poleward shift in the WAMZ experiment but the same summer ST growth change region over the Ross Sea (Figure 5.5e and f) is also shown during the autumn season (Figure 5.13e and f). Genesis density RCP8.5 change increases over the northeast of Argentina is stronger than RCP4.5 for the WAMZ experiment (Figure 5.14a and e), while the RCP4.5 WAMZ experiment has the sign changes from the SA towards Antarctic Peninsula (Figure 5.14b and f). Equatorward increases in lysis and MGDR density changes (Figures 5.15e,f and 5.16e,f) are also similar to the summer season (Figures 5.7e,f and 5.8e,f), under both scenarios, particularly at the windward of Andes Mountains on the south of SA.

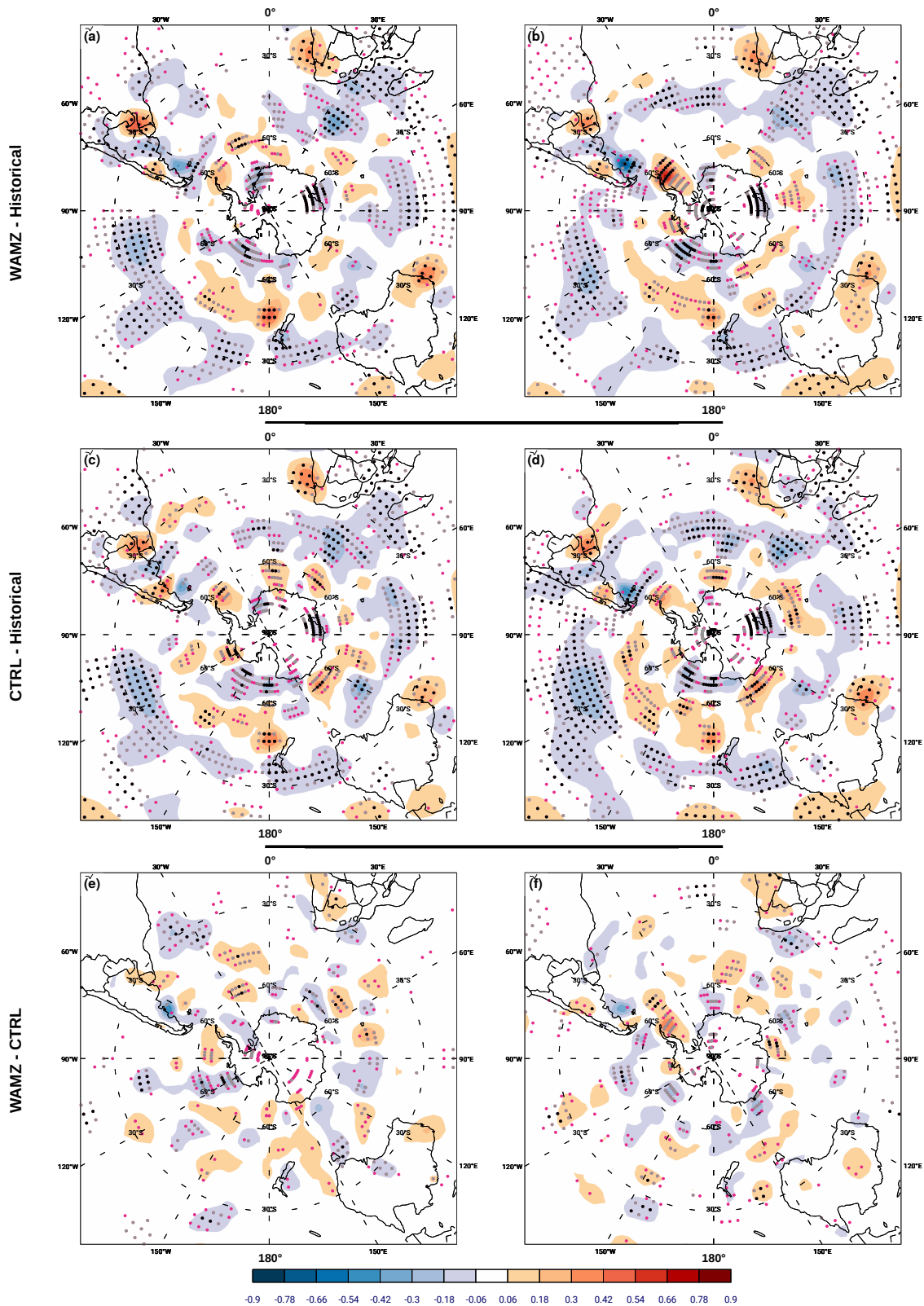
Figure 5.9 - Storm track density changes in SON for the period 2070-2099.



Future projected changes in cyclone track density for RCP8.5 (left) and RCP4.5 (right) scenarios in SON: (a) and (b) WAMZ–Historical, (c) and (d) CTRL–Historical, and (e) and (f) WAMZ–CTRL. HadGEM2-ES experiments for period of 2070-2099 and Historical for period of 1976-2005. Densities are in units of number density per month per unit area, where the unit area is equivalent to a  $5^\circ$  spherical cap ( $\sim 10^6 km^2$ ). Stippling shows Student’s t-test significance at 90% (pink), 95% (grey) and 99% (black) levels.

SOURCE: Author’s production.

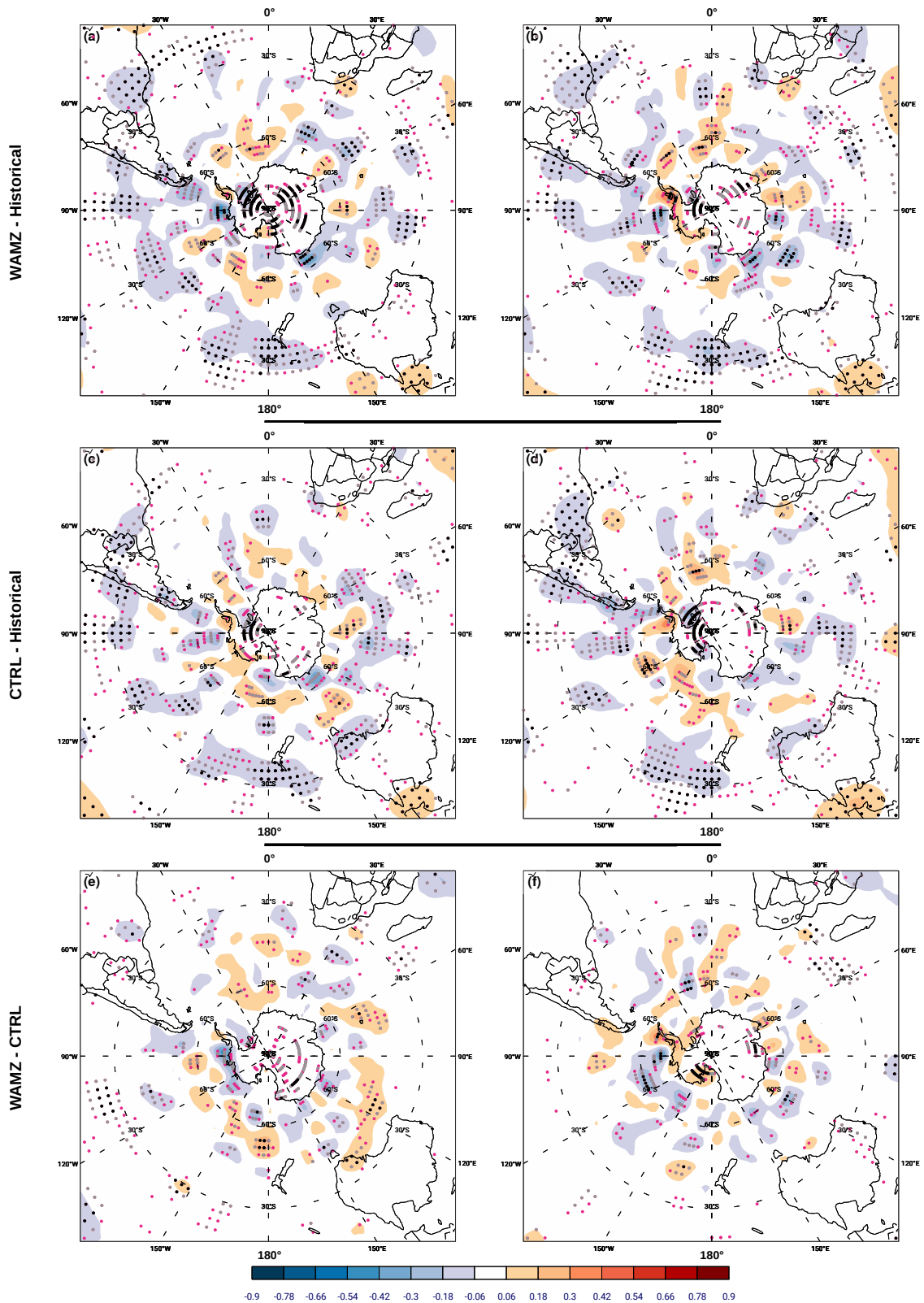
Figure 5.10 - Genesis density changes in SON for the period 2070-2099.



Future projected changes in cyclone genesis density for RCP8.5 (left) and RCP4.5 (right) scenarios in SON: (a) and (b) WAMZ–Historical, (c) and (d) CTRL–Historical, and (e) and (f) WAMZ–CTRL. HadGEM2-ES experiments for period of 2070-2099 and Historical for period of 1976-2005. Densities are in units of number density per month per unit area, where the unit area is equivalent to a  $5^\circ$  spherical cap ( $\sim 10^6 km^2$ ). Stippling shows Student’s t-test significance at 90% (pink), 95% (grey) and 99% (black) levels.

SOURCE: Author’s production.

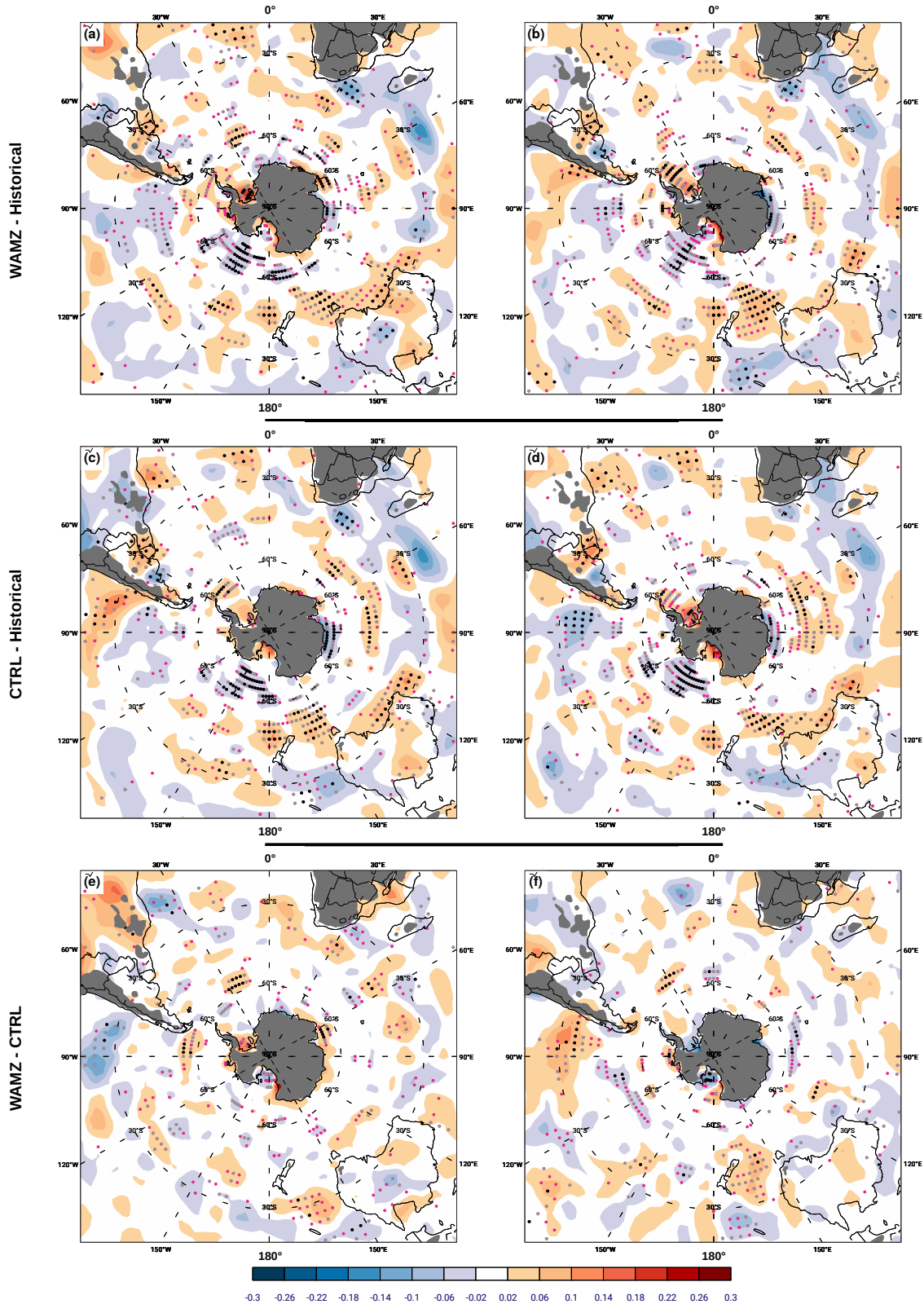
Figure 5.11 - Lysis density changes in SON for the period 2070-2099.



Future projected changes in cyclone lysis density for RCP8.5 (left) and RCP4.5 (right) scenarios in SON: (a) and (b) WAMZ–Historical, (c) and (d) CTRL–Historical, and (e) and (f) WAMZ–CTRL. HadGEM2-ES experiments for period of 2070-2099 and Historical for period of 1976-2005. Densities are in units of number density per month per unit area, where the unit area is equivalent to a  $5^\circ$  spherical cap ( $\sim 10^6 km^2$ ). Stippling shows Student’s t-test significance at 90% (pink), 95% (grey) and 99% (black) levels.

SOURCE: Author’s production.

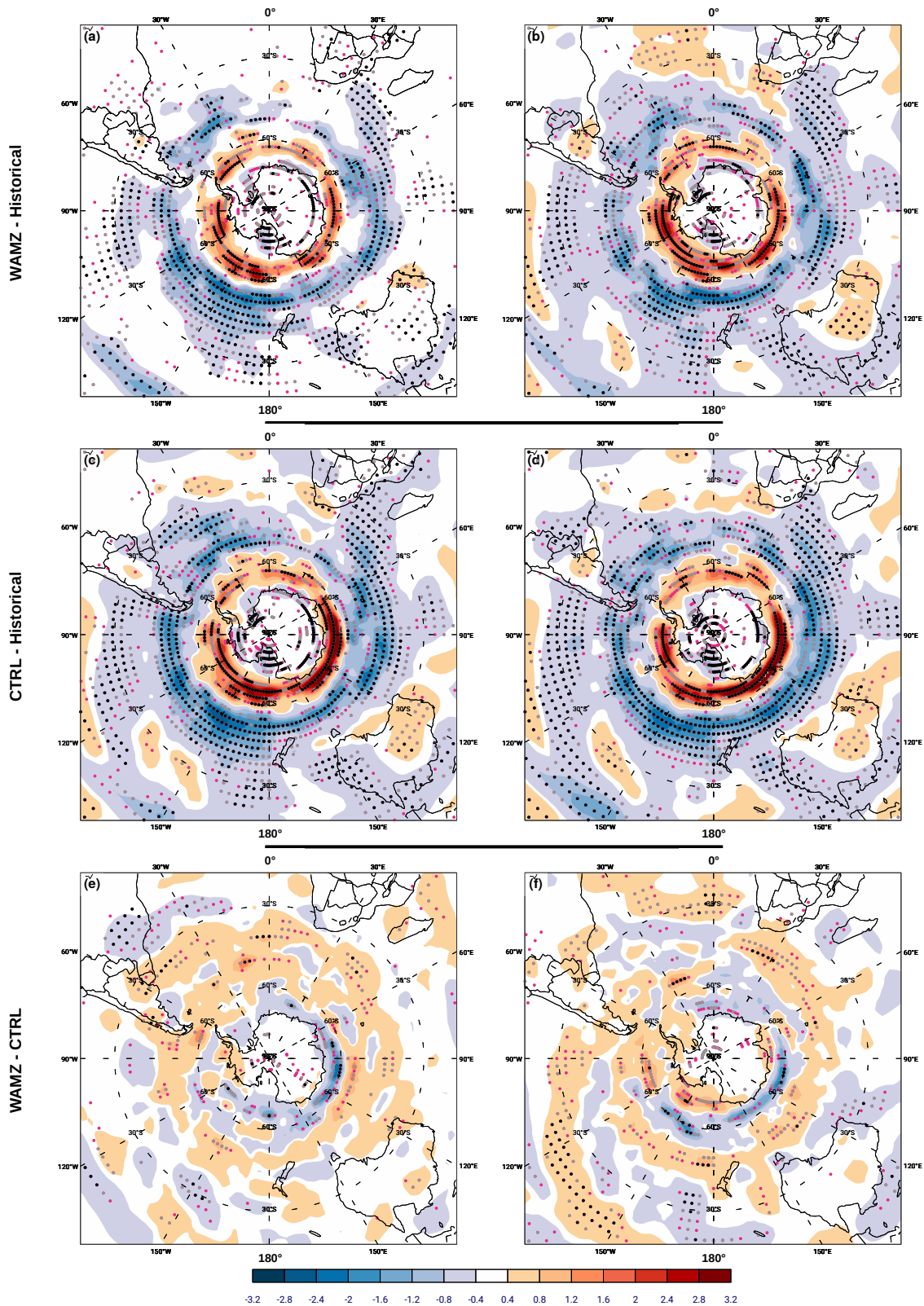
Figure 5.12 - Mean growth decay rate changes in SON for the period 2070-2099.



Future projected changes in cyclone mean growth and decay rate ( $day^{-1}$ ) for RCP8.5 (left) and RCP4.5 (right) scenarios in SON: (a) and (b) WAMZ–Historical, (c) and (d) CTRL–Historical, and (e) and (f) WAMZ–CTRL. HadGEM2-ES experiments for period of 2070-2099 and Historical for period of 1976-2005. Densities are in units of number/month/area, where the unit area is equivalent to a  $5^\circ$  spherical cap ( $\sim 10^6 km^2$ ). Stippling shows Student's t-test significance at 90% (pink), 95% (grey) and 99% (black) levels.

SOURCE: Author's production.

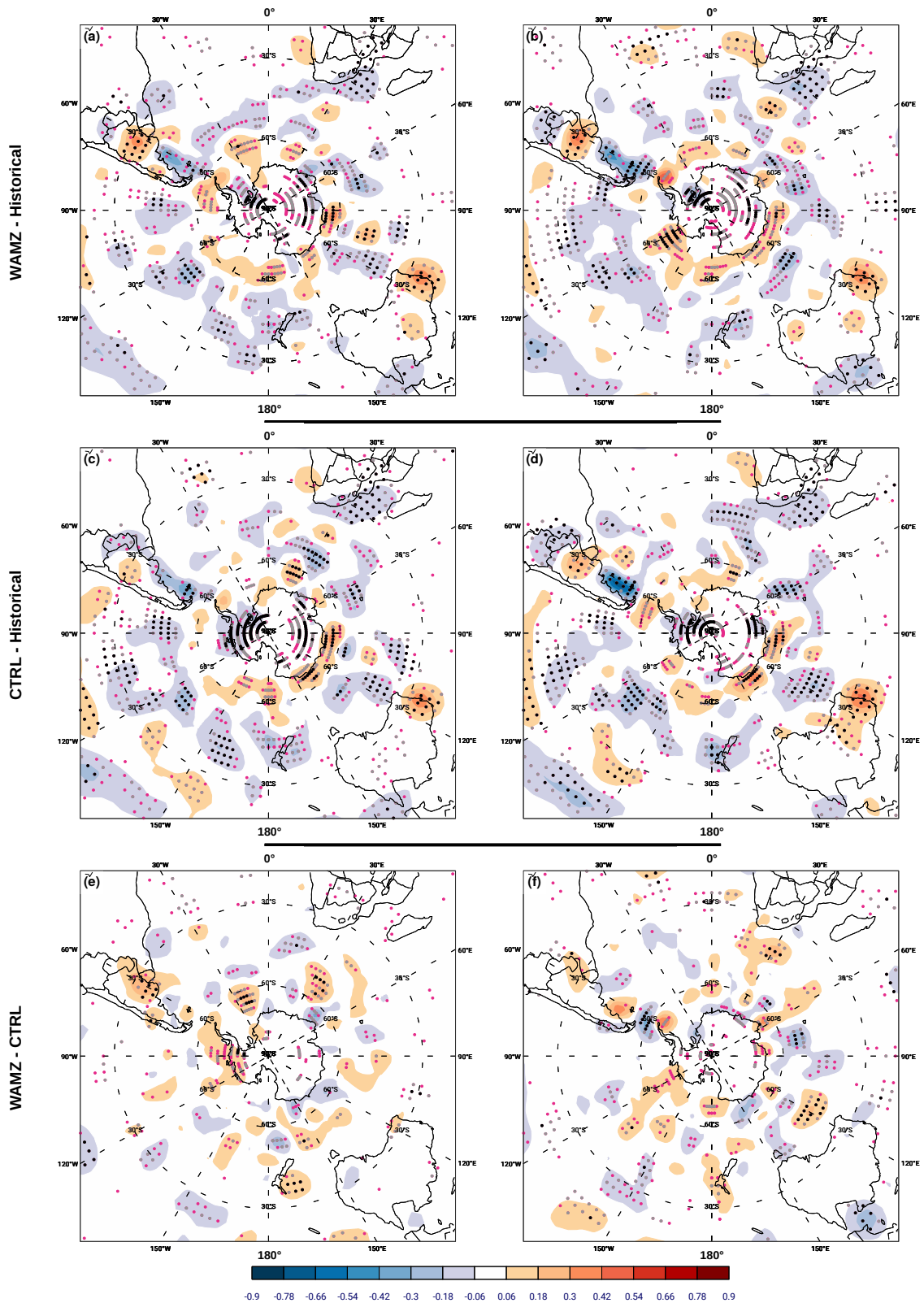
Figure 5.13 - Storm track density changes in MAM for the period 2070-2099.



Future projected changes in cyclone track density for RCP8.5 (left) and RCP4.5 (right) scenarios in MAM: (a) and (b) WAMZ–Historical, (c) and (d) CTRL–Historical, and (e) and (f) WAMZ–CTRL. HadGEM2-ES experiments for period of 2070-2099 and Historical for period of 1976-2005. Densities are in units of number density per month per unit area, where the unit area is equivalent to a  $5^\circ$  spherical cap ( $\sim 10^6 km^2$ ). Stippling shows Student’s t-test significance at 90% (pink), 95% (grey) and 99% (black) levels.

SOURCE: Author’s production.

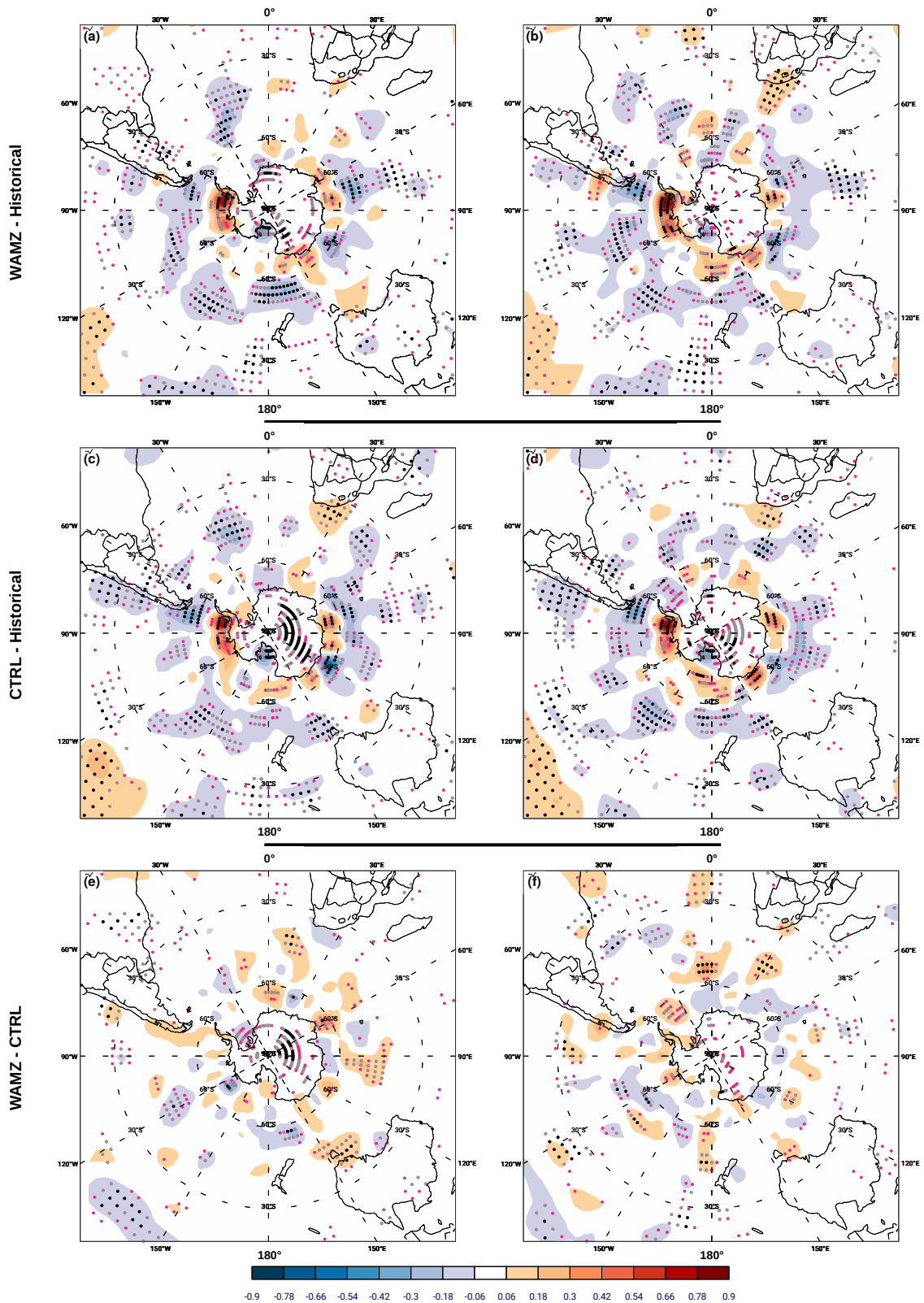
Figure 5.14 - Genesis density changes in MAM for the period 2070-2099.



Future projected changes in cyclone genesis density for RCP8.5 (left) and RCP4.5 (right) scenarios in MAM: (a) and (b) WAMZ–Historical, (c) and (d) CTRL–Historical, and (e) and (f) WAMZ–CTRL. HadGEM2-ES experiments for period of 2070-2099 and Historical for period of 1976-2005. Densities are in units of number density per month per unit area, where the unit area is equivalent to a  $5^\circ$  spherical cap ( $\sim 10^6 km^2$ ). Stippling shows Student’s t-test significance at 90% (pink), 95% (grey) and 99% (black) levels.

SOURCE: Author’s production.

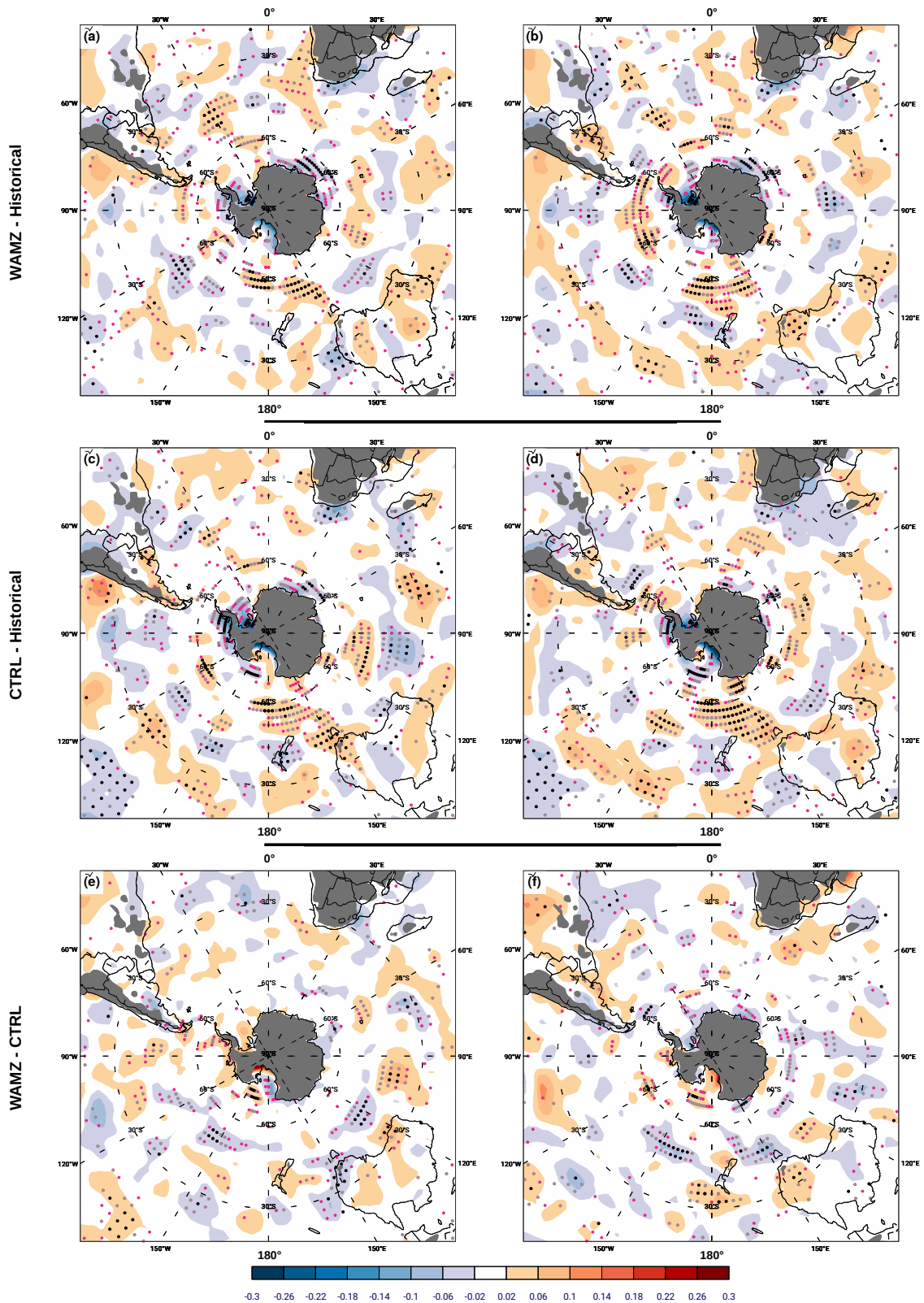
Figure 5.15 - Lysis density changes in MAM for the period 2070-2099.



Future projected changes in cyclone lysis density for RCP8.5 (left) and RCP4.5 (right) scenarios in MAM: (a) and (b) WAMZ–Historical, (c) and (d) CTRL–Historical, and (e) and (f) WAMZ–CTRL. HadGEM2-ES experiments for period of 2070-2099 and Historical for period of 1976-2005. Densities are in units of number density per month per unit area, where the unit area is equivalent to a  $5^\circ$  spherical cap ( $\sim 10^6 km^2$ ). Stippling shows Student’s t-test significance at 90% (pink), 95% (grey) and 99% (black) levels.

SOURCE: Author’s production.

Figure 5.16 - Mean growth decay rate changes in MAM for the period 2070-2099.



Future projected changes in cyclone mean growth and decay rate ( $day^{-1}$ ) for RCP8.5 (left) and RCP4.5 (right) scenarios in MAM: (a) and (b) WAMZ–Historical, (c) and (d) CTRL–Historical, and (e) and (f) WAMZ–CTRL. HadGEM2-ES experiments for period of 2070-2099 and Historical for period of 1976-2005. Densities are in units of number/month/area, where the unit area is equivalent to a  $5^\circ$  spherical cap ( $\sim 10^6 km^2$ ). Stippling shows Student's t-test significance at 90% (pink), 95% (grey) and 99% (black) levels.

SOURCE: Author's production.

### 5.1.2 Large-scale changes

This section focuses on the large-scale fields which may affect the storm track changes in the Southern Hemisphere. The large-scale changes are calculated for each HadGEM2-ES ensemble member individually and for the HadGEM2-ES ensemble mean, referred to only as HadGEM2-ES, but in this section only as the difference between the Without Amazon Forest minus Control (WAMZ–CTRL) experiment in each RCP scenario for brevity. The only difference between WAMZ and CTRL experiments is the removal of Amazon Forest, thus the emission and concentration of gases along the time for RCP8.5 and RCP4.5 scenario occur in both the experiments according to each respective RCP. The climatological patterns over the SH for the historical period are described in Chapter 4 - Section 4.2.2.

#### 5.1.2.1 Winter

The historical winter large-scale patterns are described in detail in the Chapter 4, Section 4.2.2.1, and is used as a reference for the fields analysed in this section.

The differences between WAZM and the CTRL experiments for the maximum Eady growth rate changes at upper (250hPa) and lower (850hPa) levels for both the RCPs in all seasons are shown in Figures 5.17 - 5.20.

The winter baroclinicity changes at upper levels (Figures 5.17a and 5.18a) are the smallest of all seasons for both the RCPs, being approximately 5% in relation to the CTRL experiment. Moreover, the baroclinicity decreases in the same latitudinal belt as the main baroclinic region in historical climatology (figure not shown, but see Figure 4.10a for winter ERA-Interim climatology). Both the RCPs agree in the changes over north of Argentina, Uruguay and south of Brazil, however they have opposite signs over southern Australia (Figures 5.17a and 5.18a). These areas corresponds with the changes between the RCPs for the cyclone track densities (Figures 5.1e and f). For RCP4.5 (Figure 5.18a) increases in baroclinicity are found around the latitude of 30° over south of South Africa and Australia and also correspond to the cyclone track density increases areas found in this scenario. In addition, in this scenario increases over the tropical Indian and Pacific ocean towards South America do not correspond changes in the cyclone track densities (Figures 5.1f).

At lower levels (Figures 5.19a and 5.20a ) the changes in baroclinicity are similar to the areas of changes in ST density (Figures 5.1e and f) for both RCPs. Contrasting with the upper levels, the removal of the Amazon Forest causes the largest baro-

clonicity changes of all seasons for both the RCPs, with values of between 15-20% relative to the CTRL experiment. The RCP8.5 changes are larger than for RCP4.5 and correspond to the cyclone track and genesis density changes (Figures 5.2e and 5.2e). For both the RCPs the main areas of increase are observed on the leeward side of the Andes Mountains ( $\sim 20^\circ\text{S}$ ), while the main decreases are found in the Antarctic region. For RCP8.5 (Figure 5.19a) the increases in the baroclinicity extends from South America, through South Africa and Indian Ocean, towards the Pacific Ocean where two other peaks are found over New Zealand and eastwards over the ocean. Increases are also seen along the Antarctic coastline from the Ross Sea towards the Antarctic Peninsula. While increases are observed in almost the entire field, baroclinicity decreases over the extreme south of SA, south of Madagascar, Australia eastwards over the ocean and around the latitude of  $60^\circ\text{S}$  (Figure 5.19a). However the RCP4.5 baroclinicity changes contrast with RCP8.5 over the south of South Africa and Madagascar (Figure 5.20a), but correspond to the ST density changes in RCP4.5 (Figure 5.1f).

These winter baroclinicity changes in both the RCP scenarios are directly related to two factors, the radiative forcing which causes more surface warming and enhances the baroclinicity at lower levels, and the two eddy-driven jets over the SH during the winter season, which has a branch over the south of SA and also helps to increase the genesis and storms. This hypothesis will be explored in the regional-scale changes over South America (Section 5.1.4).

The cross section of temperature changes are shown in Figure 5.21 (left column) for the Atlantic (Figure 5.21a), Indian (Figure 5.21c) and Pacific (Figure 5.21e) Oceans. The differences for WAMZ–HIST (black contours) and CTRL–HIST (grey contours) are shown in these figures to give an idea of the magnitude of changes. In general there is a heating at upper levels over all the southern oceans, while there is a cooling in middle and lower levels except in the Pacific Ocean, where there is a heating from the surface to the stratosphere at latitudes between  $70^\circ\text{S}$  and  $70^\circ\text{S}$ . The temperature decreases in RCP8.5 over the Atlantic Ocean at high latitudes. Similar to Figure 5.21, the temperature cross sections for the RCP4.5 scenario are shown in Figure 5.22 for the Atlantic (a), Indian (c) and Pacific (e), respectively. The temperature changes over the Atlantic are the largest during the winter season (Figure 5.22a), having opposite sign in relation to the RCP8.5 scenario (Figure 5.21a) at high latitudes ( $\sim 70^\circ\text{S}$ ). Over the other SH oceans, Indian and Pacific, the temperature increases in tropical and polar regions from surface to upper levels, while temperature decreases between the latitudes  $20 - 55^\circ\text{S}$ .

The cross section of zonal wind changes are shown in Figure 5.21 (right column) for Atlantic (Figure 5.21b), Indian (Figure 5.21d) and Pacific (Figure 5.21f) Oceans. During the winter season the jets are split, with the polar jet between 60°S and 40°S, and the subtropical jet, 30°S and 20°S. The same jet pattern continues in the future projected changes but are modified when the Amazon Forest is removed. The CMIP5 multi-model mean reveals a poleward shift of the storm tracks (INTERGOVERNMENTAL PANEL ON CLIMATE CHANGE (IPCC), 2013), however the removal of the Amazon Forest reduces the poleward shift and enhances the equatorward side of the polar jet. This is a new result and the zonal wind change pattern corresponds with what was found for the cyclone track density changes. The HadGEM2-ES RCP8.5 experiment shows both the jets slightly shifted to polewards, however the zonal wind for the poleward branch is reduced while the equatorward branch is enhanced. Figures 5.22b,d and e, show the zonal wind changes for the RCP4.5 experiment over the Atlantic, Indian and Pacific oceans, respectively. In this scenario the subtropical jet continues in the same position in relation to the ERA-Interim climatology (Figure 4.13). The subtropical jet increases while the polar jet decreases over the SH oceans, thus the removal of the Amazon Forest reinforces this pattern previously observed for the RCP4.5 scenario (CHENOLI, 2017) and agrees with Tandon et al. (2013) who suggest that the warming in the subtropics may play a stronger role in jet trends.

Geopotential height (HGT) anomaly changes at 500hPa are shown in Figures 5.23 and 5.24 for RCP8.5 and RCP4.5 scenarios in all seasons. This field is important to show changes in the stationary wave pattern over the SH where and negative (positive) anomalies indicate a cyclonic (anticyclonic) tendency. The RCP8.5 geopotential increases over the south of SA and the Antarctic Peninsula, south of South Africa and from east of Antarctic toward New Zealand. These geopotential height anomaly changes (WAMZ–CTRL) are consistent with the temperature increases of Figure 5.25, and the resultant anticyclonic anomalous circulation change, particularly over the southern Atlantic, which is consistent with the location of the jet speed decrease at upper levels. Therefore, the anomalous circulation may act to reduce the storm track poleward shift to a more zonal position, given the equatorward jet change over all SH oceans (Figures 5.21b, d and f). Also, HGT decreases over the Pacific may indicate a change of the Rossby wave pattern due to tropical heating mainly over the Pacific Ocean, which affects the cyclone track densities (Figures 5.1e) in the SH. The 500hPa geopotential anomaly changes for the RCP4.5 scenario (Figure 5.24a) are similar but slightly displaced, compared to the RCP8.5 scenario, over the Indian and Pacific Oceans. HGT increases (Figure 5.24a) over the south of SA are displaced to the north in relation to the RCP8.5 scenario (Figure 5.23a), however the region

of HGT decrease in the mid Atlantic Ocean are displaced towards Antarctica.

In general global skin temperature during the winter season decreases in the RCP8.5 scenario (Figure 5.25a), however this is in contrast to the temperature increases in the RCP4.5 scenario (Figure 5.26a). This field represents the surface temperature over the oceans (SST) and the surface temperature over the continents. The next analyses will focus on the SST, however the surface temperature will be explored further in the regional-scale analysis (Section 5.1.4.1).

Temperature decreases (WAMZ–CTRL,  $\sim -1.5^{\circ}\text{C}$ ) over the region of Weddell Sea and the Antarctic coast toward Indian Ocean, however increase in the same magnitudes over the Ross Sea toward Antarctic Peninsula for RCP8.5 scenario (Figure 5.25a). Therefore, this supports the hypothesis that the removal of the Amazon Forest impacts the heat transport from the tropical region to the Antarctic (Drake Passage region), which causes a temperature increase between the Ross Sea and Antarctic Peninsula (Figure 5.25a) and results in an increase of the anticyclonic motion (Figure 5.23a). This hypothesis is also consistent with the storm track RCP8.5 changes found in the Antarctic Peninsula region where there is a lysis decrease on the windward side (Figure 5.3e) and genesis increase on the leeward side (Figure 5.2e). Also, this pattern corresponds with the temperature changes in the RCP8.5 experiment in the same region, with the temperature increase over the Ross Sea and decrease over the Weddell Sea (Figure 5.25a). The temperature cross section for the RCP8.5 experiment over the Pacific (Figure 5.21e, increase between  $70^{\circ} - 80^{\circ}\text{S}$ ) and Atlantic (Figure 5.21a, decrease between  $70^{\circ} - 80^{\circ}\text{S}$ ) also support this hypothesis. The RCP8.5 SST change decreases over the major part of southern oceans and somewhat increases in the tropical latitudes (below  $30^{\circ}\text{S}$ ). Also, there is a sign contrast over the south of South Africa that may be related to the Agulhas current, however this pattern is not seen in the RCP4.5 scenario (Figure 5.26a).

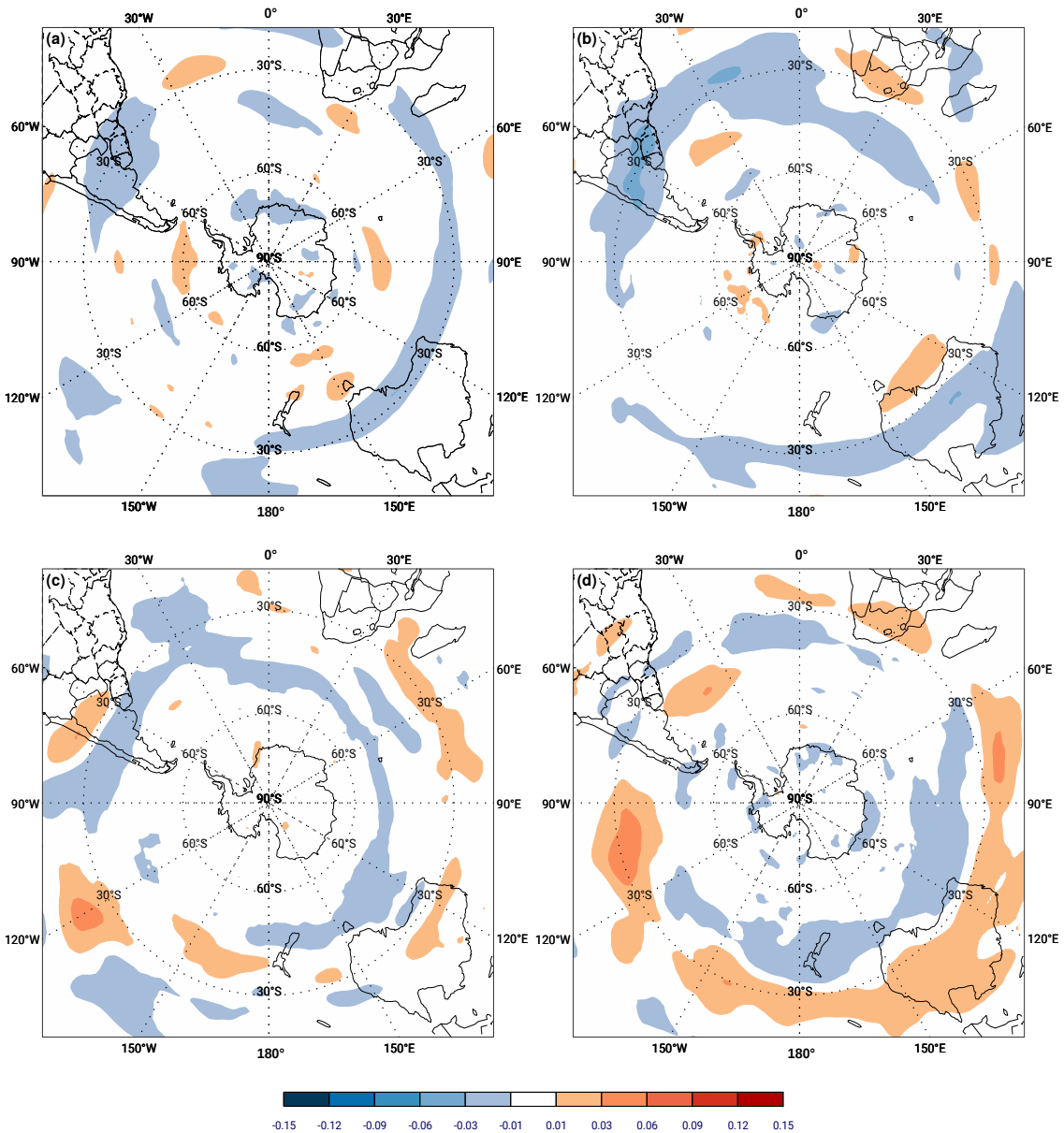
The global skin temperature is higher in the RCP4.5 scenario (Figure 5.26a) and, as discussed above, contrasts with the major part of the surface temperature reduction in the RCP8.5 scenario (Figure 5.25a). Temperature increases over the Weddell Sea is up to  $2.0^{\circ}\text{C}$  and over Wilkes and Victoria Land in Antarctica. Thus, similar to the RCP8.5 scenario, the removal of the Amazon Forest also impacts the meridional heat transport from tropics to polar regions. This change can be seen in the temperature cross section changes, particularly in the Atlantic Ocean (Figure 5.22a) at high latitudes, where the temperature increase. This temperature change also corresponds with the lysis increases windward of the Antarctic Peninsula (Figure 5.2f), but is not

seen in the geopotential anomaly changes 5.24. Therefore, in general the temperature increases for RCP4.5 may be related to Ozone recovery, similar to that found by Barnes et al. (2014) in Figures 2.b and 8.e and h) for CMIP5 climate models, since the Ozone contributes to the temperature increase over Antarctica, particularly over the Weddell Sea.

Sea surface temperature increases over the tropical Pacific Ocean is up to  $0.5^{\circ}\text{C}$  and this tendency can be seen in both the RCPs, but is stronger in the RCP4.5 scenario. Hence the removal of Amazon Forest seems to impact the the SPCZ though the feedback mechanisms between the SST and clouds. To test this hypothesis the outgoing longwave radiation (OLR) changes for WAMZ–CTRL are shown in Figures 5.27 and 5.28 for both the RCPs, where increase (decrease) indicate less (more) clouds than the CTRL experiment. In general winter OLR RCP4.5 changes are seen at tropical latitudes (Figure 5.28a), particularly over the Intertropical Convergence Zone (ITCZ), however the maximum increase areas of changes occur over the Amazon Forest region and Pacific Ocean. These areas have the feedback mechanisms acting in two ways, the temperature increase adjacent to the north of SA enhances the zonal heat transport and results in more clouds over the Pacific Ocean which contributes to enhance the latent heat and the SST. Whereas the removal of Amazon Forest reduces the clouds, the earth system increases the loss of radiation to the atmosphere and reduces the surface temperature. This feedback mechanisms will be also discussed in the regional-scale analyses (Section 5.1.4).

Finally, the precipitation changes are shown in Figures 5.29 and 5.30 for each RCP scenario in all seasons. The precipitation changes are similar in both the RCPs, being the maximum changes at tropical latitudes and over the South America. These changes correspond well with the OLR changes and the removal of Amazon Forest has impacts in global-scale. Thus, there is a constant difference between the RCPs over the Atlantic ITCZ (Figures 5.29a and 5.30a) which may associated with the Hadley Cell expansion (not shown), although this effect is stronger during the summertime in the CMIP5 models (GERBER; SON, 2014), once many of changes occurs over Northern Hemisphere. The main continental change occurs over the SA, which is direct result of the removal of Amazon Forest, and them will be discussed in the Section 5.1.4.

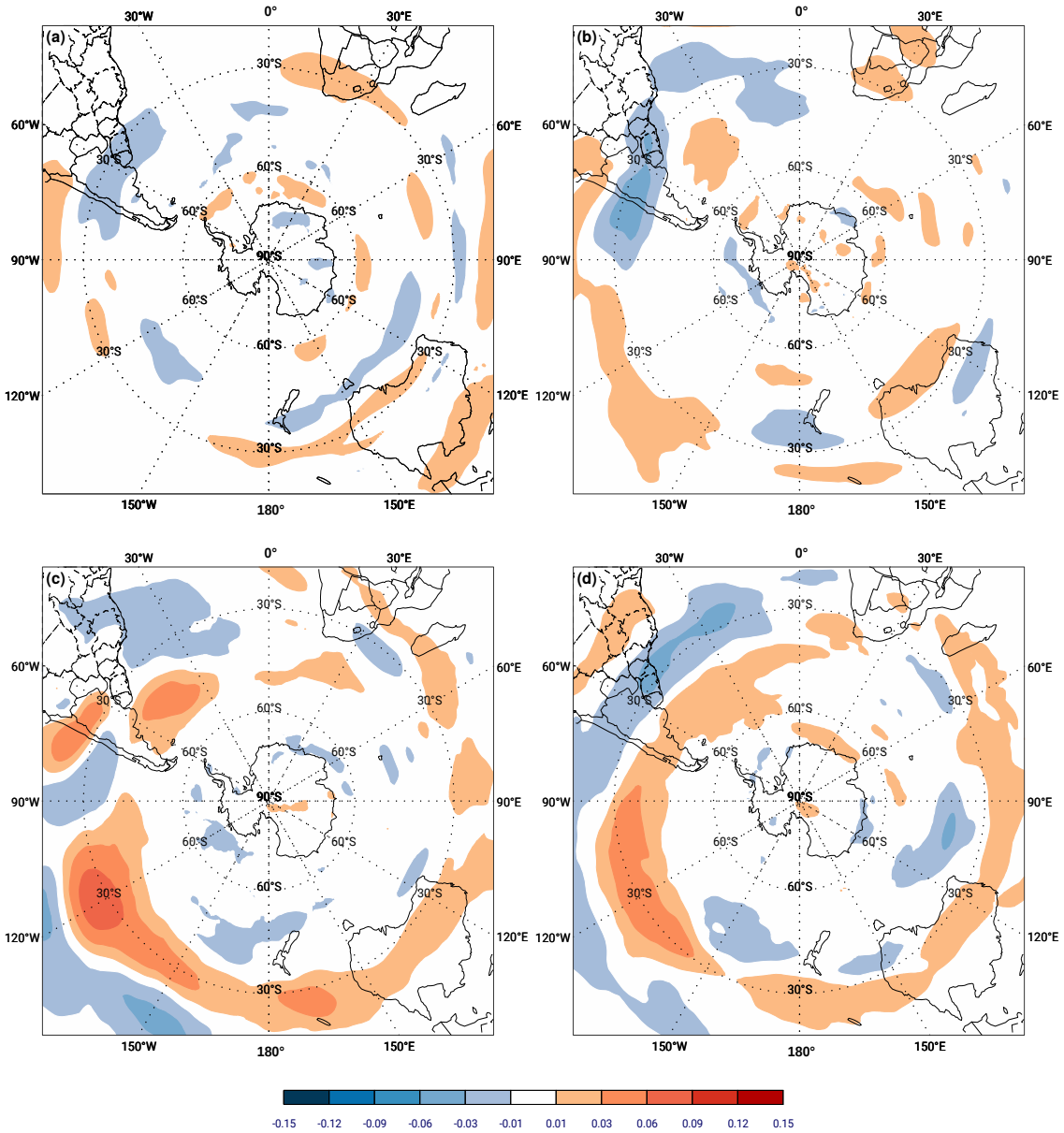
Figure 5.17 - Maximum Eady growth rate RCP8.5 changes at 250hPa for the period 2070-2099.



Maximum Eady growth rate ( $day^{-1}$ ) RCP8.5 changes (WAMZ-CTRL) at upper levels (250hPa) for the period 2070-2099 over Southern Hemisphere: (a) JJA; (b) SON; (c) DJF; and (d) MAM.

SOURCE: Author's production.

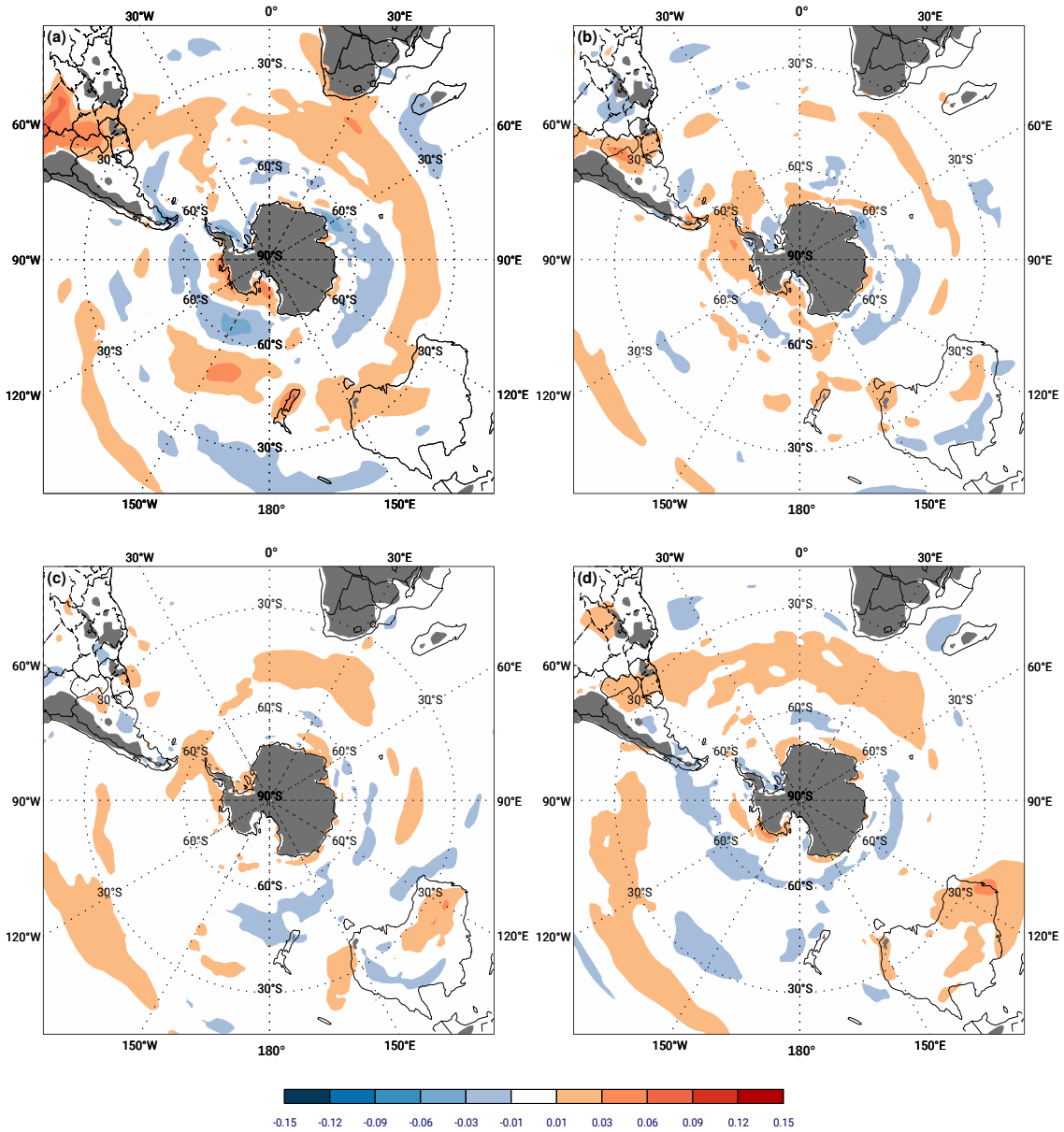
Figure 5.18 - Maximum Eady growth rate RCP4.5 changes at 250hPa for the period 2070-2099.



Maximum Eady growth rate ( $day^{-1}$ ) RCP4.5 changes (WAMZ-CTRL) at upper levels (250hPa) for the period 2070-2099 over Southern Hemisphere: (a) JJA; (b) SON; (c) DJF; and (d) MAM.

SOURCE: Author's production.

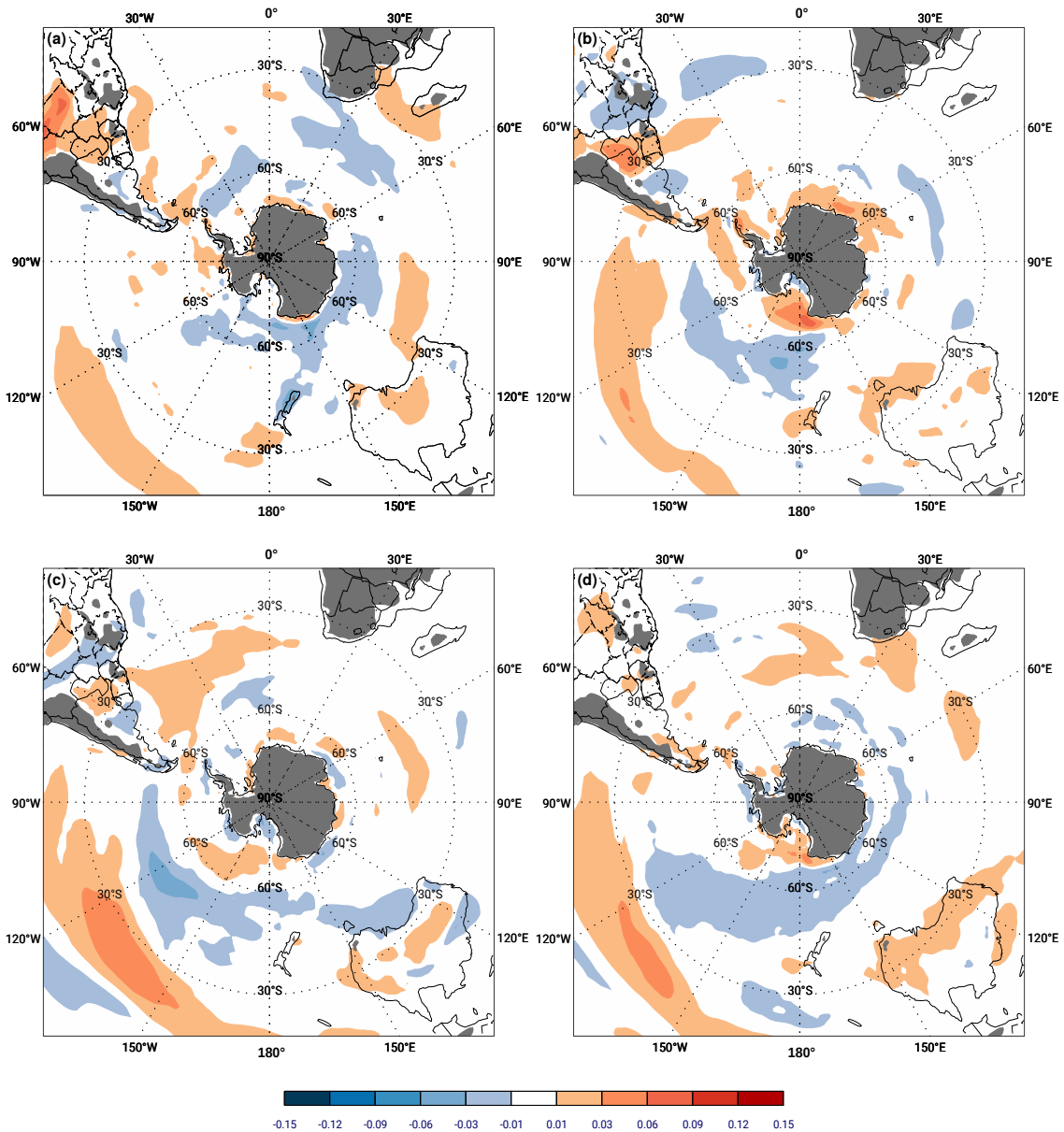
Figure 5.19 - Maximum Eady growth rate RCP8.5 changes at 850hPa for the period 2070-2099.



Maximum Eady growth rate ( $day^{-1}$ ) RCP8.5 changes (WAMZ-CTRL) at upper levels (850hPa) for the period 2070-2099 over Southern Hemisphere: (a) JJA; (b) SON; (c) DJF; and (d) MAM.

SOURCE: Author's production.

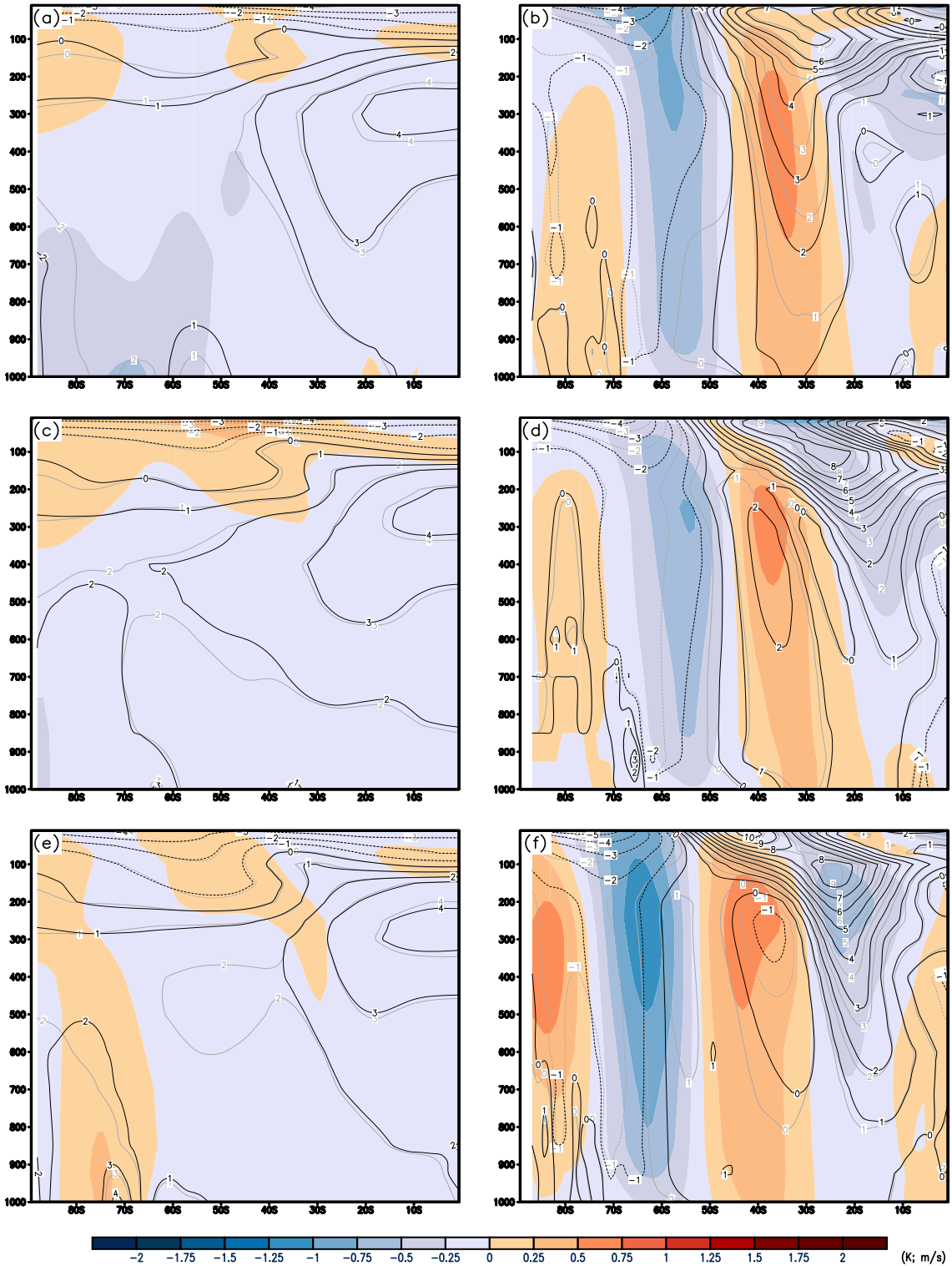
Figure 5.20 - Maximum Eady growth rate RCP4.5 changes at 850hPa for the period 2070-2099.



Maximum Eady growth rate ( $day^{-1}$ ) RCP4.5 changes (WAMZ-CTRL) at upper levels (850hPa) for the period 2070-2099 over Southern Hemisphere: (a) JJA; (b) SON; (c) DJF; and (d) MAM.

SOURCE: Author's production.

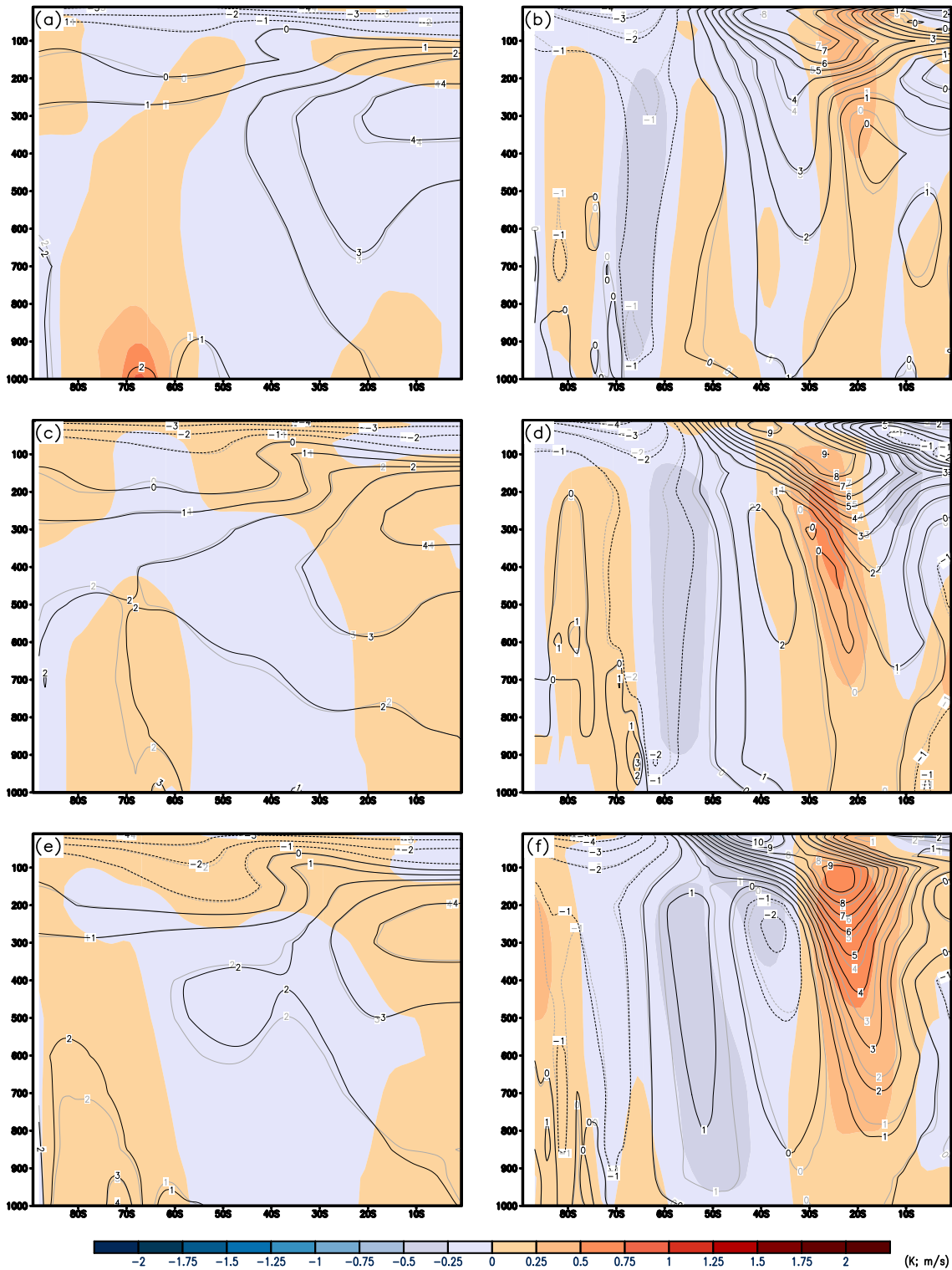
Figure 5.21 - Zonal mean temperature and zonal wind RCP8.5 changes in JJA.



Zonal mean temperature (K) (left column) and zonal mean zonal wind ( $m/s$ ) (right column) RCP8.5 changes in JJA for: (a) and (b) Atlantic; (c) and (d) Indian; and (e) and (f) Pacific. Results are calculated as the difference of the WAMZ minus CTRL experiment for the period 2070-2099 over Southern Hemisphere oceans. Black line contours show WAMZ-HIST while grey line contours show CTRL-HIST. Historical climatology is for the period 1976-2005.

SOURCE: Author's production.

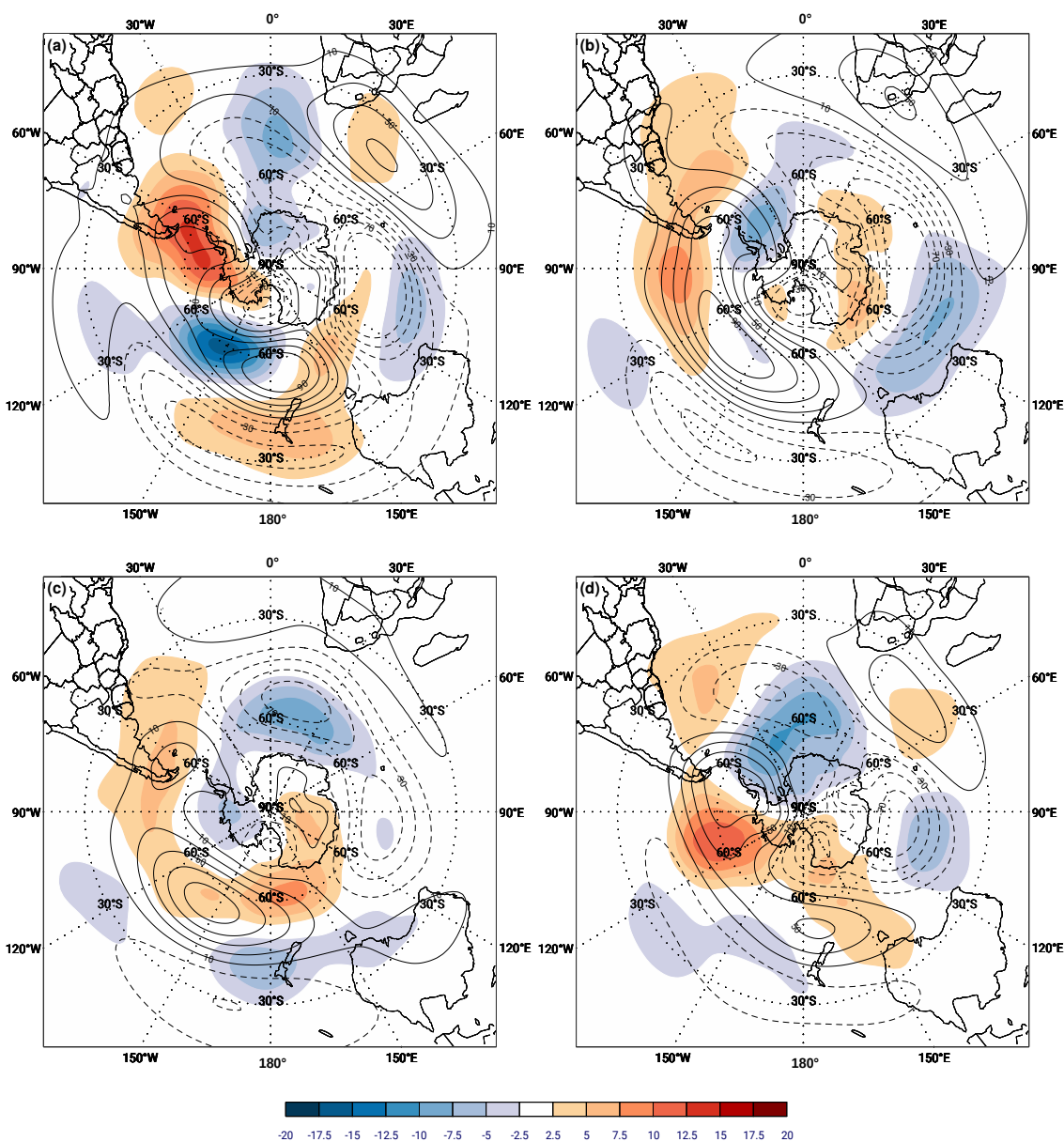
Figure 5.22 - Zonal mean temperature and zonal wind RCP4.5 changes in JJA.



Zonal mean temperature (K) (left column) and zonal mean zonal wind ( $m/s$ ) (right column) RCP4.5 changes in JJA for: (a) and (b) Atlantic; (c) and (d) Indian; and (e) and (f) Pacific. Results are calculated as the difference of the WAMZ minus CTRL experiment for the period 2070-2099 over Southern Hemisphere oceans. Black line contours show WAMZ-HIST while grey line contours show CTRL-HIST. Historical climatology is for the period 1976-2005.

SOURCE: Author's production.

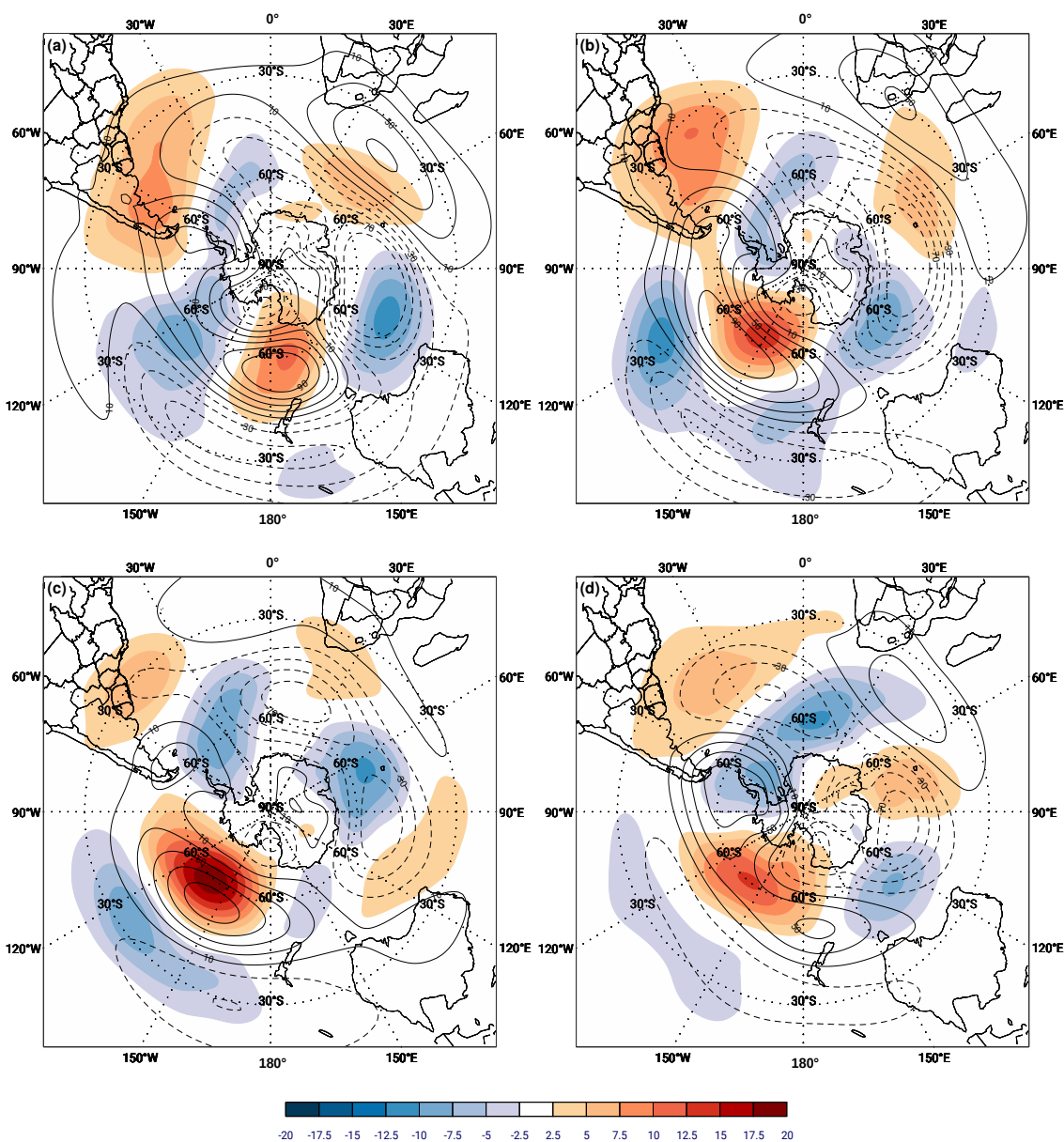
Figure 5.23 - 500hPa geopotential height anomaly RCP8.5 changes.



500hPa geopotential height anomaly (meters) RCP8.5 changes (WAMZ–CTRL) from the zonal mean for the period 2070-2099 over Southern Hemisphere: (a) JJA; (b) SON; (c) DJF; and (d) MAM. Black line contours show HadGEM2-ES Historical climatology for the period 1976-2005 and dashed contours indicate negative values.

SOURCE: Author's production.

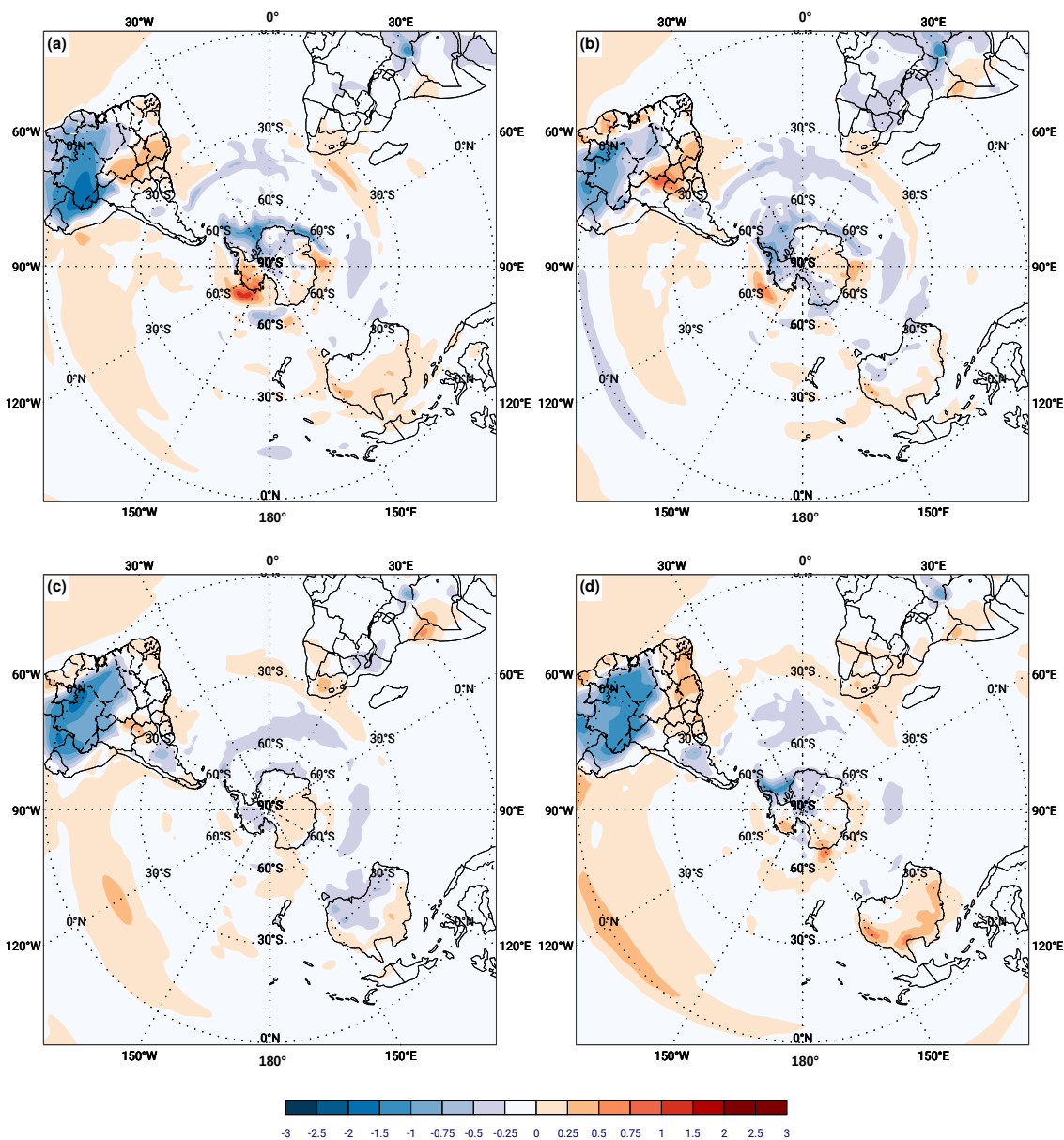
Figure 5.24 - 500hPa geopotential height anomaly RCP4.5 changes.



500hPa geopotential height anomaly (meters) RCP8.5 changes (WAMZ–CTRL) from the zonal mean for the period 2070-2099 over Southern Hemisphere: (a) JJA; (b) SON; (c) DJF; and (d) MAM. Black line contours show HadGEM2-ES Historical climatology for the period 1976-2005 and dashed contours indicate negative values.

SOURCE: Author's production.

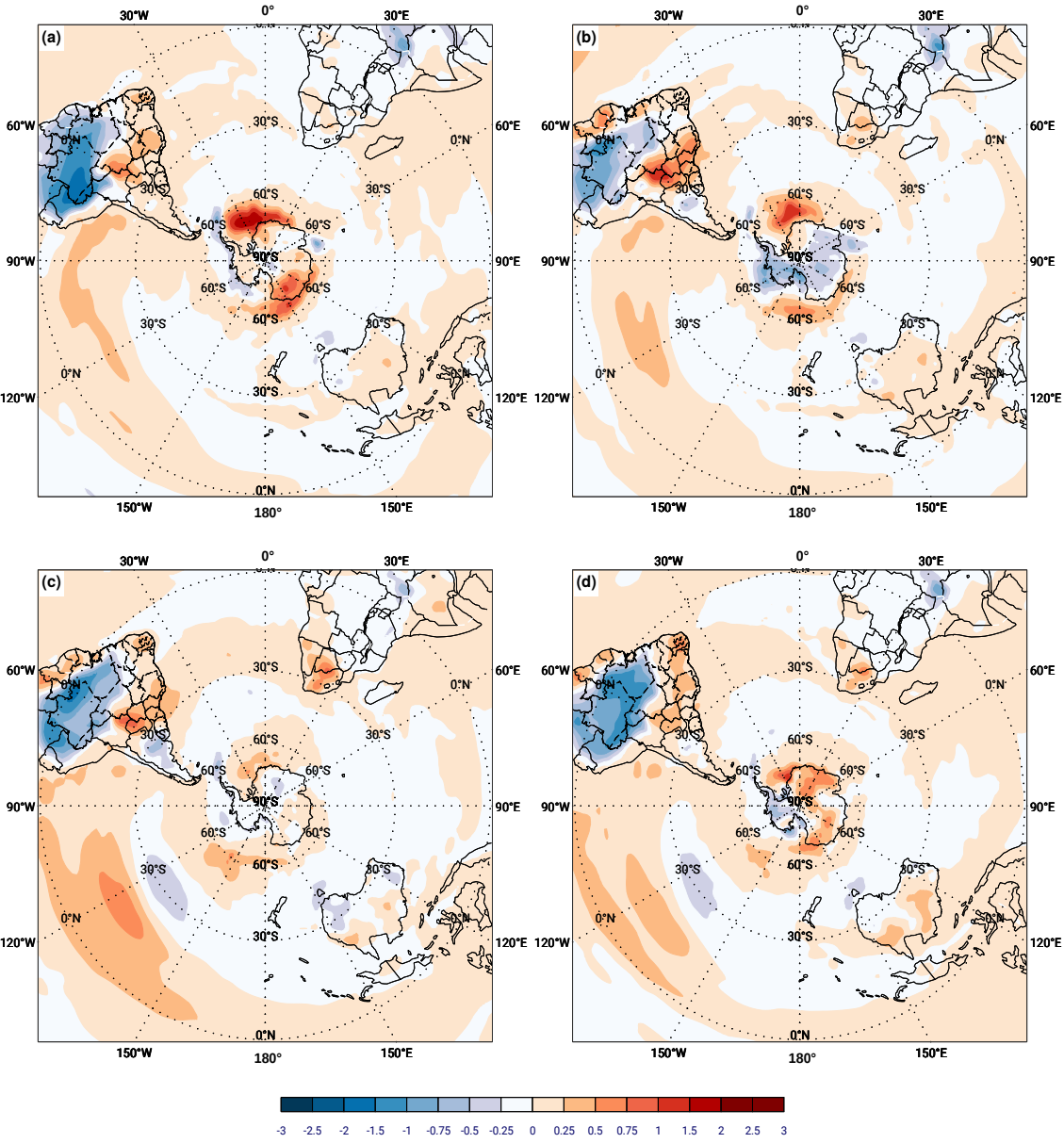
Figure 5.25 - Skin temperature RCP8.5 changes.



Skin temperature ( $^{\circ}\text{C}$ ) RCP8.5 changes (WAMZ-CTRL) for the period 2070-2099 over Southern Hemisphere: (a) JJA; (b) SON; (c) DJF; and (d) MAM. Black line contours show HadGEM2-ES Historical climatology for the period 1976-2005 and dashed contours indicate negative values.

SOURCE: Author's production.

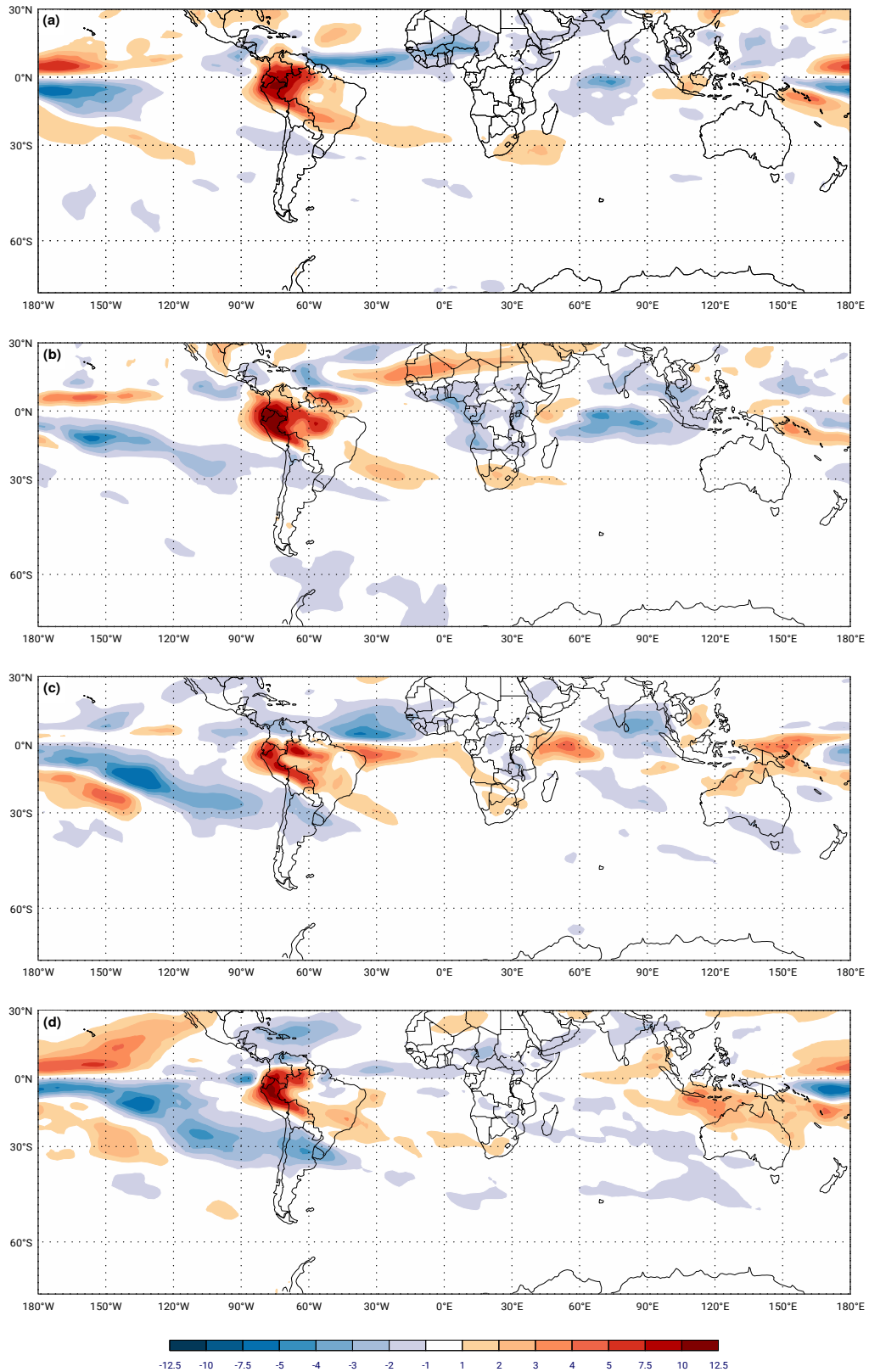
Figure 5.26 - Skin temperature RCP4.5 changes.



Skin temperature ( $^{\circ}C$ ) RCP4.5 changes (WAMZ–CTRL) for the period 2070-2099 over Southern Hemisphere: (a) JJA; (b) SON; (c) DJF; and (d) MAM. Black line contours show HadGEM2-ES Historical climatology for the period 1976-2005 and dashed contours indicate negative values.

SOURCE: Author’s production.

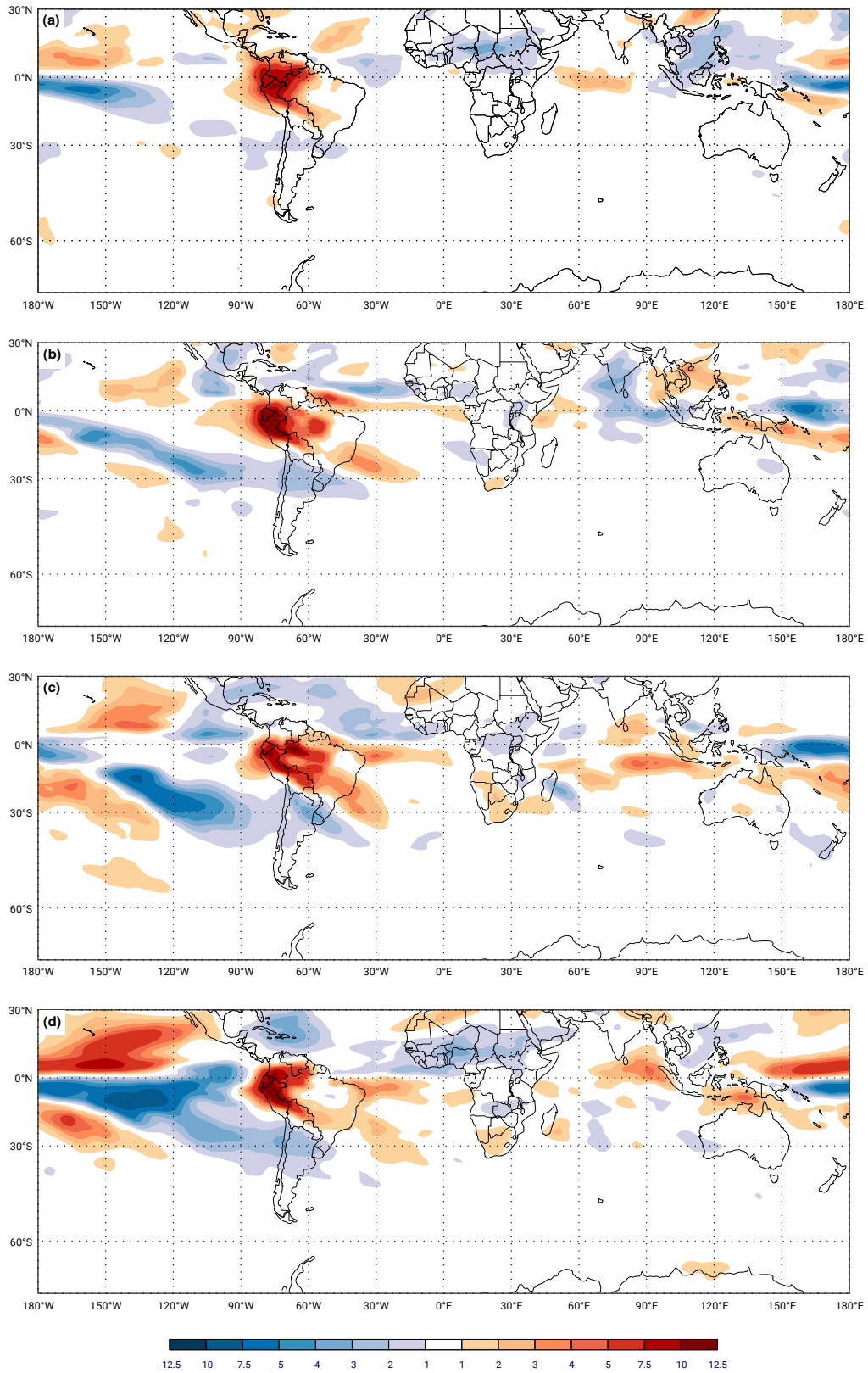
Figure 5.27 - Outgoing longwave radiation RCP8.5 changes.



Outgoing longwave radiation ( $W/m^2$ ) RCP8.5 changes (WAMZ-CTRL) for the period 2070-2099 over Southern Hemisphere: (a) JJA; (b) SON; (c) DJF; and (d) MAM.

SOURCE: Author's production.

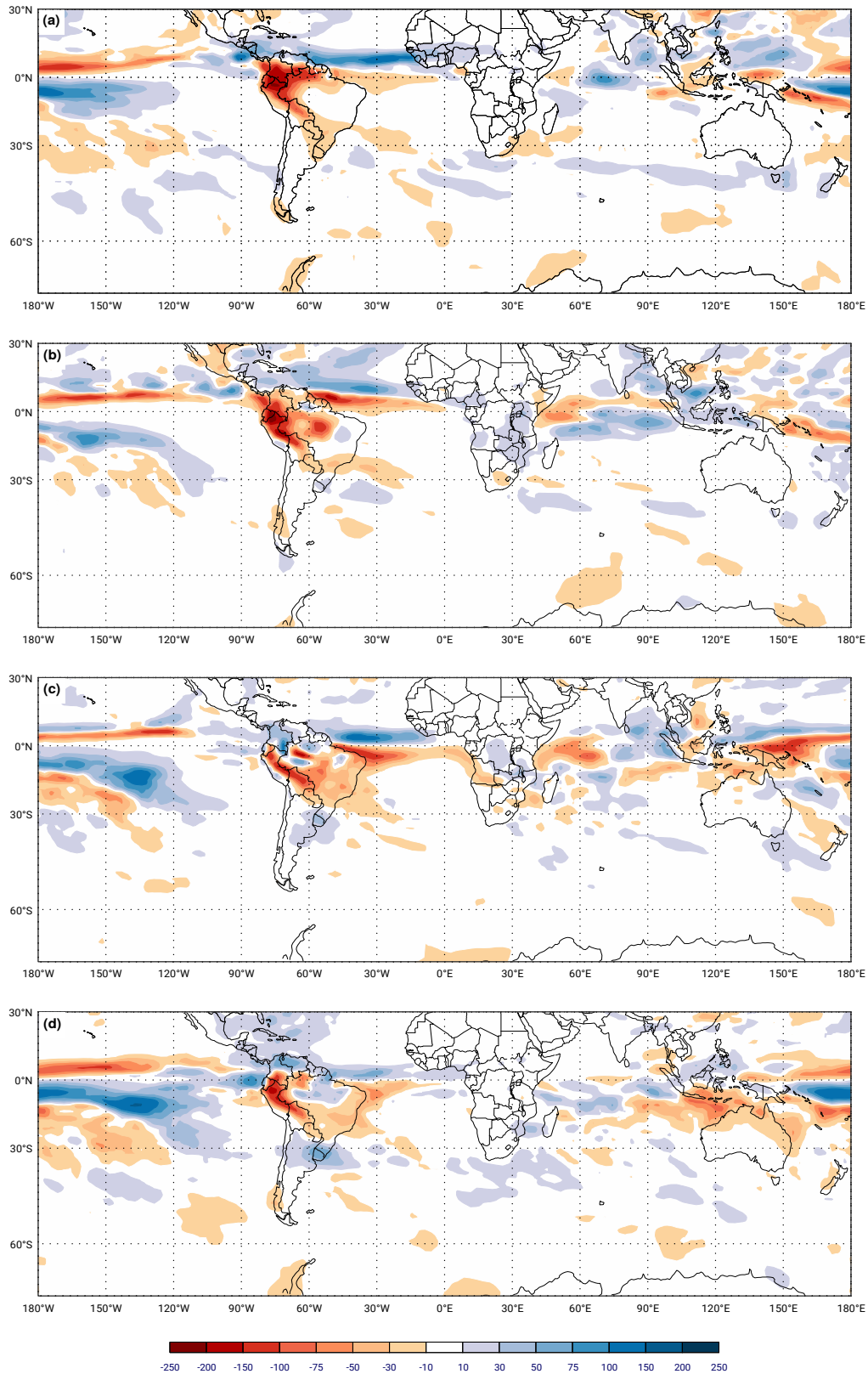
Figure 5.28 - Outgoing longwave radiation RCP4.5 changes.



Outgoing longwave radiation ( $W/m^2$ ) RCP4.5 changes (WAMZ-CTRL) for the period 2070-2099 over Southern Hemisphere: (a) JJA; (b) SON; (c) DJF; and (d) MAM.

SOURCE: Author's production.

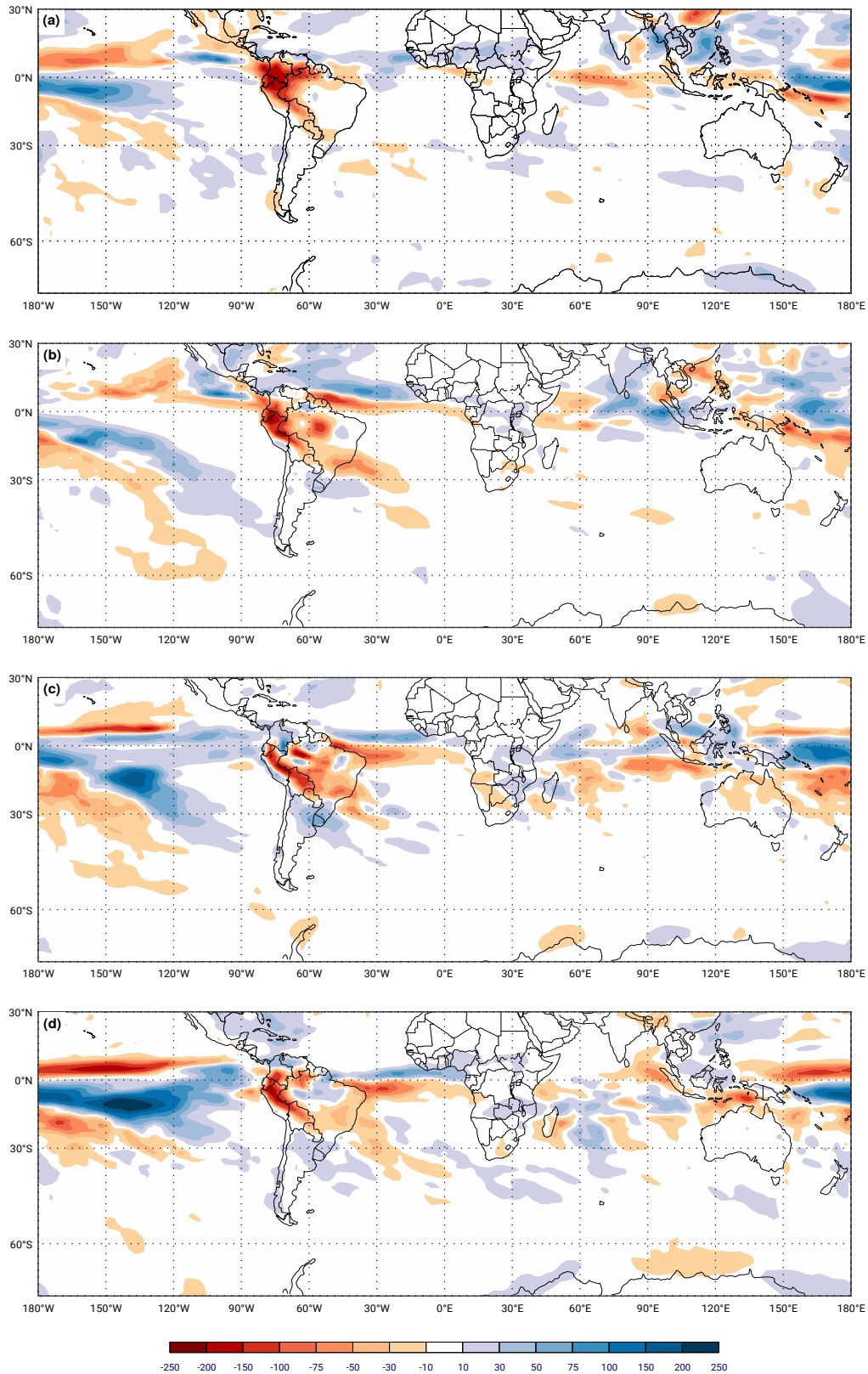
Figure 5.29 - Precipitation RCP8.5 changes.



Precipitation (mm/season) RCP8.5 changes (WAMZ-CTRL) for the period 2070-2099 over Southern Hemisphere: (a) JJA; (b) SON; (c) DJF; and (d) MAM.

SOURCE: Author's production.

Figure 5.30 - Precipitation RCP4.5 changes.



Precipitation (mm/season) RCP4.5 changes (WAMZ-CTRL) for the period 2070-2099 over Southern Hemisphere: (a) JJA; (b) SON; (c) DJF; and (d) MAM.

SOURCE: Author's production.

### 5.1.2.2 Summer

The summer large-scale patterns are described in detail in Chapter 4, Section 4.2.2.2, and the historical climatology can be used as a background reference for the fields analysed in this section.

For the differences between the WAZM and CTRL experiments the maximum Eady growth rate changes at upper (250hPa) and lower (850hPa) levels for both the RCPs during the summer season are shown in Figures 5.17c, 5.18c, 5.19c, and 5.20c.

The RCP8.5 baroclinicity changes for the summer season (Figure 5.17c) show that the main differences (WAZM–CTRL) occur at extratropical latitudes over the southern oceans. Baroclinicity decreases from the Pacific through the Atlantic toward Indian Ocean between latitudes 40 – 50°S, while increases are found at a latitude of 30°S over SA, Indian Ocean, Australia and Pacific Ocean. The area of change over the Pacific Ocean is the largest during the summer season and corresponds with the cyclone track and genesis density changes for the RCP8.5 experiment (Figures 5.5e and 5.6e). The summer baroclinicity changes for RCP4.5 at upper levels (Figure 5.18c) are the largest of all seasons and scenarios, being up to 10% of changes in relation to the CTRL experiment. Baroclinicity decreases in the same latitudinal belt as the main baroclinic region in the historical climatology (similar to Figure 4.10c for summer ERA-Interim climatology) and the main changes occur over the Pacific and Atlantic Oceans. This pattern of change in the Pacific Ocean is linked with the HadGEM2-ES RCP4.5 scenario changes at upper levels, which simulated an enhancement of the Subtropical Jet in the experiment without the Amazon Forest (Figures 5.32). Although not comparable, the CMIP5 multi-model mean does not show a similar sign of change during the summer (CHENOLI, 2017).

The summer Baroclinicity changes (WAMZ–CTRL) at lower levels are shown in Figures 5.19c and 5.20c for the RCP8.5 and RCP4.5 scenarios respectively. Contrasting with the upper levels, the removal of the Amazon Forest causes the smallest baroclinicity changes of all seasons for the RCP8.5 experiment (Figure 5.19c), with the main increases over Australia, the Pacific and the Atlantic Oceans. The increases in the extratropical latitudes contribute to reduce the poleward shift in the experiment without Amazon Forest. Hence in the WAMZ experiment under RCP8.5 scenario the baroclinicity decreases are small in relation to the CTRL experiment. Similar to the RCP8.5 scenario, the baroclinicity changes for the RCP4.5 experiment are mainly over the Indian and Atlantic Oceans (Figure 5.20c). This pattern corresponds with the cyclone track density changes and seem associated with the

wind increase on the Subtropical Jet, given the enhancement of the poleward shift when the Amazon Forest is removed in the RCP4.5 scenario. This hypothesis is also supported by the baroclinicity enhancement over the south of Brazil and the adjacent Atlantic Ocean, which corresponds with the increase of the cyclone track and genesis density changes in RCP4.5. Although in the summer season, this pattern of change is somewhat similar to the winter storm trajectories shown by Hoskins and Hodges (2005) (Figures 6 and 7) and seems associated with the wind increase on the equatorward jet (Figure 5.32). Therefore, there is strong evidence that the removal of the Amazon Forest impacts the Southern Hemisphere storm tracks.

The zonal mean temperature changes (WAMZ–CTRL) for the RCP8.5 experiment are shown in Figure 5.31 (left column) for Atlantic (Figure 5.31a), Indian (Figure 5.31c) and Pacific (Figure 5.31e) Oceans. The differences for WAMZ–HIST (black contours) and CTRL–HIST (grey contours) are shown in these figures to give an idea of the magnitude of changes. In general the temperature decreases over all oceans, similar to the winter season in this scenario, however there is a temperature increase in the lower stratosphere (above 50 hPa). Other small temperature increases occur over the Indian, middle (200hPa) and high (600-300hPa) latitudes, and Pacific Ocean (column at 60°S between 850-150hPa). Thus, the impact of the removal of the Amazon Forest during the summer results in an atmosphere cooling pattern in the RCP8.5 scenario. Contrasting this cooling pattern during summer, with the RCP4.5 changes (Figure 5.32) there is a warming pattern, particularly in the Atlantic and Pacific Oceans, where this change is concentrated at tropical (between 10 – 30°S) and middle-high latitudes. The temperature change in the Pacific Ocean around 60°S extends from surface to the lower stratosphere. This upper level change does not correspond with the maximum Eady growth rate changes at upper levels, but seems to be related to Ozone recovery suggested by Barnes et al. (2014) for CMIP5 models during the summer season.

The cross section of zonal wind changes are shown in Figure 5.31 (right column) for the Atlantic (Figure 5.31b), Indian (Figure 5.31d) and Pacific (Figure 5.31f) Oceans. The ERA-Interim climatology shows a single eddy-driven jet between 60°S and 40°S over all southern oceans during the summer season (Figure 4.17, black contour lines). However, the HadGEM2-ES simulates a split jet in this season over the Pacific Ocean for both the RCP scenarios (figure not shown), which is somewhat similar to that shown for the Historical experiment (see the equatorward positive biases in Figure 4.17f). In general the zonal wind for RCP8.5 increases over the tropical region and decreases at extratropical latitudes, which corresponds well to the baroclinicity

changes (Figures 5.17c and 5.19c) and the reduced poleward shift observed in this scenario (Figure 5.5e). This wind enhanced pattern at tropical latitudes over the southern oceans suggests a relation to the Hadley Cell, similar to that described by Gerber and Son (2014) for CMIP5 models, which found that the latitudes of the jet stream and Hadley Cell boundary are sensitive to the temperature gradient between the tropics and high latitudes in the upper troposphere lower stratosphere.

Summer geopotential height anomaly changes are shown in Figures 5.23c and 5.24c for the RCP8.5 and RCP4.5 scenarios. The RCP8.5 geopotential changes are the smallest of all seasons in this scenario and the main changes are at the middle and high latitudes. HGT increases over the south of SA, Pacific and East of Antarctica, while it decreases in the New Zealand region and Atlantic Ocean at approximately 15°E.

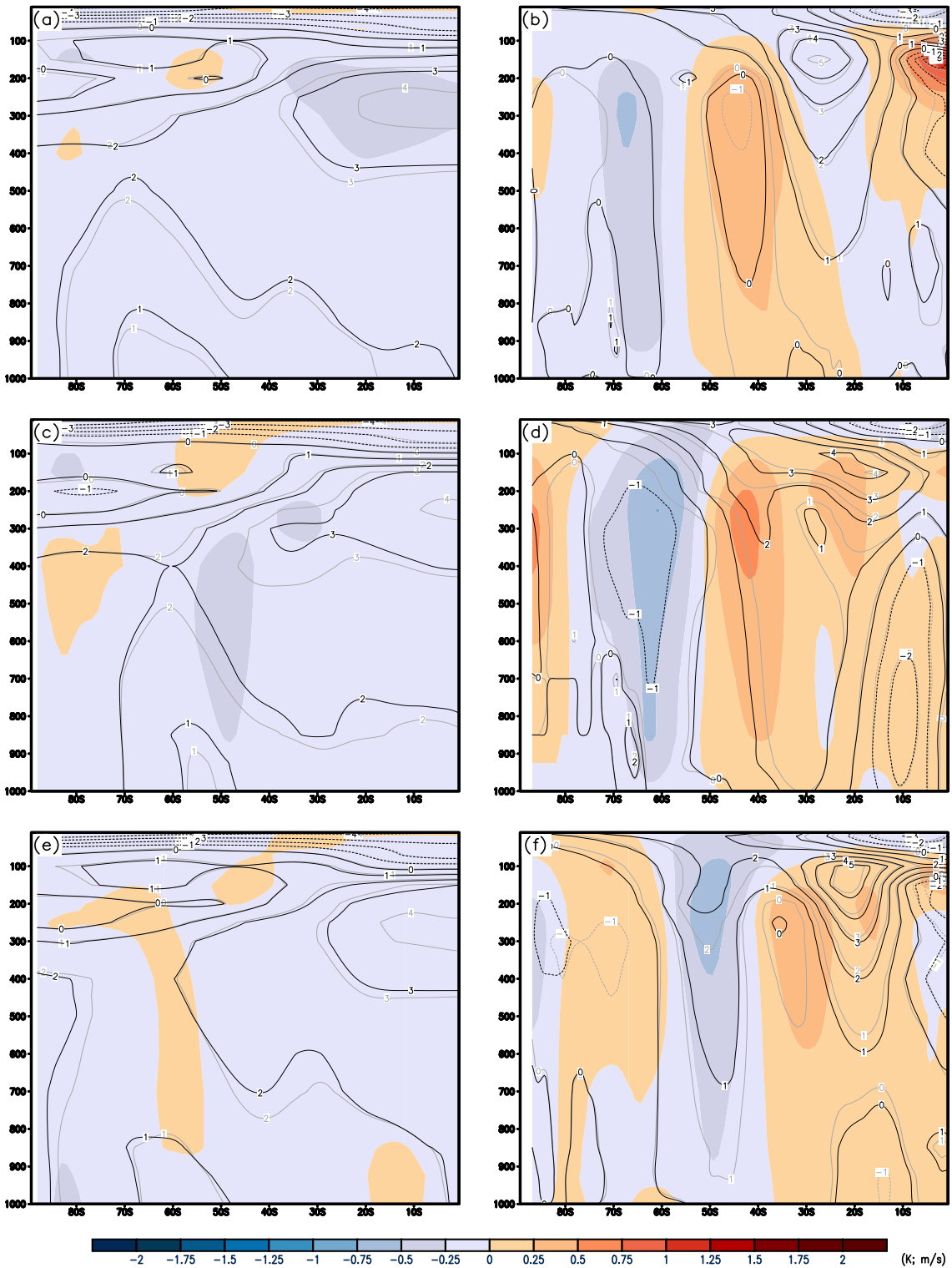
The 500hPa geopotential anomaly for the RCP4.5 scenario (Figure 5.24c) are similar but stronger than for the RCP8.5 scenario. HGT increases (Figure 5.24a) over the south of SA are displaced to the north in relation to the RCP8.5 scenario (Figure 5.23a), however the HGT decreases in the middle of the Atlantic Ocean toward the Antarctic Peninsula, the Antarctic coastline around 60°E and the tropical Pacific. The largest HGT change for RCP4.5 occurs over the Pacific Ocean (150 – 120°W) in the climatological region of the positive HGT anomaly. Contrasting to the winter season, it seems to act to enhance the poleward shift in RCP4.5, indicating that the removal of the Amazon Forest acts to increase the baroclinicity at upper levels (5.18c) and the storms towards the pole (Figure 5.5f).

Similar to the winter season, the global skin temperature during the summer season decreases in the RCP8.5 scenario (Figure 5.25c), however this contrasts with the temperature increases in the RCP4.5 scenario (Figure 5.26c). The surface temperature changes over SA will be explored further in the regional-scale analysis (Section 5.1.4.1). The RCP4.5 SST increases by up to 0.75° over the Pacific Ocean and is the largest change of all oceans in this season. This change corresponds well with the baroclinicity increase and the cyclone track density changes in RCP4.5. Hence the removal of the Amazon Forest seems to impact the SPCZ through the feedback mechanisms between the SST and clouds, as explained for the winter season, and shown in the OLR changes for both the RCPs (Figures 5.27c and 5.28c). This pattern seems stronger in the RCP4.5 scenario for the summer season and links with the wind increases, mainly over the Pacific Ocean (Figure 5.32f).

The precipitation changes for RCP8.5 (Figure 5.29c) and RCP4.5 (Figure 5.30c)

are the result of the changes in the large-scale fields. The precipitation changes are similar in both the RCPs, including the summer features of the maximum changes at tropical latitudes and over the South America. These changes correspond well with the OLR changes in both the RCPs with the removal of Amazon Forest impacts the global-scale precipitation. The RCP4.5 precipitation changes are stronger than in the RCP8.5 over South America which will be explored in detail in the regional-scale section.

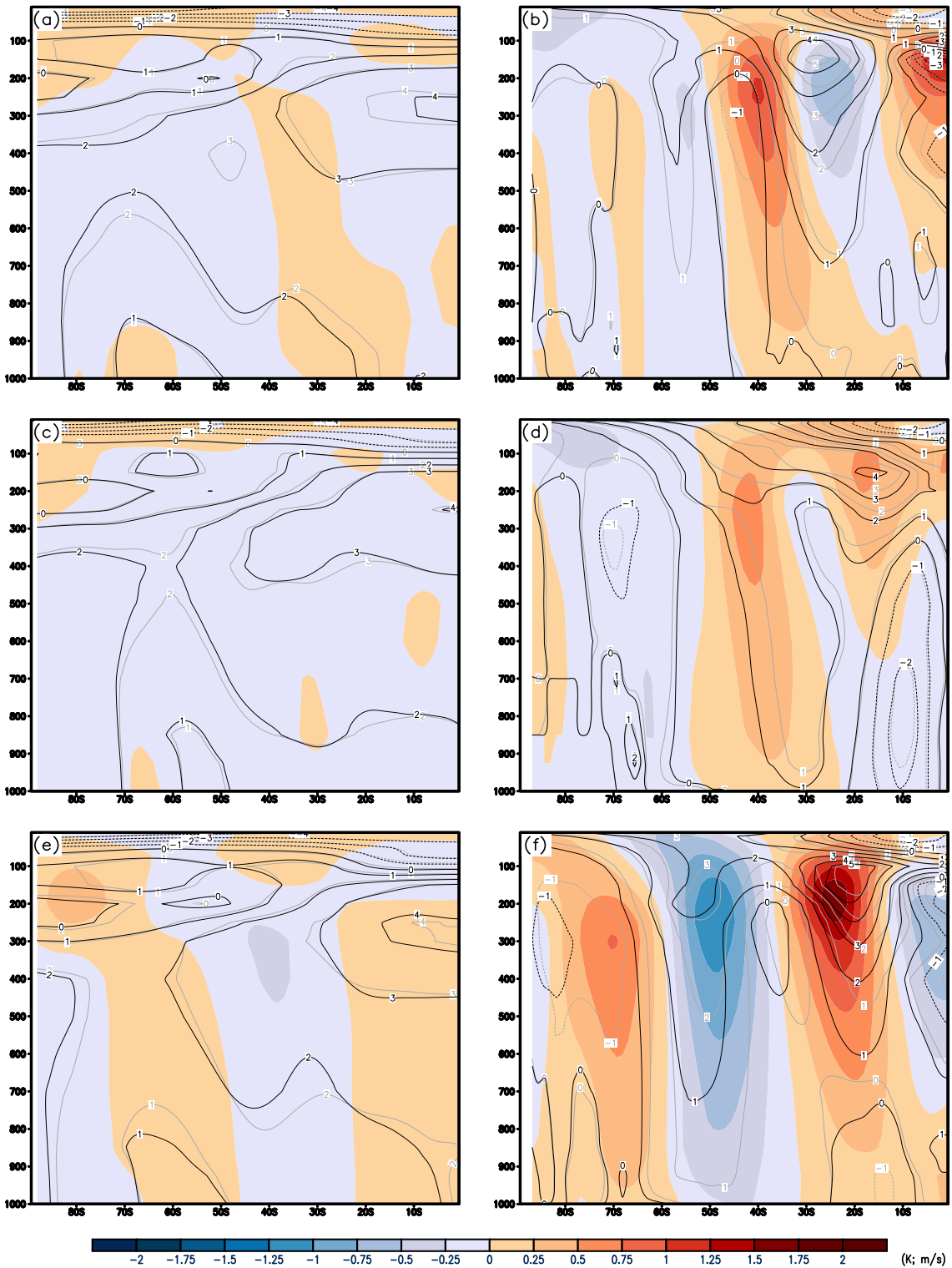
Figure 5.31 - Zonal mean temperature and zonal wind RCP8.5 changes in DJF.



Zonal mean temperature (K) (left column) and zonal mean zonal wind ( $m/s$ ) (right column) RCP8.5 changes in DJF for: (a) and (b) Atlantic; (c) and (d) Indian; and (e) and (f) Pacific. Results are calculated as the difference of the WAMZ minus CTRL experiment for the period 2070-2099 over Southern Hemisphere oceans. Black line contours show HadGEM2-ES Historical climatology for the period 1976-2005.

SOURCE: Author's production.

Figure 5.32 - Zonal mean temperature and zonal wind RCP4.5 changes in DJF.



Zonal mean temperature (K) (left column) and zonal mean zonal wind ( $m/s$ ) (right column) RCP4.5 changes in DJF for: (a) and (b) Atlantic; (c) and (d) Indian; and (e) and (f) Pacific. Results are calculated as the difference of the WAMZ minus CTRL experiment for the period 2070-2099 over Southern Hemisphere oceans. Black line contours show HadGEM2-ES Historical climatology for the period 1976-2005.

SOURCE: Author's production.

### 5.1.2.3 Transition seasons

The large-scale patterns for the spring and autumn seasons are also described in the Chapter 4, Section 4.2.2.3. The HadGEM2-ES Historical climatology can be used as a background reference for the fields analysed in this section. As described in the introduction, the analyses discussed here refer to difference between the HadGEM2-ES experiments without Amazon Forest minus with fixed land use (WAMZ–CTRL).

The baroclinicity changes at upper levels (250hPa) (Figures 5.17b and 5.18b) for the spring season have a zonal change concentrated around  $30^\circ$  over the SH, similar to the preceding season, with baroclinicity decreases over the band from the Pacific Ocean towards South America and the Atlantic Ocean ( $\sim 30^\circ\text{S}$ ), while there are increases over the southern Atlantic, South Africa and Australia. For the experiment RCP8.5 only the maximum Eady growth rate decreases in a band from the Indian ocean (northwest of Australia) towards the Pacific Ocean (Figure 5.17b), however this contrasts with the increase over the Pacific Ocean in the RCP4.5 scenario (Figure 5.18b). The autumn baroclinicity RCP8.5 changes are the largest of all seasons at upper levels, while the RCP4.5 is as strong as the summer season, which indicates a strong relation to the warming in the Pacific Ocean shown in Figures 5.25d and 5.26d in both the RCP scenarios. The Eady growth rate changes at 250hPa correspond well with the autumn cyclone track, genesis, lysis density and MGDR changes (Figures e and f of 5.13, 5.14, 5.15 and 5.16). At lower levels the changes in baroclinicity during the spring and autumn (Figures 5.19b,d and 5.20b,d) are in the same latitudes as the changes in cyclone track density changes (Figures 5.1e and f) for each respective RCP and also have the main features of the changes discussed to the preceding seasons.

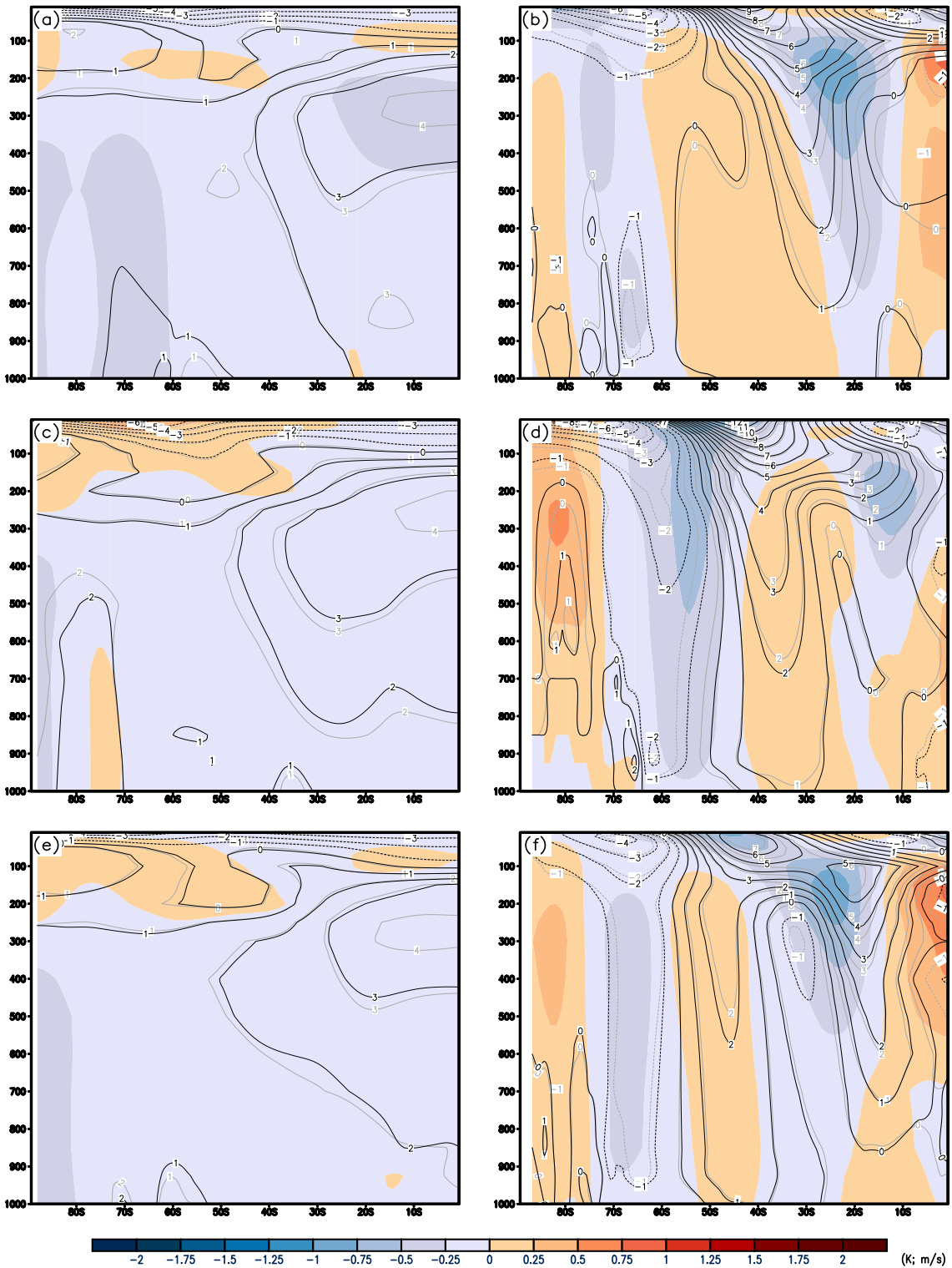
The spring and autumn zonal mean temperature and zonal wind changes are shown in Figures 5.33, 5.35, 5.34 and 5.36, for Atlantic (a,b), Indian (c,d) and Pacific (e,f) Oceans in each of the RCPs. The differences for WAMZ–HIST (black contours) and CTRL–HIST (grey contours) are shown in these figures to give an idea of the magnitude of changes. During the spring the ITCZ position is displaced to the north, similar to the winter season, while the autumn ITCZ position is more similar to the summer season. These ITCZ variabilities have direct impacts on the wind changes (Figures 5.33, 5.35, 5.34, 5.36, right side) and this seems to be related to those in the succeeding seasons, while the temperature cross sections seem to be similar to those in the preceding season, which suggests a direct relation to the large thermal inertia of the oceans in the experiments without the Amazon Forest. The autumn

zonal wind changes are very similar between the RCPs, however they are stronger at upper levels in the RCP8.5 scenario, particularly in the Atlantic and Pacific Ocean. These changes suggest a direct impact of the removal of the Amazon Forest on the adjacent oceans, which corresponds to the baroclinicity and track changes over both the oceans. Also, the temperature at lower levels increases over the Atlantic region at extratropical latitudes ( $20 - 30^{\circ}\text{S}$ ) while a decrease occurs at polar latitudes (Figure 5.35a).

Geopotential height anomaly changes during the transition seasons are similar to those in the preceding season, as are shown in Figures 5.33, 5.34, 5.35 and 5.36 for both the RCPs. The field features are described in previous Section 5.1.2.1 and 5.1.2.2. Similar to the geopotential changes, the skin temperature changes for transition seasons have similarity with those in the preceding season and are shown in Figures 5.25b,d and 5.26b,d for both the RCPs. The field features are also described in previous Section 5.1.2.1 and 5.1.2.2, however the difference between WAMZ–CTRL for spring temperature changes over the centre-southeast of Brazil is the largest of all season in both the scenarios (Figures 5.25b and 5.26b) (will be discussed in regional-scale changes, Section 5.1.4.3).

The precipitation changes during the spring and autumn seasons are shown in Figures 5.29b,d and 5.30b,d for each RCP scenario. The autumn RCP4.5 changes are stronger than RCP8.5 scenario, which also have the largest changes of all seasons. As expected, the OLR changes (Figures 5.27b,d and 5.28b,d) correspond very well with precipitation changes.

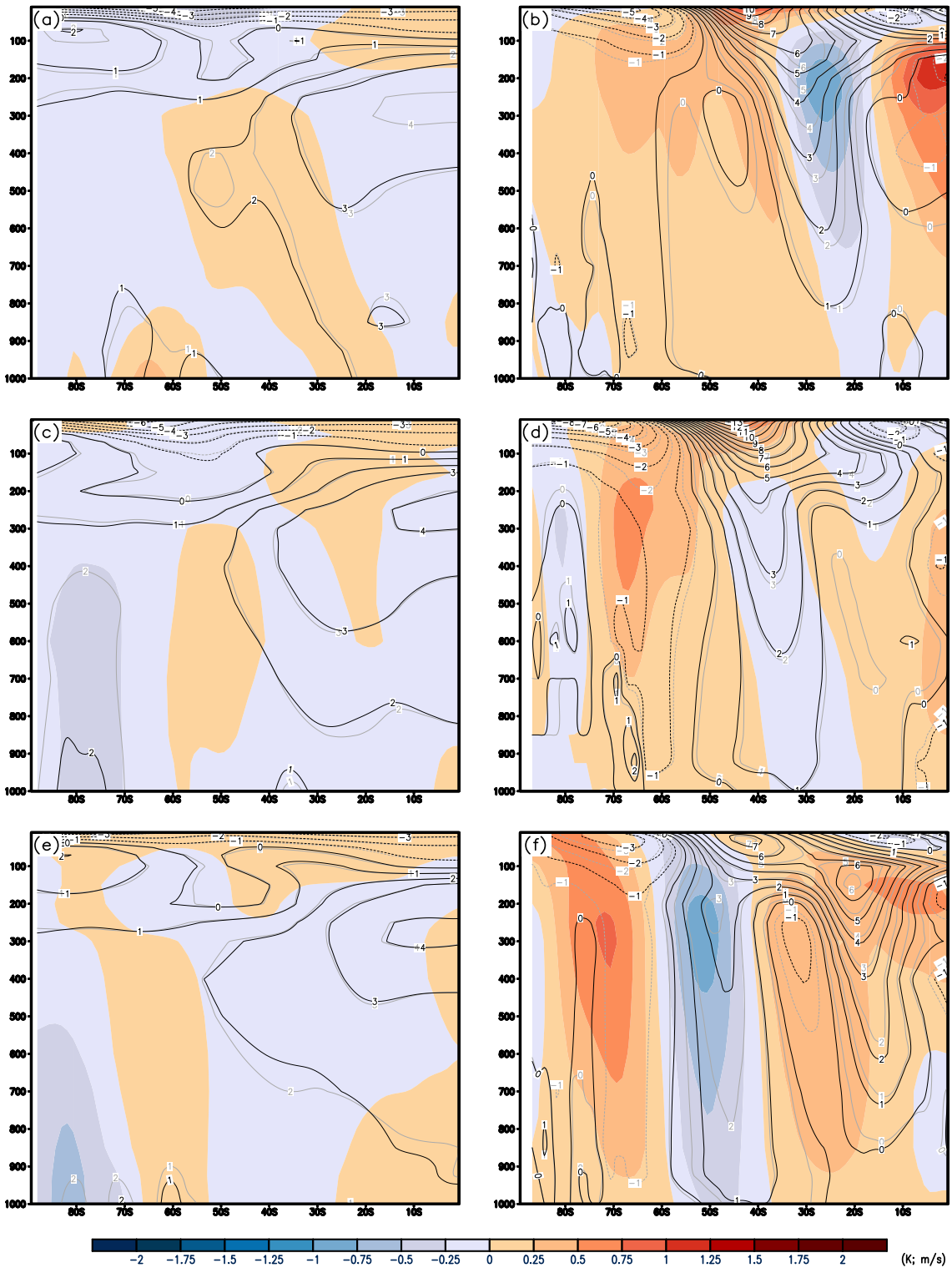
Figure 5.33 - Zonal mean temperature and zonal wind RCP8.5 changes in SON.



Zonal mean temperature (K) (left column) and zonal mean zonal wind ( $m/s$ ) (right column) RCP8.5 changes in SON for: (a) and (b) Atlantic; (c) and (d) Indian; and (e) and (f) Pacific. Results are calculated as the difference of the WAMZ minus CTRL experiment for the period 2070-2099 over Southern Hemisphere oceans. Black line contours show HadGEM2-ES Historical climatology for the period 1976-2005.

SOURCE: Author's production.

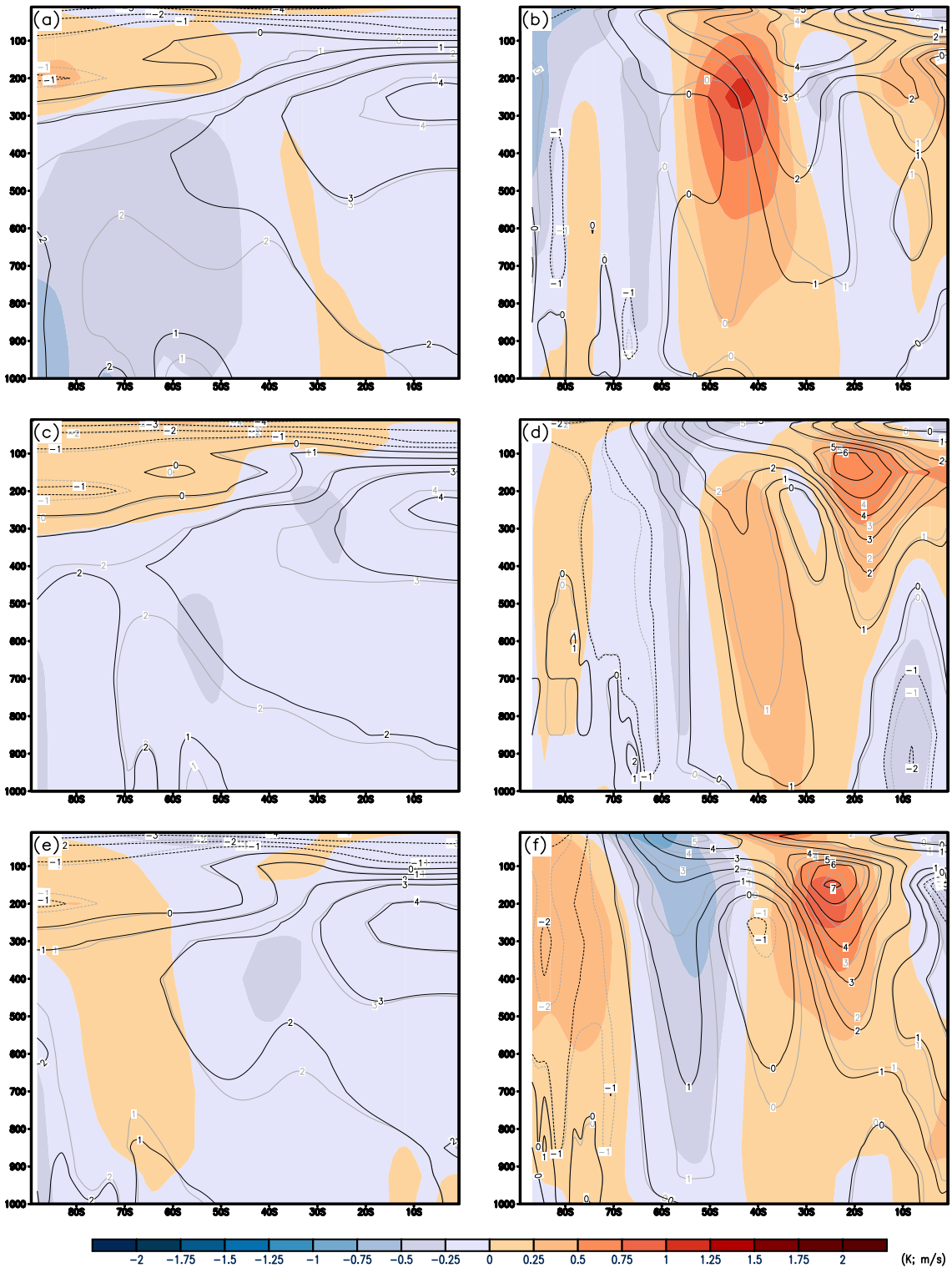
Figure 5.34 - Zonal mean temperature and zonal wind RCP4.5 changes in SON.



Zonal mean temperature (K) (left column) and zonal mean zonal wind ( $m/s$ ) (right column) RCP4.5 changes in SON for: (a) and (b) Atlantic; (c) and (d) Indian; and (e) and (f) Pacific. Results are calculated as the difference of the WAMZ minus CTRL experiment for the period 2070-2099 over Southern Hemisphere oceans. Black line contours show HadGEM2-ES Historical climatology for the period 1976-2005.

SOURCE: Author's production.

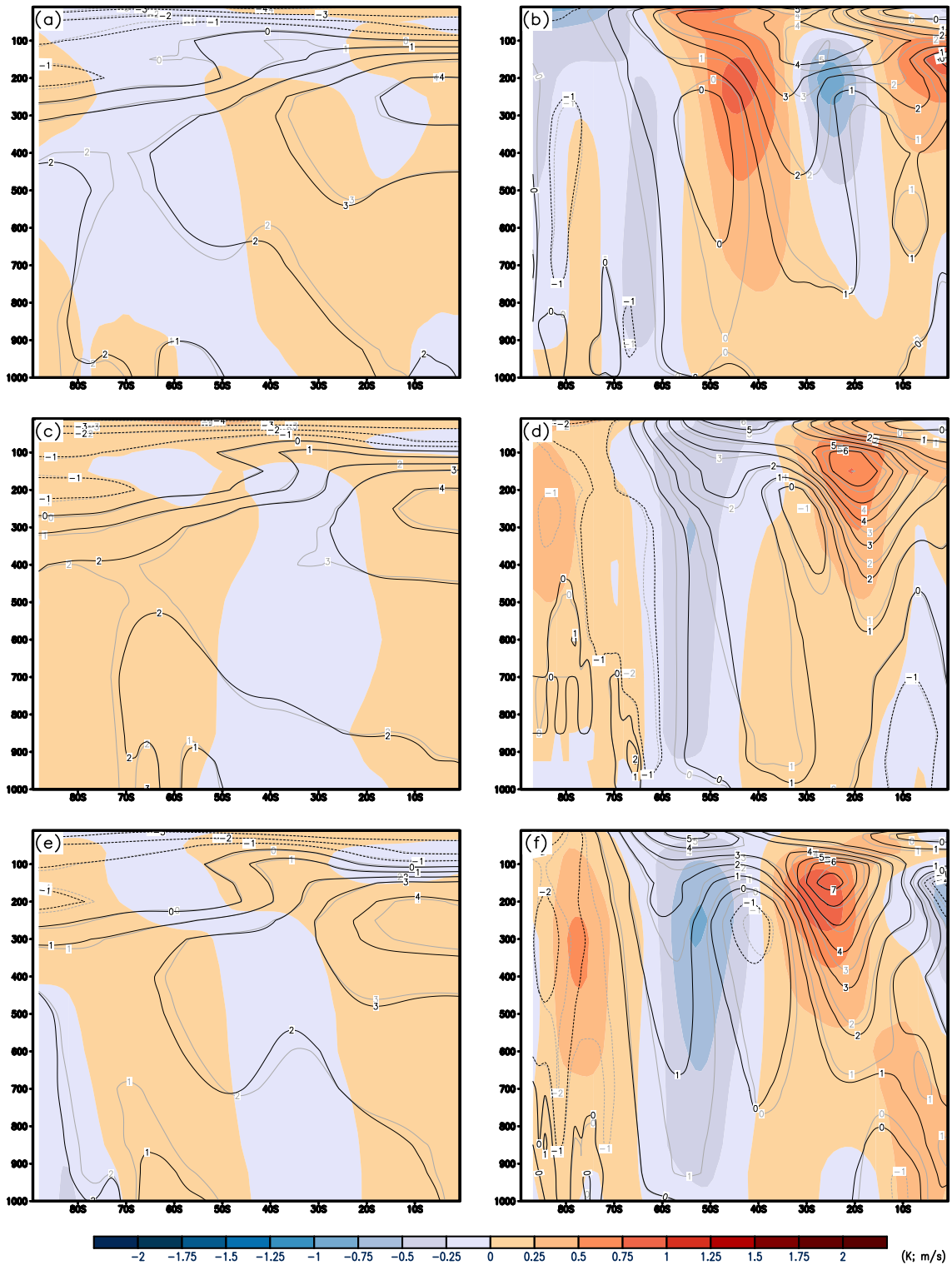
Figure 5.35 - Zonal mean temperature and zonal wind RCP8.5 changes in MAM.



Zonal mean temperature (K) (left column) and zonal mean zonal wind ( $m/s$ ) (right column) RCP8.5 changes in MAM for: (a) and (b) Atlantic; (c) and (d) Indian; and (e) and (f) Pacific. Results are calculated as the difference of the WAMZ minus CTRL experiment for the period 2070-2099 over Southern Hemisphere oceans. Black line contours show HadGEM2-ES Historical climatology for the period 1976-2005.

SOURCE: Author's production.

Figure 5.36 - Zonal mean temperature and zonal wind RCP4.5 changes in MAM.



Zonal mean temperature (K) (left column) and zonal mean zonal wind ( $m/s$ ) (right column) RCP4.5 changes in MAM for: (a) and (b) Atlantic; (c) and (d) Indian; and (e) and (f) Pacific. Results are calculated as the difference of the WAMZ minus CTRL experiment for the period 2070-2099 over Southern Hemisphere oceans. Black line contours show HadGEM2-ES Historical climatology for the period 1976-2005.

SOURCE: Author's production.

### 5.1.3 Cyclone intensity changes

The cyclone intensity biases are calculated using the vorticity field at 850hPa for each HadGEM2-ES ensemble member individually and for the HadGEM2-ES average as the difference between the HadGEM2-ES experiments without Amazon Forest and with land use change fixed in 2005 (WAMZ–CTRL). The climatology period is 2070 to 2099 for both experiments. The HadGEM2-ES HIST cyclone count are shown to give a background of the future projected changes in relation to the past climate.

#### 5.1.3.1 Cyclone count

Results show that the number of cyclones identified for RCP8.5 and RCP4.5 respectively, shown in Tables 5.1 and 5.2, are fewer than in historical period in all seasons. The removal of the Amazon Forest for both the RCPs show that the future projected climate further reduces the number of cyclones in almost all seasons and these tendencies can be seen in both the scenarios, except in MAM where there is an increase in the number of cyclones per month. In general, the differences (WAMZ–CTRL) in numbers are relatively small and may be associated with two factors.

The removal of the Amazon Forest seems to be reflected in the atmosphere in several ways, as shown in Sections 5.1.1 and 5.1.2, however the count over all the southern hemisphere may be hiding regional variability. Also, some atmospheric small-scale processes may not be represented particularly well. Thus, the lower spatial resolution may also affect the representation of cyclones over the Southern Hemisphere. This hypothesis is also supported by the biases found in the comparison between HadGEM2-ES and ERA-Interim, as shown in the Chapter 4 - Section 4.2.3. Also, Willison et al. (2013) found that the spatial resolution impacts directly the diabatic heating in cyclone development. This may be hiding the impact of the Amazon Forest on the storm track count once there are large changes in the tropical region and some of those may not be acting over the extratropical regions.

Second, the increase of the SST during the summer season associated with the large thermal inertia of the oceans may also contribute to the increases during the autumn season (MAM). Also, it may contribute to the earlier appearance of the split jet (see Figures 5.35 and 5.36, right side) that generally occurs during the winter season, as shown in Chapter 4 - Section 4.2.2.1. Therefore, these features partially contribute to the projected changes of the number of cyclones over the Southern Hemisphere.

Table 5.1 - Number of cyclones per month for each season in HadGEM2-ES experiments that are found in the SH extratropics (90°S,20°S) for all seasons in RCP8.5 scenario. The period for WAMZ and CTRL experiments is 2070-2099 and for Historical experiment is 1976-2005. Abbreviations: EM, Ensemble Member.

Experiment	JJA	SON	DJF	MAM
HIST	131.1	122.6	108.6	122.1
WAMZ EM 1	125.6	118.1	105.7	118.4
WAMZ EM 2	125.0	117.8	105.4	118.6
WAMZ EM 3	125.4	118.9	106.6	117.7
WAMZ EM 4	124.9	117.5	104.3	120.1
CTRL EM 1	125.8	119.6	107.3	117.7
CTRL EM 2	126.5	117.8	105.9	118.6
CTRL EM 3	125.9	119.0	105.5	117.5
CTRL EM 4	125.4	117.8	106.3	117.0
WAMZ	125.3	118.1	105.5	118.7
CTRL	125.9	118.5	106.3	117.7
Differences	-0.6	-0.4	-0.8	1.0

SOURCE: Author's production.

Table 5.2 - Number of cyclones per month for each season in HadGEM2-ES experiments that are found in the SH extratropics (90°S,20°S) for all seasons in RCP4.5 scenario. The period for WAMZ and CTRL experiments is 2070-2099 and for Historical experiment is 1976-2005. Abbreviations: EM, Ensemble Member.

Experiment	JJA	SON	DJF	MAM
HIST	131.1	122.6	108.6	122.1
WAMZ EM 1	125.8	117.6	105.2	118.5
WAMZ EM 2	125.2	118.5	106.4	119.0
WAMZ EM 3	124.3	118.3	105.2	119.0
WAMZ EM 4	125.8	119.2	105.4	117.7
CTRL EM 1	125.8	118.8	106.9	118.8
CTRL EM 2	126.3	118.3	105.4	117.1
CTRL EM 3	125.6	118.6	106.1	117.4
CTRL EM 4	124.7	118.9	106.8	117.6
WAMZ	125.3	118.4	105.5	118.5
CTRL	125.7	118.7	106.3	117.7
Differences	-0.4	-0.3	-0.8	0.8

SOURCE: Author's production.

### 5.1.3.2 Maximum intensity distribution

In general, the intensity distribution changes are relatively similar across all of the seasons, although there are small differences in the maximums and the total number of storms between the seasons. The maximum relative vorticity distribution comparison for RCP8.5 and RCP4.5 with the Historical experiment shows that there are fewer storms in the low-medium intensity range and more high-intensity storms ( $< -10 \times 10^{-5} s^{-1}$ ). Recent studies such as Chang (2017), highlight that the extreme storms increase in CMIP5 models under the RCP8.5 scenario. Also, the weakest intensity storms have a very small increase in all seasons for both the scenarios and experiments. As the distributions are very similar, a nonparametric method such as Kolmogorov-Smirnov ( $KS$ ) test is performed to test when and if the intensity distributions are statistically different, as shown in the Tables 5.3 and 5.4. This is similar to that applied by Hodges et al. (2011) to test the small differences between reanalysis datasets. This method tends to have less statistical power than parametric methods (e.g. Student's t-test), but do not depend on any distributional assumptions. For more detail about the method, see Chapter 3 - Section 3.4.3.

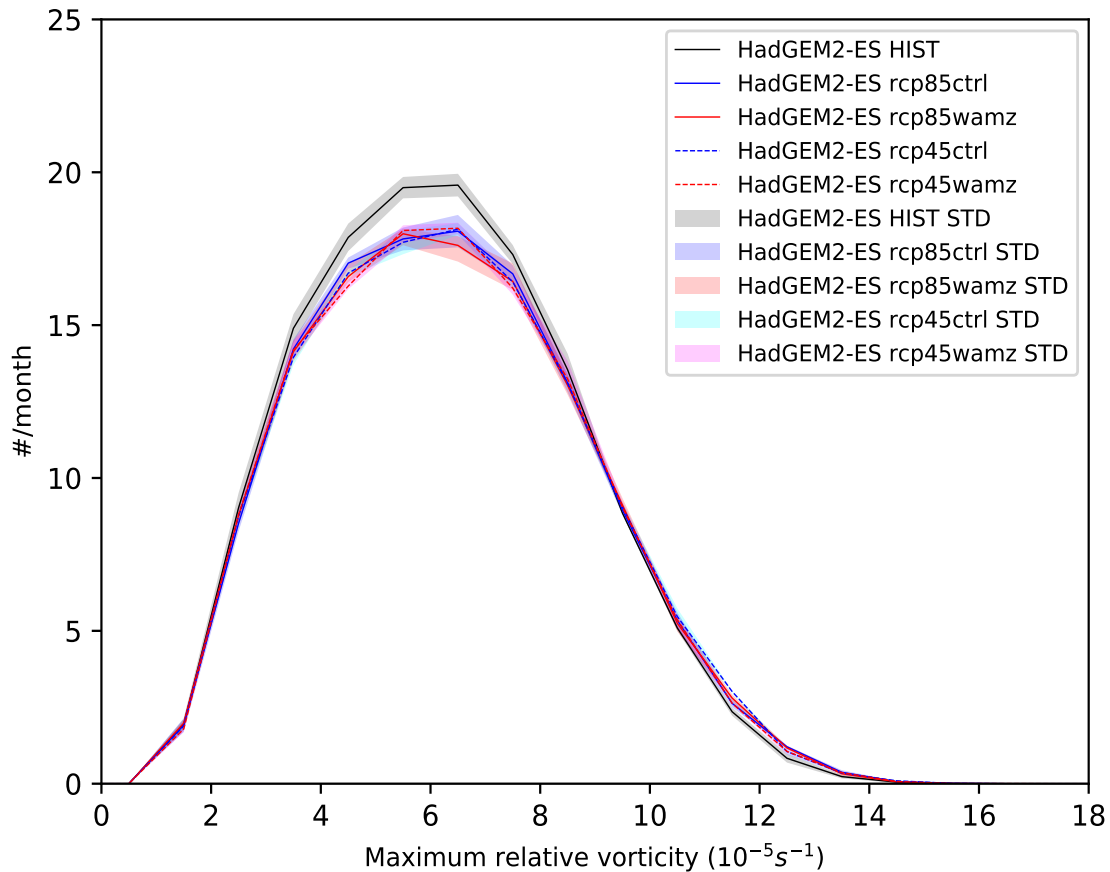
The austral winter maximum intensity distribution for future projected changes are shown Figure 5.37. The changes show the highest number and intensity of cyclones during the winter season, which the RCP4.5 WAMZ climatology (dashed red line) have larger magnitude and the maximum number of cyclones is 18.40 per month for cyclones with vorticity of  $-6.5 \times 10^{-5} s^{-1}$ . The maximum standard deviation also occurs for this distribution with 0.60 cyclones per month. These results are consistent with those shown in Chapter 4 (Section 4.2.3.2) where the highest number and intensity of cyclones were also found in the winter season.

The HADGEM2-ES CTRL experiments for both the RCPs (Figure 5.37, blue solid and dashed lines) in general tend to represent more storms during the winter season, including the shift to stronger intensity values. This indicates that the removal of Amazon Forest (WAMZ experiments) reduces the number of storms over the Southern Hemisphere during the winter season as also shown in Tables 5.1 and 5.2. However, the WAMZ experiments (Figure 5.37, red solid and dashed lines) seem to increase the medium (between  $-6.5$  and  $-7.5 \times 10^{-5} s^{-1}$ ) and very high ( $> -13 \times 10^{-5} s^{-1}$ ) intensity storms for both the RCPs. Considering all of distribution, the standard deviation is approximately 2 times larger for WAMZ experiments.

The  $KS D$  statistics (Tabs. 5.3 and 5.4) during the austral winter correspond with the results found in the previous sections (5.1 and 5.1.2). The comparison WAMZ

minus the Historical (WAMZ–HIST) shows that the WAMZ experiment tends to represent less storms in the RCP8.5 (Tab. 5.3, left side) and the percentage of ensemble members with  $D > 0.05$  is 25%, thus this mean that only an EM has  $D$  statistics greater than 0.05 (Tab. 5.3, right side). The difference is also observed for CTRL minus the Historical experiment (CTRL–HIST) in this scenario (Tab. 5.3, JJA), however the difference is statistically greater (almost two times). These difference patterns for WAMZ–HIST and CTRL–HIST are also observed under the RCP4.5 scenario (Tab. 5.4, left side), however they are greater and the ensemble members agrees more between them (Tab. 5.4, right side).

Figure 5.37 - Maximum intensity distribution for JJA during the period 2070-2099.



Maximum intensity distribution based on 850hPa relative vorticity for winter over SH ( $90^{\circ}\text{S} - 20^{\circ}\text{S}$ ). Values are number per month for the period 2070-2099 for the HadGEM2-ES experiments for RCP8.5 and RCP4.5 scenarios. Standard deviation of climatology across the each 4 HadGEM2-ES EMs are represented by light grey (HIST), light blue/cyan (CTRL) and light red/magenta (WAMZ) shading. The vorticity is scaled by  $-1$  and the bin widths are  $1 \times 10^{-5} \text{ s}^{-1}$ .

SOURCE: Author's production.

Table 5.3 - Kolmogorov-Smirnov statistical test for the RCP8.5 experiments in comparison to the Historical experiment and between them. Each experiment comparison shows the Kolmogorov-Smirnov statistic ( $D$ ) for intensity distributions of the relative vorticity in the Southern Hemisphere for the respective seasons (top side); and the percentage of individual HadGEM2-ES ensemble member in a likewise experiment comparison for each member. The period for WAMZ and CTRL experiments is 2070-2099 and for Historical experiment is 1976-2005. Abbreviations: EM, Ensemble Member.

		HadGEM2-ES Ensemble Mean				% of EM where $D > 0.05$			
		JJA	SON	DJF	MAM	JJA	SON	DJF	MAM
WAMZ-HIST	$D$	0.05682	0.05682	0.05682	0.12500	25%	25%	25%	100%
	$p$	0.99999	0.99999	0.99999	0.98393	-	-	-	-
CTRL-HIST	$D$	0.09091	0.12500	0.06818	0.14773	100%	100%	50%	100%
	$p$	0.99997	0.94987	0.99998	0.93918	-	-	-	-
WAMZ-CTRL	$D$	0.05682	0.05682	0.05682	0.09091	25%	25%	25%	75%
	$p$	0.99999	0.99999	0.99999	0.99463	-	-	-	-

SOURCE: Author's production.

Table 5.4 - Kolmogorov-Smirnov statistical test for the RCP4.5 experiments in comparison to the Historical experiment and between them. Each experiment comparison shows the Kolmogorov-Smirnov statistic ( $D$ ) for intensity distributions of the relative vorticity in the Southern Hemisphere for the respective seasons (top side); and the percentage of individual HadGEM2-ES ensemble member in a likewise experiment comparison for each member. The period for WAMZ and CTRL experiments is 2070-2099 and for Historical experiment is 1976-2005. Abbreviations: EM, Ensemble Member.

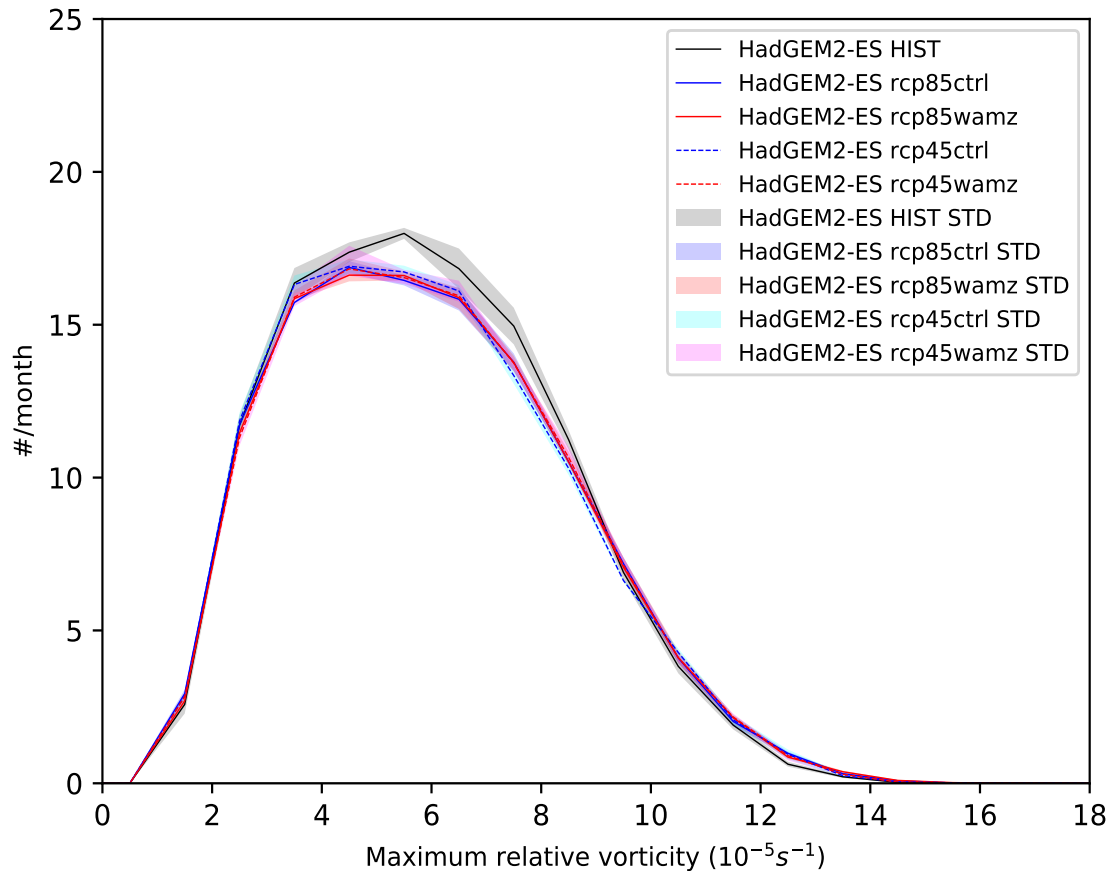
		HadGEM2-ES Ensemble Mean				% of EM where $D > 0.05$			
		JJA	SON	DJF	MAM	JJA	SON	DJF	MAM
WAMZ-HIST	$D$	0.07955	0.09091	0.06818	0.12500	75%	75%	50%	100%
	$p$	0.99998	0.99463	0.99998	0.98393	-	-	-	-
CTRL-HIST	$D$	0.11364	0.12500	0.07955	0.13636	100%	75%	75%	100%
	$p$	0.98927	0.91047	0.99998	0.97858	-	-	-	-
WAMZ-CTRL	$D$	0.07955	0.09091	0.06818	0.11364	75%	75%	50%	75%
	$p$	0.99998	0.99463	0.99998	0.98393	-	-	-	-

SOURCE: Author's production.

The spring maximum intensity distributions are shown in Figure 5.38. In general, the spring season distributions are very similar those in the winter season, but with fewer cyclones during the peak of the season for relative vorticity  $-6.0 \times 10^{-5} s^{-1}$ . Also, the peak distribution of storms is lower than historical period (Figure 5.38, solid black line). The RCP4.5 CTRL (Figure 5.38, dashed blue line) simulates more storms of all the experiments, however the RCP8.5 WAMZ simulates fewer storms. This pattern of fewer storms under the RCP8.5 scenario is also present during the spring season, however the removal of the Amazon Forest has the smallest impact of all seasons over the SH storm tracks, as shown in Table 5.1 and 5.2). The differences (WAMZ–CTRL) are the smallest in this season, which correspond with the spring baroclinicity at lower levels (850hPa) small changes discussed in the results (Section 4.2.2.3). The model also tends to decrease the intensity of future projected cyclones and the distribution being shifted for fewer number of storms. The maximum STD is 0.75 cyclones per month under RCP4.5 WAMZ for this distribution, the largest of all seasons.

The *KS D* statistic (Tabs. 5.3 and 5.4) during spring is similar to the winter season, however the *D* statistic increases and the *p* values decrease for the comparison CTRL–HIST, evidencing that the distributions are little different. The *p* values are high and do not suggest that then null hypothesis can be rejected. These results were expected for *KS D* statistics, which means that relatively high values of *D* results in smaller *p* values. However, these results will be explored in a further journal publication.

Figure 5.38 - Maximum intensity distribution for SON during the period 2070-2099.



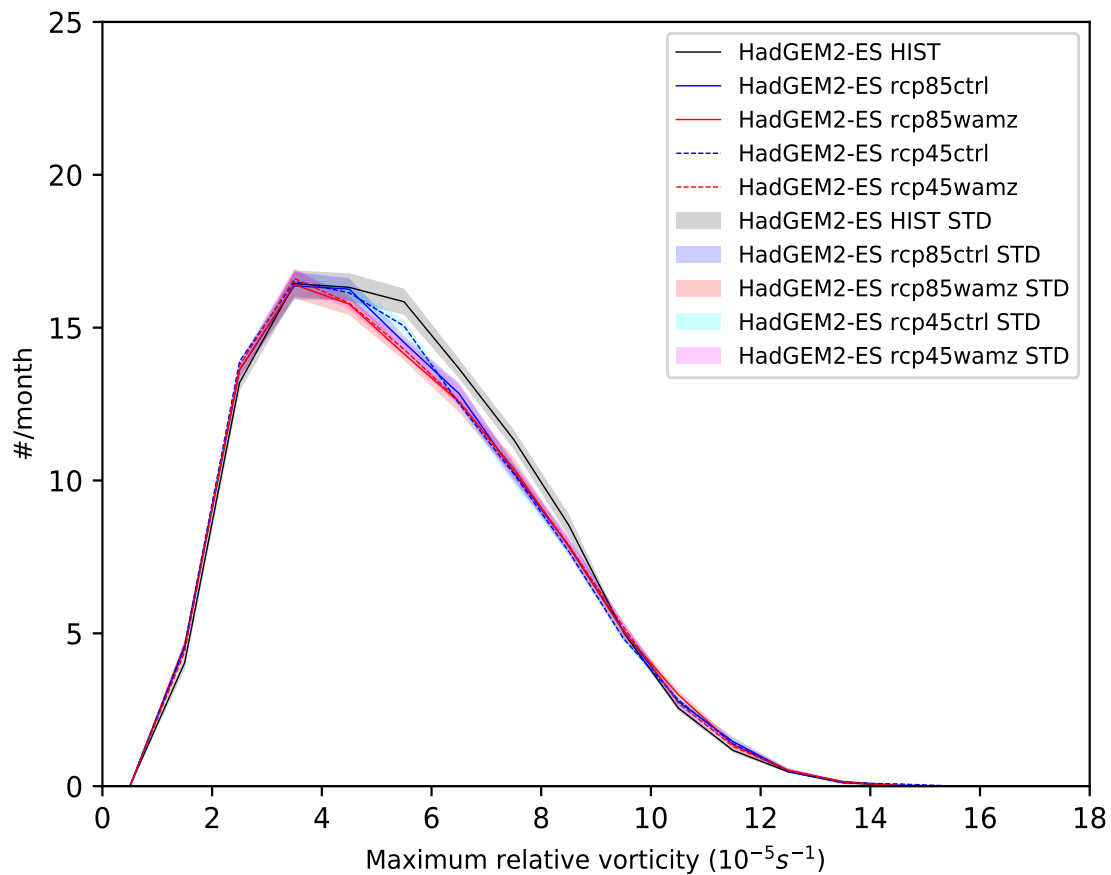
Maximum intensity distribution based on 850hPa relative vorticity for spring over SH ( $90^{\circ}\text{S} - 20^{\circ}\text{S}$ ). Values are number per month for the period 2070-2099 for the HadGEM2-ES experiments for RCP8.5 and RCP4.5 scenarios. Standard deviation of climatology across the each 4 HadGEM2-ES EMs are represented by light grey (HIST), light blue/cyan (CTRL) and light red/magenta (WAMZ) shading. The vorticity is scaled by -1 and the bin widths are  $1 \times 10^{-5} \text{ s}^{-1}$ .

SOURCE: Author's production.

The summer season intensity distributions for future projections (Figure 5.39) are narrower and weaker than other seasons, however decrease of cyclones per month is the largest of all seasons. The RCP4.5 distribution shows a slight increase of the storms for intensities between  $-3$  and  $-4 \times 10^{-5} \text{ s}^{-1}$  for the WAMZ and CTRL experiments in relation to the Historical climatology (Figure 5.39, black solid line). The RCP8.5 distribution for this intensity intervals are also near to the maximum intensity for the Historical experiment. This result corresponds with the future projected changes found for the storm track densities (Section 5.1.1.2) and large-scale (Section 5.1.2.2). Similar to the winter season, the maximum standard deviation

can be seen for WAMZ experiments are 0.53 and 0.46 cyclones per month under RCP4.5 and RCP8.5 scenario, respectively. The *KS D* statistic (Tabs. 5.3 and 5.4) during summer is also similar to the winter and spring seasons, but the comparison WAMZ–CTRL for RCP4.5 scenario has the smallest ensemble member agreement (50%) of all seasons (Tab. 5.4, right side).

Figure 5.39 - Maximum intensity distribution for DJF during the period 2070-2099.



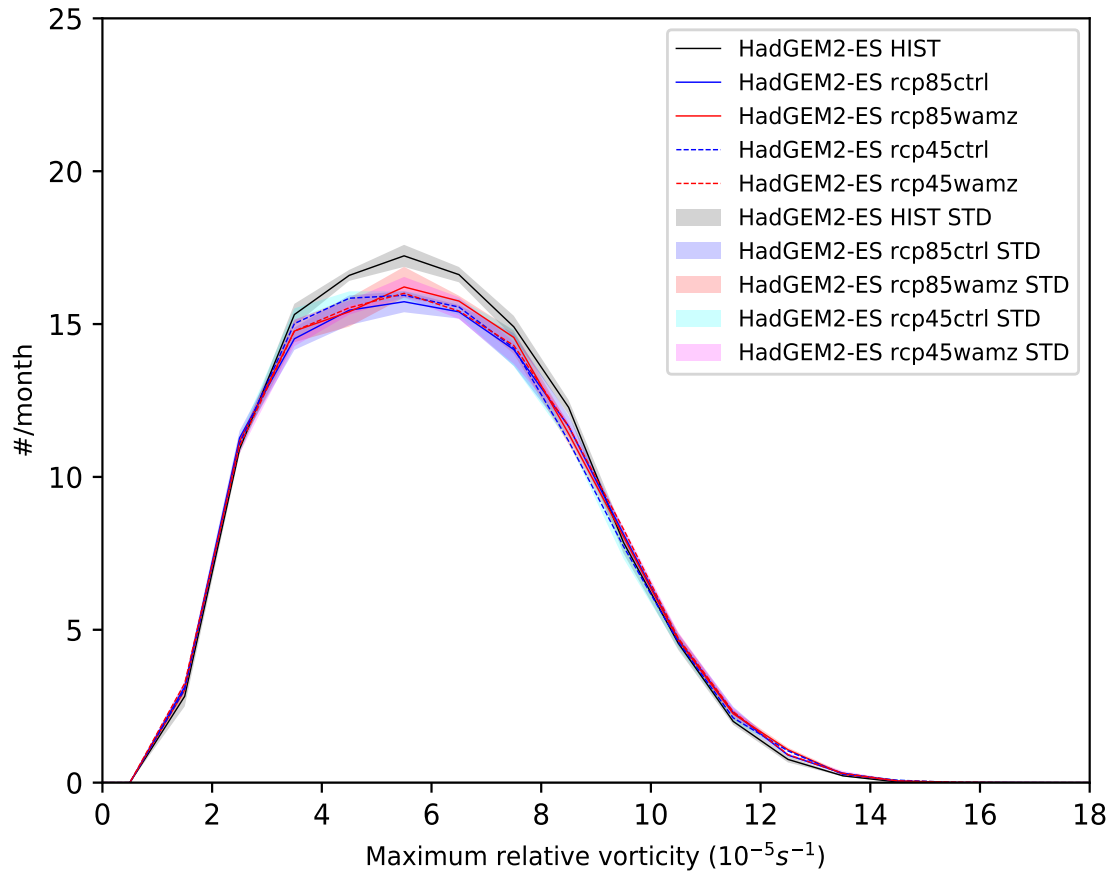
Maximum intensity distribution based on 850hPa relative vorticity for summer over SH (90°S - 20°S). Values are number per month for the period 2070-2099 for the HadGEM2-ES experiments for RCP8.5 and RCP4.5 scenarios. Standard deviation of climatology across the each 4 HadGEM2-ES EMs are represented by light grey (HIST), light blue/cyan (CTRL) and light red/magenta (WAMZ) shading. The vorticity is scaled by -1 and the bin widths are  $1 \times 10^{-5} s^{-1}$ .

SOURCE: Author's production.

In contrast with the spring season, the projected changes in autumn (Figure 5.40) have the largest cyclone differences and is the unique season where there is storm increase compared to the other seasons, as shown in Tables 5.1 and 5.2). These results correspond well with the increases shown in the storm track density (Section 5.1.1.3) and large-scale (Section 4.2.2.3) changes for both the RCP scenarios. Also, these changes are also similar to the summer intensity distribution changes. The maximum standard deviation is 0.66 cyclones per month for the RCP8.5 WAMZ distribution, which is similar to the spring season.

The  $KS$   $D$  statistic (Tabs. 5.3 and 5.4) during the autumn season has the statistically largest differences for the comparisons in all seasons, which correspond very well with the changes shown in the Sections 5.1.1.3 and 5.1.2.3. In general the differences are two times more than those in the preceding season (DJF) and the ensemble members agrees with them (100%) for the comparisons WAMZ–HIST and CTRL–HIST in both the scenarios (Tabs. 5.3 and 5.4, right side). For the comparison RCP8.5 WAMZ–CTRL (Tab. 5.3, right side), this is the period when the model ensemble members agreement is largest (75%) of all seasons in this scenario. Also, there is a  $D$  statistic increase and the  $p$  values decrease for the comparison CTRL–HIST in both the scenarios, which is similar to the spring season and evidences that the distributions are little different. As discussed previously, these  $p$  values results will be explored in a further journal publication. These results fit with the storm track changes shown for the WAMZ experiments in relation to the CTRL experiments in both the RCPs, which have the largest changes during the autumn season.

Figure 5.40 - Maximum intensity distribution for MAM during the period 2070-2099.



Maximum intensity distribution based on 850hPa relative vorticity for autumn over SH (90°S - 20°S). Values are number per month for the period 2070-2099 for the HadGEM2-ES experiments for RCP8.5 and RCP4.5 scenarios. Standard deviation of climatology across the each 4 HadGEM2-ES EMs are represented by light grey (HIST), light blue/cyan (CTRL) and light red/magenta (WAMZ) shading. The vorticity is scaled by -1 and the bin widths are  $1 \times 10^{-5} s^{-1}$ .

SOURCE: Author's production.

#### 5.1.4 Regional-scale changes

This section focuses on the regional-scale changes over South America and adjacent oceans. The novelty in the presented research is not in having advanced terrestrial surface analysis (e.g. land carbon, vegetation), it is in the comprehensiveness of the study about how the changes in land use alter the future projected climate.

The regional-scale changes are calculated for each HadGEM2-ES ensemble member individually and for the HadGEM2-ES ensemble member mean, referred to as HadGEM2-ES, but only the differences between the Without Amazon Forest minus Control (WAMZ–CTRL) experiment in each RCP scenario is shown for brevity. The fields are presented for all seasons in the same figure to show the annual variability. The main climatological patterns over SA for the historical period are described in Chapter 2 - Section 2.2.2.3 - and for a CMIP5 multi-model perspective in Torres (2014).

##### 5.1.4.1 Winter

The differences between the WAZM and CTRL experiments for skin temperature for both the RCPs in all seasons are shown in Figures 5.41 and 5.42. This field represents the surface temperature over the oceans (SST) and the surface temperature over the continents as explained previously. In general the skin temperature during the winter season decreases in the RCP8.5 scenario (Figure 5.41a), however this contrasts with temperature increases in the RCP4.5 scenario (Figure 5.42a). For the RCP8.5 scenario the temperature decreases around 2°C over the region of the removal of the Amazon Forest, with the strongest reduction (−3°C) over the west of the Amazon (Acre State - Brazil). There are other areas of decrease areas over the north of Argentina and south of the Atlantic Ocean in extratropical latitudes. However, the temperature increases over the centre-south of Brazil towards the adjacent region of the Atlantic Ocean. There are other areas of increasing temperatures over the east of northeast of Brazil and the Northern Hemisphere (NH) Atlantic Ocean, which extends to the tropical Pacific Ocean. In the RCP4.5 scenario the temperature change has the same spatial pattern over the region of the Amazon Forest ( $\sim -2.0^\circ\text{C}$ ), where the region with the largest decrease is also found over the west of the Amazon ( $\sim -2.5^\circ\text{C}$ ). In addition, there is also a decrease in temperature over the Drake Passage. While the temperature decrease is similar to the RCP8.5 scenario, the area of temperature increase over the centre-south of Brazil is larger in the RCP4.5 scenario (Figure 5.42a) with the largest change is found on the border of Brazil-Bolivia. Also, there are other regions of increase peaks the centre and north-

east of Brazil and Pacific Ocean near to Peru. Therefore, these SST increases over the Pacific and Atlantic Oceans for both the RCPs, in particularly in RCP4.5, may affect the climate on different time scales such as interdecadal (ENSO (4-7 years)) and decadal (AMO and PDO (10 years)).

The novelty of this study, in terms of regional climate change, is the temperature decrease over the Amazon Forest in both the RCP scenarios when the Amazon Forest is removed, which contrasts with several previous studies. This hypothetical scenario of the removal of Amazon Forest was explored in previous studies for climate global and regional models such as Nobre et al. (1991), Foley and Costa (2000), Oyama and Nobre (2003), Sampaio et al. (2007), Alves (2016), Pitman and Lorenz (2016) and Alves et al. (2017). For more details about how the LUC affect the atmosphere, see Section 2.2.2.4.

Although previous studies are not comparable to the simulations used here due to the use of different model physics, features and configuration, there are some features of the HadGEM2-ES model that may explain this difference as follows:

- The terrestrial ecosystems and hydrology, are tightly coupled in HadGEM2-ES;
- The surface roughness, impacts directly the wind near the surface and the climate (SUD et al., 1988);
- The feedback mechanisms, HadGEM2-ES was designed to be responsive to these.

The precipitation changes (WAMZ–CTRL) are shown in Figures 5.43 and 5.44 for each RCP scenario in all seasons. The winter precipitation in RCP8.5 decreases from the ITCZ region, through to the Amazon Forest region toward the southeast of SA, to the Atlantic Ocean at a latitude of  $\sim 30^\circ\text{S}$  (Figure 5.43a). Contrasting with this area, precipitation increases over tropical latitudes ( $\sim 10^\circ\text{N}$ ) from the Atlantic toward the Pacific Ocean. Other small areas of increase are observed in the Pacific and Atlantic Oceans at a latitude of  $40^\circ\text{S}$ . Although the spatial precipitation patterns for RCP4.5 are similar to those of RCP8.5. The areas of precipitation change are smaller for RCP 4.5 over the ITCZ region with overall less changes for RCP4.5. In addition, there is a precipitation increase over Central America (Figure 5.44a) that contrasts with the RCP8.5 scenario (Figure 5.43a). The precipitation decrease for

the experiments without the Amazon Forest correspond to previous studies such as Nobre et al. (1991), Sampaio et al. (2007) and Alves et al. (2017).

The outgoing longwave radiation change during the winter season for both the RCPs (Figures 5.45a and 5.45a) corresponds very well with the precipitation spatial patterns for each respective RCP scenario. The OLR decrease changes have been associated with more clouds (precipitation increase), while the OLR increase changes are related to less clouds (precipitation decrease).

The wind changes (WAMZ–CTRL) at 850hPa for the winter season are shown in Figures 5.43a and 5.44a for both the scenarios in all seasons. The wind intensities in the RCP8.5 scenario (shaded colours) increase mainly over the tropics ( $10^{\circ}\text{S} - 10^{\circ}\text{N}$ ) and extratropical ( $45 - 60^{\circ}\text{S}$ ) regions. The removal of the Amazon Forest decreases the roughness and increases the trade winds that flow from the South Atlantic toward the west of the normal forest region (latitudes of  $2 - 4^{\circ}\text{S}$ ). The wind at lower levels forks when at Andes Mountains (adjacent to mountain), which creates a local circulation. Moreover, the removal of the Amazon Forest enhances the natural anticyclonic circulation over the South Atlantic and the eastward wind in the extratropical latitudes ( $\sim 40^{\circ}\text{S}$ ). For the RCP4.5 scenario the wind change patterns are similar to those for the RCP8.5 scenario over the Amazon Forest region, however in general the winds have stronger intensities over the Pacific Ocean and weaker intensities over Atlantic Ocean.

The previous wind pattern gives a background to the winter maximum Eady growth rate shown in Figure 5.49a for RCP8.5 and 5.50a for RCP4.5. The baroclinic instability represents the growth of convection and links regions of cyclogenesis and cyclone growth rate with the large-scale environment. For the RCP8.5 scenario the baroclinicity increases from the south of the Amazon Forest toward the South Atlantic, with a maximum Eady growth rate change of around  $0.09 \text{ day}^{-1}$  over Mato Grosso and Rondônia State in Brazil (5.49a). However this field shows decreases over the extreme south of South America and adjacent oceans. The baroclinicity changes for RCP4.5 (5.50a) are similar to those for RCP8.5, but the area of increase area over the centre of SA is smaller and there are decreases over Argentina and Chile and increases adjacent to the Argentina coastline. These patterns correspond very well with the cyclone track changes (Figures 5.1e and f; 5.2e and f; 5.3e and f; and 5.4e and f) for each respective scenario observed mainly in latitudes below  $20^{\circ}\text{S}$  over the South America.

The winter relative humidity (RH) and omega at 850hPa changes (WAMZ–CTRL)

for both the RCPs are shown in Figures 5.41a and 5.42a. These fields relate the regions where there is lifting (negative omega, blue triangles) and humidity availability (positive RH, blue shaded) for the storm development. The RH changes are similar in both the RCPs, with larger RH increases observed over major parts of Brazil, Bolivia, northern of Paraguay and Peru towards the Tropical Pacific. This area of RH increase is higher in the RCP4.5 scenario. Moreover, omega decreases over the Tropical Atlantic and Pacific Oceans and extratropical regions, however this field tends to follow the position of the Subtropical Jet (Figures 5.21a and c, and Figures 5.22a and c) and is associated with regions of convection of South America. Thus, for RCP8.5 the region of omega decrease is displaced to the south ( $\sim 45^\circ\text{S}$ ) in relation to the RCP4.5 ( $\sim 30^\circ\text{S}$ ). The omega increase (Figures 5.41a and 5.42a, red triangles) is associated with the regions of subsidence (high pressure), which results in non-development of storms due to the less RH availability over the border of Amazon Forest and in the Atlantic Ocean.

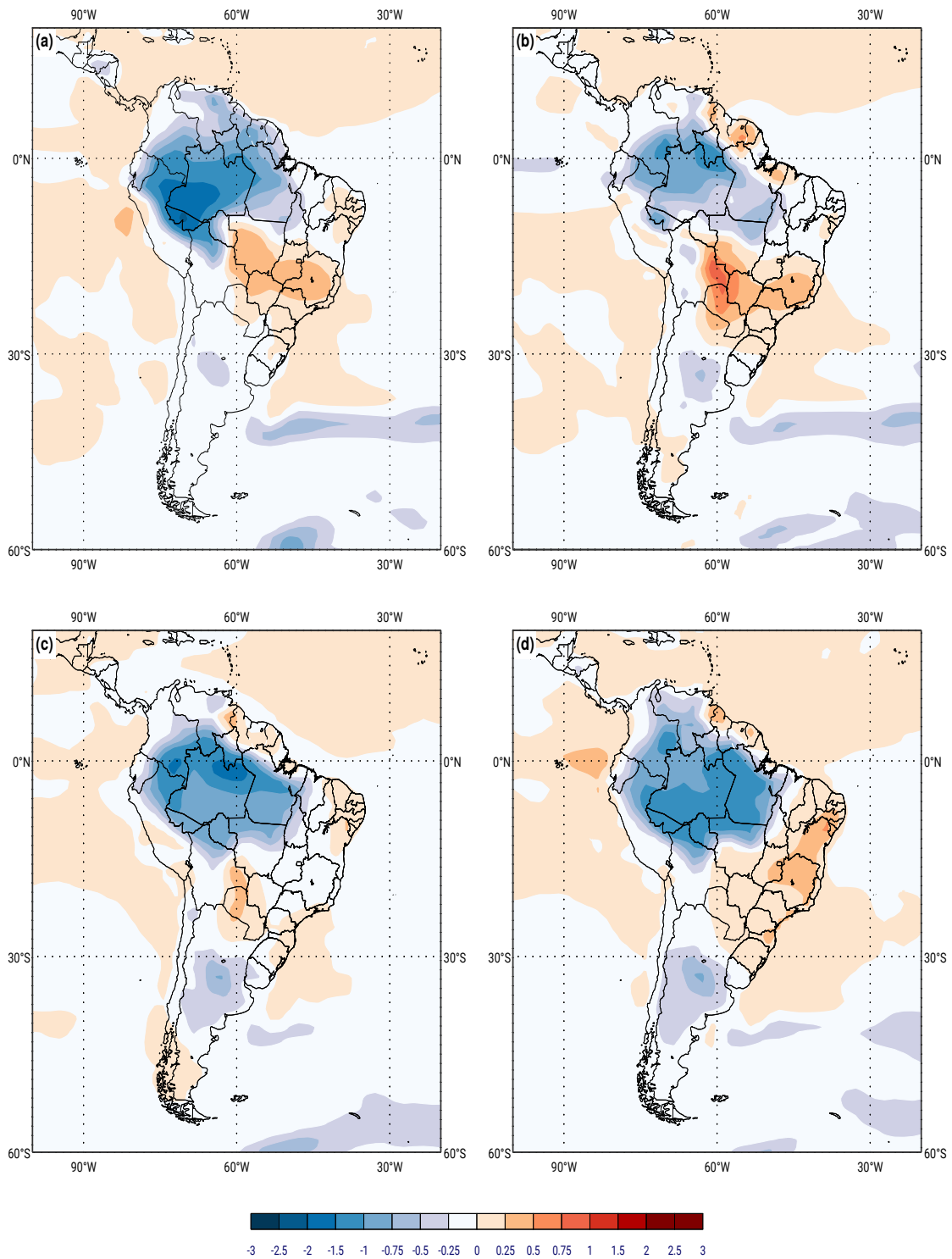
The surface latent heat (SLH) changes (WAMZ–CTRL) for RCP8.5 and RCP4.5 scenarios are shown in Figures 5.55a and 5.56a, respectively. The removal of the Amazon Forest for both the RCPs results in a decrease in the availability of SLH over the centre-north of SA with the strongest decrease occurring over the south and east of the normal Amazon Forest region. This seems associated with the northern position of the ITCZ during the austral winter. There is a tendency for latent heat increases around the region of large decrease, particularly over the Tropical Pacific and Atlantic Oceans. For the RCP8.5 (Figure 5.55a), there are more SLH changes over the extratropical region (between  $30 - 60^\circ\text{S}$ ) and the SLH increase (decrease) over the Atlantic Ocean (latitude of  $40^\circ\text{S}$ ) corresponding well with the ST density increase (decrease) (Figure 5.1e). However, the SLH for RCP4.5 (Figure 5.56a) decreases over the Tropical Atlantic (Cuba and Jamaica region) and the area of increase close to the northeast of Brazil seems displaced to the south in RCP4.5 in relation to the RCP8.5 changes.

In general the surface sensible heat (SSH) changes (WAMZ–CTRL) are concentrated over the SA in continental area and are shown in Figures 5.57a and 5.58a for the RCP8.5 and RCP4.5 scenarios. The removal of the Amazon Forest for RCP8.5 increases the SSH in the centre-north of SA, including the southeast of Brazil, with the largest increase found over the south and east of the Amazon Forest. There are other areas of increase over the Atlantic Ocean that is in the same location as the SLH changes at a latitude of  $40^\circ\text{S}$  and another region at approximately  $50^\circ\text{S}$ , which indicates that the cyclones may be stronger in these regions. This pattern

corresponds well with the RCP8.5 enhanced baroclinicity at 850hPa over the South Atlantic (Figure 5.49a). However, there are SSH RCP8.5 decreases over the band localized over the north of SA (between Suriname and Venezuela), Central America and in the Pacific Ocean adjacent to the extreme south of SA (60°S). The SSH RCP4.5 changes are similar to the RCP8.5 changes, but with smaller changes over the oceans and an increase over Central America.

Finally, the evaporation minus precipitation ( $E - P$ ) is shown in Figures 5.59a for RCP8.5 and 5.60a for RCP4.5. This relation is very important to climate change because over the ocean it affects the salinity of the mixed layer, while over continents it defines the sum of surface and subsurface runoff. Thus, the  $E - P$  represents the freshwater budget, or water balance, which the ideally should be close to 0 and negative (positive) values indicate less evaporation (more precipitation). In general the largest  $E - P$  changes occur over the continent. There is a decrease in evaporation in the Amazon Forest region in both the RCP scenarios (Figures 5.59a and 5.60a), particularly on the eastern side. Another region of decrease is found over the Tropical Atlantic at approximately 10°N, but this change only occurs for (WAMZ-CTRL) under RCP8.5. On the other hand, the  $E - P$  in both the RCPs increases over Colombia and the Equator and in the border area of Brazil-Bolivia. This corresponds well with the wind forks (Figures 5.43a and 5.44a), SSH (increase, Figures 5.55a and 5.56a), SLH (decrease, Figures 5.57a and 5.58a), OLR (decrease, Figures 5.45a and 5.46a), precipitation (Figures 5.43a and 5.44a) and temperature (Figures 5.41a and 5.42a) patterns found in this analysis. Therefore, this analysis leads to hypothesis that the feedback mechanisms are different from previous studies, since the climate response for temperature is opposite. This will be discussed in the concluding summary (Section 5.2).

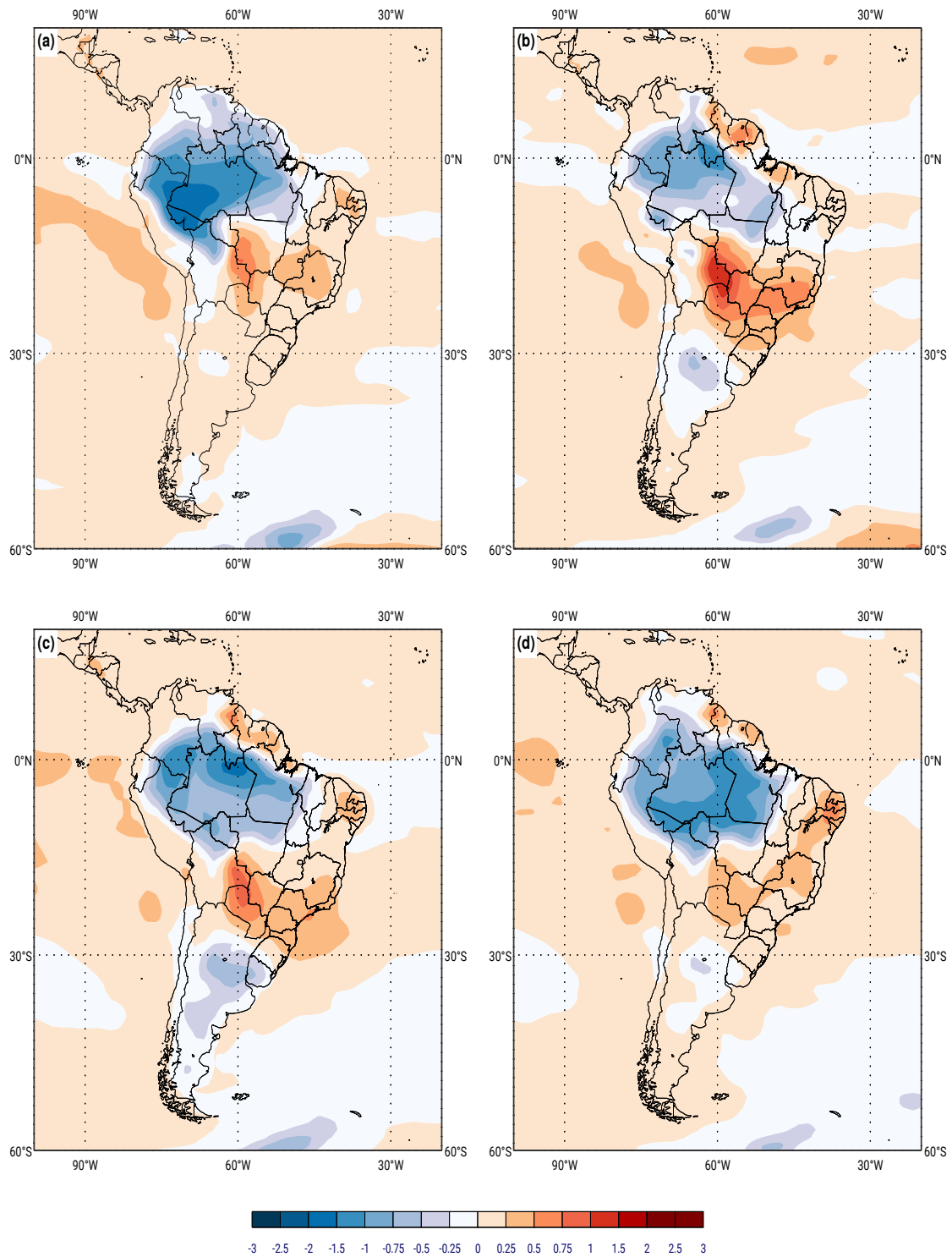
Figure 5.41 - Skin temperature RCP8.5 changes.



Skin temperature ( $^{\circ}C$ ) RCP8.5 changes (WAMZ–CTRL) for the period 2070-2099 over Southern Hemisphere: (a) JJA; (b) SON; (c) DJF; and (d) MAM. Black line contours show HadGEM2-ES Historical climatology for the period 1976-2005 and dashed contours indicate negative values.

SOURCE: Author's production.

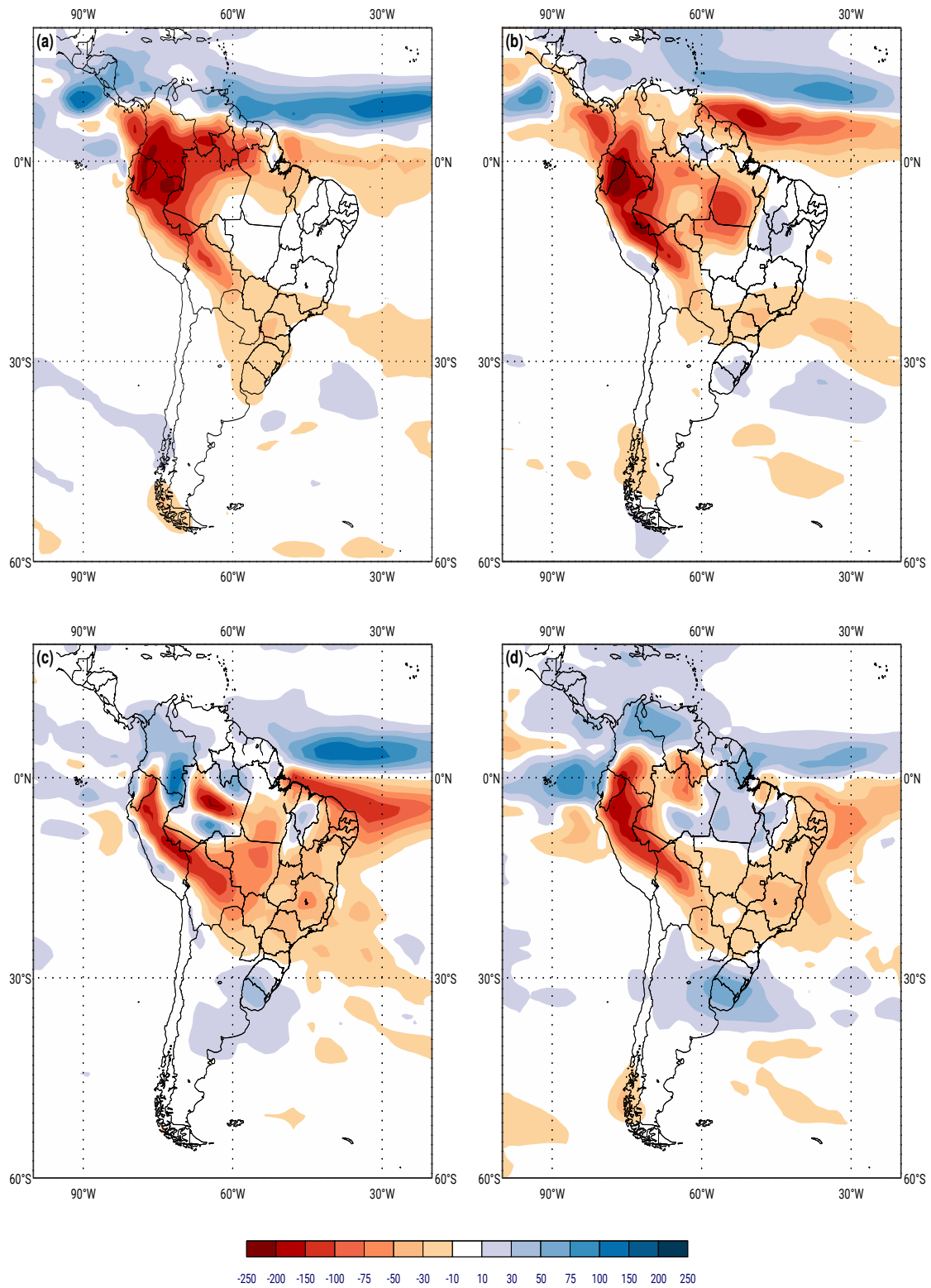
Figure 5.42 - Skin temperature RCP4.5 changes.



Skin temperature ( $^{\circ}\text{C}$ ) RCP4.5 changes (WAMZ–CTRL) for the period 2070-2099 over Southern Hemisphere: (a) JJA; (b) SON; (c) DJF; and (d) MAM. Black line contours show HadGEM2-ES Historical climatology for the period 1976-2005 and dashed contours indicate negative values.

SOURCE: Author's production.

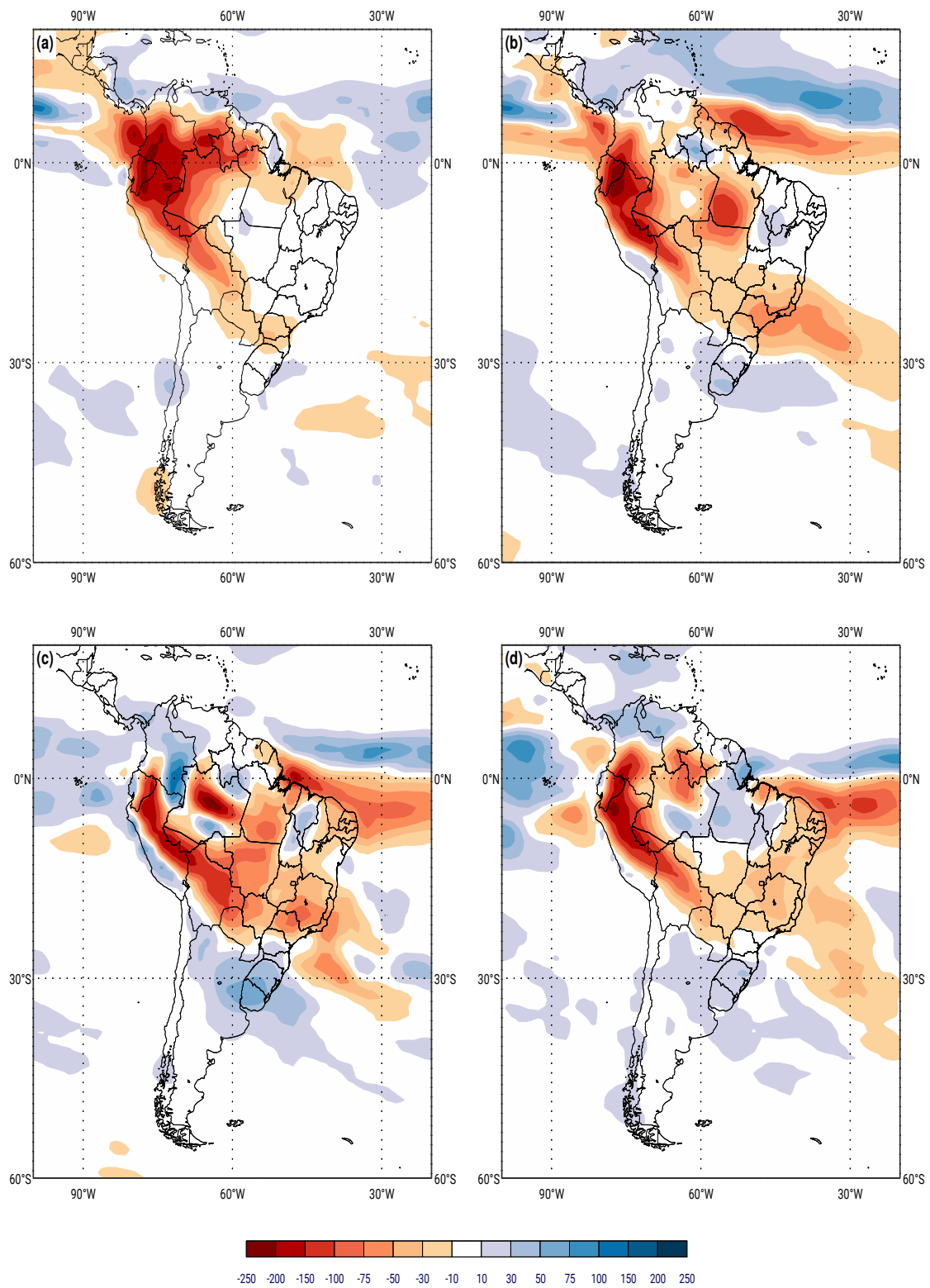
Figure 5.43 - Precipitation RCP8.5 changes.



Precipitation (mm/season) RCP8.5 changes (WAMZ-CTRL) for the period 2070-2099 over Southern Hemisphere: (a) JJA; (b) SON; (c) DJF; and (d) MAM.

SOURCE: Author's production.

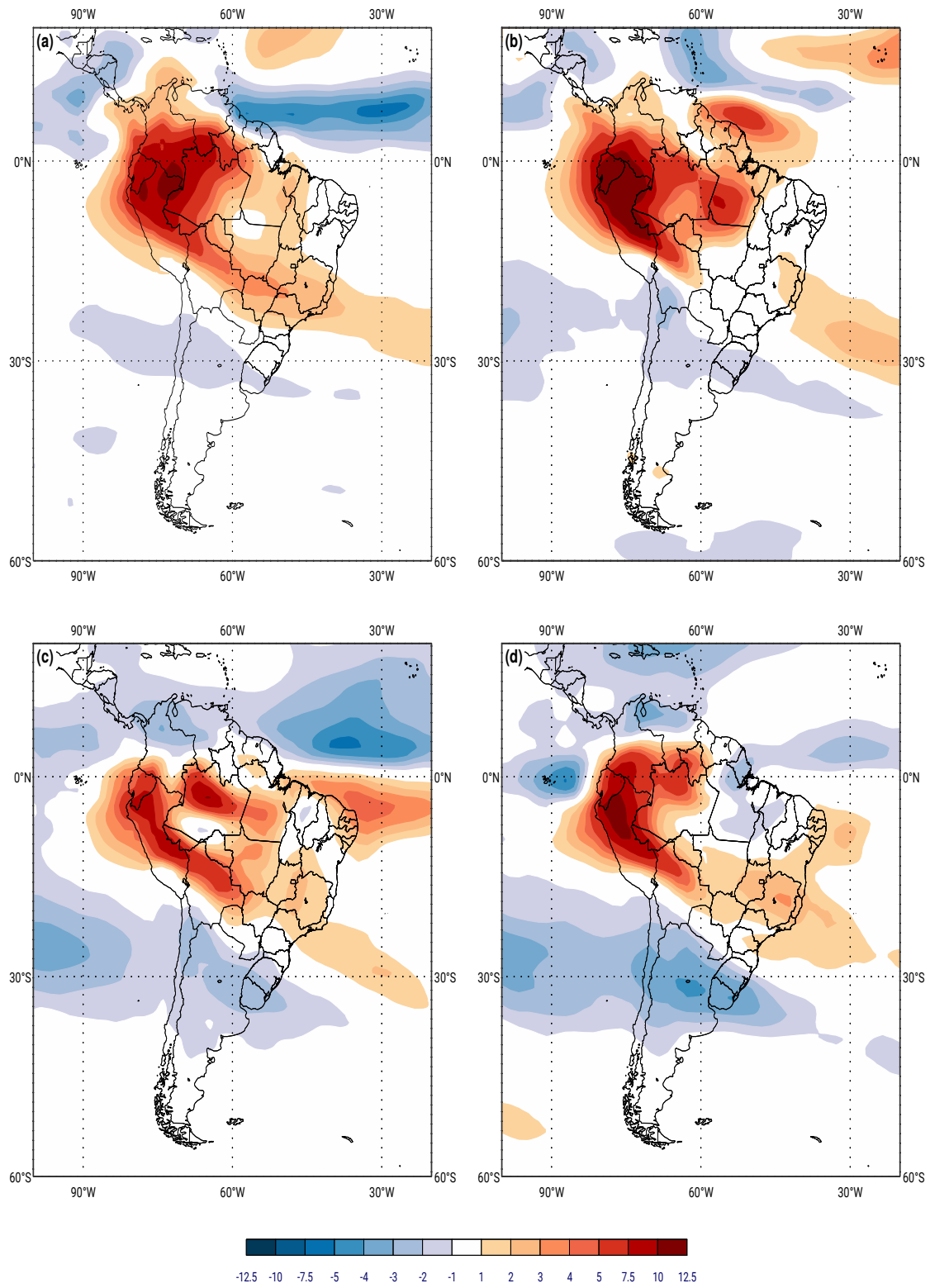
Figure 5.44 - Precipitation RCP4.5 changes.



Precipitation (mm/season) RCP4.5 changes (WAMZ-CTRL) for the period 2070-2099 over Southern Hemisphere: (a) JJA; (b) SON; (c) DJF; and (d) MAM.

SOURCE: Author's production.

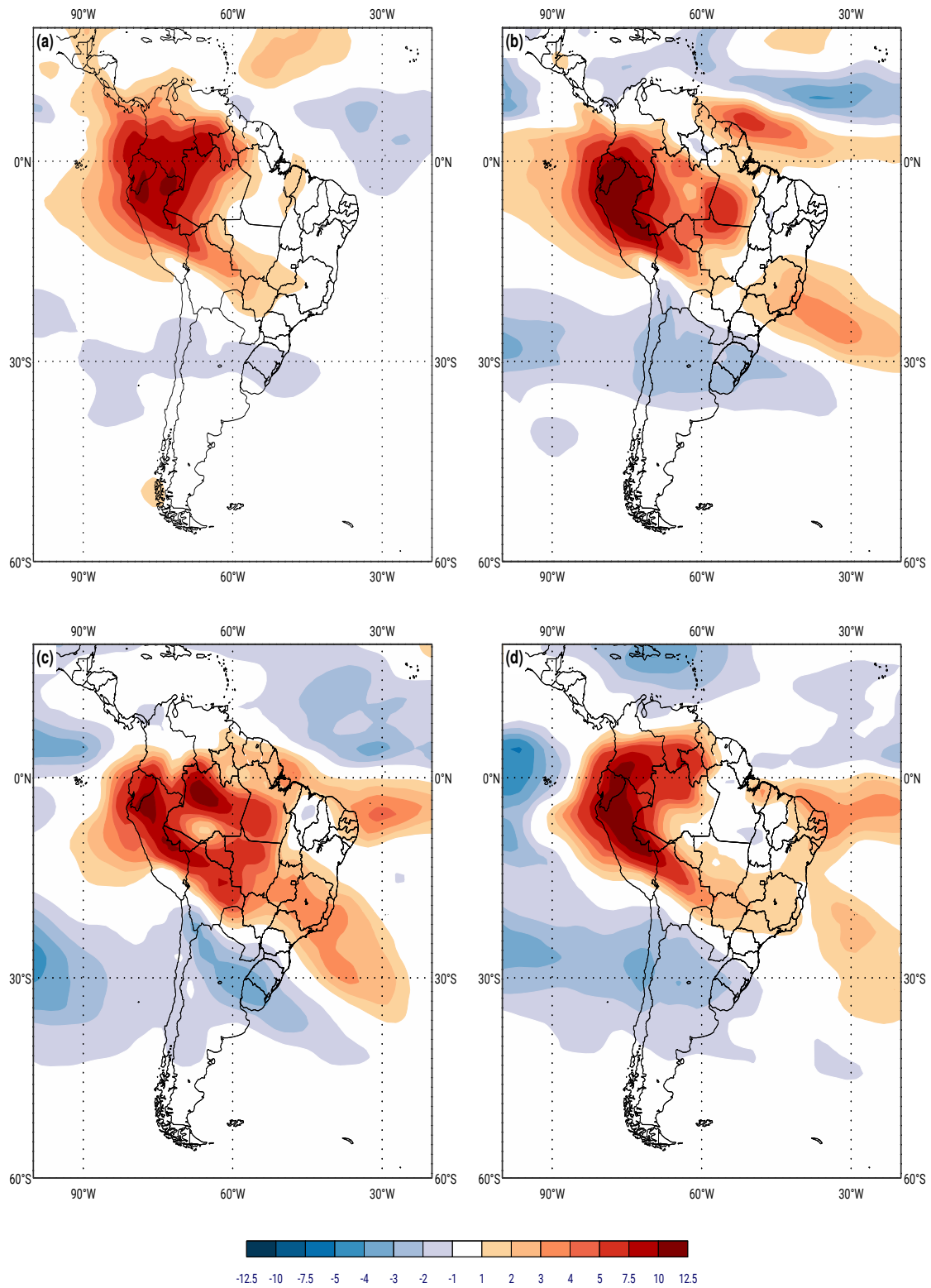
Figure 5.45 - Outgoing longwave radiation RCP8.5 changes.



Outgoing longwave radiation ( $Wm^{-2}$ ) RCP8.5 changes (WAMZ-CTRL) for the period 2070-2099 over Southern Hemisphere: (a) JJA; (b) SON; (c) DJF; and (d) MAM.

SOURCE: Author's production.

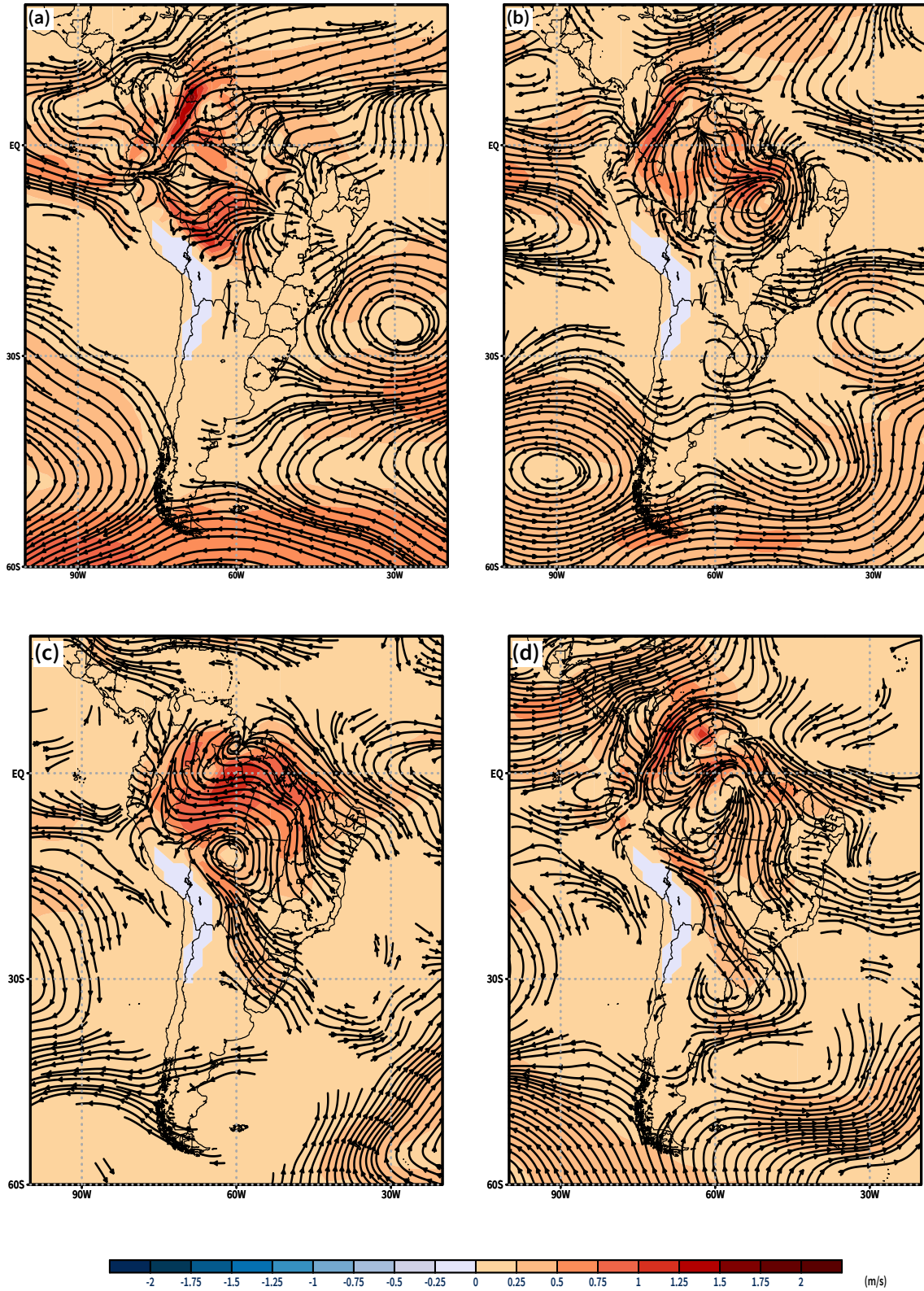
Figure 5.46 - Outgoing longwave radiation RCP4.5 changes.



Outgoing longwave radiation ( $Wm^{-2}$ ) RCP4.5 changes (WAMZ-CTRL) for the period 2070-2099 over Southern Hemisphere: (a) JJA; (b) SON; (c) DJF; and (d) MAM.

SOURCE: Author's production.

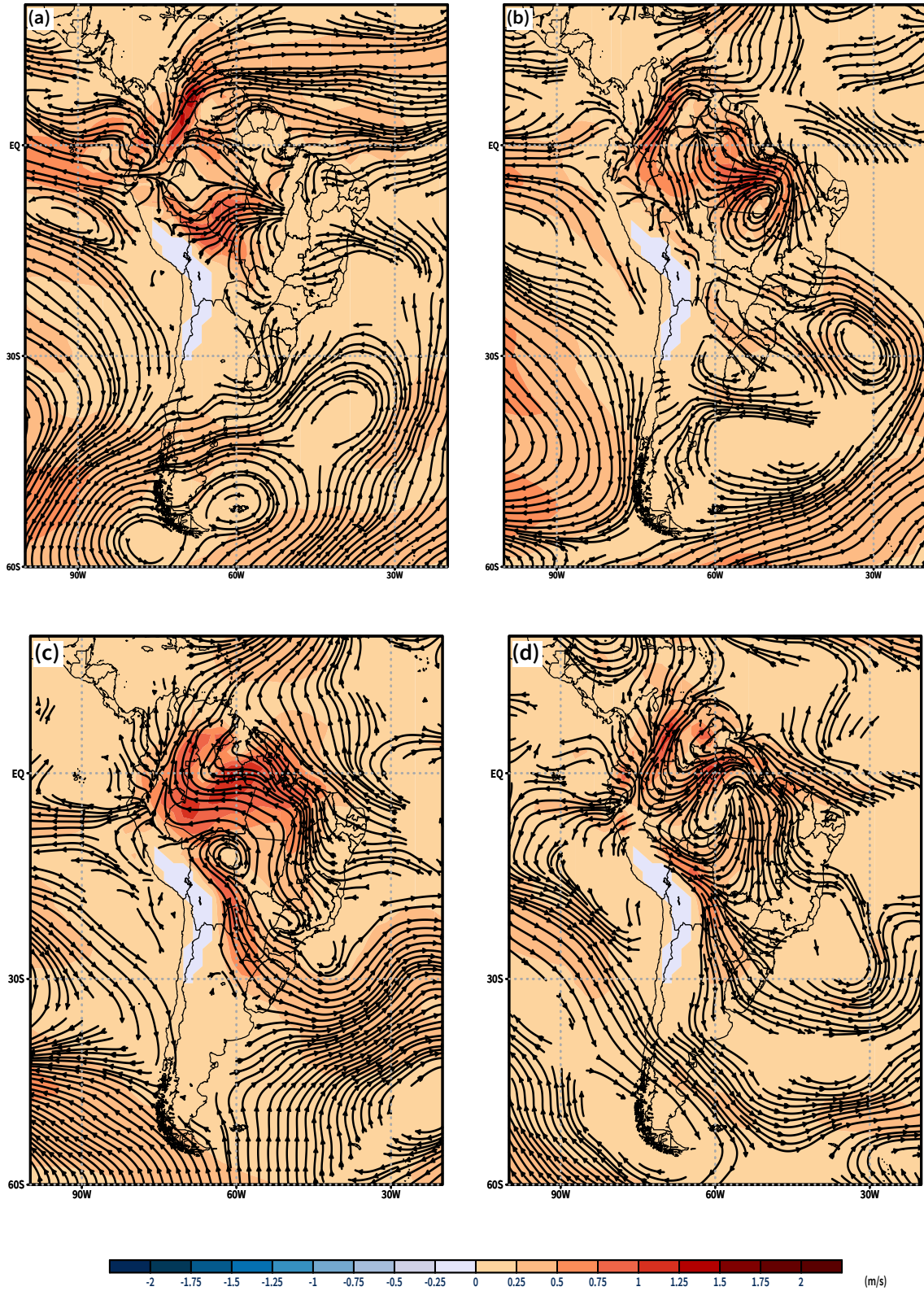
Figure 5.47 - Wind RCP8.5 changes at 850hPa.



Wind ( $m/s$ ) RCP8.5 changes (WAMZ-CTRL) for the period 2070-2099 over Southern Hemisphere: (a) JJA; (b) SON; (c) DJF; and (d) MAM.

SOURCE: Author's production.

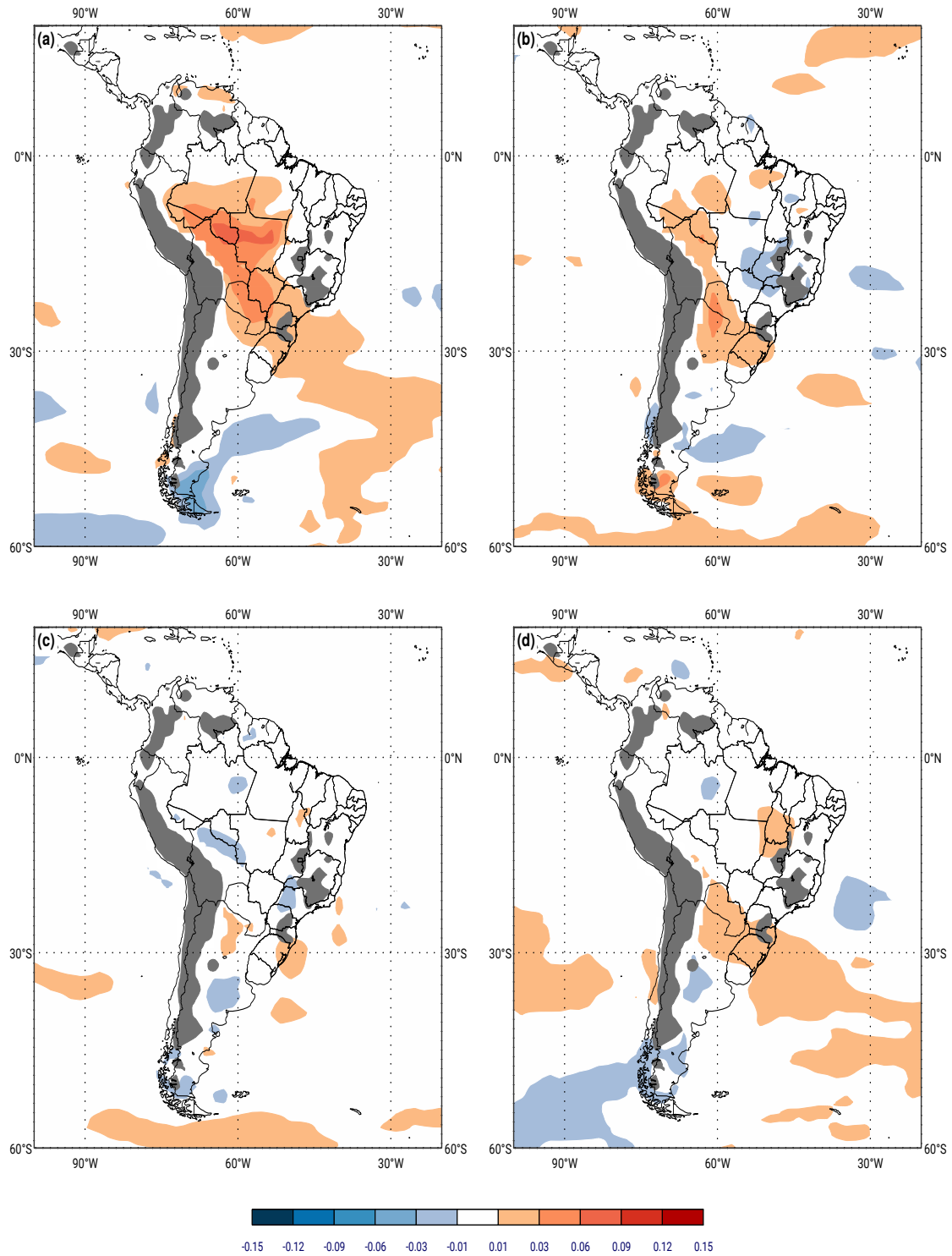
Figure 5.48 - Wind RCP4.5 changes at 850hPa.



Wind ( $m/s$ ) RCP4.5 changes (WAMZ–CTRL) for the period 2070–2099 over Southern Hemisphere: (a) JJA; (b) SON; (c) DJF; and (d) MAM.

SOURCE: Author's production.

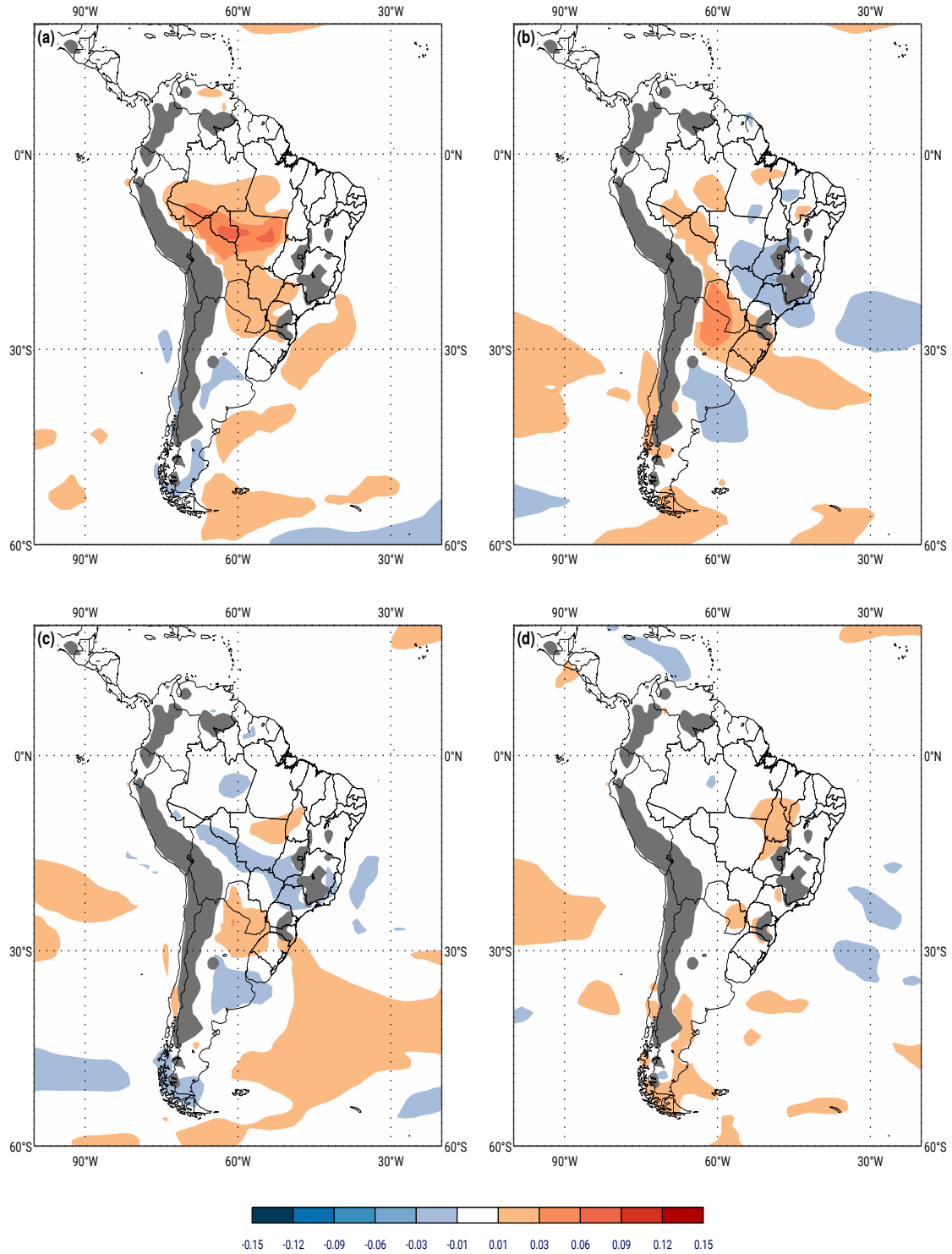
Figure 5.49 - Maximum Eady growth rate RCP8.5 changes at 850hPa for the period 2070-2099.



Maximum Eady growth rate ( $day^{-1}$ ) RCP8.5 changes (WAMZ-CTRL) at upper levels (850hPa) for the period 2070-2099 over Southern Hemisphere: (a) JJA; (b) SON; (c) DJF; and (d) MAM.

SOURCE: Author's production.

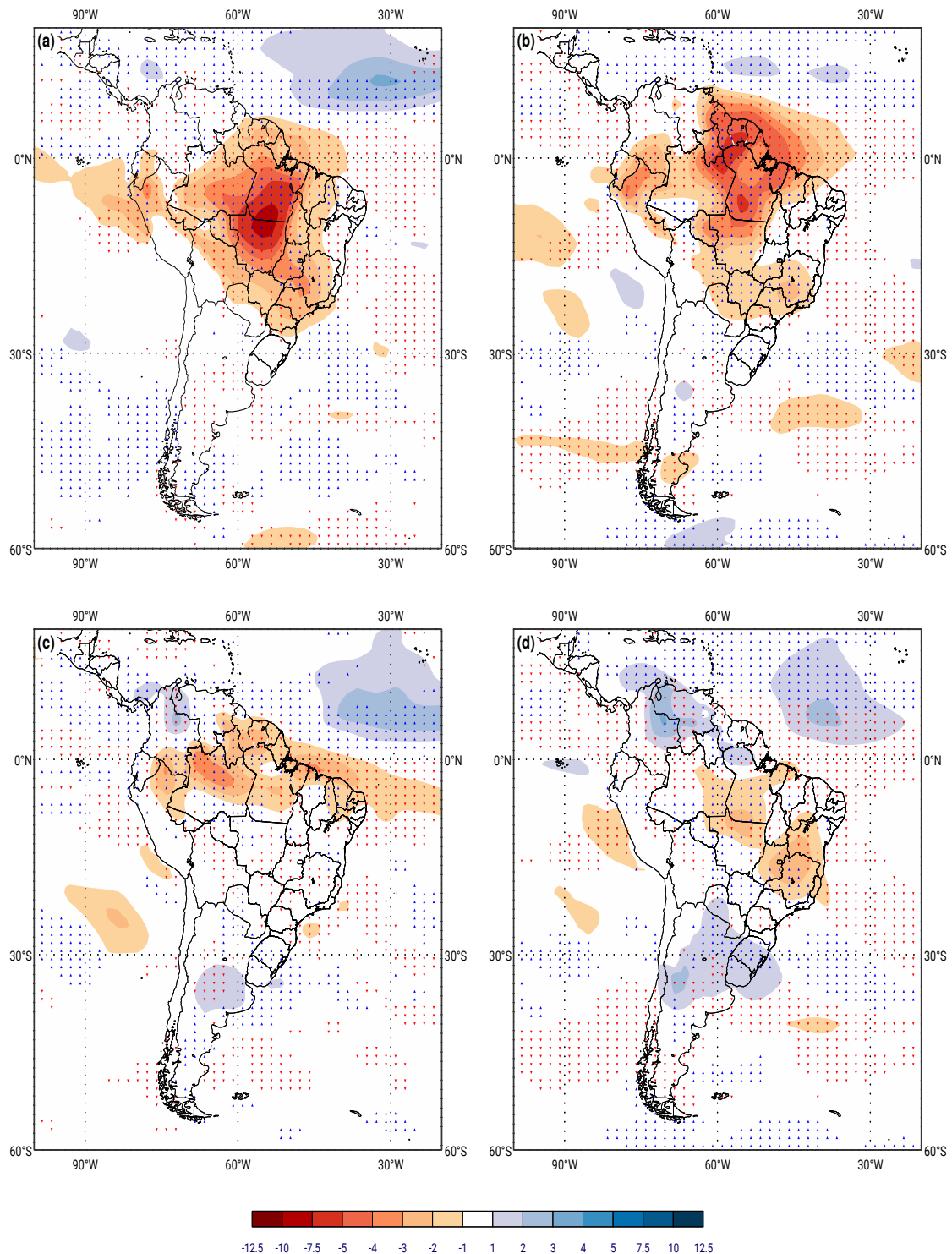
Figure 5.50 - Maximum Eady growth rate RCP4.5 changes at 850hPa for the period 2070-2099.



Maximum Eady growth rate ( $day^{-1}$ ) RCP4.5 changes (WAMZ-CTRL) at upper levels (850hPa) for the period 2070-2099 over Southern Hemisphere: (a) JJA; (b) SON; (c) DJF; and (d) MAM.

SOURCE: Author's production.

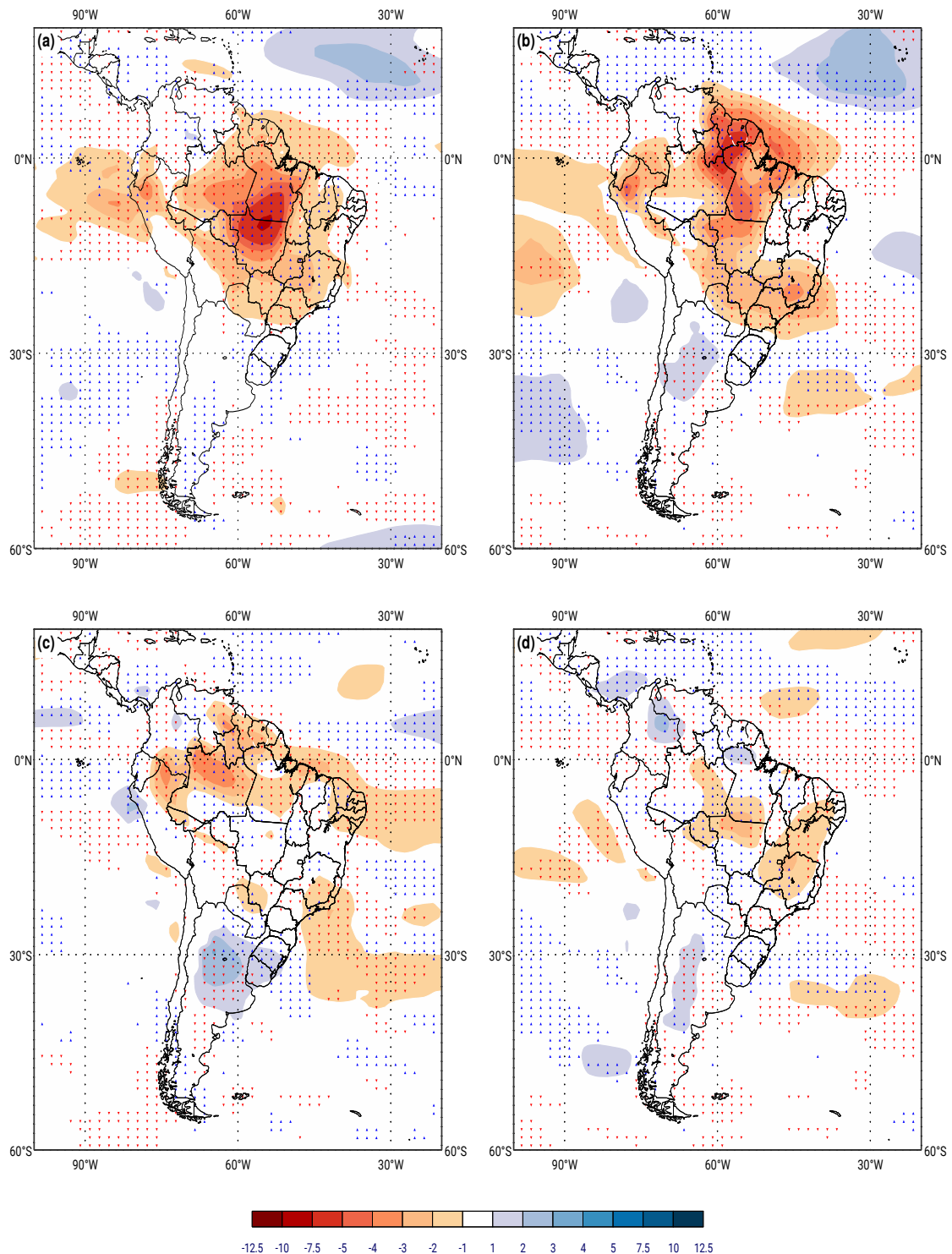
Figure 5.51 - Relative humidity and Omega RCP8.5 changes at 850hPa.



Relative humidity (%) (shaded) and Omega ( $Pa s^{-1}$ ) (triangle stipples) at 850hPa RCP8.5 changes (WAMZ–CTRL) for the period 2070–2099 over Southern Hemisphere: (a) JJA; (b) SON; (c) DJF; and (d) MAM.

SOURCE: Author's production.

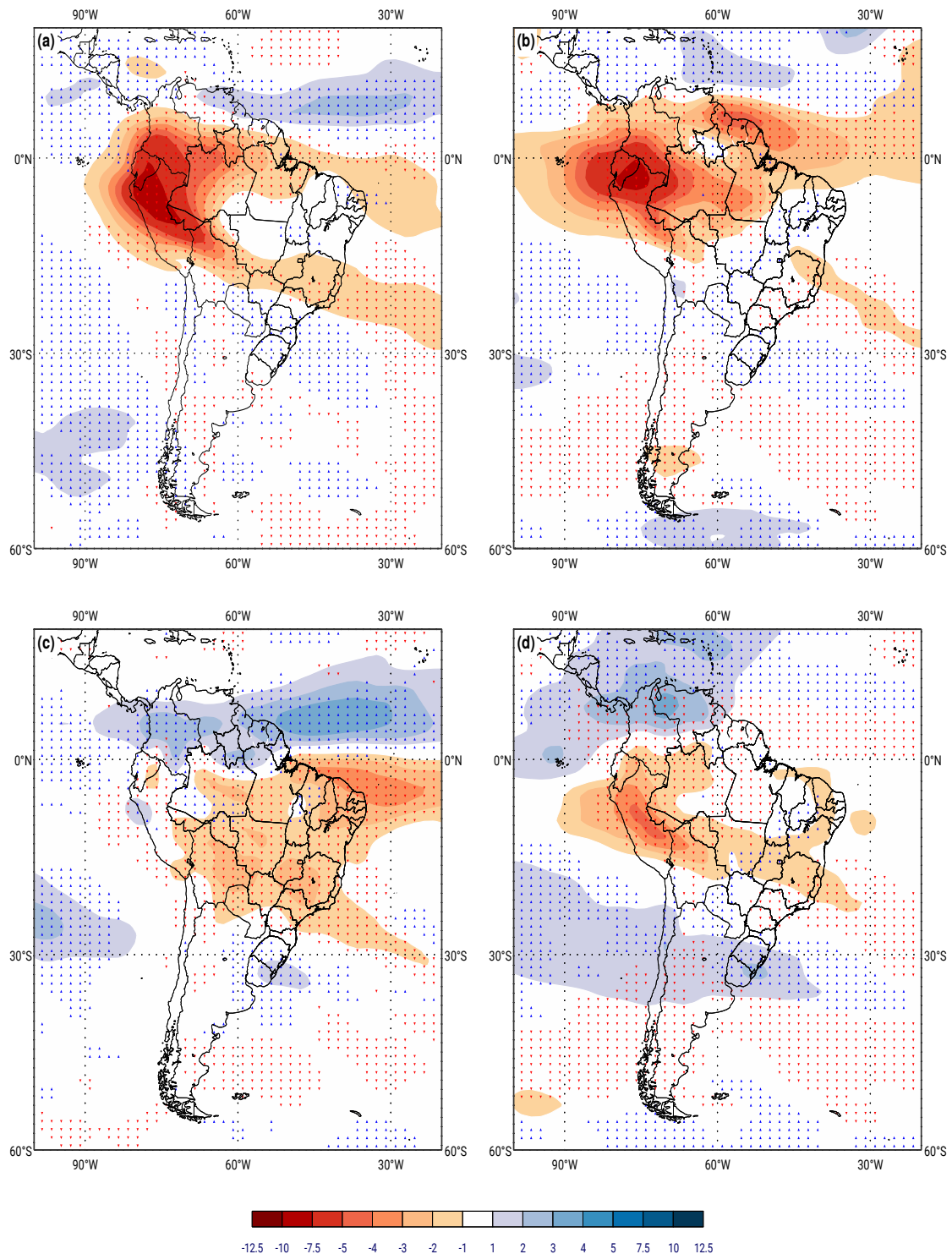
Figure 5.52 - Relative humidity and Omega RCP4.5 changes at 850hPa.



Relative humidity (%) (shaded) and Omega ( $Pa s^{-1}$ ) (triangle stippling) at 850hPa RCP4.5 changes (WAMZ-CTRL) for the period 2070-2099 over Southern Hemisphere: (a) JJA; (b) SON; (c) DJF; and (d) MAM.

SOURCE: Author's production.

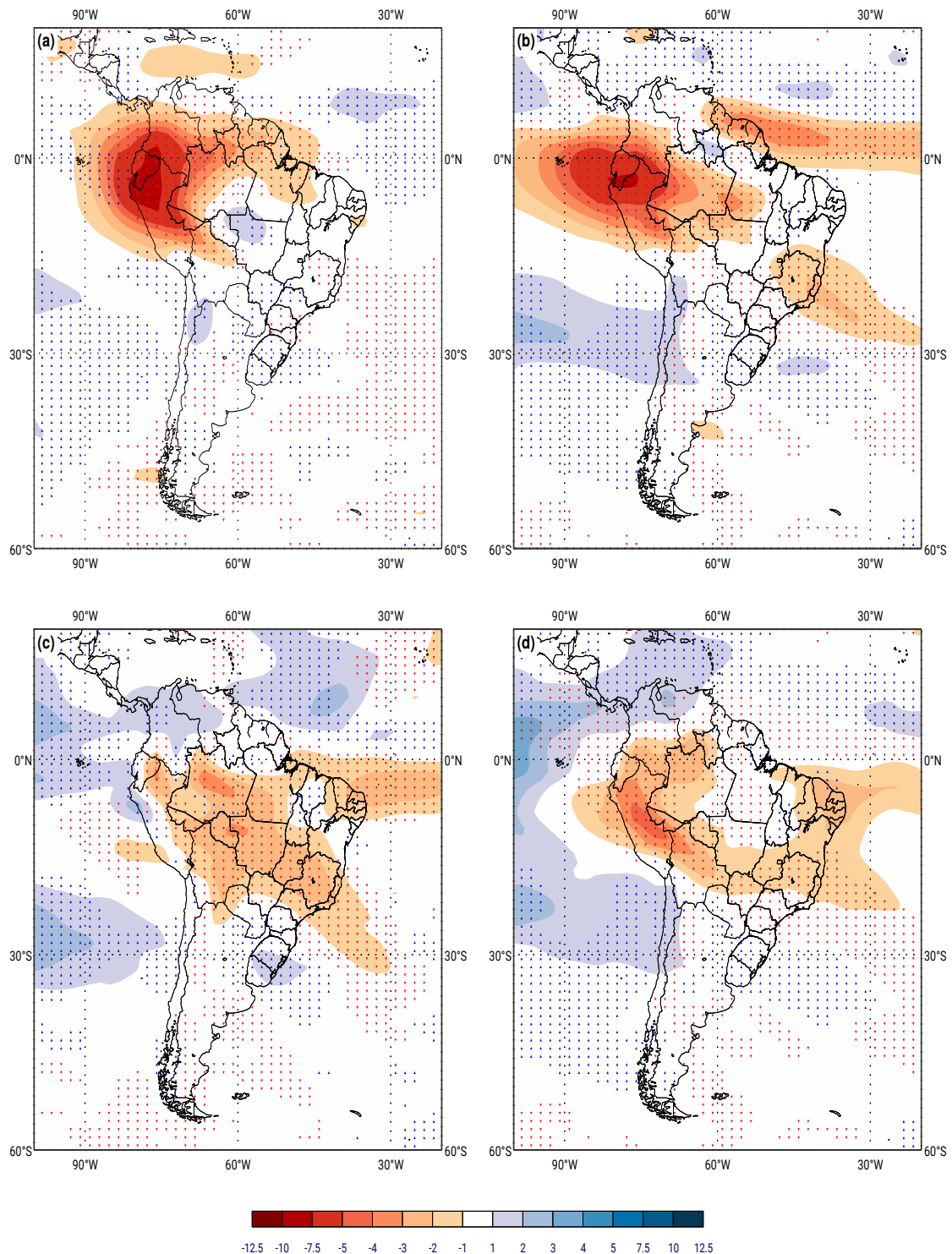
Figure 5.53 - Relative humidity and Omega RCP8.5 changes at 500hPa.



Relative humidity (%) (shaded) and Omega ( $Pas^{-1}$ ) (triangle stipples) at 500hPa RCP8.5 changes (WAMZ-CTRL) for the period 2070-2099 over Southern Hemisphere: (a) JJA; (b) SON; (c) DJF; and (d) MAM.

SOURCE: Author's production.

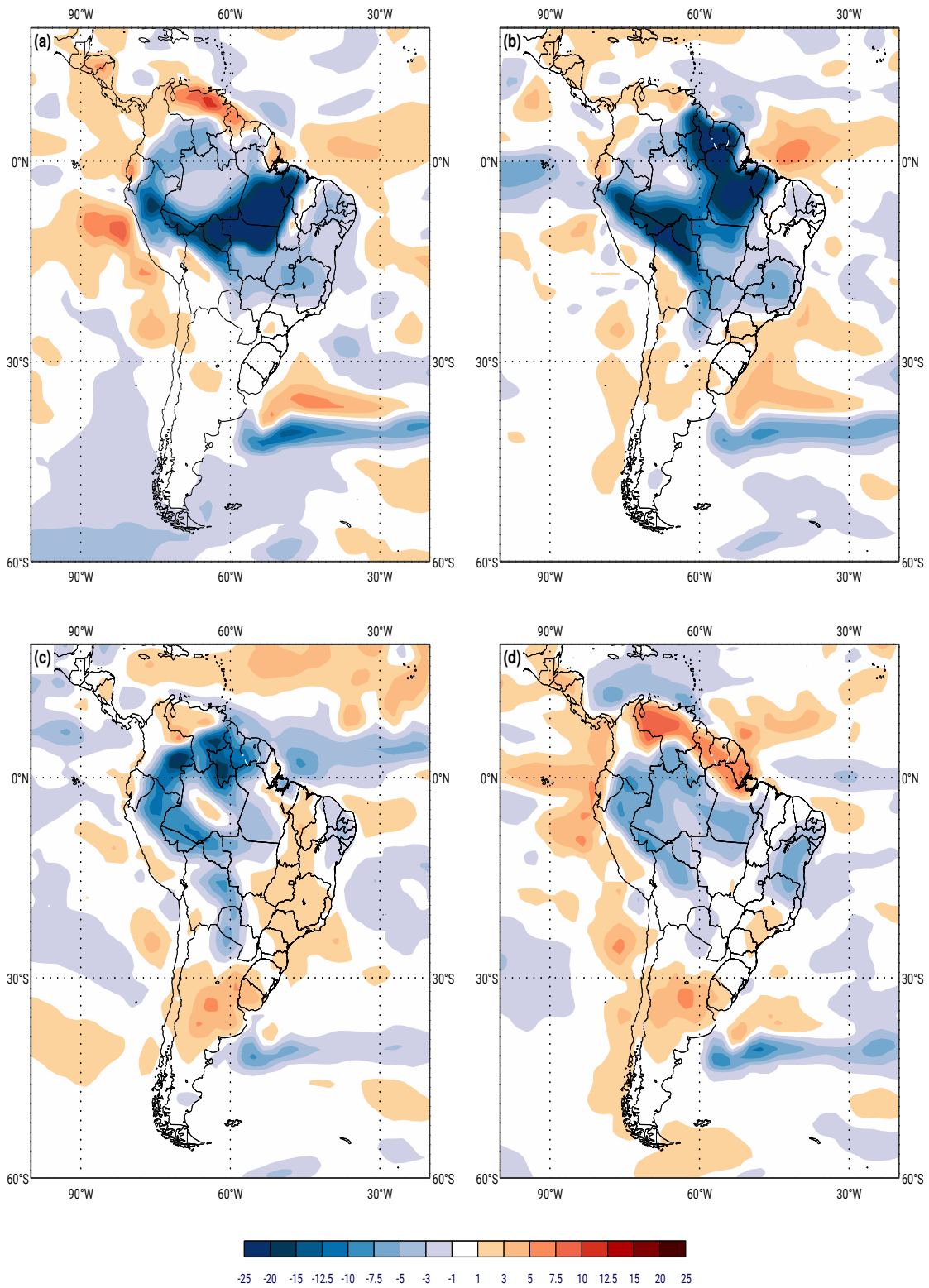
Figure 5.54 - Relative humidity and Omega RCP4.5 changes at 500hPa.



Relative humidity (%) (shaded) and Omega ( $Pas^{-1}$ ) (triangle stippling) at 500hPa RCP4.5 changes (WAMZ-CTRL) for the period 2070-2099 over Southern Hemisphere: (a) JJA; (b) SON; (c) DJF; and (d) MAM.

SOURCE: Author's production.

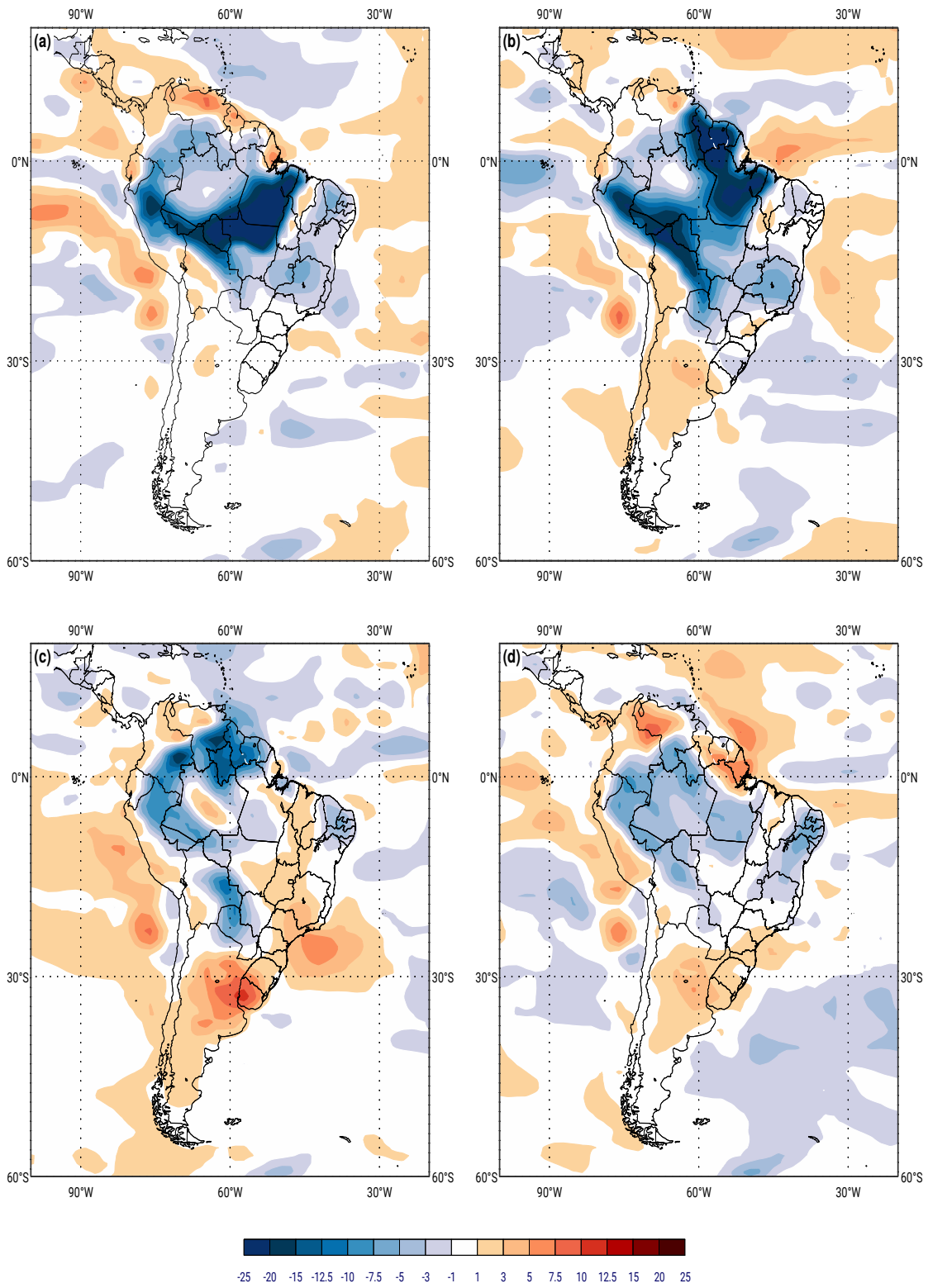
Figure 5.55 - Latent heat RCP8.5 changes.



Latent heat ( $Wm^{-2}$ ) RCP8.5 changes (WAMZ–CTRL) for the period 2070-2099 over Southern Hemisphere: (a) JJA; (b) SON; (c) DJF; and (d) MAM.

SOURCE: Author's production.

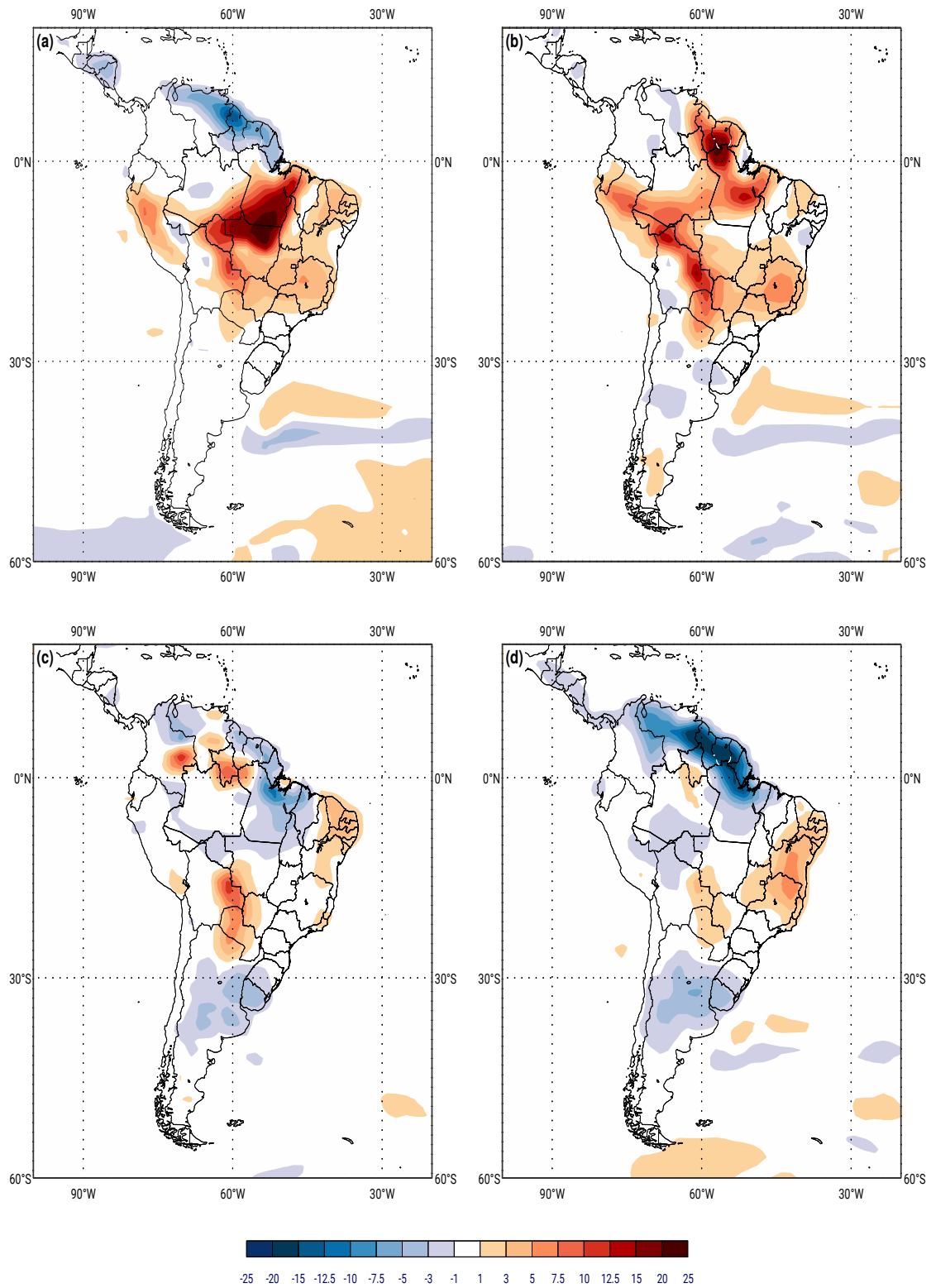
Figure 5.56 - Latent heat RCP4.5 changes.



Latent heat ( $Wm^{-2}$ ) RCP4.5 changes (WAMZ–CTRL) for the period 2070-2099 over Southern Hemisphere: (a) JJA; (b) SON; (c) DJF; and (d) MAM.

SOURCE: Author's production.

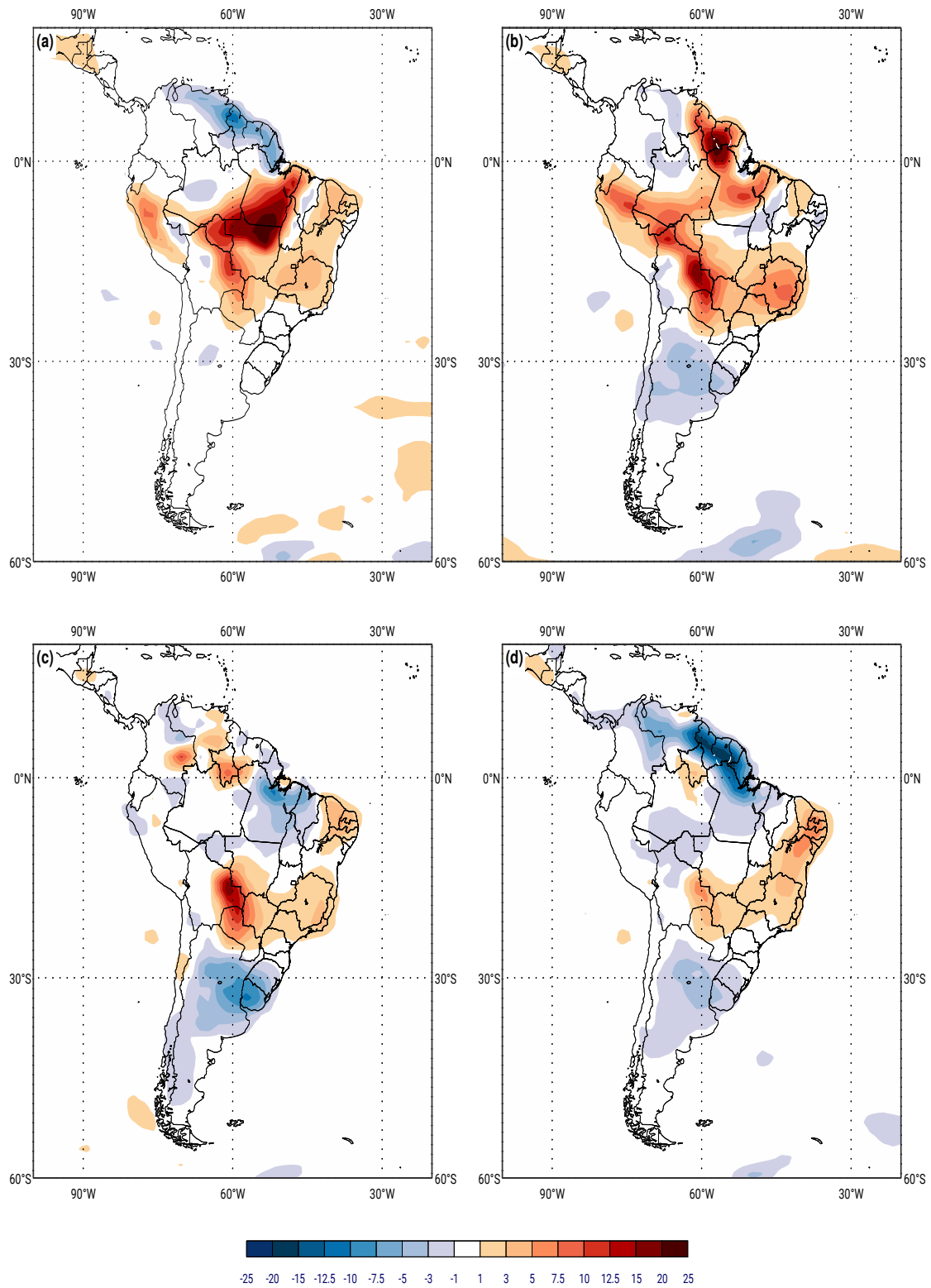
Figure 5.57 - Sensible heat RCP8.5 changes.



Sensible heat ( $Wm^{-2}$ ) RCP8.5 changes (WAMZ-CTRL) for the period 2070-2099 over Southern Hemisphere: (a) JJA; (b) SON; (c) DJF; and (d) MAM.

SOURCE: Author's production.

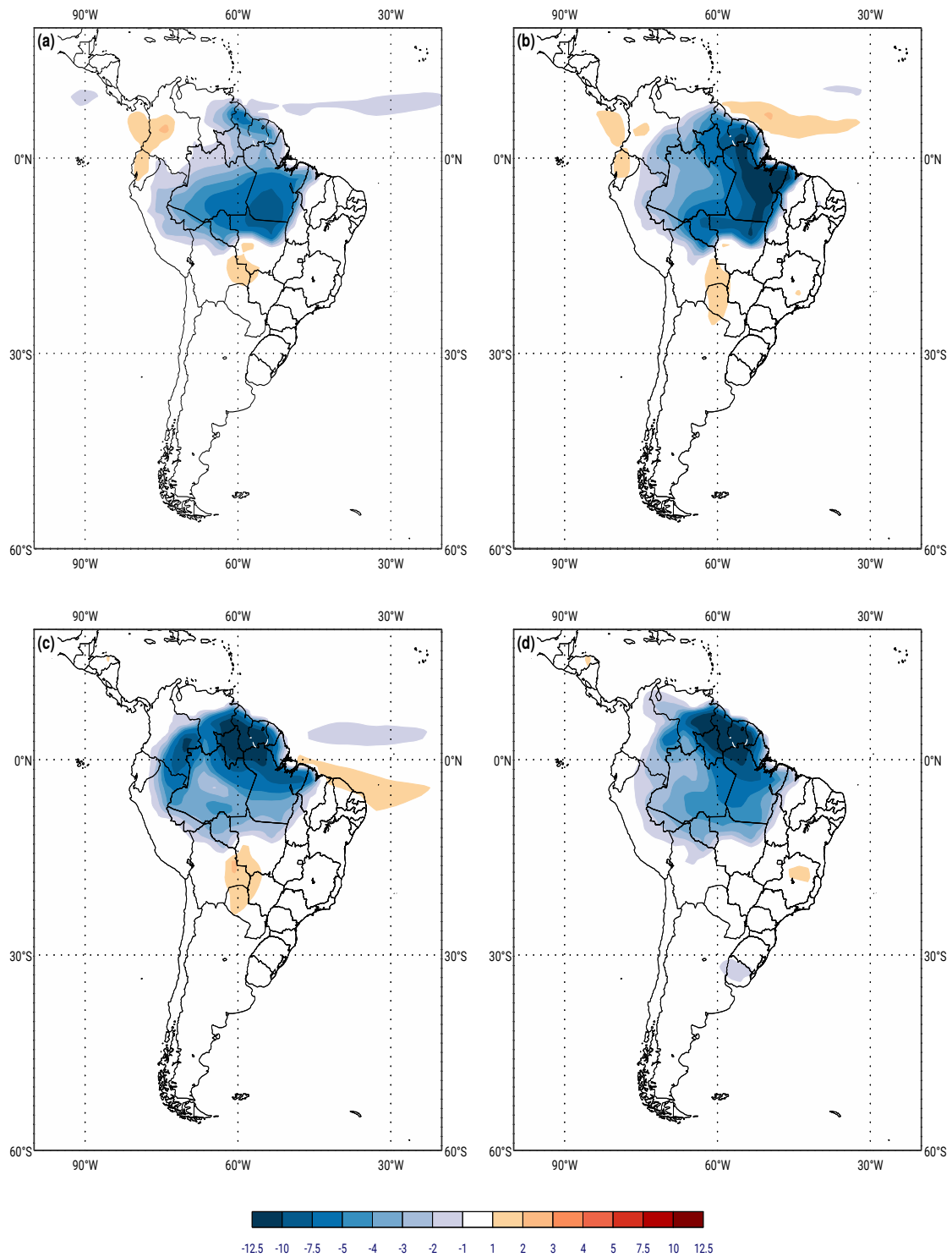
Figure 5.58 - Sensible heat RCP4.5 changes.



Sensible heat ( $Wm^{-2}$ ) RCP4.5 changes (WAMZ-CTRL) for the period 2070-2099 over Southern Hemisphere: (a) JJA; (b) SON; (c) DJF; and (d) MAM.

SOURCE: Author's production.

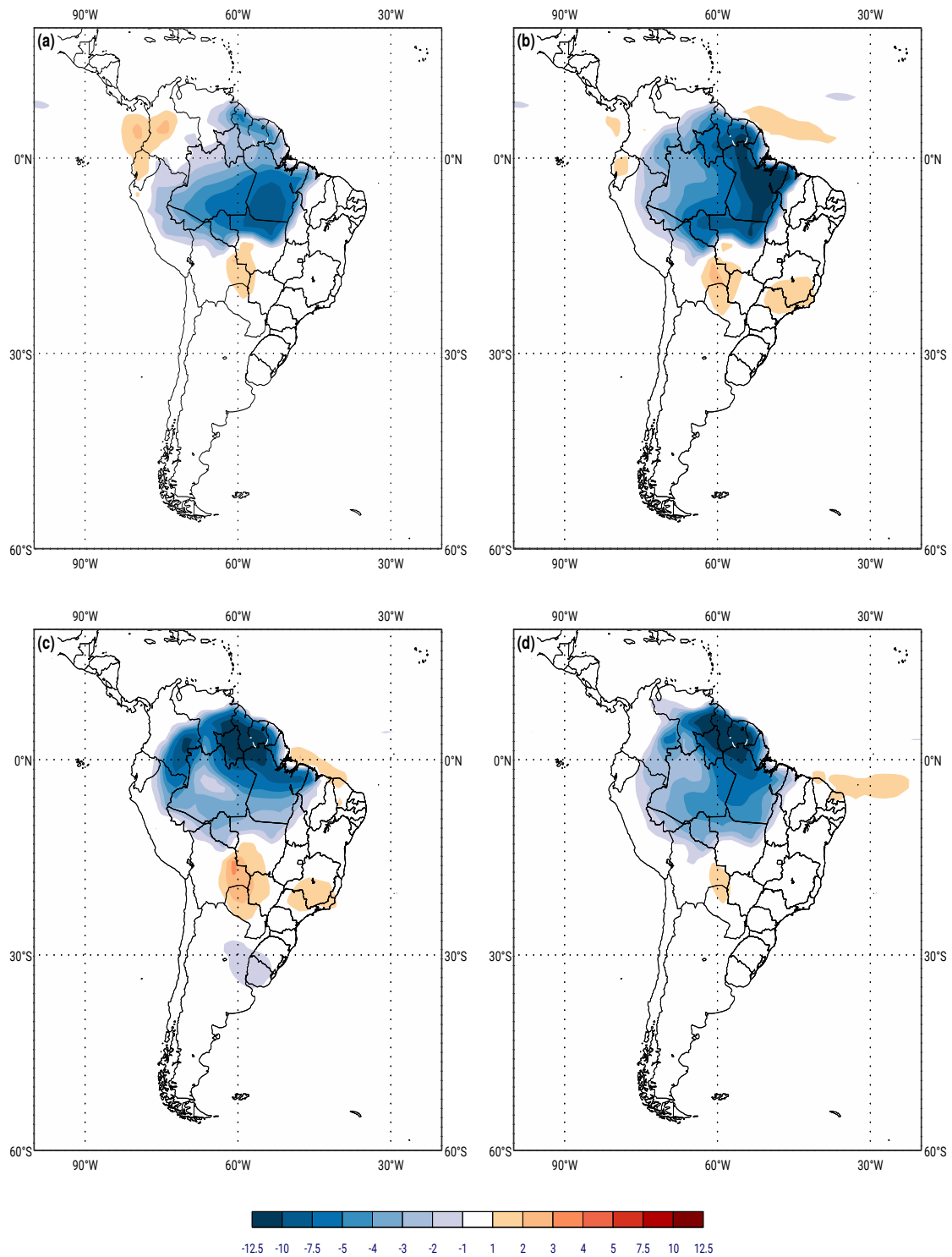
Figure 5.59 - Evaporation minus Precipitation RCP8.5 changes.



Evaporation minus Precipitation (mm/day) RCP8.5 changes (WAMZ–CTRL) for the period 2070-2099 over Southern Hemisphere: (a) JJA; (b) SON; (c) DJF; and (d) MAM.

SOURCE: Author's production.

Figure 5.60 - Evaporation minus Precipitation RCP4.5 changes.



Evaporation minus Precipitation (mm/day) RCP4.5 changes (WAMZ–CTRL) for the period 2070-2099 over Southern Hemisphere: (a) JJA; (b) SON; (c) DJF; and (d) MAM.

SOURCE: Author's production.

#### 5.1.4.2 Summer

The summer storm track and large-scale patterns are described in detail in the Chapter 4, Sections 4.1.2 and 4.2.2.2, where the historical climatology can be used as a background reference for the fields analysed in this section. In addition, the large-scale changes (WAMZ–CTRL) are described in Section 5.1.2.2, as well as the storm track changes in Section 5.1.1.2.

The temperature changes for both the RCPs during the summer season are shown in Figures 5.41c and 5.42c. Similar to the winter season, in general the skin temperature during the summer season decreases in the RCP8.5 scenario (Figure 5.41c), however this contrasts with temperature increases in the RCP4.5 scenario (Figure 5.42c). Also, the temperature decreases over the Amazon Forest region but the largest change in temperature occurs over the border between Amazonas and Roraima States in Brazil. This region is very close to the frontier of Brazil-Venezuela where the highest mountain in Brazil, Pico da Neblina, with 2,995.3 meters, is found and appears to affect the local circulation. However, there are orography height biases over this region as shown in Chapter 4 - Figure 4.9. Moreover, the ITCZ is displaced to the south during the summer which can also affect the temperature changes in both the scenarios.

The temperature changes in RCP8.5 (WAMZ–CTRL) increases over the region between Paraguay, north of Argentina, east of Bolivia and west of Centre-West of Brazil. Moreover, the temperature increase over the south of Brazil toward the adjacent Atlantic Ocean, northeast of Brazil and in the band between Roraima and northeast of Venezuela. Also, there are other areas of increase over the Tropical Atlantic Ocean (NH side) and another large region from the extreme south of SA to the Tropical Pacific Ocean. However, there are other areas of decrease over the centre of Argentina ( $-0.5^{\circ}\text{C}$ ) and other small decreases ( $-0.25^{\circ}\text{C}$ ) in parts of Brazil and the Pacific and Atlantic Oceans. For the RCP4.5 scenario the changes are higher than in RCP8.5 mainly over the central region of SA ( $\sim 1^{\circ}\text{C}$ ) and over the adjacent oceans (SSTs higher than RCP8.5).

The summer precipitation changes (WAMZ–CTRL) are shown in Figures 5.43c for RCP8.5 and 5.44c for RCP4.5. The main increase is found over the south of Brazil, Uruguay and east of Argentina, which seems directly related to the intensity increases of the SA Low-Level Jet East of the Andes (SALLJ, Marengo et al. (2004)). The increase of the winds in the SALLJ (Figures 5.47c and 5.48c) seems increase the instability over these areas, which gives the dynamical features to support the

hypothesis that the removal of Amazon Forest may increase the number of cyclones (Figure 5.5e and f) and genesis (5.6e and f). In addition, this combination of wind (5.47c and 5.48c), humidity and lifting (Figures 5.51c and 5.52c), and SLH (Figures 5.55c and 5.56c), may also lead to the hypothesis that an increase in the number of Mesoscale Convective Complex (MCC), particularly in the RCP4.5 scenario. Also, the increase of wind intensities in SALLJ contributes to the heat advection along the Andes Mountains from Amazon Forest region toward Paraguay, which enhances the sensible heat over this region as shown in Figures 5.57c and 5.58c.

Another precipitation increase over the Amazon Forest region (peaks on northeast, south, west, and in the border over Maranhão and PiauÍ - Brazil) seems to be the result of the wind changes (Figures 5.47c and 5.48c) associated with the ITCZ position to south (Figures 5.45c and 5.46c), which provides a humidity support in both the scenarios. This precipitation change is larger over the Tropical Atlantic in the RCP8.5 scenario (Figure 5.45c). In addition, the SLH increase in both the RCPs in the centre of the Amazon Forest, which corresponds to the precipitation increase and indicates that it is the result of the combination of the humidity from the ITCZ and lifting associated with the wind shear at upper levels (700 and 500hPa, not shown).

The precipitation decreases over the major part of SA and over the Tropical and South Atlantic sectors. The strongest decreases are found over northeast of Brazil (coastline), centre of Amazonas State and between Acre State and Peru. These changes are very similar between the RCPs, however they are larger in the RCP4.5 scenario particularly over the southeast of Brazil. These precipitation changes are directly related to the removal of Amazon Forest and correspond with the OLR (Figures 5.45c and 5.46c) increases (less clouds). During summer there is a decrease in the humidity at 500hPa in the Amazon Forest region and an increase in the subsidence (Figures 5.53c and 5.54c, red shaded colors and red triangles), which support the hypothesis that the removal of the Amazon Forest reduces the dynamical support for the South Atlantic Convergence Zone (SACZ). This means that, even with the greater availability of heat (latent heat - Figures 5.55c and 5.56c; and sensible heat - Figs 5.57c and 5.58c.), the SACZ pattern is reduced as discussed previously. This corresponds well with the maximum Eady growth rate decrease shown in Figures 5.49c and 5.49c, particularly to RCP4.5 scenario.

The main patterns of SLH changes (Figures 5.55c and 5.56c) were discussed previously. However, the SLH RCP4.5 increase near to the southeast of Brazil do not

correspond with the storm track and genesis densities (Figures 5.5e and f, and 5.6e and f) during the summer season. This seems related to the anticyclonic circulation (Figure 5.48c) associated with the omega increase at lower (Figure 5.52c) and middle (Figure 5.54c) levels that inhibits the genesis and growth of storms.

Finally, the summer evaporation minus precipitation ( $E - P$ ) is shown in Figures 5.59c and 5.60c for the RCP8.5 and RCP4.5 scenarios, respectively. The main change occurs over the north of South America where there is a decrease of the evaporation over the continent, where the ITCZ displaced to the south is the main source of humidity when the Amazon Forest is removed. Another main change occurs over the centre of SA where there is an increase of the evaporation as a result of the sensible heat increases in both the RCPs (Figures 5.57c and 5.58c). The evaporation increase over the coastline of northeast of Brazil is related to the precipitation decrease in the Tropical Atlantic (Figures 5.43c and 5.44c). Another evaporation increase is observed over São Paulo State only for RCP4.5 and it may be related to the SACZ pattern reduction discussed previously.

#### 5.1.4.3 Transition seasons

The spring and autumn storm track and large-scale patterns are described in detail in the Chapter 4, Sections 4.1.3 and 4.2.2.3. The historical climatology can be used as a background reference for the fields analysed in this section. Moreover, the large-scale changes (WAMZ–CTRL) are described in Section 5.1.2.3, as well as storm track changes in Section 5.1.1.3.

The temperature changes for both the RCPs during the transition seasons are shown in Figures 5.41b and d and 5.42b and d. The spring temperature decrease over the Amazon Forest region is the smallest of all seasons in both the scenarios, while the increase over the central region of SA is the largest. In summary, the temperature changes are similar to those in the previous season.

The precipitation changes (WAMZ–CTRL) are shown in Figures 5.43c for RCP8.5 and 5.44c for RCP4.5. These are similar to those in the previous season, but they are larger over the south of Brazil region during the autumn for RCP4.5 scenario. This dynamical pattern during the autumn season is similar to discussed previously for the summer season in this region where the SALLJ (Figures 5.47d; 5.48d) may increase the convective systems. For both the seasons the spatial pattern of change in precipitation and OLR (Figures 5.45b and d; and 5.46b and d) corresponds very well in both the RCPs.

The changes (WAMZ–CTRL) in both the RCP scenarios during the spring and autumn seasons for wind (Figures 5.47b,d and 5.47b,d), baroclinicity (Figures 5.49b,d and 5.50b,d), humidity and omega (Figures 5.51b,d and 5.52b,d), latent heat (Figures 5.55b,d and 5.56b,d), sensible heat (Figures 5.57b,d and 5.58b,d), and  $E - P$  (Figures 5.59b,d and 5.60b,d), are similar to those in previous season (spring to winter and autumn to summer).

## 5.2 Discussion and conclusion

First, in relation to the Historical experiment, in general the storm track changes in the CTRL experiment (Figures 5.1c and d) show a consistent poleward shift for both of the RCPs, with the track density decreasing on the equatorward and increasing on the poleward side. This is consistent with the previous results found from CMIP5 (CHANG, 2013; HARVEY et al., 2014; LEE, 2014; REBOITA et al., 2018) and CMIP3 (BENGTSSON et al., 2006). The largest ST density changes occur during the summer and autumn seasons. The genesis and growth rates tend to be found close the climatological region but the changes are larger during the summer and spring season, particularly in the WAMZ–HIST experiments. The summer lysis density changes around the Antarctic coast have the largest projected increases under both the RCPs, where the maximum change occurs near to the Antarctic Peninsula. The results show that the genesis and lysis future projection changes indicate that both are slightly displaced to the south.

Constrasting the WAMZ with CTRL experiments, the storm track changes are constrained between 20°S and 75°S over the SH and are shifted poleward in the future projected climate. The changes are stronger in the CTRL experiments compared to the HIST experiment, particularly under the RCP4.5 scenario, with the summer poleward shift being larger than the other seasons. However, the results show that the WAMZ RCP8.5 experiment have a reduce ST poleward shift, which is reflected directly in the decreases of mean growth decay rates over the southern oceans. The removal of the Amazon Forest impacts the ST mainly over the Atlantic and Pacific Oceans.

A summary of the results are outlined below. In this study the experiments were designed with land use change fixed at 2005 conditions (CTRL) and without the Amazon Forest (WAMZ), thus the previous using the CMIP5 climate model studies of the STs cannot be used to assess the results found here, but they can be used only as a reference.

- The future projected storm tracks in the Southern Hemisphere have larger width than in the historical period with less cyclones on the equatorward side and more on the poleward side. This poleward shift pattern has high correspondence with the upper level jet differences. Similar results were also found by Barnes and Polvani (2013) using the actual CMIP5 climate models. The poleward shift means that the storm tracks are slightly latitu-

dinally narrower ( $1 - 3^\circ$ , depending the season) due to the larger extension (not intensity) of the equatorward track density decreases relative to the poleward track density increases. For RCP4.5 scenario this pattern is larger because the spatial extent also decreases but the Subtropical Jet increases, as shown in Section 5.1.2.

- For the WAMZ–CTRL difference, the poleward track density decreases for RCP8.5 compared to the RCP4.5 scenario, highlights that the changes are also dependent on the emission scenario. Therefore, not only the removal of the Amazon Forest reduces the poleward shift, but also the emission scenario. These changes fit with the results found by [Lorenz and DeWeaver \(2007\)](#), where both the tropical warming and the polar cooling at upper levels increases the pole-to-equator temperature gradient and results in a rise in the height of the tropopause and a poleward shift in the zonal winds in the mid-latitude circulation. Moreover, the reduced poleward shift of the STs for the WAMZ experiments corresponds with the results found by [Harvey et al. \(2014\)](#), where the enhanced lower level tropical temperature, in relation to the pole, weakens the equator-to-pole temperature gradient and acts to shift the storm track towards the equator.
- The variance of the storm tracks in a future projected climate can be related to the lower level temperature changes. These changes are larger in the winter season and seem related to the land-sea contrast changes. [Harvey et al. \(2014\)](#) studied the equator-to-pole temperature differences at lower levels and found this relation with a high correlation. These changes may affect the baroclinicity at lower levels through the static stability, however it was not separate in this study. Recent studies such as [Lu et al. \(2010\)](#) indicate an increase in the subtropical and extratropical static stability that contribute to a poleward shift, while [Raible \(2007\)](#) highlights the importance of static stability to the NH genesis regions. Thus, there is evidence that it may be affecting the SH ST which will be addressed in further studies. In relation to the historical period, the genesis changes decrease over the extreme south of SA (one of the three climatological regions) in all seasons, being weaker during the autumn. The autumn lysis changes have larger increases of all seasons and are concentrated at high latitudes (above  $60^\circ\text{S}$ ).
- The variances for WAMZ–CTRL show that the genesis changes increase over the north of Argentina under the RCP8.5 scenario during all seasons,

while they tend to decrease over the Atlantic Ocean under the RCP4.5 scenario in the summer season. The main lysis changes occur between the extreme south of SA ( $\sim 45^\circ\text{S}$ ) and Antarctic Peninsula and are somewhat responsive to the RCP scenario.

- In general, large-scale changes (WAMZ–CTRL) tend to have a similar pattern to the ST biases. In the upper levels, large changes were found over the subtropical and extratropical latitudes, in particular under RCP4.5 during DJF and MAM which is a result of the equatorward jet position of the Subtropical Jet. At lower levels, over the continent the main changes occur during the winter season for the RCP8.5 experiments due to the lower level temperature changes discussed above, while over the southern oceans the main changes are concentrated over the Atlantic and Pacific. Baroclinicity changes at upper levels correspond well with the zonal mean zonal wind changes, being the main changes also seen over both the oceans.
- The pattern of temperature changes discussed above seem to impact the 500hPa geopotential height anomaly changes (WAMZ–CTRL), which show an increase during all seasons over the SA. There is also evidence that the removal of the Amazon Forest impacts the stationary wave pattern that affects the Australian Blocking by changes in the Rossby Wave source. These changes are stronger over the Pacific Ocean, which leads to the hypothesis that the well-know Rossby Wave source close to New Zealand is also modified, however this will be addressed in future work. In addition, there is evidence of changes in the SAM. The precipitation changes are similar and concentrated over the tropical regions in both the RCP scenarios, however the increases are larger under RCP4.5 while decreases are larger under RCP8.5 scenario.
- The *KS D* statistics (Tables 5.3 and 5.4) correspond with the results found in the previous sections (5.1 and 5.1.2) and show that the removal of the Amazon Forest (WAMZ–CTRL) for both the RCPs reduces the number of cyclones in almost all seasons, except in MAM. Moreover, the WAMZ experiments for both the RCPs, particularly for RCP8.5 scenario, have less agreement between the ensemble members. In addition, the experiments under the RCP4.5 scenario, particularly for the CTRL experiment, tends to represent more storms than the experiments under the RCP8.5 scenario.
- The regional-scale changes (WAMZ–CTRL) were analysed over the South America region. However, there are also many changes over Africa and

the Australia - New Zealand region that will be addressed in future work. These changes should be analysed separately because there is evidence of teleconnections (MO; WHITE, 1984; CAVALCANTI, 2009), as shown in the large-scale changes (Section 5.1.2) at the 500hPa level. For the future projected climate, the removal of the Amazon Forest impacts directly the main climate pattern over South America during all seasons of the year. In this study were shown the main mechanisms that impact the storm track densities over the SA are shown, including the temperature, precipitation, winds, relative humidity and other diagnostics.

- In general, the changes have similar features in both the RCP scenarios, but there are some patterns of increase during the seasons. During the winter and part of the spring season the ITCZ is displaced to the north which removes the humidity support over the north of SA. The trade winds increase due to less roughness (no obstacles), passing over the Amazon Forest region, until they fork when they encounter the Andes Mountains. This pattern is somewhat related to the large-scale changes and affects the sensible and latent heating, temperature, humidity, precipitation and OLR. In addition, the South Atlantic Subtropical Anticyclone (SASA) over the ocean is enhanced. Thus, these creates other resultant changes that affects directly the water cycle, shown as  $E - P$  changes. On the other hand, during the summer and part of the autumn, the ITCZ is displaced to the south and gives some humidity support to the north of SA, thus it creates some small scale circulation over the Amazon region and enhances the SALLJ. The SALLJ is the most important humidity support for the centre-south of SA, however because of the removal of Amazon Forest it doesn't have the humidity which increases the sensible heat and temperature between the border of Brazil-Bolivia. Moreover, the SALLJ with strong winds contributes to enhance the wind shear over south of Brazil, Uruguay and north of Argentina, which may enhance the MCCs.
- The feedback mechanisms seem stronger than the regional-scale changes, which explain the temperature change decreases in all seasons for both the scenarios. Over the Amazon Forest region, a positive feedback acts to reduce the temperature as follows:
  - a) there is high sensible heat due to the removal of the forest;
  - b) the surface accumulates more heat, which reduces the latent heating because there is less humidity available to be converted;

- c) the evaporation reduces because there is no forest (evapotranspiration) and less humidity (only coming from adjacent oceans);
- d) the albedo increases and results in radiation loss to the atmosphere;
- e) the OLR increases (less clouds);
- f) the radiation loss increases;
- g) the temperature decreases.

These results have shown that there is a considerable agreement between the climate change when the Amazon Forest is removed in both the RCP scenarios. The ecosystems and hydrology is consistent with the physical improvements in the HadGEM2-ES climate model, which includes many improvements in the coupled fluxes passed from the atmosphere to the land, feedback mechanism and many others (more details in [Martin \(2011\)](#)). In addition, changes are still apparent in the storm track density over all Southern Hemisphere, however, there are several changes over tropical and Northern Hemisphere that were not explored in this study.

## 6 CONCLUSIONS

### 6.1 Overview

Extratropical cyclones play an important role in the transport of energy and moisture from low latitudes to Polar Regions. They are synoptic scale weather systems of meteorological, climatic and socioeconomic importance for South America regional climate. The aim of this study was to perform a comprehensive study of the Storm Tracks over the Southern Hemisphere and to investigate the impact on cyclones and the STs in an idealized experiment, using the UK Met Office HadGEM2-ES coupled climate model, of changes in the land cover over the Amazon Forest. To this, re-analysis data and numerical simulation results were used to answer the key science questions presented in Chapter 1 and reproduced as follows:

- How well does the HadGEM2-ES Coupled Model represent the Southern Hemisphere Storm Tracks?
- What are the main factors that contribute to biases in the storm tracks?
- What are future storm track changes predicted by the HadGEM2-ES model for the two IPCC future climate change scenarios?
- How might Amazon land use cover change affect the storm track and climate over South America?

To answer these scientific questions, the historical and future projected climate were investigated. Chapter 4 highlights the climatology and biases of the extratropical cyclones and the large-scale fields in the HadGEM2-ES model for the historical period between 1979-2005. Chapter 5 focuses in the future projected climate of the extratropical cyclones and large-scale changes using the HadGEM2-ES model for four experiments with and without Amazon Forest, including a regional-scale analysis, for a 30-year climatology between 2070-2099.

The Section 6.2 is addressed to answer each of the key questions using the results of Chapters 4 and 5. Section 6.3 shows the suggestions and directions for future work based in the results found in this study.

## 6.2 Conclusions

### 6.2.1 How well does the HadGEM2-ES Coupled Model represent the Southern Hemisphere Storm Tracks?

Although there are a few errors that will be described in the next answer, the HadGEM2-2 climate model represents well the storm tracks when contrasted with the ERA-Interim reanalysis. This conclusion is based on the results of Chapter 4, as follows:

- For austral winter, HadGEM2-ES shows the main characteristic of the ST that is the spiral from South America, around Antarctic, through the Atlantic and Indian Oceans, and to the Antarctic Peninsula (FYFE, 2003; HOSKINS; HODGES, 2005). The largest track density region can be seen around the Antarctic coast between 120°E, and 80°W. The lowest track densities tend to be found to the south of New Zealand and are most apparent in the winter. The model shows that the cyclogenesis occurs throughout the main ST region due to secondary cyclogenesis and downstream development (CHANG, 1993; INATSU; HOSKINS, 2004; HOSKINS; HODGES, 2005; HODGES et al., 2011). More concentrated cyclogenesis occurs in two well-known regions in the southeast of South America, specifically leeward of the natural barrier of the Andes Mountains, one stronger in the northeast of Argentina related with the Subtropical Jet and mountain effect, and the second found in the extreme south of SA, which is related to where the ST from the Pacific Ocean crosses the mountains. Other major genesis densities maxima are found on the Antarctic coast, the first with center at 65°S e 165°E and a second near to Drake Passage, with both associated with upstream decay and lysis, which enhances the local baroclinicity resulting in reinvigoration or secondary cyclogenesis. Another cyclogenesis region can be seen close to the Australian coast, also found by Hoskins and Hodges (2005), and is related with the winter split jet. The region between 20°S and 50°S is dominated by cyclone growth rates where the maximum may be seen on the east side of Andes Mountains. The lysis maximum regions are concentrated around the Antarctic coast, with a maximum near to the Antarctic Peninsula and another at the same longitude of Australia. Also an important region may be seen on the windward side of the South America related to where the ST intercepts the Andes Mountains, causing a lysis on the upslope. The cyclone decay rate regions are seen in tropical

and high latitudes around the SH, with a maximum close to the Andes Mountains and Antarctic coast.

- During the summer season, the model shows that the main characteristics of the STs are that they are narrower, more zonal and symmetric than in the winter season. These differences are associated mainly with a single eddy-driven jet, in contrast with the split jet during the winter. The track density maximum is located between South America and the Antarctic Peninsula, which is related with the single eddy-driven jet over the South Pacific Ocean and the orography of the Andes Mountains that tends divert it to the south. The HadGEM2-ES also shows that the two main peaks of genesis density may be seen over Argentina on the eastern side of the Andes Mountains, one stronger to the south that occurs mainly as the jet stream moves to a poleward position during the summer and the other in the northeast, both are also related to mountain effect (HOSKINS; HODGES, 2005). In addition, other regions of cyclogenesis are seen near the southeast of Brazil around 25°S, along the southern edge of the South Atlantic Convergence Zone and around 150°S along the southern edge of the South Pacific convergence zone. There are other cyclogenesis maxima on the Antarctic Peninsula, that are weaker than in winter, near to Western Australia and over the Indian Oceans. The cyclone growth rate is, in general, smaller than in winter with the peak areas found near to the genesis areas. However, over the cyclogenesis regions close to South Africa, the growth rates are larger than in the winter. Moreover, the lysis density pattern in the summer is similar to the winter season with a slightly reduced maxima in the main regions near to Antarctic. The cyclolysis peak over South America in this season is shifted slightly to the south and with smaller magnitude in comparison to the winter season. Also, other lysis peaks may be seen in the Eastern Northeast of Brazil related to the propagation of Easterly Wave Disturbances (GOMES et al., 2015). During the summer season the mean decay rates are qualitatively similar in most parts of the SH, however with a smaller maximum rate. In comparison with winter, the decrease of decay rate may be seen in the Andes Mountains that is slightly moved to the south.
- For spring season, the model shows that the track density climatology has similar features to the winter and summer seasons. This pattern was observed by Hoskins and Hodges (2005), where the transition seasons tend

to have similarity with those in the preceding season, and Shaw (2013), where the less abrupt changes in the SH, in comparison with the NH, are related to the lack of a leading-order monsoon-anticyclone transport via planetary-scale waves. The ST over the SH is more zonal than in winter, however some features over the Pacific and Atlantic are somewhat similar to the winter season and the spiral tends to be more poleward. The genesis, lysis and mean growth decay rate densities are similar to the patterns discussed for winter.

- Finally, HadGEM2-ES shows that the ST during the autumn is also similar to the spatial pattern in austral summer, however slightly broader in latitudes and less zonal and symmetric. The genesis and mean growth decay rate densities are similar to summer though the lysis seems more similar to the winter season around the coast of Antarctic.

### **6.2.2 What are the main factors that contribute to biases in the storm tracks?**

The HadGEM2-2 climate model represents well the Southern Hemisphere storm track, however biases were found in regional and large-scale. This conclusion is also based on analyses of Chapter 4, as follows:

- The storm track (ST) climatology of HadGEM2-ES presents similar patterns to those of the reanalysis. However, the model tends to represent the austral winter ST position with an equatorward bias and a zonal bias in the spiral towards the pole. The main differences were found during the austral winter and spring, with large track density biases over the Indian Ocean indicating a poor representation of the ST in this specific region. This was found to be related to two factors. First, the large negative genesis biases over South America, Antarctic Peninsula and the Antarctic coast. Second, the model resolution and the representation of the Andes Mountains in South America.
- The link between STs and the large-scale circulation was examined and at upper levels a large cold bias was found over the extratropical and Polar Regions, which is a result of the equatorward jet position bias of the subtropical jet and a negative bias in the eddy-driven. The analysis of the large-scale circulation showed that the split jet bias during winter is associated with geopotential anomaly and sea surface temperature biases.

As a consequence, in general the track densities over the Southern oceans are underestimated in the austral winter. During the summer season, the results showed that the STs move poleward and there is a single eddy-driven jet, which is represented relatively well compared with the winter situation. These factors tend to reduce the differences seen in the cyclone track distribution biases. Although the model has biases in the ST behavior in the SH, it is still considered that these do not preclude this model being used for perturbation and future projection studies.

### **6.2.3 What are future storm track changes predicted by the HadGEM2-ES model for the two IPCC future climate change scenarios?**

First, to answer this science question comparison between the historical experiment and the CTRL experiments for RCP8.5 and RCP4.5 scenarios, which they are similar (but not equal) to the CMIP5 experiments, will be considered. The WAMZ experiments changes are somewhat similar to CTRL experiments and their differences (WAMZ–CTRL) will be addressed in the next science question.

The HadGEM2-2 climate model represents the Southern Hemisphere storm track future projections (2070-2099) similar to the historical period (1976-2005), including the seasonal variations, however shows a consistent poleward shift for both the RCP scenarios. This conclusion is based on the results of Chapter 5, as follows:

- The SH storm track future projected changes during the austral winter show a consistent poleward shift for both of the RCPs, with the track density decreasing on the equatorward side and increasing on the poleward side of the main ST, which is similar to the results found with the CMIP5 climate models (CHANG, 2013; HARVEY et al., 2014). During the austral winter season the ST density future changes for RCP8.5 seem stronger than for RCP4.5, however some positive changes are stronger for RCP4.5. The ST spatial pattern changes are similar for both RCPs (Figure 5.1) and the largest changes are commonly negative over southern Australia, northern New Zealand and towards south of South America. Positive areas are found around Antarctica and in the Atlantic Ocean ( $\sim 50^{\circ}\text{S}$ ). The RCP8.5 genesis density changes are larger than for those of RCP4.5 in both the experiments. In SA, the region leeward of the Andes Mountains shows a decrease in genesis over the usual climatological winter maximum region over the south of Argentina of up to 20% relative to the Historical

experiment. Over this same region in SA, the HadGEM2-ES model tends to overestimate the genesis density for the Historical experiment compared with the reanalysis (see Section 4.2.1.1 for the winter season biases), which may indicate that the projected future changes may have a larger decrease than simulated. Further north, over the second climatological maximum between northeast Argentina and the south of Brazil, there are increases in genesis density of up to 20% over a region extending eastwards to the Atlantic Ocean in the RCP8.5 experiment. This area of genesis density increase may be seen in the other experiments for both the RCPs. Lysis density changes show a consistent decrease in extratropical latitudes, while there are some increases in regions around the Antarctica coast. The main changes occur between the south of SA and the Antarctic Peninsula. There is a sign contrast related to the ST position which is more equatorward for RCP8.5 than RCP4.5, causing lysis when the cyclones meet the Andes and Transantarctic Mountains. The MGDR changes are concentrated mainly above the extratropical latitudes in both the experiments. The pattern of changes discussed above contrast with those using older CMIP/AMIP climate models such as used by Yin (2005) using the older IPCC A1B scenario and found a poleward ST shift but without the equatorward decrease. Similar results have also been found for more recent CMIPs such as by Chang et al. (2013) for AR4/CMIP3 and Chang et al. (2012) for CMIP5, which found changes in the multi-model mean similar to that found here for the CTRL experiment.

- The summer season storm track for future projected climate continues narrower, more zonal and symmetric than in the winter season, but the ST is also poleward shifted. This is highlighted by the cyclone track density changes which are concentrated around the Antarctic region. The second largest difference between the austral winter and summer seasons may be seen by comparing the RCP8.5 results with those of the RCP4.5 scenario. The summer ST changes are largest under the RCP4.5 scenario, which contrast to Bengtsson et al. (2006), Chang et al. (2012) once the largest changes were found for the RCP8.5 scenario. The projected future changes show increases around Antarctica ( $\sim 60^\circ\text{S}$ ) of up to approximately 15% relative to the Historical experiment. Regionally, the RCP4.5 changes show increases over the Atlantic, through the Indian Ocean towards the Pacific Ocean at a latitude of ( $\sim 45^\circ\text{S}$ ). In the Atlantic Ocean, the growth of the RCP4.5 changes correspond to the genesis density increases over the north-

east of Argentina in SA for the RCP4.5 scenario. Also, there are increases in the track density changes over the Pacific Ocean at high latitudes in both the RCPs. Changes in the genesis densities are also linked to the future projected changes in cyclone track density discussed previously. The genesis density decreases over tropical latitudes of the Pacific Ocean and in two of the three climatological cyclogenesis regions in SA, in the south of Argentina and in the Atlantic Ocean close to the southeast of Brazil, compared to the Historical experiment. However, the HadGEM2-ES experiments show an increase in the future projected genesis density around the Antarctic coast and on the west coast of Australia. The genesis density increases in the north of Argentina and corresponds to the increase of the track density changes over the Atlantic Ocean, which is more evident in the RCP4.5 experiment. The lysis densities around the Antarctic coast have the largest projected increases under both the RCPs, with the maximum change near to the Antarctic Peninsula.

- The differences for the spring and autumn seasons of the projected ST changes under both the RCPs are similar to the preceding seasons, winter and summer, respectively. This is somewhat similar to the ST climatological patterns found in the Southern Hemisphere and seems associated with the large thermal inertia of the oceans. However, there is a linear decreasing poleward trend in the track density response in all seasons under the RCP8.5 scenario. These projected future changes in the RCP4.5 (minor radiative forcing) support the hypothesis that the feedback mechanisms may partially link these larger ST density changes in this scenario.

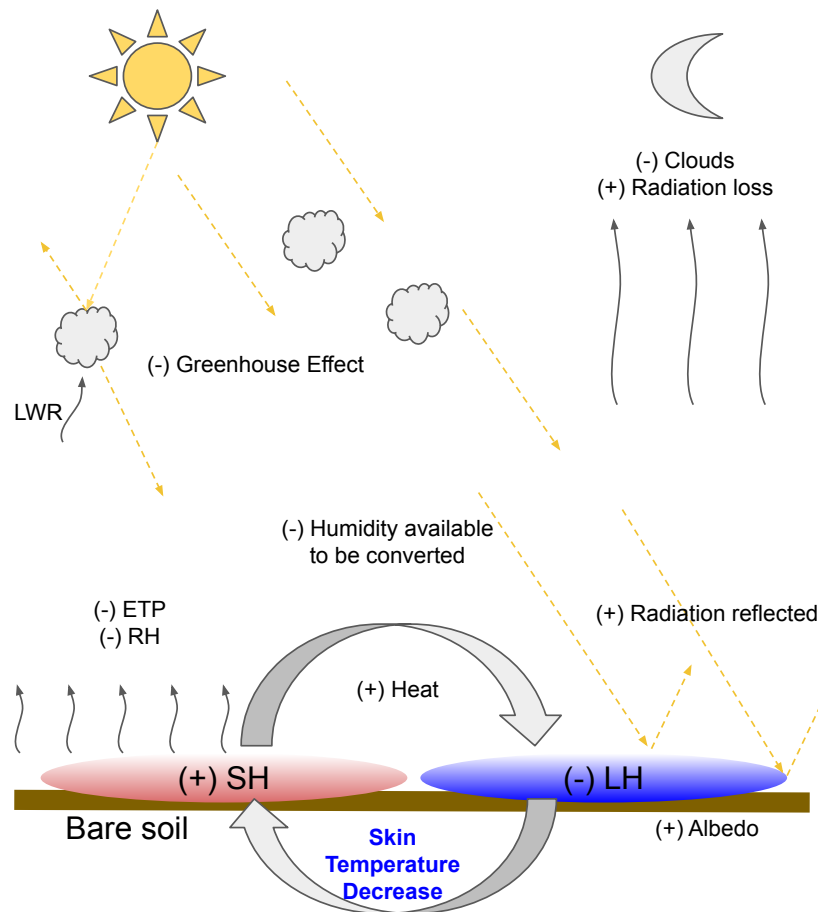
#### **6.2.4 How might Amazon land use cover change affect the storm track and climate over South America?**

The only difference between WAMZ and CTRL experiments is the removal of the Amazon Forest. Therefore, changes in the concentration of gases over time occur in both the experiments according to their respective RCP (RCP8.5 and RCP4.5).

The HadGEM2-ES climate model without the Amazon Forest (WAMZ) indicates future changes in the Southern Hemisphere storm track future projected changes similar to those indicated by HadGEM2-ES with the Amazon Forest (CTRL experiment), however the consistent poleward shift for both the RCP scenarios is smoothed. This conclusion is based on the results of the Chapter 5, as follows:

- The main spatial patterns of changes were discussed in the previous answer, however the ST changes in the WAMZ experiment show a consistent reduction in the poleward shift, compared with the CTRL experiment, with the track density showing smaller increases on the equatorward side and decreases on the poleward side. This corresponds to the track, genesis and lysis future projected changes in WAMZ experiments for both the RCPs.
- The poleward track density decreases under RCP8.5 in relation to the RCP4.5 scenario, which evidences that there are also a correlation with the emission scenarios. Therefore, not only the removal of the Amazon Forest reduces the poleward shift, but also the emission scenario. These changes agree with the results found by [Lorenz and DeWeaver \(2007\)](#), in which both tropical warming and polar cooling at upper levels increases the pole-to-equator temperature gradient and result in a rise in the height of the tropopause and a poleward shift in the zonal winds in mid-latitude circulation. The large and regional-scale patterns correspond well with the ST changes in WAMZ experiments in both the RCPs.
- The feedback mechanism seems stronger than the regional-scale changes, which explain the temperature change decrease in all seasons for both the scenarios. This feedback mechanism is shown in [Figure 6.1](#). Over the Amazon Forest region, after the removal of land cover and change to bare soil, the sensible heat increases and the surface accumulate more heat, which reduces the latent because there is less humidity available to be converted. Consequently, the evaporation reduces because there is no evapotranspiration and less humidity (only coming from adjacent oceans). In addition, the albedo increases and results in radiation loss to the atmosphere, which is enhanced by the the OLR increase (less clouds). During the night, the radiation loss and winds increase, which collaborates to create a positive feedback mechanism that acts to reduce the skin temperature.

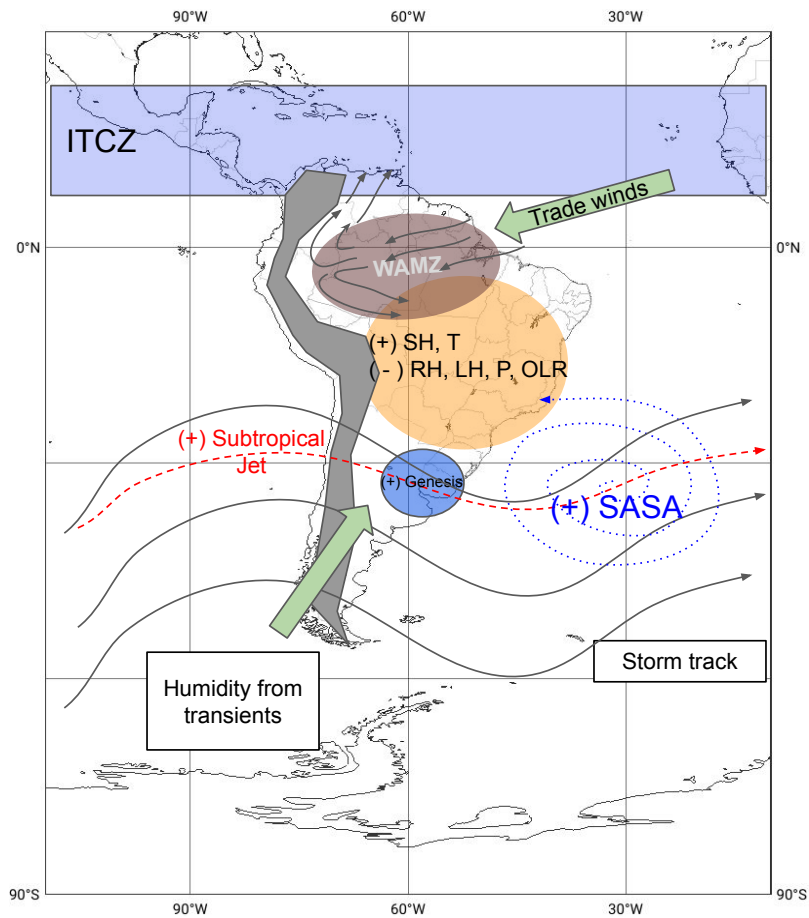
Figure 6.1 - Schematic of the positive feedback mechanism after the removal of Amazon Forest.



SOURCE: Author's production.

- During the winter and part of the spring season the ITCZ is displaced to the north which removes the humidity support over the north of SA. The trade winds increase due to less roughness (no obstacles), passing over the Amazon Forest region, until they fork when reach the Andes Mountains. This pattern is somewhat related to the large-scale changes and affects the sensible and latent heating, temperature, humidity, precipitation and OLR. In addition, the South Atlantic Subtropical Anticyclone (SASA) over the ocean is enhanced. This creates other resultant changes that affect directly the water cycle, shown as  $E - P$  changes. These circulations are shown in Figure 6.2.

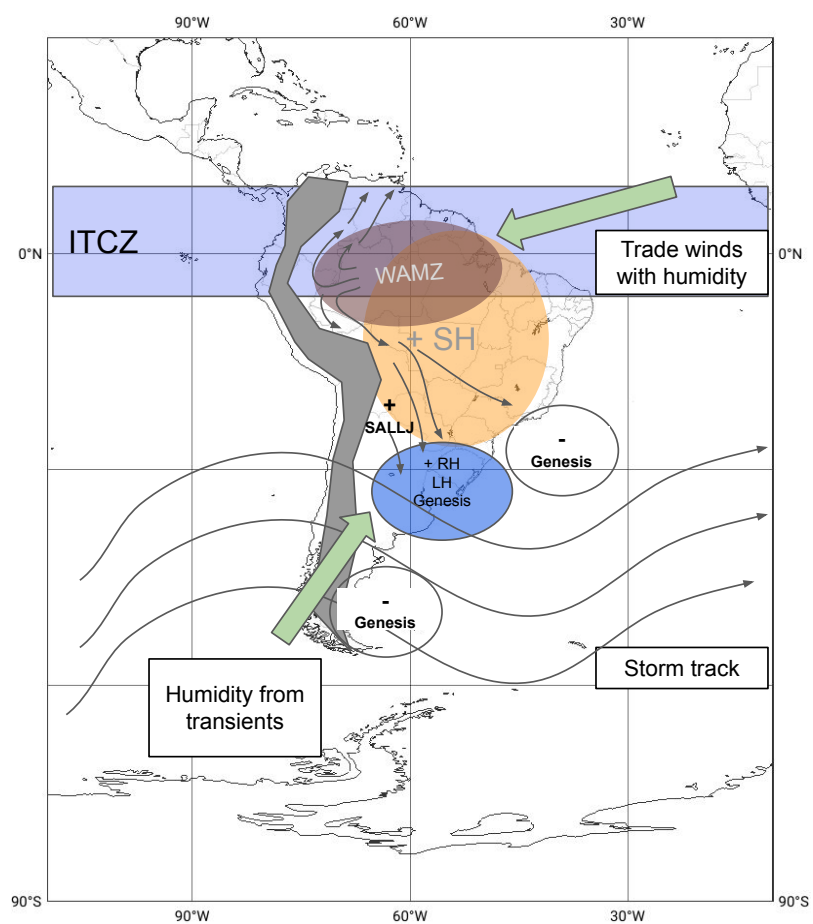
Figure 6.2 - Schematic of South America circulation for WAMZ experiment in winter.



SOURCE: Author's production.

- For summer and part of the autumn, the ITCZ is displaced to the south and gives some humidity support to the north of SA, thus it creates some small scale circulation over the Amazon region and enhances the SALLJ. The SALLJ is the most important humidity support for the centre-south of SA, however because of the removal of Amazon Forest it doesn't have humidity, which increases the sensible heat and temperature between the border of Brazil-Bolivia and centre-south of Brazil. Moreover, the SALLJ with strong winds contributes to enhance the wind shear over south of Brazil, Uruguay and north of Argentina, which may enhance the cyclogenesis and MCCs. These circulations are shown in Figure 6.3.

Figure 6.3 - Schematic of South America circulation for WAMZ experiment in summer.



SOURCE: Author's production.

### 6.3 Recommendations and future work

Some different experiments and analyses have been left for the future due to main aim of the thesis and the lack of time because the experiments with and without Amazon Forest are usually very time consuming, requiring up to 4 months to finish a single run. However, it is important that the land-atmosphere coupling and the feedbacks in the Earth system are well represented in the model used to run land use/change experiments (e.g. removal of the Amazon Forest). Future work concerns deeper analysis of particular mechanisms and new analyses with different methods, as follows:

- Investigate the effects of the removal of Amazon Forest in the Northern Hemisphere storm tracks, particularly in North Atlantic;
- Investigate the land cover changes and their impacts on the carbon cycle;
- Perform the same experiments using the new generation of the HadGEM climate model and other Earth system models that will participate in CMIP6;
- Investigate the low-level jet over South America (Low-Level Jet East of the Andes) in the CMIP6 protocol due to the high spatial resolution;
- Investigate the impact of the removal of the Amazon Forest on the El Nino Southern Oscillation, PSA, SAM, and change on the Australia blocking pattern;
- Investigate the impact of the removal of the Amazon Forest on the Ozone in the stratosphere, since during the analyses of the results temperature changes were observed in the lower stratosphere (between 30-1hPa, not shown).

## REFERENCES

ADAM, O.; SCHNEIDER, T.; HARNIK, N. Role of changes in mean temperatures versus temperature gradients in the recent widening of the Hadley circulation. **Journal of Climate**, v. 27, n. 19, p. 7450–7461, oct 2014. ISSN 08948755. 2, 20

ADLER, R. F.; HUFFMAN, G. J.; CHANG, A.; FERRARO, R.; XIE, P.-P.; JANOWIAK, J.; RUDOLF, B.; SCHNEIDER, U.; CURTIS, S.; BOLVIN, D.; GRUBER, A.; SUSSKIND, J.; ARKIN, P.; NELKIN, E. The Version-2 Global Precipitation Climatology Project (GPCP) monthly precipitation analysis (1979-present). **Journal of Hydrometeorology**, v. 4, n. 6, p. 1147–1167, 2003. ISSN 1525-755X. Available from:

<[http://dx.doi.org/10.1175/1525-7541\(2003\)004{ }3C1147:TVGPCP{ }3E2.0.CO{ }5Cn2](http://dx.doi.org/10.1175/1525-7541(2003)004{ }3C1147:TVGPCP{ }3E2.0.CO{ }5Cn2)>. 44

ADLER, R. F.; SAPIANO, M. R.; HUFFMAN, G. J.; WANG, J. J.; GU, G.; BOLVIN, D.; CHIU, L.; SCHNEIDER, U.; BECKER, A.; NELKIN, E.; XIE, P.; FERRARO, R.; SHIN, D. B. The Global Precipitation Climatology Project (GPCP) monthly analysis (New Version 2.3) and a review of 2017 global precipitation. **Atmosphere**, v. 9, n. 4, 2018. ISSN 20734433. 44

ALVES, L. **Análise estatística da sazonalidade e tendências das estações chuvosas e seca na Amazônia: clima presente e projeções futuras**. 158 p. PhD Thesis (Tese de Doutorado) — Instituto Nacional de Pesquisas Espaciais, São José dos Campos, 2016. 27, 168

ALVES, L. M.; MARENGO, J. A.; FU, R.; BOMBARDI, R. J. Sensitivity of Amazon regional climate to deforestation. **American Journal of Climate Change**, v. 06, n. 01, p. 75–98, 2017. ISSN 2167-9495. 26, 168, 169

BARNES, E. A.; BARNES, N. W.; POLVANI, L. M. Delayed southern hemisphere climate change induced by stratospheric ozone recovery, as projected by the CMIP5 models. **Journal of Climate**, v. 27, n. 2, p. 852–867, 2014. ISSN 08948755. 20, 33, 130, 146

BARNES, E. A.; GARFINKEL, C. I. Barotropic impacts of surface friction on Eddy kinetic energy and momentum fluxes: an alternative to the barotropic governor. **Journal of the Atmospheric Sciences**, v. 69, n. 10, p. 3028–3039, 2012. ISSN 0022-4928. 85

BARNES, E. A.; POLVANI, L. Response of the midlatitude jets, and of their variability, to increased greenhouse gases in the CMIP5 models. **Journal of Climate**, v. 26, n. 18, p. 7117–7135, 2013. ISSN 08948755. 196

BARRY, R.; CARLETON, A. **Synoptic and dynamic climatology**. [S.l.]: Psychology Press, 2001. 640 p. 9

BELLOUIN, N. et al. The HadGEM2 family of Met Office Unified Model Climate configurations. **Geoscientific Model Development Discussions**, v. 4, n. 2, p. 765–841, apr 2011. ISSN 1991-962X. Available from:  
<<http://www.geosci-model-dev-discuss.net/4/765/2011/>>. 30, 31, 33

BENGTSSON, L.; HODGES, K. I.; ROECKNER, E. Storm tracks and climate change. **Journal of Climate**, v. 19, n. 15, p. 3518–3543, 2006. ISSN 08948755. 1, 14, 45, 61, 96, 98, 99, 105, 196, 206

BERBERY, E. H.; BARROS, V. R. The hydrologic cycle of the La Plata Basin in South America. **Journal of Hydrometeorology**, v. 3, p. 630–645, 2002. ISSN 1525-755X. Available from:  
<[http://dx.doi.org/10.1175/1525-7541\(2002\)003{%-}3C0630:THCOTL{%-}3E2.0.CO;2](http://dx.doi.org/10.1175/1525-7541(2002)003{%-}3C0630:THCOTL{%-}3E2.0.CO;2)>. 10

BERBERY, E. H.; VERA, C. S. Characteristics of the Southern Hemisphere winter storm track with filtered and unfiltered data. **Journal of the Atmospheric Sciences**, feb 1996. ISSN 0022-4928. 1, 8, 10, 11, 28, 73

BETTS, R. A.; BOUCHER, O.; COLLINS, M.; COX, P. M.; FALLOON, P. D.; GEDNEY, N.; HEMMING, D. L.; HUNTINGFORD, C.; JONES, C. D.; SEXTON, D. M. H.; WEBB, M. J. Projected increase in continental runoff due to plant responses to increasing carbon dioxide. **Nature**, v. 448, n. 7157, p. 1037–1041, aug 2007. ISSN 0028-0836. Available from:  
<<http://www.nature.com/doifinder/10.1038/nature06045>>. 37

BETTS, R. A.; COX, P. M.; COLLINS, M.; HARRIS, P. P.; HUNTINGFORD, C.; JONES, C. D. The role of ecosystem-atmosphere interactions in simulated Amazonian precipitation decrease and forest dieback under global climate warming. **Theoretical and Applied Climatology**, v. 78, n. 1-3, p. 157–175, 2004. ISSN 0177798X. 26, 27

BETTS, R. A.; GOLDING, N.; GONZALEZ, P.; GORNALL, J.; KAHANA, R.; KAY, G.; MITCHELL, L.; WILTSHIRE, A. Climate and land use change impacts

on global terrestrial ecosystems and river flows in the HadGEM2-ES Earth system model using the representative concentration pathways. **Biogeosciences**, v. 12, n. 5, p. 1317–1338, 2015. ISSN 17264189. 37

BJERKNES, V.; SOLBERG, H. Life cycle of cyclones and the polar front theory of atmospheric circulation. **Geofysiske Publikasjoner**, v. 3, n. 1, p. 3–18, 1922. 59

BLACKMON, M. L. A climatological spectral study of the 500 mb geopotential height of the Northern Hemisphere. **Journal of the Atmospheric Sciences**, v. 33, n. 8, p. 1607–1623, aug 1976. ISSN 0022-4928. Available from: [http://journals.ametsoc.org/doi/abs/10.1175/1520-0469\(1976\)033<1607:ACSSOT%3E2.0.CO;2](http://journals.ametsoc.org/doi/abs/10.1175/1520-0469(1976)033<1607:ACSSOT%3E2.0.CO;2). 7, 8, 28

BLACKMON, M. L.; WALLACE, J. M.; LAU, N.-C.; MULLEN, S. L. An Observational Study of the Northern Hemisphere Wintertime Circulation. **Journal of the Atmospheric Sciences**, v. 34, n. 7, p. 1040–1053, 1977. ISSN 0022-4928. 1, 7, 8, 28

BLUESTEIN, H. B. **Synoptic-dynamic meteorology in midlatitudes. Volume II. Observations and theory of weather systems**. 2. ed. New York: Oxford University Press, 1993. 283 p. 8

BROVKIN, V.; BOYSEN, L.; ARORA, V. K.; BOISIER, J. P.; CADULE, P.; CHINI, L.; CLAUSSEN, M.; FRIEDLINGSTEIN, P.; GAYLER, V.; HURK, B. J. Van den; HURTT, G. C.; JONES, C. D.; KATO, E.; DUCOUDRE, N. De noblet; PACIFICO, F.; PONGRATZ, J.; WEISS, M. Effect of anthropogenic land-use and land-cover changes on climate and land carbon storage in CMIP5 projections for the twenty-first century. **Journal of Climate**, v. 26, n. 18, p. 6859–6881, sep 2013. ISSN 08948755. Available from: <http://journals.ametsoc.org/doi/abs/10.1175/JCLI-D-12-00623.1>. 23, 26

BUTCHART, N.; CHARLTON-PEREZ, A. J.; CIONNI, I.; HARDIMAN, S. C.; HAYNES, P. H.; KRÜGER, K.; KUSHNER, P. J.; NEWMAN, P. A.; OSPREY, S. M.; PERLWITZ, J.; SIGMOND, M.; WANG, L.; AKIYOSHI, H.; AUSTIN, J.; BEKKI, S.; BAUMGAERTNER, A.; BRAESICKE, P.; BRHL, C.; CHIPPERFIELD, M.; DAMERIS, M.; DHOMSE, S.; EYRING, V.; GARCIA, R.; GARNY, H.; JÖCKEL, P.; LAMARQUE, J. F.; MARCHAND, M.; MICHOU, M.; MORGENSTERN, O.; NAKAMURA, T.; PAWSON, S.; PLUMMER, D.; PYLE, J.; ROZANOV, E.; SCINOCCHA, J.; SHEPHERD, T. G.; SHIBATA, K.; SMALE,

D.; TEYSSÈDRE, H.; TIAN, W.; WAUGH, D.; YAMASHITA, Y. Multimodel climate and variability of the stratosphere. **Journal of Geophysical Research Atmospheres**, v. 116, n. 5, p. 1–21, 2011. ISSN 01480227. 86

BUTLER, A. H.; THOMPSON, D. W.; HEIKES, R. The steady-state atmospheric circulation response to climate change-like thermal forcings in a simple general circulation model. **Journal of Climate**, v. 23, n. 13, p. 3474–3496, jul 2010. ISSN 08948755. Available from:

<<http://journals.ametsoc.org/doi/abs/10.1175/2010JCLI3228.1>>. 19

CAI, W.; RENSCH, P. van; COWAN, T.; HENDON, H. H. Teleconnection pathways of ENSO and the IOD and the mechanisms for impacts on Australian rainfall. **Journal of Climate**, v. 24, n. 15, p. 3910–3923, 2011. ISSN 08948755. 73

CARLETON, A. M. Monthly variability of satellite-derived cyclonic activity for the southern hemisphere winter. **Journal of Climatology**, v. 1, n. 1, p. 21–38, jan 1981. ISSN 01961748. Available from:

<<http://doi.wiley.com/10.1002/joc.3370010105>>. 11

CATTO, J. L. Extratropical cyclone classification and its use. **Reviews of Geophysics**, p. 486–520, 2016. ISSN 87551209. 14

CATTO, J. L.; SHAFFREY, L. C.; HODGES, K. I. Can climate models capture the structure of extratropical cyclones? **Journal of Climate**, v. 23, n. 7, p. 1621–1635, apr 2010. ISSN 08948755. Available from:

<<http://journals.ametsoc.org/doi/abs/10.1175/2009JCLI3318.1>>. 1, 14

\_\_\_\_\_. Northern Hemisphere Extratropical Cyclones in a Warming Climate in the HiGEM High-Resolution Climate Model. **Journal of Climate**, v. 24, n. 20, p. 5336–5352, oct 2011. ISSN 0894-8755. Available from:

<<http://journals.ametsoc.org/doi/abs/10.1175/2011JCLI4181.1>>. 1, 14

CAVALCANTI, I. F. A. et al. **Tempo e clima no Brasil**. São Paulo, Brasil: Oficina de Textos, 2009. 463 p. 2, 10, 199

CEPPI, P.; HARTMANN, D. L. On the speed of the Eddy-driven Jet and the width of the Hadley Cell in the Southern Hemisphere. **Journal of Climate**, v. 26, n. 10, p. 3450–3465, may 2013. ISSN 08948755. 2, 20

CHANG, E. K. Downstream development of baroclinic waves as inferred from regression analysis. **Journal of the Atmospheric Sciences**, v. 50, n. 13, p. 2038–2053, 1993. ISSN 0022-4928. 9, 54, 202

\_\_\_\_\_. Projected significant increase in the number of extreme Extratropical Cyclones in the Southern Hemisphere. **Journal of Climate**, v. 30, n. 13, p. 4915–4935, 2017. ISSN 08948755. 159

CHANG, E. K. M. Characteristics of wave packets in the Upper Troposphere. Part II: Seasonal and Hemispheric Variations. **Journal of the Atmospheric Sciences**, v. 56, n. 11, p. 1729–1747, 1999. ISSN 0022-4928. 73, 81

\_\_\_\_\_. CMIP5 projection of significant reduction in extratropical cyclone activity over North America. **Journal of Climate**, v. 26, n. 24, p. 9903–9922, 2013. ISSN 08948755. 1, 103, 196, 205

CHANG, E. K. M.; FU, Y. Interdecadal variations in Northern Hemisphere winter storm track intensity. **Journal of Climate**, v. 15, n. 6, p. 642–658, 2002. ISSN 08948755. 8, 28

CHANG, E. K. M.; GUO, Y.; XIA, X. CMIP5 multimodel ensemble projection of storm track change under global warming. **Journal of Geophysical Research Atmospheres**, v. 117, n. 23, p. 1–19, 2012. ISSN 01480227. 105, 110, 206

CHANG, E. K. M.; GUO, Y.; XIA, X.; ZHENG, M. Storm-track activity in IPCC AR4/CMIP3 model simulations. **Journal of Climate**, v. 26, n. 1, p. 246–260, jan 2013. ISSN 0894-8755. Available from:  
<<http://journals.ametsoc.org/doi/abs/10.1175/JCLI-D-11-00707.1>>. 96, 98, 99, 105, 206

CHANG, E. K. M.; YU, D. B. Characteristics of wave packets in the upper troposphere. Part I: Northern Hemisphere winter. **Journal of the Atmospheric Sciences**, v. 56, n. 11, p. 1708–1728, jun 1999. ISSN 0022-4928. 10, 11

CHARLTON-PEREZ, A. J.; BALDWIN, M. P.; BIRNER, T.; BLACK, R. X.; BUTLER, A. H.; CALVO, N.; DAVIS, N. A.; GERBER, E. P.; GILLETT, N.; HARDIMAN, S.; KIM, J.; KRÜGER, K.; LEE, Y. Y.; MANZINI, E.; MCDANIEL, B. A.; POLVANI, L.; REICHLER, T.; SHAW, T. A.; SIGMOND, M.; SON, S. W.; TOOHEY, M.; WILCOX, L.; YODEN, S.; CHRISTIANSEN, B.; LOTT, F.; SHINDELL, D.; YUKIMOTO, S.; WATANABE, S. On the lack of stratospheric dynamical variability in low-top versions of the CMIP5 models. **Journal of Geophysical Research Atmospheres**, v. 118, n. 6, p. 2494–2505, 2013. ISSN 21698996. 85

CHARNEY, J.; STONE, P. H.; QUIRK, W. J. Drought in the Sahara: a biogeophysical feedback mechanism. **Science**, v. 187, n. 4175, p. 434–435, 1975. ISSN 0036-8075. 2

CHARNEY, J. G. The dynamics of long waves in a baroclinic westerly current. **Journal of Meteorology**, v. 4, n. 5, p. 136–162, oct 1947. ISSN 0095-9634. Available from: <[http://journals.ametsoc.org/doi/abs/10.1175/1520-0469\(1947\)004{%-}3C0136:TDOLWI{%-}3E2.0.CO;2](http://journals.ametsoc.org/doi/abs/10.1175/1520-0469(1947)004{%-}3C0136:TDOLWI{%-}3E2.0.CO;2)>. 8

CHARNOCK, H. Wind stress on a water surface. **Quarterly Journal of the Royal Meteorological Society**, v. 81, n. 350, p. 639–640, oct 1955. ISSN 00359009. Available from: <<http://doi.wiley.com/10.1002/qj.49708135027>>. 86

CHEN, G.; HELD, I. M.; ROBINSON, W. A. Sensitivity of the latitude of the surface westerlies to surface friction. **Journal of the Atmospheric Sciences**, v. 64, n. 8, p. 2899–2915, 2007. ISSN 0022-4928. 86

CHENOLI, S. N. et al. Historical and projected changes in the Southern Hemisphere Sub-tropical Jet during winter from the CMIP5 models. **Climate Dynamics**, v. 48, n. 1-2, p. 661–681, 2017. ISSN 14320894. 128, 145

CLARKE, L. E.; EDMONDS, J. A.; JACOBY, H. D.; PITCHER, H. M.; REILLY, J. M.; RICHEL, R. G. **Scenarios of greenhouse gas emissions and atmospheric concentrations**. [S.l.], 2007. 164 p. (Synthesis and Assessment Product 2.1 by the U.S. Climate Change Science Program and the Subcommittee on Global Change Research, July). Available from: <<http://www.ncbi.nlm.nih.gov/pubmed/22275275>>. 21

COLLINS, W. J.; BELLOUIN, N.; DOUTRIAUX-BOUCHER, M.; GEDNEY, N.; HALLORAN, P.; HINTON, T.; HUGHES, J.; JONES, C. D.; JOSHI, M.; LIDDICOAT, S.; MARTIN, G.; O'CONNOR, F.; RAE, J.; SENIOR, C.; SITCH, S.; TOTTERDELL, I.; WILTSHIRE, A.; WOODWARD, S. Development and evaluation of an Earth-System model - HadGEM2. **Geoscientific Model Development**, v. 4, n. 4, p. 1051–1075, 2011. ISSN 1991-9603. Available from: <<http://www.geosci-model-dev.net/4/1051/2011/>>. 31, 32, 33

COSTA, M. H.; YANAGI, S. N.; SOUZA, P. J.; RIBEIRO, A.; ROCHA, E. J. Climate change in Amazonia caused by soybean cropland expansion, as compared to caused by pastureland expansion. **Geophysical Research Letters**, v. 34, n. 7, p. 2–5, 2007. ISSN 00948276. 27

COX, P. M. **Description of the "TRIFFID" dynamic global vegetation model, Hadley Centre. Technical Note 24.** Exeter - UK, 2001. 17 p. 32, 34, 35, 36

COX, P. M.; BETTS, R. A.; JONES, C. D.; SPALL, S. A.; TOTTERDELL, I. J. Acceleration of global warming due to carbon-cycle feedbacks in a coupled climate model. **Nature**, v. 408, p. 184–187, 2000. 31, 35

CUBASCH, U.; WUEBBLES, D.; CHEN, D.; FACCHINI, M.; FRAME, D.; MAHOWALD, N.; WINTHER, J. Introduction. In: **INTERGOVERNMENTAL PANEL ON CLIMATE CHANGE. Climate Change 2013 - The Physical Science Basis.** Geneva: IPCC: [s.n.], 2013. p. 119–158. ISBN ISBN 978-1-107-66182-0. Available from: <http://srren.ipcc-wg3.de/report/IPCC{ }SRREN{ }Ch02.pdf><http://ebooks.cambridge.org/ref/id/CB09781107415324A015>>. 16, 18, 40

DAI, A.; QIAN, T.; TRENBERTH, K. E.; MILLIMAN, J. D. Changes in continental freshwater discharge from 1948 to 2004. **Journal of Climate**, v. 22, n. 10, p. 2773–2792, may 2009. ISSN 0894-8755. Available from: <http://journals.ametsoc.org/doi/abs/10.1175/2008JCLI2592.1>>. 27

D'ALMEIDA, C.; VÖRÖSMARTY, C. J.; HURTT, G. C.; MARENGO, J. A.; DINGMAN, S. L.; KEIM, B. D. The effects of deforestation on the hydrological cycle in Amazonia: a review on scale and resolution. **International Journal of Climatology**, v. 27, n. 5, p. 633–647, apr 2007. ISSN 08998418. Available from: <http://doi.wiley.com/10.1002/joc.1475>>. 27

DAVIES-BARNARD, T.; VALDES, P. J.; SINGARAYER, J. S.; PACIFICO, F. M.; JONES, C. D. Full effects of land use change in the representative concentration pathways. **Environmental Research Letters**, v. 9, n. 11, p. 114014, nov 2014. ISSN 1748-9326. Available from: <http://stacks.iop.org/1748-9326/9/i=11/a=114014?key=crossref.7d48f87396d830ca0fac6d9e8a4f1fe8>>. 21

DEE, D. P.; UPPALA, S. M.; SIMMONS, A. J.; BERRISFORD, P.; POLI, P.; KOBAYASHI, S.; ANDRAE, U.; BALMASEDA, M. A.; BALSAMO, G.; BAUER, P.; BECHTOLD, P.; BELJAARS, A. C. M.; BERG, L. van de; BIDLOT, J.; BORMANN, N.; DELSOL, C.; DRAGANI, R.; FUENTES, M.; GEER, A. J.; HAIMBERGER, L.; HEALY, S. B.; HERSBACH, H.; HÓLM, E. V.; ISAKSEN, I.; KÅLLBERG, P.; KÖHLER, M.; MATRICARDI, M.; MCNALLY, A. P.;

MONGE-SANZ, B. M.; MORCRETTE, J.-J.; PARK, B.-K.; PEUBEY, C.; ROSNAY, P. de; TAVOLATO, C.; THÉPAUT, J.-N.; VITART, F. The ERA-Interim reanalysis: configuration and performance of the data assimilation system. **Quarterly Journal of the Royal Meteorological Society**, v. 137, n. 656, p. 553–597, apr 2011. ISSN 00359009. Available from: <<http://doi.wiley.com/10.1002/qj.828>>. 43, 44

EADY, E. T. Long waves and cyclone waves. **Tellus A**, 1949. ISSN 0280-6495. 8, 51

EDSON, J. B.; WELLER, R. A.; VICKERS, D.; MAHRT, L.; HERSBACH, H.; BIGORRE, S. P.; PLUEDDEMANN, A. J.; FAIRALL, C. W.; MILLER, S. D.; JAMPANA, V. On the exchange of momentum over the open ocean. **Journal of Physical Oceanography**, v. 43, n. 8, p. 1589–1610, 2013. ISSN 0022-3670. 86

EDWARDS, P. N. History of climate modeling. **Wiley Interdisciplinary Reviews: Climate Change**, v. 2, n. 1, p. 128–139, jan 2011. ISSN 17577780. Available from: <<http://doi.wiley.com/10.1002/wcc.95>>. 18

ELLIS, E. C. Anthropogenic transformation of the terrestrial biosphere. **Philosophical Transactions of the Royal Society A: Mathematical, Physical and Engineering Sciences**, v. 369, n. 1938, p. 1010–1035, 2011. ISSN 1364503X. 25

ENFIELD, D. B.; MESTAS-NUÑEZ, A. M.; TRIMBLE, P. J. The Atlantic Multidecadal Oscillation and its relation to rainfall and river flows in the continental U.S. **Geophysical Research Letters**, v. 28, n. 10, p. 2077–2080, may 2001. ISSN 00948276. Available from: <<http://doi.wiley.com/10.1029/2000GL012745>>. 38

ESSERY, R. L. H.; BEST, M. J.; BETTS, R. A.; COX, P. M.; TAYLOR, C. M. Explicit representation of subgrid heterogeneity in a GCM land surface scheme. **Journal of Hydrometeorology**, v. 4, n. 3, p. 530–543, 2003. ISSN 1525-755X. Available from: <[http://journals.ametsoc.org/doi/abs/10.1175/1525-7541\(2003\)004{%-}3C0530:EROSHI{%-}3E2.O.CO;2](http://journals.ametsoc.org/doi/abs/10.1175/1525-7541(2003)004{%-}3C0530:EROSHI{%-}3E2.O.CO;2)>. 34

FIGUEROA, S.; NOBRE, C. A. Precipitation distribution over central and western tropical South America. *Climanálise*. **Climanalise**, 1990. 27

FISCH, G.; MARENGO, J. A.; NOBRE, C. A. Uma revisão geral sobre o clima da Amazônia. **Acta Amazonica**, v. 28, n. 2, p. 101–101, jun 1998. ISSN 0044-5967.

Available from: <[http://www.scielo.br/scielo.php?script=sci\\_arttext&pid=S0044-59671998000200101&lng=pt&tlng=pt](http://www.scielo.br/scielo.php?script=sci_arttext&pid=S0044-59671998000200101&lng=pt&tlng=pt)>. 27

FLATO, G.; MAROTZKE, J.; ABIODUN, B.; BRACONNOT, P.; CHOU, S.; COLLINS, W.; COX, P.; DRIOUECH, F.; EMORI, S.; EYRING, V.; FOREST, C.; GLECKLER, P.; GUILYARDI, E.; JAKOB, C.; KATTSOV, V.; REASON, C.; RUMMUKAINEN, M. Climate Change 2013 - The Physical Science Basis.

**Climate Change 2013 - The Physical Science Basis**, p. 741–866, 2014. ISSN 1476-4687. 38

FOLEY, J. A.; COSTA, M. H. Combined effects of deforestation and doubled atmospheric CO<sub>2</sub> concentrations on the climate of Amazonia. **Journal of Climate**, v. 13, n. 1, p. 18–34, 2000. Available from:

<[https://journals.ametsoc.org/doi/full/10.1175/1520-0442\(2000\)013%3C0018:CEODAD%3E2.0.CO;2](https://journals.ametsoc.org/doi/full/10.1175/1520-0442(2000)013%3C0018:CEODAD%3E2.0.CO;2)><http://ams.allenpress.com/archive/1520-0442/13/1/pdf/i1520-0442-13-1-18.pdf>>. 168

FUJINO, J.; NAIR, R.; KAINUMA, M.; MASUI, T.; MATSUOKA, Y. Multi-gas mitigation analysis on stabilization scenarios using aim global model. **Energy Journal**, v. 27, p. 343–353, 2006. ISSN 01956574. 21

FYFE, J. C. Extratropical Southern Hemisphere cyclones: harbingers of climate change? **Journal of Climate**, v. 16, n. 17, p. 2802–2805, sep 2003. ISSN 0894-8755. 20, 54, 202

GALLEGO, D.; RIBERA, P.; GARCIA-HERRERA, R. A new look for the Southern Hemisphere jet stream. **Climate Dynamics**, v. 24, n. 6, p. 607–621, mar 2005. ISSN 0930-7575. Available from:

<<http://www.springerlink.com/index/10.1007/s00382-005-0006-7><http://www.springerlink.com/index/T287522233807876.pdf>>. 12

GAN, M. A. **Ciclogêneses e ciclones sobre a América do Sul**. 185 p. PhD Thesis (Tese de Doutorado) — Instituto Nacional de Pesquisas Espaciais, São José dos Campos, 1992. 13

GAN, M. A.; RAO, V. B. Surface Cyclogenesis over South America. **Monthly Weather Review**, v. 119, n. 5, p. 1293–1302, may 1991. ISSN 0027-0644. 1, 54, 59, 96

\_\_\_\_\_. **The Influence of the Andes Cordillera on Transient Disturbances**. 1994. 1141–1157 p. 10, 54

\_\_\_\_\_. Case studies of cyclogenesis over South America. **Meteorological Applications**, v. 3, n. 4, p. 359–367, jan 1996. ISSN 13504827. Available from: <<http://doi.wiley.com/10.1002/met.5060030410>>. 10, 54

GARFINKEL, C. I.; MOLOD, A. M.; OMAN, L. D.; WAUGH, D. W.; HURWITZ, M. H.; BARNES, E. A. Connections between the Spring Breakup of the Southern Hemisphere Polar Vortex, Stationary Waves, and Air-Sea Roughness. **Journal of the Atmospheric Sciences**, v. 70, n. 7, p. 2137–2151, 2013. ISSN 0022-4928. 85, 86

GARFINKEL, C. I.; OMAN, L. D. Effect of gravity waves from small islands in the Southern Ocean on the Southern Hemisphere atmospheric circulation. **Journal of Geophysical Research: Atmospheres**, v. 123, n. 3, p. 1552–1561, 2018. ISSN 21698996. 86

GERBER, E. P.; SON, S. W. Quantifying the summertime response of the Austral jet stream and hadley cell to stratospheric ozone and greenhouse gases. **Journal of Climate**, v. 27, n. 14, p. 5538–5559, 2014. ISSN 08948755. 130, 147

GOMES, H. B.; AMBRIZZI, T.; HERDIES, D. L.; HODGES, K.; SILVA, B. F. P. da. Easterly wave disturbances over Northeast Brazil: An observational analysis. **Advances in Meteorology**, v. 2015, p. 1–20, 2015. ISSN 1687-9309. Available from: <<http://www.hindawi.com/journals/amete/2015/176238/>>. 60, 203

GUIA, C. V. F. da. **Análises das características sinóticas das trajetórias dos ciclones extratropicais que atuam na América do Sul e vizinhanças**. Dissertação (Mestrado em Meteorologia) - Instituto Nacional de Pesquisas Espaciais, São José dos Campos, 2010. 120 p. Available from: <<http://urlib.net/sid.inpe.br/mtc-m19/2010/11.26.17.17>>. 45, 53

HARTMANN, D. L. et al. Observations: Atmosphere and surface. In: **Climate Change 2013 the Physical Science Basis: Working Group I Contribution to the Fifth Assessment Report of the Intergovernmental Panel on Climate Change**. Geneva: IPCC, 2013. ISBN 9781107415324. 14

HARVEY, B. J.; SHAFFREY, L. C.; WOOLLINGS, T. J. Equator-to-pole temperature differences and the extra-tropical storm track responses of the CMIP5 climate models. **Climate Dynamics**, v. 43, n. 5-6, p. 1171–1182, 2014. ISSN 14320894. 19, 103, 196, 197, 205

HAWCROFT, M.; DACRE, H.; FORBES, R.; HODGES, K.; SHAFFREY, L.; STEIN, T. Using satellite and reanalysis data to evaluate the representation of

latent heating in extratropical cyclones in a climate model. **Climate Dynamics**, v. 48, n. 7-8, p. 2255–2278, apr 2017. ISSN 0930-7575. Available from: <<http://link.springer.com/10.1007/s00382-016-3204-6>>. 1

HELD, I. M. Large-scale dynamics and global warming. **Bulletin of the American Meteorological Society**, v. 74, n. 2, p. 228–241, feb 1993. ISSN 0003-0007. Available from: <[http://journals.ametsoc.org/doi/abs/10.1175/1520-0477\(1993\)29074\(3C0228\)3ALSDAGW\(3E2.0.CO\(3\)3B2](http://journals.ametsoc.org/doi/abs/10.1175/1520-0477(1993)29074(3C0228)3ALSDAGW(3E2.0.CO(3)3B2)>. 19

HELD, I. M.; SODEN, B. J. Robust responses of the hydrological cycle to global warming. **Journal of Climate**, v. 19, n. 21, p. 5686–5699, nov 2006. ISSN 0894-8755. Available from: <<http://journals.ametsoc.org/doi/abs/10.1175/JCLI3990.1>>. 19

HIJIOKA, Y.; MATSUOKA, Y.; NISHIMOTO, H.; MASUI, T.; KAINUMA, M. Global GHG emission scenarios under GHG concentration stabilization targets. **Journal of Global Environment Engineering**, v. 13, p. 97–108, 2008. ISSN 13411268. 21

HODGES, K. I. A general method for tracking analysis and its application to meteorological data. **Monthly Weather Review**, v. 122, n. 11, p. 2573–2586, nov 1994. ISSN 0027-0644. 8, 28, 45, 46

\_\_\_\_\_. Feature tracking on the unit sphere. **Monthly Weather Review**, v. 123, n. 12, p. 3458–3465, 1995. ISSN 0027-0644. 45, 48

\_\_\_\_\_. Spherical nonparametric estimators applied to the UGAMP Model Integration for AMIP. **Monthly Weather Review**, v. 124, n. 12, p. 2914–2932, dec 1996. ISSN 0027-0644. Available from:

<[http://centaur.reading.ac.uk/166/http://journals.ametsoc.org/doi/abs/10.1175/1520-0493\(1996\)124\(3C2914:SNEATT\(3E2.0.CO;2](http://centaur.reading.ac.uk/166/http://journals.ametsoc.org/doi/abs/10.1175/1520-0493(1996)124(3C2914:SNEATT(3E2.0.CO;2)>. 45, 48

\_\_\_\_\_. Adaptive constraints for feature tracking. **Monthly Weather Review**, v. 127, n. 6, p. 1362–1373, jun 1999. ISSN 0027-0644. Available from: <[http://centaur.reading.ac.uk/163/http://journals.ametsoc.org/doi/abs/10.1175/1520-0493\(1999\)127\(3C1362:ACFFT\(3E2.0.CO;2](http://centaur.reading.ac.uk/163/http://journals.ametsoc.org/doi/abs/10.1175/1520-0493(1999)127(3C1362:ACFFT(3E2.0.CO;2)>. 8, 28, 45, 46, 47, 48

HODGES, K. I.; HOSKINS, B. J.; BOYLE, J.; THORNCROFT, C. A comparison of recent reanalysis datasets using objective feature tracking: Storm Tracks and Tropical Easterly Waves. **Monthly Weather Review**, v. 131, n. 9, p. 2012–2037, sep 2003. ISSN 0027-0644. 45

HODGES, K. I.; LEE, R. W.; BENGTTSSON, L. A comparison of extratropical cyclones in recent reanalyses ERA-Interim, NASA MERRA, NCEP CFSR, and JRA-25. **Journal of Climate**, v. 24, n. 18, p. 4888–4906, sep 2011. ISSN 0894-8755. Available from:

<<http://journals.ametsoc.org/doi/abs/10.1175/2011JCLI4097.1>>. 1, 14, 45, 49, 50, 53, 54, 61, 90, 91, 93, 96, 98, 159, 202

HOLTON, J. R. **An introduction to dynamic meteorology**. [S.l.]: Elsevier Academic Press, 2004. 553 p. ISBN 0123540151. 7, 8, 9

HOSKINS, B. J.; AMBRIZZI, T. Rossby Wave Propagation on a Realistic Longitudinally Varying Flow. **Journal of the Atmospheric Sciences**, v. 50, n. 12, p. 1661–1671, jun 1993. ISSN 0022-4928. 73

HOSKINS, B. J.; HODGES, K. I. New Perspectives on the Northern Hemisphere Winter Storm Tracks. **Journal of the Atmospheric Sciences**, v. 59, n. 6, p. 1041–1061, mar 2002. ISSN 0022-4928. 8, 45, 48

\_\_\_\_\_. A new perspective on Southern Hemisphere Storm Tracks. **Journal of Climate**, v. 18, n. 20, p. 4108–4129, oct 2005. ISSN 0894-8755. Available from: <<http://journals.ametsoc.org/doi/abs/10.1175/JCLI3570.1>>. 1, 2, 8, 10, 12, 13, 45, 53, 54, 59, 60, 73, 81, 96, 146, 202, 203

HOSKINS, B. J.; MCINTYRE, M. E.; ROBERTSON, A. W. On the use and significance of isentropic potential vorticity maps. **Quarterly Journal of the Royal Meteorological Society**, v. 111, n. 470, p. 877–946, aug 1985. ISSN 00359009. Available from: <<http://doi.wiley.com/10.1002/qj.49711147002>>. 1

HOSKINS, B. J.; VALDES, P. J. On the existence of Storm-tracks. **Journal of the Atmospheric Sciences**, v. 47, n. 15, p. 1854–1864, aug 1990. ISSN 0022-4928. 1, 9, 51

HURRELL, J. W.; LOON, H. van; SHEA, D. J. The mean state of the Troposphere. In: KAROLY, D. J.; VINCENT, D. G. (Ed.). **Meteorology of the Southern Hemisphere**. Boston, MA: American Meteorological Society, 1998. p. 1–46. ISBN 978-1-935704-10-2. Available from: <[https://doi.org/10.1007/978-1-935704-10-2\\_{\\_}1](https://doi.org/10.1007/978-1-935704-10-2_{_}1)>. 45

HURTT, G. C. et al. Harmonization of land-use scenarios for the period 1500 - 2100: 600 years of global gridded annual land-use transitions, wood harvest, and

resulting secondary lands. **Climatic Change**, v. 109, n. 1-2, p. 117–161, aug 2011. ISSN 0165-0009. Available from:

<<http://link.springer.com/10.1007/s10584-011-0153-2>>. 23, 26, 39

INATSU, M. The neighbor enclosed area tracking algorithm for extratropical wintertime cyclones. **Atmospheric Science Letters**, v. 10, n. October, 2009. ISSN 1530261X. Available from: <<http://doi.wiley.com/10.1002/asl.238>>. 8, 28

INATSU, M.; HOSKINS, B. J. The zonal asymmetry of the Southern Hemisphere winter storm track. **Journal of Climate**, v. 17, n. 24, p. 4882–4892, 2004. ISSN 08948755. 10, 12, 54, 202

\_\_\_\_\_. The seasonal and wintertime interannual variability of the Split Jet and the Storm-track activity minimum near New Zealand. **Journal of the Meteorological Society of Japan**, v. 84, n. 3, p. 433–445, 2006. ISSN 0026-1165. Available from: <<http://joi.jlc.jst.go.jp/JST.JSTAGE/jmsj/84.433?from=CrossRef>>. 54, 73, 81

INTERGOVERNMENTAL PANEL ON CLIMATE CHANGE (IPCC). **Climate change 2001: the scientific basis: contribution of the Working Group I to the third assessment report of the Intergovernmental Panel on Climate Change**. Geneva: IPCC, 2001. 881 p. ISBN 0521014956. Available from: <<http://www.cambridge.org/uk/earthsciences/climatechange/scientific.htm>>. 40

\_\_\_\_\_. IPCC Fourth Assessment Report (AR4). **IPCC**, v. 1, p. 976, 2007. Available from: <[http://www.ipcc.ch/publications\\_and\\_data/publications\\_ipcc\\_fourth\\_assessment\\_report\\_wg2\\_report\\_impacts\\_adaptation/](http://www.ipcc.ch/publications_and_data/publications_ipcc_fourth_assessment_report_wg2_report_impacts_adaptation/)>. 40

\_\_\_\_\_. Working Group I Contribution to the IPCC Fifth Assessment Report - Summary for Policymakers. In: **Climate Change 2013: The Physical Science Basis**. [s.n.], 2013. p. 1–36. Available from: <<http://eprints.utas.edu.au/4774/>>. 1, 2, 3, 26, 38, 128

IPCC Expert Meeting Report. **Towards New Scenarios for Analysis of Emissions, Climate Change, Impacts and Response Strategies**. Intergovernmental Panel on Climate Change, 2007. 132 p. Available from: <<http://www.ipcc.ch/pdf/expert-meeting-report/>>

[//www.osti.gov/energycitations/product.biblio.jsp?osti\\_id=940991](http://www.osti.gov/energycitations/product.biblio.jsp?osti_id=940991)>. 20

IPCC WORKING GROUP 1, I.; STOCKER, T.; QIN, D.; PLATTNER, G.-K.; TIGNOR, M.; ALLEN, S.; BOSCHUNG, J.; NAUELS, A.; XIA, Y.; BEX, V.; MIDGLEY, P. INTERGOVERNMENTAL PANEL ON CLIMATE CHANGE (IPCC): Climate Change 2013: The physical science basis. Contribution of Working Group I to the Fifth Assessment Report of the Intergovernmental Panel on Climate Change. **IPCC**, AR5, p. 1535, 2013. 14

JOHNS, T. C.; DURMAN, C. F.; BANKS, H. T.; ROBERTS, M. J.; MCLAREN, A. J.; RIDLEY, J. K.; SENIOR, C. A.; WILLIAMS, K. D.; JONES, A.; RICKARD, G. J.; CUSACK, S.; INGRAM, W. J.; CRUCIFIX, M.; SEXTON, D. M.; JOSHI, M. M.; DONG, B. W.; SPENCER, H.; HILL, R. S.; GREGORY, J. M.; KEEN, A. B.; PARDAENS, A. K.; LOWE, J. A.; BODAS-SALCEDO, A.; STARK, S.; SEARL, Y. The new Hadley Centre Climate Model (HadGEM1): evaluation of coupled simulations. **Journal of Climate**, v. 19, n. 7, p. 1327–1353, 2006. ISSN 08948755. 31

JONES, C. D. et al. **The HadGEM2-ES implementation of CMIP5 centennial simulations**. 2011. 689–763 p. 30, 38

JONES, P. D.; HARPHAM, C. Estimation of the absolute surface air temperature of the Earth. **Journal of Geophysical Research: Atmospheres**, v. 118, n. 8, p. 3213–3217, apr 2013. ISSN 2169897X. Available from: <<http://doi.wiley.com/10.1002/jgrd.50359>>. 72

KIDSTON, J.; VALLIS, G. K. The Relationship between the Speed and the Latitude of an Eddy-Driven Jet in a Stirred Barotropic Model. **Journal of the Atmospheric Sciences**, v. 69, n. 11, p. 3251–3263, 2012. ISSN 0022-4928. Available from: <<http://journals.ametsoc.org/doi/abs/10.1175/JAS-D-11-0300.1>>. 73, 86

KNUTTI, R. The end of model democracy? **Climatic Change**, v. 102, n. 3-4, p. 395–404, 2010. ISSN 0165-0009. 15

KONIG, W.; SAUSEN, R.; SIELMANN, F. Objective identification of cyclones in GCM simulations. **Journal of Climate**, v. 6, n. 12, p. 2217–2231, 1993. ISSN 08948755. 8, 28

KORTY, R. L.; SCHNEIDER, T. Extent of Hadley circulations in dry atmospheres. **Geophysical Research Letters**, v. 35, n. 23, p. L23803, dec 2008.

ISSN 0094-8276. Available from:

<<http://doi.wiley.com/10.1029/2008GL035847>>. 2, 20

LAMBERT, S.; SHENG, J.; BOYLE, J. Winter cyclone frequencies in thirteen models participating in the Atmospheric Model Intercomparison Project (AMIP1). **Climate Dynamics**, v. 19, n. 1, p. 1–16, may 2002. ISSN 0930-7575. Available from: <<http://link.springer.com/10.1007/s00382-001-0206-8>>. 96

LAWRENCE, D.; VANDECAR, K. Effects of tropical deforestation on climate and agriculture. **Nature Climate Change**, v. 5, n. 1, p. 27–36, 2015. ISSN 17586798. 27

LEE, R. W. **Storm track biases and changes in a warming climate from an extratropical cyclone perspective using CMIP5**. PhD Thesis (PhD) — University of Reading, Reading, 2014. 14, 196

LEVINE, X. J.; SCHNEIDER, T. Baroclinic eddies and the extent of the Hadley Circulation: an idealized GCM study. **Journal of the Atmospheric Sciences**, v. 72, n. 7, p. 2744–2761, jul 2015. ISSN 0022-4928. Available from: <<http://journals.ametsoc.org/doi/10.1175/JAS-D-14-0152.1>>. 2, 20

LEVIS, S. Modeling vegetation and land use in models of the Earth System. **Wiley Interdisciplinary Reviews: Climate Change**, v. 1, n. 6, p. 840–856, nov 2010. ISSN 17577780. Available from: <<http://doi.wiley.com/10.1002/wcc.83>>. 25

LIMA, M. V. **Avaliação do sistema de previsão de tempo global por conjunto do CPTEC na previsão de ciclones no sul da América do Sul**. Dissertação (Mestrado em Meteorologia) - Instituto Nacional de Pesquisas Espaciais, São José dos Campos, 2011. 89 p. 45

LIN, J. L.; QIAN, T.; SHINODA, T. Stratocumulus clouds in Southeastern Pacific simulated by eight CMIP5-CFMIP global climate models. **Journal of Climate**, v. 27, n. 8, p. 3000–3022, 2014. ISSN 08948755. 85

LOON, H. van. A climatological Study of the Atmospheric Circulation in the Southern Hemisphere during the IGY, Part I: 1 July 1957-31 March 1958. **Journal of Applied Meteorology**, v. 4, n. 4, p. 479–491, aug 1965. ISSN 0021-8952. Available from: <[http://journals.ametsoc.org/doi/abs/10.1175/1520-0450\(1965\)004{ }3C0479:ACSOTA{ }3E2.O.CO;2](http://journals.ametsoc.org/doi/abs/10.1175/1520-0450(1965)004{ }3C0479:ACSOTA{ }3E2.O.CO;2)>. 10

\_\_\_\_\_. **The Half-Yearly Oscillations in Middle and High Southern Latitudes and the Coreless Winter**. 1967. 472–486 p. 45

LORENZ, D. J.; DEWEAVER, E. T. Tropopause height and zonal wind response to global warming in the IPCC scenario integrations. **Journal of Geophysical Research Atmospheres**, v. 112, n. 10, p. 1–11, 2007. ISSN 01480227. 19, 197, 208

LORENZ, E. N. Available potential energy and the maintenance of the general circulation. **Tellus**, v. 7, n. 2, p. 157–167, may 1955. ISSN 00402826. Available from: <<http://doi.wiley.com/10.1111/j.1469-1809.1958.tb01442.xhttp://tellusa.net/index.php/tellusa/article/view/8796>>. 9

LU, J.; CHEN, G.; FRIERSON, D. M. W. The Position of the midlatitude Storm Track and Eddy-driven westerlies in aquaplanet AGCMs. **Journal of the Atmospheric Sciences**, v. 67, n. 12, p. 3984–4000, 2010. ISSN 0022-4928. 20, 197

MAGRIN, G.; MARENGO, J.; Boulanger, J.-P. Buckeridge, M.; CASTELLANOS, E.; POVEDA, G.; SCARANO, F.; VICUÑA, S. Central and South America. In: Climate Change 2014: Impacts, Adaptation, and Vulnerability. Part B: Regional Aspects. Contribution of Working Group II to the Fifth Assessment Report of the Intergovernmental Panel on Climate Change. **Climate Change 2014: Impacts, Adaptation, Vulnerability. Part B: Regional Aspects. Contribution of Working Group II to the Fifth Assessment Report of the Intergovernmental Panel on Climate Change**, p. 1499–1566, 2014. Available from: <[http://ipcc.ch/pdf/assessment-report/ar5/wg2/WGIIAR5-Chap27\\_{\\_}FINAL.pdf](http://ipcc.ch/pdf/assessment-report/ar5/wg2/WGIIAR5-Chap27_{_}FINAL.pdf)>. 26

MANABE, S.; SMAGORINSKY, J.; STRICKLER, R. F. SIMULATED CLIMATOLOGY OF A GENERAL CIRCULATION MODEL WITH A HYDROLOGIC CYCLE 1. **Monthly Weather Review**, v. 93, n. 12, p. 769–798, 1965. ISSN 0027-0644. Available from: <<http://journals.ametsoc.org/doi/abs/10.1175/1520-0493{ }281965{ }29093{ }3C0769{ }3ASCOAGC{ }3E2.3.CO{ }3B2>>. 25

MARENGO, J. A.; ESPINOZA, J. C. Extreme seasonal droughts and floods in Amazonia: causes, trends and impacts. **International Journal of Climatology**, v. 36, n. 3, p. 1033–1050, mar 2016. ISSN 08998418. Available from: <<http://doi.wiley.com/10.1002/joc.4420>>. 26

MARENGO, J. A.; SOARES, W. R.; SAULO, C.; NICOLINI, M. Climatology of the low-level jet east of the Andes as derived from the NCEP-NCAR reanalyses:

characteristics and temporal variability. **Journal of Climate**, v. 17, n. 12, p. 2261–2280, 2004. ISSN 08948755. 59, 192

MARENGO, J. A.; SOUZA, C. M.; THONICKE, K.; BURTON, C.; HALLADAY, K.; BETTS, R. A.; ALVES, L. M.; SOARES, W. R. Changes in climate and land use over the Amazon region: current and future variability and trends. **Frontiers in Earth Science**, v. 6, n. December, p. 1–21, 2018. 26, 27

MARTIN, G. M. et al. The HadGEM2 family of Met Office Unified Model climate configurations. **Geoscientific Model Development**, v. 4, n. 3, p. 723–757, 2011. ISSN 1991959X. 33, 200

MBENGUE, C.; SCHNEIDER, T. Storm-Track shifts under climate change: toward a mechanistic understanding using Baroclinic Mean Available Potential Energy. **Journal of the Atmospheric Sciences**, v. 74, n. 1, p. 93–110, jan 2017. ISSN 0022-4928. 2, 20

MCCONNELL, W. Meeting in the middle: the challenge of meso-level integration. **Land Use Policy**, v. 19, p. 99–101, 2002. ISSN 02648377. 25

MCLANDRESS, C.; SHEPHERD, T. G.; POLAVARAPU, S.; BEAGLEY, S. R. Is missing orographic gravity wave drag near 60°S the cause of the stratospheric zonal wind biases in chemistry-climate models? **Journal of the Atmospheric Sciences**, v. 69, n. 3, p. 802–818, 2011. ISSN 0022-4928. 86

MEADOWS, D.; WRIGHT, D. **Thinking in systems: a primer**. [S.l.]: Chelsea Green Publishing, 2008. ISBN 9781603581486. 16

MEINSHAUSEN, M.; SMITH, S. J.; CALVIN, K.; DANIEL, J. S.; KAINUMA, M. L.; LAMARQUE, J.; MATSUMOTO, K.; MONTZKA, S. A.; RAPER, S. C.; RIAHI, K.; THOMSON, A.; VELDERS, G. J.; VUUREN, D. P. van. The RCP greenhouse gas concentrations and their extensions from 1765 to 2300. **Climatic Change**, v. 109, n. 1, p. 213–241, 2011. ISSN 01650009. 38

MENDES, D.; SOUZA, E. P.; MARENGO, J. A.; MENDES, M. C. D. Climatology of extratropical cyclones over the South American-southern oceans sector. **Theoretical and Applied Climatology**, v. 100, n. 3-4, p. 239–250, may 2010. ISSN 0177-798X. Available from:

<<http://link.springer.com/10.1007/s00704-009-0161-6>>. 13

METOFFICE. **Met Office delivers new climate simulations to international modelling activity.** 2015. 1 p. Available from: <<http://www.metoffice.gov.uk/research/news/cmip5>>. 34

MEYER, W. B.; TURNER, B. L. **Changes in land use and land cover: a global perspective.** [S.l.]: Cambridge University Press, 1994. (Global Change Institute: Office for Interdisciplinary Earth Studies Global Change Institute). ISBN 9780521470858. 25

MO, K. C.; WHITE, G. H. Teleconnections in the Southern Hemisphere. **Monthly Weather Review**, v. 113, n. 1, p. 22–37, jan 1984. ISSN 0027-0644. Available from: <[http://journals.ametsoc.org/doi/abs/10.1175/1520-0493\(2015\)29113\(3C0022\)3ATITSH\(3E2.0.CO;3B2](http://journals.ametsoc.org/doi/abs/10.1175/1520-0493(2015)29113(3C0022)3ATITSH(3E2.0.CO;3B2)>. 199

MOSS, R. H.; EDMONDS, J. A.; HIBBARD, K. A.; MANNING, M. R.; ROSE, S. K.; VUUREN, D. P. van; CARTER, T. R.; EMORI, S.; KAINUMA, M.; KRAM, T.; MEEHL, G. A.; MITCHELL, J. F. B.; NAKICENOVIC, N.; RIAHI, K.; SMITH, S. J.; STOUFFER, R. J.; THOMSON, A. M.; WEYANT, J. P.; WILBANKS, T. J. The next generation of scenarios for climate change research and assessment. **Nature**, v. 463, n. 7282, p. 747–756, feb 2010. ISSN 0028-0836. Available from: <<http://www.ncbi.nlm.nih.gov/pubmed/20148028http://www.nature.com/doi/10.1038/nature08823>>. 40, 101

MOSS, R. H. et al. **Towards new scenarios for analysis of emissions, climate change, impacts.**, [S.l.], 2007. 40

MURRAY, R. J.; SIMMONDS, I. A numerical scheme for tracking cyclone centres from digital data. Part I: development and operation of the scheme. **Australian Meteorological Magazine**, v. 39, n. 3, p. 155–166, 1991. ISSN 0894-8755. Available from: <<http://www.bom.gov.au/amoj/docs/1991/murray1.pdf>>. 8, 28

NAKAMURA, H.; SHIMPO, A. Seasonal variations in the Southern Hemisphere storm tracks and jet streams as revealed in a reanalysis dataset. **Journal of Climate**, v. 17, n. 9, p. 1828–1844, 2004. ISSN 08948755. 12, 73

NAKAMURA, M. Impacts of SST anomalies in the Agulhas current system on the regional climate variability. **Journal of Climate**, v. 25, n. 4, p. 1213–1229, feb 2012. ISSN 0894-8755. Available from: <<http://journals.ametsoc.org/doi/abs/10.1175/JCLI-D-11-00088.1>>. 74

- NOBRE, A. **The Future Climate of Amazonia Scientific Assessment Report**. 1. ed. São José dos Campos: Articulação Regional Amazônica, 2014. 42 p. ISBN 9788517000744. 26
- NOBRE, C. A.; SAMPAIO, G.; BORMA, L. S.; CASTILLA-RUBIO, J. C.; SILVA, J. S.; CARDOSO, M. Land-use and climate change risks in the Amazon and the need of a novel sustainable development paradigm. **Proceedings of the National Academy of Sciences**, v. 113, n. 39, p. 10759–10768, 2016. ISSN 0027-8424. Available from: <http://www.pnas.org/lookup/doi/10.1073/pnas.1605516113>. 26, 27
- NOBRE, C. A.; SELLERS, P. J.; SHUKLA, J. Amazonian deforestation and regional climate change. **Journal of Climate**, v. 4, n. 10, p. 957–988, oct 1991. ISSN 0894-8755. Available from: [http://journals.ametsoc.org/doi/abs/10.1175/1520-0442\(1991\)29004\(1991\)3C0957\(1991\)3AADARCC\(1991\)3E2.0.CO\(1991\)3B2](http://journals.ametsoc.org/doi/abs/10.1175/1520-0442(1991)29004(1991)3C0957(1991)3AADARCC(1991)3E2.0.CO(1991)3B2). 26, 27, 168, 169
- OLIVEIRA, J. T. S. **Extratropical transition of subtropical cyclones over the southwestern atlantic ocean**. PhD Thesis (Tese de Doutorado) — Instituto Nacional de Pesquisas Espaciais, São José dos Campos, 2019. 45
- O'REILLY, C. H.; CZAJA, A. The response of the Pacific storm track and atmospheric circulation to Kuroshio Extension variability. **Quarterly Journal of the Royal Meteorological Society**, v. 141, n. 686, p. 52–66, jan 2015. ISSN 00359009. Available from: <http://doi.wiley.com/10.1002/qj.2334>. 74
- ORLANSKI, I. What controls recent changes in the circulation of the southern hemisphere: polar stratospheric or equatorial surface temperatures? **Atmospheric and Climate Sciences**, v. 03, n. 04, p. 497–509, 2013. ISSN 2160-0414. 20
- ORLANSKI, I.; CHANG, E. K. M. Ageostrophic geopotential fluxes in downstream and upstream development of baroclinic waves. **Journal of the Atmospheric Sciences**, v. 50, n. 2, p. 212–225, 1993. ISSN 0022-4928. 9
- OYAMA, M. D.; NOBRE, C. A. A new climate-vegetation equilibrium state for Tropical South America. **Geophysical Research Letters**, v. 30, n. 23, p. 10–13, 2003. ISSN 00948276. 168
- PALMER, J. R.; TOTTERDELL, I. J. Production and export in a global ocean ecosystem model. **Deep-Sea Research Part I: Oceanographic Research Papers**, v. 48, n. 5, p. 1169–1198, 2001. ISSN 09670637. 32

PARISE, C. K. **Sensitivity and memory of the current mean climate to increased Antarctic sea ice: The role of sea ice dynamics**. PhD Thesis (Tese de Doutorado) — Instituto Nacional de Pesquisas Espaciais, São José dos Campos, 2014. 45

PARISE, C. K.; CALLIARI, L. J.; KRUSCHE, N. Extreme storm surges in the south of Brazil: Atmospheric conditions and shore erosion. **Brazilian Journal of Oceanography**, v. 57, n. 3, p. 175–188, 2009. ISSN 16798759. 1

PIELKE, R. A.; PITMAN, A.; NIYOGI, D.; MAHMOOD, R.; MCALPINE, C.; HOSSAIN, F.; GOLDEWIJK, K. K.; NAIR, U.; BETTS, R.; FALL, S.; REICHSTEIN, M.; KABAT, P.; NOBLET, N. de. Land use/land cover changes and climate: modeling analysis and observational evidence. **Wiley Interdisciplinary Reviews: Climate Change**, v. 2, n. 6, p. 828–850, nov 2011. ISSN 17577780. Available from: <<http://doi.wiley.com/10.1002/wcc.144>>. 15

PINHEIRO, H. R. **Validação do método TRACK para identificação objetiva dos vórtices ciclônicos de altos níveis em regiões subtropicais**. Dissertação (Mestrado em Meteorologia) - Instituto Nacional de Pesquisas Espaciais, São José dos Campos, 2010. 45

PINHEIRO, H. R. **Cut-off lows in the Southern Hemisphere: climatology, structure and energetics**. PhD Thesis (Tese de Doutorado) — Instituto Nacional de Pesquisas Espaciais, São José dos Campos, 2018. 45

PIRES, G. F.; COSTA, M. H. Deforestation causes different subregional effects on the Amazon bioclimatic equilibrium. **Geophysical Research Letters**, v. 40, n. 14, p. 3618–3623, 2013. ISSN 00948276. 27

PITMAN, A. J.; LORENZ, R. Scale dependence of the simulated impact of Amazonian deforestation on regional climate. **Environmental Research Letters**, v. 11, n. 9, 2016. ISSN 17489326. 168

PITMAN, A. J. et al. Uncertainties in climate responses to past land cover change: First results from the LUCID intercomparison study. **Geophysical Research Letters**, v. 36, 2009. ISSN 00948276. 23

POWER, S.; CASEY, T.; FOLLAND, C.; COLMAN, A.; MEHTA, V. Inter-decadal modulation of the impact of ENSO on Australia. **Climate Dynamics**, v. 15, n. 5, p. 319–324, 1999. ISSN 09307575. 38

RAIBLE, C. C. On the relation between extremes of midlatitude cyclones and the atmospheric circulation using ERA40. **Geophysical Research Letters**, v. 34, n. 7, p. 1–6, 2007. ISSN 00948276. 20, 197

RAO, V. B.; CARMO, a. M. C. do; FRANCHITO, S. H. Seasonal variations in the Southern Hemisphere Storm Tracks and associated wave propagation. **Journal of the Atmospheric Sciences**, v. 59, n. 6, p. 1029–1040, 2002. ISSN 0022-4928. 10, 11, 12, 73, 81

REBOITA, M. S.; ROCHA, R. P. da; AMBRIZZI, T.; CAETANO, E. An assessment of the latent and sensible heat flux on the simulated regional climate over Southwestern South Atlantic Ocean. **Climate Dynamics**, v. 34, n. 6, p. 873–889, 2010. ISSN 09307575. 14

REBOITA, M. S.; ROCHA, R. P. da; AMBRIZZI, T.; SUGAHARA, S. South Atlantic Ocean cyclogenesis climatology simulated by regional climate model (RegCM3). **Climate Dynamics**, v. 35, n. 7, p. 1331–1347, dec 2010. ISSN 09307575. Available from:

<<http://dx.doi.org/10.1007/s00382-009-0668-7><http://link.springer.com/10.1007/s00382-009-0668-7>>. 54

REBOITA, M. S.; ROCHA, R. P. da; SOUZA, M. R. de; LLOPART, M. Extratropical cyclones over the southwestern South Atlantic Ocean: HadGEM2-ES and RegCM4 projections. **International Journal of Climatology**, v. 38, n. 6, p. 2866–2879, 2018. ISSN 10970088. 14, 196

RIAHI, K.; GRÜBLER, A.; NAKICENOVIC, N. Scenarios of long-term socio-economic and environmental development under climate stabilization. **Technological Forecasting and Social Change**, v. 74, p. 887–935, 2007. ISSN 00401625. 22

RIENECKER, M. M.; SUAREZ, M. J.; GELARO, R.; TODLING, R.; BACMEISTER, J.; LIU, E.; BOSILOVICH, M. G.; SCHUBERT, S. D.; TAKACS, L.; KIM, G.-K.; BLOOM, S.; CHEN, J.; COLLINS, D.; CONATY, A.; SILVA, A. da; GU, W.; JOINER, J.; KOSTER, R. D.; LUCCHESI, R.; MOLOD, A.; OWENS, T.; PAWSON, S.; PEGION, P.; REDDER, C. R.; REICHLE, R.; ROBERTSON, F. R.; RUDDICK, A. G.; SIENKIEWICZ, M.; WOOLLEN, J. MERRA: NASA's Modern-Era Retrospective Analysis for Research and Applications. **Journal of Climate**, v. 24, n. 14, p. 3624–3648, jul 2011. ISSN 0894-8755. Available from:

<<http://journals.ametsoc.org/doi/abs/10.1175/JCLI-D-11-00015.1>>. 53

RIVIÈRE, G. A dynamical interpretation of the poleward shift of the jet streams in global warming scenarios. **Journal of the Atmospheric Sciences**, v. 68, n. 6, p. 1253–1272, jun 2011. ISSN 0022-4928. 81

ROBINSON, W. A. Dissipation dependence of the jet latitude. **Journal of Climate**, v. 10, n. 2, p. 176–182, 1997. ISSN 08948755. 86

ROECKNER, E.; BROKOPF, R.; ESCH, M.; GIORGETTA, M.; HAGEMANN, S.; KORNBLUEH, L.; MANZINI, E.; SCHLESE, U.; SCHULZWEIDA, U. Sensitivity of simulated climate to horizontal and vertical resolution in the ECHAM5 atmosphere model. **Journal of Climate**, v. 19, n. 16, p. 3771–3791, aug 2006. ISSN 0894-8755. Available from:  
<<http://journals.ametsoc.org/doi/abs/10.1175/JCLI3824.1>>. 96

SAHA, S.; MOORTHI, S.; PAN, H. L.; WU, X.; WANG, J.; NADIGA, S.; TRIPP, P.; KISTLER, R.; WOOLLEN, J.; BEHRINGER, D.; LIU, H.; STOKES, D.; GRUMBINE, R.; GAYNO, G.; WANG, J.; HOU, Y. T.; CHUANG, H. Y.; JUANG, H. M. H.; SELA, J.; IREDELL, M.; TREADON, R.; KLEIST, D.; Van Delst, P.; KEYSER, D.; DERBER, J.; EK, M.; MENG, J.; WEI, H.; YANG, R.; LORD, S.; Van Den Dool, H.; KUMAR, A.; WANG, W.; LONG, C.; CHELLIAH, M.; XUE, Y.; HUANG, B.; SCHEMM, J. K.; EBISUZAKI, W.; LIN, R.; XIE, P.; CHEN, M.; ZHOU, S.; HIGGINS, W.; ZOU, C. Z.; LIU, Q.; CHEN, Y.; HAN, Y.; CUCURULL, L.; REYNOLDS, R. W.; RUTLEDGE, G.; GOLDBERG, M. The NCEP climate forecast system reanalysis. **Bulletin of the American Meteorological Society**, v. 91, n. 8, p. 1015–1057, aug 2010. ISSN 00030007. Available from:

<<http://journals.ametsoc.org/doi/abs/10.1175/2010BAMS3001.1>>. 53

SALATI, E.; DALL’OLIO, A.; MATSUI, E.; GAT, J. R. Recycling of water in the Amazon Basin: an isotopic study. **Water Resources Research**, v. 15, n. 5, p. 1250–1258, oct 1979. ISSN 00431397. Available from:

<<http://doi.wiley.com/10.1029/WR015i005p01250>>. 26

SAMPAIO, G.; NOBRE, C.; COSTA, M. H.; SATYAMURTY, P.; SOARES-FILHO, B. S.; CARDOSO, M. Regional climate change over eastern Amazonia caused by pasture and soybean cropland expansion. **Geophysical Research Letters**, v. 34, n. 17, 2007. ISSN 00948276. 27, 168, 169

SAWYER, J. S. Observational characteristics of atmospheric fluctuations with a time scale of a month. **Quarterly Journal of the Royal Meteorological**

**Society**, v. 96, n. 410, p. 610–625, oct 1970. ISSN 00359009. Available from: <<http://doi.wiley.com/10.1002/qj.49709641005>>. 7, 8, 28

SELLERS, P. J.; BOUNOUA, L.; COLLATZ, G. J.; RANDALL, D. A.; DAZLICH, D. A.; LOS, S. O.; BERRY, J. A.; FUNG, I.; TUCKER, C. J.; FIELD, C. B.; JENSEN, T. G. Comparison of radiative and physiological effects of doubled atmospheric CO<sub>2</sub> on climate. **Science**, v. 271, n. 5254, p. 1402–1406, 1996. ISSN 00368075. 25

SELUCHI, M. E. Diagnostico y prognostico de situaciones sinopticas conducentes a desarrollos ciclónicos sobre el este de Suamérica. **Geofísica Internacional**, v. 34, p. 171–186, 1995. 10

SHAW, T. A. On the role of planetary-scale waves in the abrupt seasonal transition of the Northern Hemisphere general circulation. **Journal of the Atmospheric Sciences**, v. 71, n. 5, p. 1724–1746, 2013. ISSN 0022-4928. 60, 204

SHAW, T. A.; BALDWIN, M.; BARNES, E. A.; CABALLERO, R.; GARFINKEL, C. I.; HWANG, Y.-T.; LI, C.; O’GORMAN, P. A.; RIVIÈRE, G.; SIMPSON, I. R.; VOIGT, A. Storm track processes and the opposing influences of climate change. **Nature Geoscience**, v. 9, p. 656–665, 2016. ISSN 1752-0894. Available from: <<http://www.nature.com/doi/10.1038/ngeo2783>>. 14, 19

SHIMIZU, M. H.; CAVALCANTI, I. F. d. A. Variability patterns of Rossby wave source. **Climate Dynamics**, v. 37, n. 3-4, p. 441–454, aug 2011. ISSN 0930-7575. Available from: <<http://link.springer.com/10.1007/s00382-010-0841-z>>. 82

SILVA DIAS, M. A. F.; DIAS, J.; CARVALHO, L. M. V.; FREITAS, E. D.; SILVA DIAS, P. L. Changes in extreme daily rainfall for São Paulo, Brazil. **Climatic Change**, v. 116, n. 3-4, p. 705–722, 2013. ISSN 01650009. 1

SILVA, L. D. **Storm-Track na America do Sul e Vizinhanças: Climatologia, Variabilidade e Mudanças Climáticas**. Dissertação (Mestrado em Meteorologia) - Instituto Nacional de Pesquisas Espaciais, São José dos Campos, 2010. 14, 45, 53

SIMMONDS, I.; BURKE, C.; KEAY, K. Arctic climate change as manifest in cyclone behavior. **Journal of Climate**, v. 21, n. 22, p. 5777–5796, 2008. ISSN 08948755. 8, 28

SIMMONDS, I.; KEAY, K. Mean southern hemisphere extratropical cyclone behavior in the 40-year NCEP-NCAR reanalysis. **Journal of Climate**, v. 13, n. 5, p. 873–885, 2000. ISSN 08948755. 1

SIMPSON, I. R.; HITCHCOCK, P.; SHEPHERD, T. G.; SCINOCCA, J. F. Southern Annular Mode dynamics in observations and models. Part I: the influence of climatological zonal wind biases in a comprehensive GCM. **Journal of Climate**, v. 26, n. 11, p. 3953–3967, 2013. ISSN 0894-8755. 72, 82, 85

SIMPSON, I. R.; SHEPHERD, T. G.; HITCHCOCK, P.; SCINOCCA, J. F. Southern Annular Mode dynamics in observations and models. Part II: Eddy feedbacks. **Journal of Climate**, v. 26, n. 14, p. 5220–5241, 2013. ISSN 0894-8755. 82

SINCLAIR, M. R. An objective cyclone climatology for the Southern Hemisphere. **Monthly Weather Review**, v. 122, n. 10, p. 2239–2256, oct 1994. ISSN 0027-0644. Available from: <[http://journals.ametsoc.org/doi/abs/10.1175/1520-0493\(1994\)122{%-}3C2239:A0CCFT{%-}3E2.O.CO;2](http://journals.ametsoc.org/doi/abs/10.1175/1520-0493(1994)122{%-}3C2239:A0CCFT{%-}3E2.O.CO;2)>. 96

\_\_\_\_\_. A climatology of cyclogenesis for the Southern Hemisphere. **Monthly Weather Review**, v. 123, n. 6, p. 1601–1619, jun 1995. ISSN 0027-0644. 2, 96

\_\_\_\_\_. Objective identification of cyclones and their circulation intensity, and climatology. **Weather and Forecasting**, v. 12, n. 3, p. 595–612, 1997. ISSN 0882-8156. 1, 8, 28, 96

SMITH, P.; GREGORY, P. J.; VUUREN, D. van; OBERSTEINER, M.; HAVLÍK, P.; ROUNSEVELL, M.; WOODS, J.; STEHFEST, E.; BELLARBY, J. Competition for land. **Philosophical transactions of the Royal Society of London. Series B, Biological sciences**, v. 365, p. 2941–2957, 2010. ISSN 0962-8436. 22, 23

SPRACKLEN, D. V.; GARCIA-CARRERAS, L. The impact of Amazonian deforestation on Amazon basin rainfall. **Geophysical Research Letters**, v. 42, n. 21, p. 9546–9552, nov 2015. ISSN 00948276. Available from: <<http://doi.wiley.com/10.1002/2015GL066063>>. 27

SPRENGER, M.; MARTIUS, O.; ARNOLD, J. Cold surge episodes over southeastern Brazil - a potential vorticity perspective. **International Journal of Climatology**, v. 33, n. 12, p. 2758–2767, 2013. ISSN 08998418. 1

STRETEN, N. A.; TROUP, A. J. A synoptic climatology of satellite observed cloud vortices over the Southern Hemisphere. **Quarterly Journal of the Royal Meteorological Society**, v. 99, n. 419, p. 56–72, jan 1973. ISSN 00359009.

Available from: <<http://doi.wiley.com/10.1002/qj.49709941906>>. 11

SUD, Y. C.; SHUKLA, J.; MINTZ, Y. **Influence of land surface roughness on atmospheric circulation and precipitation: a sensitivity study with a General Circulation Model**. 1988. 1036–1054 p. 168

SUN, L.; CHEN, G.; ROBINSON, W. A. The role of stratospheric polar vortex breakdown in Southern Hemisphere climate trends. **Journal of the Atmospheric Sciences**, v. 71, n. 7, p. 2335–2353, jul 2014. ISSN 0022-4928. Available from: <<http://journals.ametsoc.org/doi/abs/10.1175/JAS-D-13-0290.1>>. 20, 82

TALJAARD, J. J. Synoptic meteorology of the southern hemisphere. In: NEWTON, C. W. (Ed.). **Meteorology of the Southern Hemisphere**. Boston: American Meteorological Society, 1972. chapter 35, p. 263. 1, 11, 59, 73, 96

TAMARIN, T.; KASPI, Y. Mechanisms controlling the downstream poleward deflection of midlatitude Storm Tracks. **Journal of the Atmospheric Sciences**, v. 74, n. 2, p. 553–572, 2017. ISSN 0022-4928. Available from: <<http://journals.ametsoc.org/doi/10.1175/JAS-D-16-0122.1>>. 62

TANDON, N. F.; GERBER, E. P.; SOBEL, A. H.; POLVANI, L. M. Understanding Hadley Cell expansion versus contraction: insights from simplified models and implications for recent observations. **Journal of Climate**, v. 26, n. 12, p. 4304–4321, 2013. ISSN 08948755. 128

TAYLOR, K. E.; STOUFFER, R. J.; MEEHL, G. A. An overview of CMIP5 and the experiment design. **Bulletin of the American Meteorological Society**, v. 93, p. 485–498, 2012. ISSN 00030007. 33, 39, 40

TORRES, R. R. **Análise de incertezas em projeções de mudanças climáticas na América do Sul**. PhD Thesis (Tese de Doutorado) — Instituto Nacional de Pesquisas Espaciais, São José dos Campos, 2014. Available from: <[sid.inpe.br/mtc-m19/2014/01.13.12.37-TDI](http://sid.inpe.br/mtc-m19/2014/01.13.12.37-TDI)>. 27, 167

TORRES, R. R.; LAPOLA, D. M.; MARENGO, J. A.; LOMBARDO, M. A. Socio-climatic hotspots in Brazil. **Climatic Change**, v. 115, n. 3-4, p. 597–609, 2012. ISSN 01650009. 27

TRENBERTH, K. E. Storm Tracks in the Southern Hemisphere. **Journal of the Atmospheric Sciences**, v. 48, n. 19, p. 2159–2178, 1991. ISSN 0022-4928. 2, 9, 11

ULBRICH, U.; LECKEBUSCH, G. C.; GRIEGER, J.; SCHUSTER, M.; AKPEROV, M.; BARDIN, M. Y.; FENG, Y.; GULEV, S.; INATSU, M.; KEAY, K.; KEW, S. F.; LIBERATO, M. L.; LIONELLO, P.; MOKHOV, I. I.; NEU, U.; PINTO, J. G.; RAIBLE, C. C.; REALE, M.; RUDEVA, I.; SIMMONDS, I.; TILININA, N. D.; TRIGO, I. F.; ULBRICH, S.; WANG, X. L.; WERNLI, H. Are greenhouse gas signals of Northern Hemisphere winter extra-tropical cyclone activity dependent on the identification and tracking algorithm? **Meteorologische Zeitschrift**, v. 22, n. 1, p. 61–68, 2013. ISSN 09412948. 49

ULBRICH, U.; LECKEBUSCH, G. C.; PINTO, J. G. Extra-tropical cyclones in the present and future climate: a review. **Theoretical and Applied Climatology**, v. 96, n. 1-2, p. 117–131, apr 2009. ISSN 0177-798X. Available from: <<http://link.springer.com/10.1007/s00704-008-0083-8>>. 1, 98, 99

UMMENHOFER, C. C.; MCINTOSH, P. C.; POOK, M. J.; RISBEY, J. S. Impact of surface forcing on southern hemisphere atmospheric blocking in the Australia-New Zealand sector. **Journal of Climate**, v. 26, n. 21, p. 8476–8494, 2013. ISSN 08948755. 83

UPPALA, S. M.; KALLBERG, P. W.; SIMMONS, A. J.; ANDRAE, U.; BECHTOLD, V. D. C.; FIORINO, M.; GIBSON, J. K.; HASELER, J.; HERNANDEZ, A.; KELLY, G. A.; LI, X.; ONOGI, K.; SAARINEN, S.; SOKKA, N.; ALLAN, R. P.; ANDERSSON, E.; ARPE, K.; BALMASEDA, M. A.; BELJAARS, A. C. M.; BERG, L. V. D.; BIDLOT, J.; BORMANN, N.; CAIRES, S.; CHEVALLIER, F.; DETHOF, A.; DRAGOSAVAC, M.; FISHER, M.; FUENTES, M.; HAGEMANN, S.; HÓLM, E.; HOSKINS, B. J.; ISAKSEN, L.; JANSSEN, P. A. E. M.; JENNE, R.; MCNALLY, A. P.; MAHFOUF, J.-F.; MORCRETTE, J.-J.; RAYNER, N. A.; SAUNDERS, R. W.; SIMON, P.; STERL, A.; TRENBERTH, K. E.; UNTCH, A.; VASILJEVIC, D.; VITERBO, P.; WOOLLEN, J. The ERA-40 re-analysis. **Quarterly Journal of the Royal Meteorological Society**, v. 131, n. 612, p. 2961–3012, oct 2005. ISSN 00359009. Available from: <<http://doi.wiley.com/10.1256/qj.04.176>>. 43, 53

VASCONCELLOS, F. C. **A Oscilacao Antartica - Mecanismos Fisicos e Relacao com Caracteristicas Atmosfericas sobre a America do Sul /Oceanos Adjacentes**. PhD Thesis (Tese de Doutorado) — Instituto Nacional de Pesquisas Espaciais, São José dos Campos, 2012. 82

VERA, C. Interannual and interdecadal variability of atmospheric synoptic-scale activity in the Southern Hemisphere. **Journal of Geophysical Research**, v. 108, n. C4, p. 8077, 2003. ISSN 0148-0227. Available from:

<<http://doi.wiley.com/10.1029/2000JC000406>>. 2

VUUREN, D. P. van; EDMONDS, J.; KAINUMA, M.; RIAHI, K.; THOMSON, A.; HIBBARD, K.; HURTT, G. C.; KRAM, T.; KREY, V.; LAMARQUE, J.-F.; MASUI, T.; MEINSHAUSEN, M.; NAKICENOVIC, N.; SMITH, S. J.; ROSE, S. K. The representative concentration pathways: an overview. **Climatic Change**, v. 109, n. 1-2, p. 5–31, nov 2011. ISSN 0165-0009. Available from:

<<http://link.springer.com/10.1007/s10584-011-0148-z>>. 3, 38, 101

VUUREN, D. P. van; ELZEN, M. G. J. den; LUCAS, P. L.; EICKHOUT, B.; STRENGERS, B. J.; RUIJVEN, B. van; WONINK, S.; HOUDT, R. van. Stabilizing greenhouse gas concentrations at low levels: an assessment of reduction strategies and costs. **Climatic Change**, v. 81, n. 2, p. 119–159, feb 2007. ISSN 0165-0009. Available from:

<<http://link.springer.com/10.1007/s10584-006-9172-9>>. 21

VUUREN, D. P. van; RIAHI, K. The relationship between short-term emissions and long-term concentration targets. **Climatic Change**, v. 104, n. 3-4, p. 793–801, dec 2011. ISSN 0165-0009. Available from:

<<http://link.springer.com/10.1007/s10584-010-0004-6>>. 20, 21, 23, 25

WALLACE, J. M.; BLACKMON, M. L. Observations of low-frequency atmospheric variability. **Large-scale Dynamical Processes in the Atmosphere**, p. 55–94, 1983. 8, 28

WILLISON, J.; ROBINSON, W. A.; LACKMANN, G. M. The Importance of Resolving Mesoscale Latent Heating in the North Atlantic Storm Track. **Journal of the Atmospheric Sciences**, v. 70, n. 7, p. 2234–2250, 2013. ISSN 0022-4928. 157

WISE, M.; CALVIN, K.; THOMSON, A.; CLARKE, L.; BOND-LAMBERTY, B.; SANDS, R.; SMITH, S. J.; JANETOS, A.; EDMONDS, J. Implications of limiting CO<sub>2</sub> concentrations for land use and energy. **Science**, v. 324, n. 5931, p. 1183–6, may 2009. ISSN 1095-9203. Available from:

<<http://www.ncbi.nlm.nih.gov/pubmed/19478180>>. 21

WOOLLINGS, T. Dynamical influences on European climate: an uncertain future. **Philosophical Transactions of the Royal Society A: Mathematical,**

**Physical and Engineering Sciences**, v. 368, n. 1924, p. 3733–3756, aug 2010. ISSN 1364-503X. Available from: <<http://rsta.royalsocietypublishing.org/cgi/doi/10.1098/rsta.2010.0040>>. 73

WOOLLINGS, T.; HOSKINS, B.; BLACKBURN, M.; HASSELL, D.; HODGES, K. Storm track sensitivity to sea surface temperature resolution in a regional atmosphere model. **Climate Dynamics**, v. 35, n. 2-3, p. 341–353, aug 2010. ISSN 0930-7575. Available from: <<http://link.springer.com/10.1007/s00382-009-0554-3>>. 74

YIN, J. H. A consistent poleward shift of the storm tracks in simulations of 21st century climate. **Geophysical Research Letters**, v. 32, n. 18, p. 1–4, 2005. ISSN 00948276. 105, 206

ZAPPA, G.; MASATO, G.; SHAFFREY, L.; WOOLLINGS, T.; HODGES, K. Linking Northern Hemisphere blocking and storm track biases in the CMIP5 climate models. **Geophysical Research Letters**, v. 41, n. 1, p. 135–139, jan 2014. ISSN 00948276. Available from: <<http://doi.wiley.com/10.1002/2013GL058480>>. 99

ZAPPA, G.; SHAFFREY, L. C.; HODGES, K. I. The ability of CMIP5 models to simulate North Atlantic Extratropical Cyclones. **Journal of Climate**, v. 26, n. 15, p. 5379–5396, aug 2013. ISSN 0894-8755. 99

ZAPPA, G.; SHAFFREY, L. C.; HODGES, K. I.; SANSOM, P. G.; STEPHENSON, D. B. A multimodel assessment of future projections of North Atlantic and European Extratropical Cyclones in the CMIP5 climate models. **Journal of Climate**, v. 26, n. 16, p. 5846–5862, aug 2013. ISSN 0894-8755. Available from: <<http://journals.ametsoc.org/doi/10.1175/JCLI-D-12-00573.1>>. 1

## APPENDIX A - ARTICLE

### Climate Dynamics

#### How well does the HadGEM2-ES Coupled Model represent the Southern Hemisphere Storm Tracks?

--Manuscript Draft--

<b>Manuscript Number:</b>	CLDY-D-19-00238	
<b>Full Title:</b>	How well does the HadGEM2-ES Coupled Model represent the Southern Hemisphere Storm Tracks?	
<b>Article Type:</b>	Original Article	
<b>Keywords:</b>	Cyclones; Storm Tracks; Climatology; HadGEM2-ES; ERA-Interim; Southern Hemisphere	
<b>Corresponding Author:</b>	Philipp Edson Dias da Silva, M.D. Center of Earth System Science (CCST), National Institute for Space Research (INPE) São José dos Campos, São Paulo BRAZIL	
<b>Corresponding Author Secondary Information:</b>		
<b>Corresponding Author's Institution:</b>	Center of Earth System Science (CCST), National Institute for Space Research (INPE)	
<b>Corresponding Author's Secondary Institution:</b>		
<b>First Author:</b>	Philipp Edson Dias da Silva, M.D.	
<b>First Author Secondary Information:</b>		
<b>Order of Authors:</b>	Philipp Edson Dias da Silva, M.D. Kevin Ivan Hodges, Ph.D Mariane Mendes Coutinho, Ph.D	
<b>Order of Authors Secondary Information:</b>		
<b>Funding Information:</b>	National Institute for Space Research (INPE)	Mr. Philipp Edson Dias da Silva
<b>Abstract:</b>	<p>This study presents an assessment of the ability of the Hadley Centre Global Environment Model version 2 - Earth system configuration (HadGEM2-ES) - in simulating the mid-latitude storm tracks over the Southern Hemisphere (SH). The storm tracks are primarily assessed using cyclone tracking using data from a 4 member ensemble of 27-year simulations of HadGEM2-ES over the historical period, and the European Centre for Medium-Range Weather Forecasts (ECMWF) Interim Reanalysis (ERA-Interim). Both winter and summer periods are considered and contrasted. Results show that the storm track (ST) climatology of HadGEM2-ES presents similar patterns to those of the reanalysis. However, the model tends to represent the austral winter ST position with an equatorward bias and a zonal bias in the spiral towards the pole. The main differences were found during the austral winter, with large track density biases over the Indian Ocean indicating a poor representation of the ST in this specific region. This was found to be related to two factors. First, the large negative genesis biases over South America, Antarctic Peninsula and the Antarctic coast. Second, the model resolution and the representation of the Andes Mountains in South America. The link between STs and the large-scale circulation is examined and shows at upper levels a large cold bias over the extratropical and Polar Regions, which is a result of the equatorward jet position bias of the subtropical jet and a negative bias in the eddy-driven. The analysis of the large-scale circulation shows that the split jet during winter has a problem in the model linked to these biases, including geopotential anomaly and sea surface temperature biases. As a consequence, in general the track densities over the Southern oceans are underestimated in the austral winter. During summer, the results show the STs move poleward and there is a single eddy-driven jet, which is represented relatively well compared with the winter situation. These factors tend to reduce the differences seen in the cyclone track distribution biases. Although the model has biases in the ST</p>	

Powered by Editorial Manager® and ProduXion Manager® from Aries Systems Corporation

	behavior in the SH it is still considered that these do not preclude this model being used for perturbation and future projection studies.
<b>Suggested Reviewers:</b>	<p>Michel Mesquita, Ph.D  Research Scientist, University of Bergen  Michel.Mesquita@uni.no  Dr. Mesquita is an important researcher in the area of interest, he has many publications on large-scale dynamics, including storm tracks, teleconnectivity, downscaling and climate modeling.</p>
	<p>Caroline Susana Vera, Ph.D  Professor/Researcher, University of Buenos Aires / Argentina National Council of Sciences (CONICET)  carolina@cima.fcen.uba.ar  Dr. Vera has long research experience on understanding, simulating and predicting climate variability and change mainly over southern hemisphere. She made important contributions about cyclone development.</p>
	<p>Manoel Alonso Gan, Ph.D  Senior Researcher, Instituto Nacional de Pesquisas Espaciais (INPE)  manoel.gan@inpe.br  Dr. Gan is pionner in the area of interest and made a lot of contributions for theory of cyclone development in the Andes Mountains region and synoptic meteorology. He has many publications and more than a thousand of citations.</p>
	<p>Jennifer Catto, Ph.D  Lecturer, University of Exeter  j.catto@exeter.ac.uk  Dr. Catto is a important researcher in the area of interest and have experience in southern hemisphere storm tracks. Actually Dr. Catto developed new methods to cyclone classification and she can contribute with a different point of view for the article.</p>

## **PUBLICAÇÕES TÉCNICO-CIENTÍFICAS EDITADAS PELO INPE**

### **Teses e Dissertações (TDI)**

Teses e Dissertações apresentadas nos Cursos de Pós-Graduação do INPE.

### **Manuais Técnicos (MAN)**

São publicações de caráter técnico que incluem normas, procedimentos, instruções e orientações.

### **Notas Técnico-Científicas (NTC)**

Incluem resultados preliminares de pesquisa, descrição de equipamentos, descrição e ou documentação de programas de computador, descrição de sistemas e experimentos, apresentação de testes, dados, atlas, e documentação de projetos de engenharia.

### **Relatórios de Pesquisa (RPQ)**

Reportam resultados ou progressos de pesquisas tanto de natureza técnica quanto científica, cujo nível seja compatível com o de uma publicação em periódico nacional ou internacional.

### **Propostas e Relatórios de Projetos (PRP)**

São propostas de projetos técnico-científicos e relatórios de acompanhamento de projetos, atividades e convênios.

### **Publicações Didáticas (PUD)**

Incluem apostilas, notas de aula e manuais didáticos.

### **Publicações Seriadas**

São os seriados técnico-científicos: boletins, periódicos, anuários e anais de eventos (simpósios e congressos). Constam destas publicações o Internacional Standard Serial Number (ISSN), que é um código único e definitivo para identificação de títulos de seriados.

### **Programas de Computador (PDC)**

São a seqüência de instruções ou códigos, expressos em uma linguagem de programação compilada ou interpretada, a ser executada por um computador para alcançar um determinado objetivo. Aceitam-se tanto programas fonte quanto os executáveis.

### **Pré-publicações (PRE)**

Todos os artigos publicados em periódicos, anais e como capítulos de livros.